From bulk to structural failure: fracture of hyperelastic materials

Dissertation

by

Philipp Laurens Rosendahl, M.Sc.

from Berlin

submitted in fulfillment of the requirements
for the degree of Doktor-Ingenieur (Dr.-Ing.)

**at the Department of Mechanical Engineering
of the Technical University of Darmstadt**

Examiner: Prof. Dr.-Ing. Wilfried Becker
Co-examiner: Prof. Dr.-Ing. Dr. h. c. mult. Holm Altenbach

Darmstadt 2020

Philipp Laurens Rosendahl
From bulk to structural failure: fracture of hyperelastic materials

Darmstadt, Technische Universität Darmstadt
Published online on TUprints in 2020
Date of oral exam: May 27, 2020

URN: urn:nbn:de:tuda-tuprints-86934
URL: https://tuprints.ulb.tu-darmstadt.de/8693

Preface

This dissertation is the result of my work as a doctoral student at the Institute of Structural Mechanics at Technische Universität Darmstadt. On this occasion I would like to thank everyone who contributed to the success of this work.

I would like to thank Prof. Dr.-Ing. Wilfried Becker for his support and promotion of my scientific work, and the freedom he has given me. I thank Prof. Dr.-Ing. Dr. h. c. mult. Holm Altenbach for his interest in my work and for reviewing this thesis.

Many thanks to all colleagues and friends in and outside the institute for exciting projects and good times in Darmstadt.

Abstract

Adhesive bonding is a versatile joining technology used across many industries and is capable of addressing very specific needs. For instance, structural silicone adhesives provide excellent properties for joining brittle and low-toughness materials such as glass. Silicones are soft, hyperelastic, often nearly incompressible, amorphous, cross-linked elastomers that transfer loads homogeneously and can compensate large deformation differences. They are not only used as fillers or sealings but as structural elements. Hence, they require accurate analysis and design tools, which are the subject of research to the present day.

Modeling fracture of nearly incompressible hyperelastic media is challenging for several reasons: different failure modes such as dilatational and distortional failure may occur, notches induce weak singularities with infinite stresses but vanishing energy release rates, the onset of interface cracks is a mixed-mode fracture problem and the nonlinear elastic constitutive behavior must be accounted for. The present work addresses all of these points using two exemplary hyperelastic silicones: DOWSIL™ 993 Structural Glazing Sealant and DOWSIL™ Transparent Structural Silicone Adhesive (TSSA).

For this purpose, the materials' constitutive behavior, their multiaxial bulk material failure properties and their fracture mechanical properties are identified from a large set of unnotched and notched samples. The constitutive behavior is described using models from literature. For the assessment of multiaxial bulk material failure, a generally applicable, phenomenological failure criterion describing a single, smooth and convex failure surface is proposed. Exploiting the properties of this criterion, a strain-based description of the bulk material failure of hyperelastic elastomers is derived. Extending the concept of finite fracture mechanics to nonlinear elasticity provides a physical model for notch-induced crack nucleation in hyperelastic materials and, hence, structural failure. A coupled strain and energy criterion that predicts crack nucleation when both a strain and an energy condition are met simultaneously is proposed. The failure model is validated using experiments on different hyperelastic adhesive joints.

Adhesive joints are often composed of thin and flat substrates bonded by thin adhesive layers across large surfaces. This particular geometry allows for treating the adhesive layer as an interface and permits the development of an easy-to-use and efficient stress and strain analysis model of the adhesive. The combination of this so-called weak

interface model with the above coupled strain and energy failure criterion provides a powerful design tool for thin hyperelastic adhesive joints.

Kurzfassung

Kleben ist eine vielseitige Fügetechnologie, die in vielen Branchen eingesetzt wird und sehr spezifische Anforderungen erfüllen kann. Beispielsweise sind Struktursilikonklebstoffe prädestiniert für die Verbindung von spröden Materialien mit geringem Bruchwiderstand, wie zum Beispiel Glas. Silikone sind weiche, hyperelastische, oft nahezu inkompressible, amorphe, vernetzte Elastomere, die Lasten vergleichmäßigen und große Verformungsunterschiede ausgleichen können. Sie stellen nicht nur Füllstoffe oder Dichtungen dar, sondern werden auch als tragende Verbindungen eingesetzt. Zur Auslegung solcher Verbindungen werden genaue Analyse- und Entwurfswerkzeuge benötigt, die bis heute Gegenstand der Forschung sind.

Die Modellierung des Versagens nahezu inkompressibler hyperelastischer Medien ist in vielerlei Hinsicht eine Herausforderung: Versagen kann durch Volumen- oder Formänderung auftreten, Kerben stellen schwache Spannungssingularitäten mit unendlich hohen Spannungsspitzen aber verschwindenden Energiefreisetzungsraten dar, Grenzflächenrisse entstehen unter gemischter Beanspruchung und das nichtlineare Materialverhalten ist zu berücksichtigen. Die vorliegende Arbeit widmet sich den genannten Punkten am Beispiel zweier hyperelastischer Silikone: DOWSIL™ 993 Structural Glazing Sealant und DOWSIL™ Transparent Structural Silicone Adhesive (TSSA).

Dazu werden das Konstitutivverhalten der Materialien, ihre Festigkeiten unter mehrachsiger Beanspruchung und ihre bruchmechanischen Eigenschaften anhand eines umfangreichen Satzes an Experimenten bestimmt. Materialgesetze werden mit Hilfe von Modellen aus der Literatur beschrieben. Zur Bewertung des mehrachsigen Versagensverhaltens wird ein allgemein anwendbares, phänomenologisches Versagenskriterium vorgeschlagen, das eine geschlossene, glatte und konvexe Versagensfläche beschreibt. Für hyperelastische Elastomere lässt sich von diesem Kriterium ein mehrachsiges dehnungsbasiertes Versagenskriterium ableiten. Die Erweiterung des Konzepts der finiten Bruchmechanik auf nichtlineare Elastizität liefert ein physikalisches Modell für die kerbeninduzierte Rissbildung in hyperelastischen Werkstoffen. Es wird ein gekoppeltes Dehnungs- und Energiekriterium vorgeschlagen, das Rissbildung erlaubt, wenn sowohl eine Dehnungs- als auch eine Energiebedingung gleichzeitig erfüllt sind. Das Versagensmodell wird durch Experimente an verschiedenen hyperelastischen Klebeverbindungen validiert.

Kurzfassung

Klebeverbindungen bestehen oft aus flachen, dünnen Fügeteilen, die durch dünne Klebeschichten über große Kontaktflächen verbunden sind. Diese spezielle Geometrie erlaubt es, die Klebeschicht als vereinfachtes Kontinuum zu behandeln und ein einfaches und effizientes Modell für die Spannungs- und Dehnungsanalyse des Klebstoffs zu entwickeln. Die Kombination dieses so genannten Weak-Interface-Modells mit dem zuvor eingeführten gekoppelten Dehnungs- und Energiekriterium stellt ein leistungsfähiges Entwurfswerkzeug für dünne hyperelastische Klebeverbindungen dar.

Table of contents

Nomenclature

Abbreviations

3PB	Three-point bending
993	DOWSIL™ 993 Structural Glazing Sealant
BT	Biaxial tension
CFRP	Carbon fiber reinforced composite
CT	Compact tension
CZM	Cohesive zone model
DCB	Double cantilever beam
DIC	Digital image correlation
DLJ	Double-lap joint
ELSJ	End-loaded shear joint
ENF	End-notched flexure
FEA	Finite element analysis
FEM	Finite element method
FFM	Finite fracture mechanics
FMC	Failure mode concept
FSDT	First-order shear deformation theory
ICM	Imaginary crack method
LM	Line method
MAZ	Modified Altenbach–Zolochevsky
NR	Natural rubber
ODCB	Out-of-plane double cantilever beam
PE	Polyethylene
PM	Point method
PTFE	Polytetrafluoroethylene
RDCB	Rigid double cantilever beam
RDF	Robust deviatoric function
SBR	Styrene–butadiene rubber
SD	Standard deviation
SED	Strain energy density
SLJ	Single-lap joint
TCD	Theory of critical distances

TDCB	Tapered double cantilever beam
TSSA	DOWSIL™ Transparent Structural Silicone Adhesive
UT	Uniaxial tension

Indices and notations

$\dot{\bigcirc}$	Time derivative
$\bigcirc'$	Derivative of a function of one variable
$\bigcirc^{\mathsf{T}}$	Transposed
$\bigcirc_{\times}$	Value at failure
$\bigcirc_{\parallel}$	Parallel
$\bigcirc_{\perp}$	Perpendicular
$\bigcirc_{0}$	Initial, with respect to the reference configuration
$\bigcirc_{\mathrm{c}}$	Critical
$\bigcirc_{\mathrm{con}}$	Heat conduction
$\bigcirc_{\mathrm{coup}}$	Coupling
$\bigcirc_{\mathrm{dev}}$	Deviatoric
$\bigcirc_{\mathrm{eq}}$	Equivalent
$\bigcirc_{\mathrm{ext}}$	External
$\bigcirc_{\mathrm{f}}$	Failure
$\bigcirc_{\mathrm{int}}$	Internal
$\bigcirc_{\mathrm{iso}}$	Isochoric (distortional)
$\bigcirc_{\mathrm{G}}$	Gaussian
$\bigcirc_{\mathrm{L}}$	Langevin
$\bigcirc_{\mathrm{n}}$	Normal
$\bigcirc_{\mathrm{p}}$	Plastic
$\bigcirc_{\mathrm{s}}$	Sliding
$\bigcirc_{\mathrm{sph}}$	Spherical
$\bigcirc_{\mathrm{t}}$	Tearing, prescribed tractions
$\bigcirc_{\mathrm{T}}$	Uniaxial tension
$\bigcirc_{\mathrm{u}}$	Prescribed displacements
$\bigcirc_{\mathrm{vol}}$	Volumetric (dilatational)
$\bigcirc_{\mathrm{y}}$	Yield

Latin symbols

a	Crack length
A	Surface area, constant
$\boldsymbol{A}$	Euler–Almansi strain tensor
Δa, ΔA	Finite crack length, surface area
b	Out-of-plane width

B	Constant
$\boldsymbol{B}, \bar{\boldsymbol{B}}$	Left Cauchy–Green strain tensor, modified (isochoric)
$\mathcal{B}$	Configuration
c, C	Constants
$\boldsymbol{C}, \bar{\boldsymbol{C}}$	Right Cauchy–Green strain tensor, modified (isochoric)
$\mathbb{C}$	Elasticity tensor
d, D	Constants
$\boldsymbol{D}$	Rate of deformation tensor
$\boldsymbol{e}$	Unit vector
E	Young's modulus
$\boldsymbol{E}$	Green–Lagrange strain tensor
$\boldsymbol{\mathcal{E}}$	Third-order permutation tensor
$\boldsymbol{f}$	Body force vector
F	Force
$\boldsymbol{F}, \bar{\boldsymbol{F}}$	Deformation gradient, modified (isochoric)
$\mathcal{G}$ ($\mathcal{G}_{\mathrm{I}}, \mathcal{G}_{\mathrm{II}}, \mathcal{G}_{\mathrm{III}}$)	Differential energy release rate (opening, sliding, tearing)
$\bar{\mathcal{G}}$ ($\bar{\mathcal{G}}_{\mathrm{I}}, \bar{\mathcal{G}}_{\mathrm{II}}, \bar{\mathcal{G}}_{\mathrm{III}}$)	Incremental energy release rate (opening, sliding, tearing)
$\mathcal{G}_{\mathrm{c}}$ ($\mathcal{G}_{\mathrm{Ic}}, \mathcal{G}_{\mathrm{IIc}}, \mathcal{G}_{\mathrm{IIIc}}$)	Fracture toughness (opening, sliding, tearing)
h	Height, thickness
I_y	Moment of inertia with respect to the y-axis
$I_{\boldsymbol{Y}}, II_{\boldsymbol{Y}}, III_{\boldsymbol{Y}}$	Principal scalar invariants of $\boldsymbol{Y}$
$I'_{\boldsymbol{Y}}, II'_{\boldsymbol{Y}}, III'_{\boldsymbol{Y}}$	Principal scalar invariants of the deviatoric part of $\boldsymbol{Y}$
$\boldsymbol{I}$	Identity matrix, unit tensor
J	Volume ratio, J-integral
k	Shear correction factor
$\mathrm{k_B}$	Boltzmann constant
K	Bulk modulus
$K_{\mathrm{I}}, K_{\mathrm{II}}, K_{\mathrm{II}}$	Mode I, II and III stress intensity factors
$K_{\mathrm{Ic}}, K_{\mathrm{IIc}}, K_{\mathrm{IIc}}$	Mode I, II and III fracture toughness
$\mathcal{K}$	Kinetic energy
l	Length
$\boldsymbol{l}$	Vector of angular momentum
L	Contour length
$\boldsymbol{L}$	Spatial velocity gradient
$\mathcal{L}$	Langevin function
m	Mass, coefficient of interaction
M	Section bending moment
n	Positive integer, number of chain segments
$\boldsymbol{n}$	Normal vector
N	Normal section force, positive integer

$\boldsymbol{p}$	Vector of linear momentum
P	Scalar load parameter
$\boldsymbol{P}$	First Piola–Kirchhoff stress tensor
$\mathcal{P}$	Mechanical power
$\boldsymbol{q}$	Heat flux vector
$\boldsymbol{Q}$	Orthogonal tensor
$\mathcal{Q}$	Thermal power
r	Radius, end-to-end distance, heat source per unit volume
$\boldsymbol{R}$	Proper orthogonal rotation tensor
$\boldsymbol{S}$	Second Piola–Kirchhoff stress tensor
u	Displacement, specific internal energy
$\boldsymbol{u}$	Displacement vector
$\boldsymbol{U}$	Right (material) stretch tensor
$\mathcal{U}$	Total internal energy
$\boldsymbol{v}$	Velocity vector
V	Transverse shear section force, volume
$\boldsymbol{V}$	Left (spatial) stretch tensor
w	Out-of-plane width, deflection
W	Mechanical work
$\boldsymbol{W}$	Spin tensor
$\mathcal{W}$	Strain energy density potential
$\boldsymbol{x}$	Spatial (Eulerian) coordinates
$\boldsymbol{X}$	Material (Lagrangian) coordinates
s	Specific entropy
t	Time, adhesive thickness
$\boldsymbol{t}$	Cauchy (true) traction vector
$\boldsymbol{t}_0$	First Piola–Kirchhoff (nominal) traction vector
T	Absolute temperature

Greek symbols

α	Constant, shape parameter
β	Constant, shape parameter
γ	Shear strain, constant, shape parameter
Γ	Energy dissipation, boundary
δ	Crack tip opening displacement
ε_0	Nominal strain
$\varepsilon_{\mathrm{I}}, \varepsilon_{\mathrm{II}}, \varepsilon_{\mathrm{III}}$	Principal Hencky (true) strains
$\boldsymbol{\varepsilon}$	Spatial Hencky strain tensor
$\boldsymbol{\varepsilon}_0$	Infinitesimal strain tensor
ζ	Scaling function

η_1, η_2	Locations of tensile and compressive hydrostatic nodes
θ	Angle of rotation, meridian angle
κ	Constant
$\lambda, \overline{\lambda}$	Principal stretch, modified (isochoric)
Λ	Lamé constant
μ	Shear modulus
ν	Poisson's ratio
ξ	Deviatoric plane coordinate
Ξ	Shape function
Π	Total potential energy
$\Delta\Pi$	Change of total potential energy
ρ	Density, radial distance from hydrostatic axis
σ, σ_0	True/nominal normal stress
σ_+, σ_-	Uniaxial tensile/compressive strength
$\sigma_\mathrm{I}, \sigma_\mathrm{II}, \sigma_\mathrm{III}$	Principal stresses
$\boldsymbol{\sigma}$	Cauchy stress tensor
τ, τ_0	True/nominal shear stress
$\boldsymbol{\tau}$	Kirchhoff stress tensor
φ	Angular coordinate, meridian angle
Φ	Failure surface
ξ	Internal variable
ψ	Midplane rotation angle
Ψ	Helmholtz free energy
ω	Shape function
Ω	Problem domain

Chapter 1

Introduction

Dealing with the limited supply of resources is one of the biggest challenges of our time. Hence, technical structures must aim at maximum resource efficiency. This encourages lightweight design, which not only reduces resource requirements for the structure itself but also the energy consumption during its life, for instance, in the form of fuel for means of transportation.

Mass reduction can be achieved in different ways: using lightweight materials, reducing material usage through optimized load transfer, or using lightweight manufacturing techniques. A key technology among the latter is adhesive bonding. It allows for joining dissimilar materials and enables composite designs, it does not require holes introducing stress concentrations and weakening the adherends, and it does not require additional parts such as screws or rivets.

For these reasons, adhesive bonding has become a popular and established joining technology across many industries. Adhesives in vehicle bodies act as energy absorbers in the case of a crash, increase the vehicle's stiffness and enable multi-material designs reducing the vehicle's weight (Fig. 1.1). In facades, adhesives are used for acoustic damping, as weather seals and to fasten structural elements (Fig. 1.2). In all these applications, they are not only fillers or seals but structural elements. Hence, they require accurate engineering and design tools, and precise testing and application procedures.

1.1 Motivation

Besides the above general features of adhesive bonds, special purpose adhesives can satisfy very specific needs. For instance, structural silicone adhesives provide excellent properties for joining brittle and low toughness materials such as glass. Silicones are amorphous cross-linked elastomers with strong silicon–oxygen backbones. Their glass transition temperature lies well below ambient temperatures, which allows for considerable segmental motion at ambient conditions. Silicones typically exhibit hyperelastic

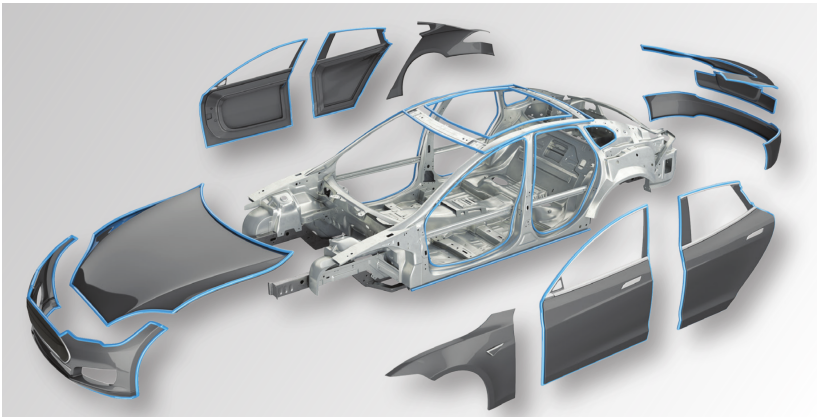

Fig. 1.1 Use of adhesives in vehicle bodies for joining dissimilar materials such as carbon and glass fiber composites, sheet molding compound, aluminum, and steel (Dow Automotive Systems, 2019).

behavior, high failure strain and low elastic modulus, excellent adhesion to many materials, and a good resistance against environmental impacts and aging. When used as adhesives, they transfer loads homogeneously and can compensate large deformation differences originating, e.g., from a thermal mismatch (Fig. 1.3). However, at bi-material corners between adherends and adhesive, stress singularities owing to geometrical and material discontinuities are present. Applying classical local strength-of-materials or fracture mechanics approaches yields contradictory and unphysical predictions, and concepts that accurately capture notch-induced crack nucleation in hyperelastic materials and that describe the physics of the failure process are yet unknown.

Assuming the spontaneous formation of a finite sized crack instead of infinitesimal crack growth allows for deriving a failure model capable of bridging this gap. The approach is known as finite fracture mechanics and has proved successful in many structural applications, in particular for adhesive joints. However, it has not been applied to nonlinear elastic materials, yet.

1.2 State of the art

Fracture of hyperelastic materials is a complex phenomenon that requires the characterization and modeling of many different individual aspects: i) the material's constitutive behavior must be identified and described by a model, ii) bulk material failure properties must be measured and approximated by a mathematical expression for the failure

Fig. 1.2 Use of adhesives in facades. **1** Glass–glass joints, **2** glass–metal joints, **3** facade panel fixings, **4** translucent joints, **5** natural stone and concrete joints, **6** sealings (Sika Services AG, 2019a).

surface, and iii) a fracture mechanical model for notch-induced crack nucleation is required, which necessitates the measurement of the fracture toughness of the nonlinear material. A comprehensive overview of relevant studies on each of these topics is given in the beginning of the respective chapter. This section only provides a brief overview of the state of the art and open points in order to derive objectives for the present work.

Constitutive models and experimental material characterization. Literature provides a vast number of constitutive equations and giving a comprehensive overview is nearly impossible. Khiêm and Itskov (2016) summarize selected materials models that have proven practical and successful in their application. The challenge lies in a reliable experimental characterization and in choosing a model that captures the material behavior well but has minimum complexity.

Experimental methods for the characterization of the constitutive behavior are largely standardized, even for hyperelastic materials (ASTM Standard D624, 2000; ASTM Standard D3492, 2016). This holds for the identification of bulk failure properties, as well (ASTM Standard D412, 2016). However, measuring the fracture toughness of nonlinear materials is challenging. Classical (Irwin and Kies, 1954) and standardized (BS Standard 7991, 2001) methods often rely on the assumption of linearity. Recent J-integral based models allow for calculating properties of interest from experimentally accessible quantities (Marzi et al., 2009a) but consider only thin nonlinear adhesive layers.

Bulk material failure. Determining a material's critical states under multiaxial loading requires extensive experimental programs and not all possible stress or strain states can

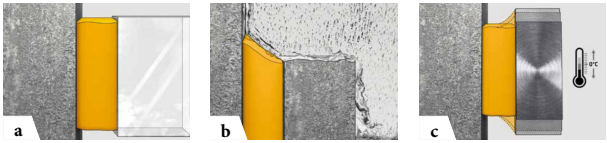

Fig. 1.3 Advantages of soft elastic adhesives. **a** Excellent adhesion to many materials permits bonding of dissimilar materials, **b** good resistance against environmental impacts provides tight sealings, **c** high failure strain and low elastic modulus allow for compensating large deformation differences (Sika Services AG, 2019b).

be examined. In order to understand the limits of structural integrity in any situation, failure criteria have been used since the origins of the field of mechanics (Coulomb, 1773). Classical failure criteria are often too primitive to accurately describe experimental data and to capture complex multiaxial behavior (Kolupaev, 2018), in particular for hyperelastic materials. Although several sophisticated generalized criteria were formulated (Altenbach et al., 1995; Bigoni and Piccolroaz, 2004), they are still only applicable to a certain class of materials and no universal failure criterion exists. More importantly, no criterion capable of accurately describing multiaxial bulk material failure of different hyperelastic materials has been identified.

Models for crack nucleation in hyperelastic materials. At notches, so-called weak stress singularities, i.e., indefinitely large stress concentrations, are present (Weißgraeber et al., 2016b). In order to describe notch-induced crack nucleation, classical strength-of-materials and fracture mechanics concepts can only be applied using an additional length parameter: strength criteria must be evaluated in a certain distance from the singularity (Neuber, 1936) and fracture mechanics requires the assumption of pre-existing cracks (Waddoups et al., 1971). Different nonlocal approaches were successfully applied to hyperelastic materials (Clift et al., 2014; Miehe and Schänzel, 2014; Berto, 2015; Ayatollahi et al., 2016). However, the length parameter involved is not known a priori and lacks definite physical meaning.

Finite fracture mechanics introduces a length scale with clear physical meaning – the finite size of the nucleating crack (Hashin, 1996). In this context, Leguillon (2002) showed that crack nucleation is not governed by strength or toughness alone but by both simultaneously. The corresponding coupled stress and energy criterion provides excellent failure predictions for many different problems and structures (Weißgraeber et al., 2016b), and requires only experimentally accessible material parameters as inputs. Although it is generally applicable to hyperelastic materials, the coupled criterion has not been used for this class of materials.

Normative background. The lack of proper models for crack nucleation in hyperelastic materials is also documented by available standards for hyperelastic adhesive bonds. Guidelines such as the European Technical Approval Guideline for Structural Sealant Glazing Systems, ETAG 002 (EOTA, 2012), or the ASTM Standard Guide for Evaluating Failure of Structural Sealant Glazing (ASTM Standard C1401, 2014) do not account for hyperelasticity and assume linear elastic material behavior. They neglect multiaxial stress states and assume uniform stresses within the adhesive. An assessment of notch-induced failure is only provided using specimen tests and corresponding design factors accounting for all unconsidered effects.

1.3 Objectives and structure

This work aims to develop models, tools and procedures for the design of hyperelastic adhesive bonds, and for the assessment of fracture of nonlinear elastic materials. By extending the scope of finite fracture mechanics to hyperelastic materials, it provides a physical model for notch-induced crack nucleation. Enabling the application of the coupled criterion of finite fracture mechanics to nonlinear elastic materials requires addressing two open points: i) a bulk material failure criterion for multiaxial loads and ii) a model that allows for measuring the fracture toughness of thick hyperelastic adhesive bonds. This is complemented by a comprehensive experimental characterization of the constitutive behavior and measurements of multiaxial bulk failure data. The procedure is demonstrated using two structural silicone adhesives.

Chapter 2 introduces a consistent nomenclature and summarizes relevant theoretical concepts. Chapter 3 describes the preparation and testing of samples used for material characterization and benchmark tests. It includes details on the finite element models used to reproduce the experiments. Chapter 4 is dedicated to the experimental characterization of the constitutive behavior, bulk material failure properties and the fracture toughness of the hyperelastic materials used throughout the present work. Chapter 5 reports on the development of a novel generalized deviatoric function capable of describing failure surfaces of a multitude of materials. The properties of this novel failure criterion are used to provide an accurate representation of the failure surfaces of hyperelastic materials. Chapter 6 uses the findings of previous chapters to extend finite fracture mechanics to hyperelasticity and to formulate a coupled strain and energy criterion for notch-induced crack nucleation in hyperelastic materials. Using material parameters characterized in independent experiments, the failure criterion is validated by comparison to experimentally measured effective joint strengths. Chapter 7 exploits characteristic properties of adhesive bonds to develop an efficient semi-analytical stress and strain analysis model for nonlinear elastic adhesive joints. In combination with the

coupled strain and energy failure criterion, the model provides an easy-to-use and fast design tool for a certain class of hyperelastic adhesive joints.

Chapter 2

Theoretical background

The present work is concerned with fracture of hyperelastic materials. To allow for a mathematical description of the phenomenon, the following sections provide a brief introduction of the basic principles of continuum mechanics, relevant concepts of constitutive modeling, methods for the description of bulk material failure and fundamentals of classical and modern fracture mechanics.

The chapter attempts to establish a consistent nomenclature. Mathematical operators and abbreviations are written in upright roman font. Variables are represented by italic symbols. For zeroth-order tensors (scalars), we use italic symbols in normal font weight. First-order tensors (vectors) are written in bold italics using lower case letters and second-order tensors using upper case symbols. Fourth-order tensors are represented by double struck symbols (blackboard bold). Occasionally, the limited number of typographic symbols will demand a deviation from these general rules. Vectors are assumed as column vectors and their scalar product is expressed by $\boldsymbol{a} \cdot \boldsymbol{b} = \boldsymbol{a}^{\mathsf{T}} \boldsymbol{b}$. For convenience, the matrix product (e.g., of a tensor and a vector, or two tensors) will not be indicated by a dot.

2.1 Fundamentals of continuum mechanics

Continuum mechanics is a branch of mechanics that studies the motion of deformable bodies in response to external forces. It disregards the microscopic structure of matter and approximates the object of investigation as a continuous medium characterized by certain field quantities associated with the internal structure, such as density, temperature and velocity. The basic ingredients of continuum mechanics are kinematics, i.e., the study of motion and deformation, stress, i.e., the study of internal forces, and balance principles, i.e., the mathematical description of fundamental laws of physics. All of the above hold for all materials and all times. They are supplemented by constitutive equations for the material-specific response to stresses or deformation (Chaves, 2013).

In the following, we will discuss the basics of continuum mechanics relevant for the description of hyperelastic solids. The discussion is based on the monographs by Ziegler (1983), Ogden (1997), Holzapfel (2000), Parisch (2003), and Altenbach (2015), which the interested reader can refer to for more detailed information.

2.1.1 Kinematics

The motion of a body in space is composed of rigid body motions and shape changes. While rigid body motions only change the position and orientation of the body in space, shape changes cause deformations, which result in internal stresses. In the description of kinematics, i.e., the motion of a body in space, the separation of translations and rotations from changes in shape and size is crucial. In the following, we will introduce state variables that capture the state of deformation independent of rigid body motions. Quantities satisfying this requirement are called objective (Parisch, 2003).

Configurations. The regions occupied by a continuum body at times t are known as the configurations of the body. The (fixed) undeformed configuration at initial time $t = 0$ is called reference configuration $\mathcal{B}_0$. The deformed configuration at a given time $t > 0$ is denoted current configuration $\mathcal{B}$. The coordinates of a material point in the reference configuration $\mathcal{B}_0$ are described by the material position vector $\boldsymbol{X}$. The spatial coordinates of the same point in the current configuration $\mathcal{B}$ are described by the spatial position vector $\boldsymbol{x}$. Characterizing a motion with respect to the material coordinates $\boldsymbol{X}$ is referred to as Lagrangian description. The representation of a motion in terms of spatial coordinates $\boldsymbol{x}$ is denoted Eulerian description (Ogden, 1997).

Displacements and velocity. The position $\boldsymbol{x}$ of a material point in the deformed configuration is related to its position $\boldsymbol{X}$ in the undeformed configuration through the displacement vector

$$\boldsymbol{u} = \boldsymbol{x} - \boldsymbol{X}. \tag{2.1}$$

The first derivative of the displacement vector (2.1) with respect to time yields the velocity vector

$$\boldsymbol{v} = \frac{\partial \boldsymbol{u}}{\partial t} = \dot{\boldsymbol{u}}. \tag{2.2}$$

With Eq. (2.1) and fixed material coordinates $\boldsymbol{X}$, the velocity vector can also be expressed as the material time derivative $\boldsymbol{v} = \dot{\boldsymbol{x}}$ (Holzapfel, 2000).

Deformation gradient. Spatial and material coordinates $\boldsymbol{x}$ and $\boldsymbol{X}$, respectively, as well as the displacement vector $\boldsymbol{u}$ (2.1) characterize the location of particles of a continuum body when moved from the reference configuration $\mathcal{B}_0$ to the current configuration $\mathcal{B}$. For the description of its deformation, i.e., changes in size and shape, we consider the spatial and material tangent vectors $\mathrm{d}\boldsymbol{x}$ and $\mathrm{d}\boldsymbol{X}$. The tangent vectors are infinitesimal vector elements in the current and reference configuration and often referred to as spatial (deformed) and material (undeformed) line elements. Material tangent vectors $\mathrm{d}\boldsymbol{X}$ map into spatial tangent vectors $\mathrm{d}\boldsymbol{x}$ according to the fundamental relation

$$\mathrm{d}\boldsymbol{x} = \boldsymbol{F}\,\mathrm{d}\boldsymbol{X}, \tag{2.3}$$

where the second-order tensor

$$\boldsymbol{F} = \frac{\partial \boldsymbol{x}}{\partial \boldsymbol{X}}, \tag{2.4}$$

is called deformation gradient. The deformation gradient (2.4) is the primary measure of deformation in continuum mechanics. It is a so-called two-point tensor involving points in two distinct configurations. In general, it has nine components for all times t and characterizes the motion in the neighborhood of a point (Holzapfel, 2000). Expression (2.3) defines a linear transformation also known as *push forward* operation (of a covariant vector). The corresponding inverse transformation

$$\mathrm{d}\boldsymbol{X} = \boldsymbol{F}^{-1}\mathrm{d}\boldsymbol{x}, \tag{2.5}$$

is called *pull back* operation (of a covariant vector) and maps the spatial tangent vector $\mathrm{d}\boldsymbol{x}$ into the material tangent vector $\mathrm{d}\boldsymbol{X}$. The inverse of the deformation gradient $\boldsymbol{F}^{-1}$ is often referred to as spatial deformation gradient (Parisch, 2003).

Volume ratio. The Jacobian determinant of the deformation gradient is known as volume ratio

$$J = \det \boldsymbol{F}. \tag{2.6}$$

Denoting infinitesimal volume elements in the current and reference configuration as $\mathrm{d}V$ and $\mathrm{d}V_0$, respectively, it expresses the volume change between the two configurations, i.e.,

$$J = \frac{\mathrm{d}V}{\mathrm{d}V_0}. \tag{2.7}$$

Because the linear transformation (2.3) is invertible and volume elements cannot have negative volumes, we obtain $J > 0$ (Holzapfel, 2000).

Polar decomposition. The deformation gradient can be decomposed uniquely into a pure stretch and a pure rotation according to

$$\boldsymbol{F} = \boldsymbol{R}\boldsymbol{U}, \tag{2.8a}$$

$$\boldsymbol{F} = \boldsymbol{V}\boldsymbol{R}, \tag{2.8b}$$

where $\boldsymbol{R}$ is a proper orthogonal tensor, i.e., $\boldsymbol{R}^{\mathsf{T}}\boldsymbol{R} = \boldsymbol{I}$ with $\det \boldsymbol{R} = 1$, called rotation tensor. $\boldsymbol{U}$ and $\boldsymbol{V}$ are unique, positive definite, symmetric tensors called right (material) and left (spatial) stretch tensor, respectively. They describe local stretching, i.e., local change of shape, with respect to the reference and current configuration, respectively. The rotation tensor $\boldsymbol{R}$ measures the change of local orientation. It maps between the reference and the current configuration and, therefore, is a two-point tensor like $\boldsymbol{F}$ (Holzapfel, 2000).

Strain tensors. While displacements are measurable quantities, strains are introduced as a concept to simplify analyses. Therefore, numerous definitions and names of strain tensors exist (Holzapfel, 2000). We will limit the discussion to select strain tensors relevant for this work. Equation (2.8) yields the symmetric stretch tensors

$$\boldsymbol{U} = \left(\boldsymbol{F}^{\mathsf{T}}\boldsymbol{F}\right)^{\frac{1}{2}}, \tag{2.9a}$$

$$\boldsymbol{V} = \left(\boldsymbol{F}\boldsymbol{F}^{\mathsf{T}}\right)^{\frac{1}{2}}. \tag{2.9b}$$

describing local stretching of line elements independent of rigid body motions. However, because they involve square roots, i.e., irrational mathematical operations, they are rarely used as strain measures. Considering the transformation of the squares of line elements instead, yields the right and left Cauchy–Green strain tensors[1]

$$\boldsymbol{C} = \boldsymbol{U}^2 = \boldsymbol{F}^{\mathsf{T}}\boldsymbol{F}, \tag{2.10a}$$

$$\boldsymbol{B} = \boldsymbol{V}^2 = \boldsymbol{F}\boldsymbol{F}^{\mathsf{T}}, \tag{2.10b}$$

as important strain measures in material and spatial coordinates, respectively (Altenbach, 2015). They transform squared material (reference) line elements $\mathrm{d}\boldsymbol{X} \cdot \mathrm{d}\boldsymbol{X}$ and squared spatial (current) line elements $\mathrm{d}\boldsymbol{x} \cdot \mathrm{d}\boldsymbol{x}$ according to

$$\mathrm{d}\boldsymbol{x} \cdot \mathrm{d}\boldsymbol{x} = \mathrm{d}\boldsymbol{X} \cdot \boldsymbol{C}\,\mathrm{d}\boldsymbol{X}, \qquad \mathrm{d}\boldsymbol{X} \cdot \mathrm{d}\boldsymbol{X} = \mathrm{d}\boldsymbol{x} \cdot \boldsymbol{B}^{-1}\,\mathrm{d}\boldsymbol{x}. \tag{2.11}$$

[1] The term strain tensor refers to tensors that are based on quadratic stretch measures, i.e., the squared lengths of line elements $\mathrm{d}S^2 = \mathrm{d}\boldsymbol{X} \cdot \mathrm{d}\boldsymbol{X}$ and $\mathrm{d}s^2 = \mathrm{d}\boldsymbol{x} \cdot \mathrm{d}\boldsymbol{x}$. In contrast, stretch tensors are based on linear stretch measures, i.e., $\mathrm{d}S = |\mathrm{d}\boldsymbol{X}|$ and $\mathrm{d}s = |\mathrm{d}\boldsymbol{x}|$ (Parisch, 2003).

The tensors $\boldsymbol{U}$ and $\boldsymbol{V}$ as well as the tensors $\boldsymbol{C}$ and $\boldsymbol{B}$ have the same eigenvalues. Their determinants are related to the Jacobian determinant (2.6) according to

$$\begin{aligned} \det \boldsymbol{U} &= \det \boldsymbol{V} = \det \boldsymbol{F} = J, \\ \det \boldsymbol{C} &= \det \boldsymbol{B} = (\det \boldsymbol{F})^2 = J^2. \end{aligned} \tag{2.12}$$

In the undeformed reference configuration and for pure rigid body motions, all strain tensors introduced until this point equal the unit tensor $\boldsymbol{U} = \boldsymbol{V} = \boldsymbol{C} = \boldsymbol{B} = \boldsymbol{I}$. For many applications, in particular for the formulation of constitutive laws, it is convenient to introduce deformation measures that vanish for pure rigid body motions and in the reference configuration (Altenbach, 2015). Considering Eq. (2.11), we can express the change in the squared lengths of line elements between the reference and the current configuration by

$$\mathrm{d}\boldsymbol{x} \cdot \mathrm{d}\boldsymbol{x} - \mathrm{d}\boldsymbol{X} \cdot \mathrm{d}\boldsymbol{X} = \mathrm{d}\boldsymbol{X} \cdot (\boldsymbol{C} - \boldsymbol{I})\, \mathrm{d}\boldsymbol{X} = \mathrm{d}\boldsymbol{x} \cdot \left(\boldsymbol{I} - \boldsymbol{B}^{-1}\right) \mathrm{d}\boldsymbol{x}. \tag{2.13}$$

With Eq. (2.10) and introducing a normalization factor 1/2, this yields the symmetric material strain tensor

$$\boldsymbol{E} = \frac{1}{2}\left(\boldsymbol{F}^{\top}\boldsymbol{F} - \boldsymbol{I}\right), \tag{2.14}$$

known as Green–Lagrange strain tensor and the spatial Euler–Almansi strain tensor

$$\boldsymbol{A} = \frac{1}{2}\left(\boldsymbol{I} - \boldsymbol{F}^{-\top}\boldsymbol{F}^{-1}\right). \tag{2.15}$$

The purpose of the normalization factor in Eqs. (2.14) and (2.15) will become apparent in the linearization of the respective strain measures. The spatial Euler–Almansi strain tensor $\boldsymbol{A}$ is connected to the covariant Green–Lagrange strain tensor $\boldsymbol{E}$ by the *push forward* operation

$$\boldsymbol{A} = \boldsymbol{F}^{-\top}\boldsymbol{E}\boldsymbol{F}^{-1}. \tag{2.16}$$

Accordingly, the material Green–Lagrange strain tensor $\boldsymbol{E}$ is the *pull back* of the covariant Euler–Almansi strain tensor

$$\boldsymbol{E} = \boldsymbol{F}^{\top}\boldsymbol{A}\boldsymbol{F}. \tag{2.17}$$

Other covariant tensors, which transform according to Eqs. (2.16) and (2.17), are the right Cauchy–Green strain tensor $\boldsymbol{C}$ and the inverse of the left Cauchy–Green strain tensor $\boldsymbol{B}^{-1}$ (Holzapfel, 2000). As will be shown in the following, the above strain tensors can be decomposed multiplicatively into volume-changing and volume-preserving parts. A particularly interesting strain measure is the spatial Hencky strain tensor

$$\boldsymbol{\varepsilon} = \ln \boldsymbol{V}. \tag{2.18}$$

Because of the logarithmic function, it decomposes additively into volumetric and isochoric parts (Becker, 1893; Hencky, 1928, 1931, 1933). The material Hencky strain tensor $\ln \boldsymbol{U}$ has similar properties.

Volumetric–isochoric split. Hyperelastic materials often behave quite differently in bulk and shear. Therefore, we split the deformation locally into a volumetric part and an isochoric part. This split can be interpreted as two consecutive deformations

$$\boldsymbol{F} = \boldsymbol{F}_{\mathrm{vol}}\,\boldsymbol{F}_{\mathrm{iso}}, \tag{2.19}$$

corresponding to a multiplicative decomposition of the deformation gradient. The first term

$$\boldsymbol{F}_{\mathrm{vol}} = J^{1/3}\boldsymbol{I}, \tag{2.20}$$

is associated with volume-changing deformations. The second term

$$\boldsymbol{F}_{\mathrm{iso}} = J^{-1/3}\boldsymbol{F} = \overline{\boldsymbol{F}}, \tag{2.21}$$

is referred to as modified deformation gradient $\overline{\boldsymbol{F}}$ with $\det\overline{\boldsymbol{F}} = 1$. It corresponds to volume-preserving deformations (Flory, 1961; Lubliner, 1985). The eigenvalues of $\overline{\boldsymbol{F}}$ are called modified principal stretches

$$\overline{\lambda}_i = J^{-1/3}\lambda_i, \quad i = 1, 2, 3. \tag{2.22}$$

For finite element formulations, the volumetric–isochoric decompositions of the left and right Cauchy–Green strain tensors

$$\boldsymbol{C}_{\mathrm{vol}} = J^{2/3}\boldsymbol{I}, \qquad \boldsymbol{C}_{\mathrm{iso}} = J^{-2/3}\boldsymbol{C} = \overline{\boldsymbol{C}}, \tag{2.23a}$$

$$\boldsymbol{B}_{\mathrm{vol}} = J^{2/3}\boldsymbol{I}, \qquad \boldsymbol{B}_{\mathrm{iso}} = J^{-2/3}\boldsymbol{B} = \overline{\boldsymbol{B}}, \tag{2.23b}$$

are particularly important. On account of Eq. (2.18), the volumetric–isochoric split of the spatial Hencky strain tensor is performed additively. Using $\boldsymbol{V} = \boldsymbol{V}_{\mathrm{vol}}\boldsymbol{V}_{\mathrm{iso}}$, we obtain

$$\boldsymbol{\varepsilon} = \ln\left(J^{1/3}\boldsymbol{I}\right) + \ln\left(J^{-1/3}\boldsymbol{V}\right) = \frac{\operatorname{tr}\boldsymbol{\varepsilon}}{3}\,\boldsymbol{I} + \boldsymbol{\varepsilon}_{\mathrm{dev}}, \tag{2.24}$$

where $\operatorname{tr}\boldsymbol{\varepsilon} = \varepsilon_{11} + \varepsilon_{22} + \varepsilon_{33}$ denotes the trace and $\boldsymbol{\varepsilon}_{\mathrm{dev}} = \boldsymbol{\varepsilon} - (\operatorname{tr}\boldsymbol{\varepsilon}/3)\boldsymbol{I}$ the deviatoric part of the spatial Hencky strain tensor (Neff et al., 2016). A material, for which dilatational changes require a much higher exterior work than distortional changes, is called nearly incompressible.

Spectral decomposition. The left and right stretch tensors have the same eigenvalues λ_i, $i = 1, 2, 3$, called principal stretches. Their mutually orthogonal and normalized sets of eigenvectors, $\boldsymbol{n}_i$ and $\boldsymbol{n}_i^0$, are called principal spatial and principal referential directions, respectively, and their spectral decomposition reads

$$\boldsymbol{U} = \sum_{i=1}^{3}\lambda_i\,\boldsymbol{n}_i^0 \otimes \boldsymbol{n}_i^0, \qquad \boldsymbol{V} = \sum_{i=1}^{3}\lambda_i\,\boldsymbol{n}_i \otimes \boldsymbol{n}_i. \tag{2.25}$$

The principal referential directions transform onto the principal spatial directions according to $\boldsymbol{n}_i = \boldsymbol{R}\boldsymbol{n}_i^0$. The eigenvectors of the left and right Cauchy–Green strain tensors equal the eigenvectors of the left and right stretch tensor, respectively. However, their eigenvalues are the squares of the principal stretches, i.e.,

$$\boldsymbol{C} = \sum_{i=1}^{3} \lambda_i^2 \, \boldsymbol{n}_i^0 \otimes \boldsymbol{n}_i^0, \qquad \boldsymbol{B} = \sum_{i=1}^{3} \lambda_i^2 \, \boldsymbol{n}_i \otimes \boldsymbol{n}_i. \tag{2.26}$$

The eigenvalues of the material and spatial Hencky strain tensors $\varepsilon_i = \ln \lambda_i$ are called true or logarithmic strains and we obtain

$$\ln \boldsymbol{U} = \sum_{i=1}^{3} (\ln \lambda_i) \, \boldsymbol{n}_i^0 \otimes \boldsymbol{n}_i^0, \qquad \boldsymbol{\varepsilon} = \ln \boldsymbol{V} = \sum_{i=1}^{3} (\ln \lambda_i) \, \boldsymbol{n}_i \otimes \boldsymbol{n}_i. \tag{2.27}$$

Again, their eigenvectors are the principal referential and principal spatial directions.

Linearization. Using Eq. (2.1), we can split the deformation gradient into the unit tensor and the displacement gradient $\boldsymbol{F} = \boldsymbol{I} + \partial \boldsymbol{u} / \partial \boldsymbol{X}$. Plugging this result into Eq. (2.14) yields

$$\boldsymbol{E} = \frac{1}{2} \left(\frac{\partial \boldsymbol{u}}{\partial \boldsymbol{X}} + \left(\frac{\partial \boldsymbol{u}}{\partial \boldsymbol{X}} \right)^{\mathsf{T}} \right) + \frac{1}{2} \left(\frac{\partial \boldsymbol{u}}{\partial \boldsymbol{X}} \right)^{\mathsf{T}} \frac{\partial \boldsymbol{u}}{\partial \boldsymbol{X}}. \tag{2.28}$$

For small deformations we can neglect the quadratic second term in Eq. (2.28). Then, the Green–Lagrange tensor $\boldsymbol{E}$ coincides with the infinitesimal strain tensor

$$\boldsymbol{\varepsilon}_0 = \frac{1}{2} \left(\frac{\partial \boldsymbol{u}}{\partial \boldsymbol{X}} + \left(\frac{\partial \boldsymbol{u}}{\partial \boldsymbol{X}} \right)^{\mathsf{T}} \right), \tag{2.29}$$

used in linear elasticity and with the Euler–Almansi strain tensor $\boldsymbol{A}$. This equality in the case of small strains motivates the normalization factor 1/2 in Eqs. (2.14) and (2.15).

Rates of deformation tensors. The derivative of the velocity field (2.2) with respect to spatial coordinates is given by the spatial velocity gradient

$$\boldsymbol{L} = \frac{\partial \boldsymbol{v}}{\partial \boldsymbol{x}} = \boldsymbol{D} + \boldsymbol{W}. \tag{2.30}$$

In general, the second-order tensor $\boldsymbol{L}$ is not symmetric and, therefore, can be decomposed additively into its symmetric and antisymmetric parts

$$\boldsymbol{D} = \frac{1}{2} \left(\boldsymbol{L} + \boldsymbol{L}^{\mathsf{T}} \right), \tag{2.31a}$$

$$\boldsymbol{W} = \frac{1}{2} \left(\boldsymbol{L} - \boldsymbol{L}^{\mathsf{T}} \right). \tag{2.31b}$$

The symmetric part $\boldsymbol{D}$ is called rate of deformation tensor. The antisymmetric part $\boldsymbol{W}$ is known as spin tensor (Holzapfel, 2000).

2.1.2 Stress

Subjecting a body to an external force displaces its particles according to the kinematics discussed in the previous chapter. Interatomic forces create a resistance against this particle movement. Interpreting the average of the interatomic forces of a certain set of atoms as the internal force yields a macroscopic variable on the continuum level. The internal force at each material point (particle) of the continuum is described by the traction vector field (force per unit area) representing the starting point to establish the stress state at a material point (Chaves, 2013).

Surface tractions. Let a continuum body in its current configuration $\mathcal{B}$ at time t be cut by a plane surface passing through the spatial point $\boldsymbol{x}$. Consider a spatial element of this surface ΔA at the tail of a unit outward normal vector $\boldsymbol{n}$ at $\boldsymbol{x}$. Internal forces transmitted through this surface element are denoted $\Delta \boldsymbol{f}$. According to Cauchy's postulate, the limit

$$\boldsymbol{t} = \lim_{\Delta A \to 0} \frac{\Delta \boldsymbol{f}}{\Delta A}, \tag{2.32}$$

exists and the vector $\boldsymbol{t}$ is called Cauchy (true) traction vector. In Eq. (2.32), we omit so-called resultant couples, which can be interpreted as a torque acting on the surface element. Considering a surface element ΔA_0 at a material point $\boldsymbol{X}$ in a cut of the body in its reference configuration $\mathcal{B}_0$ characterized by the unit outward normal vector $\boldsymbol{n}_0$, yields the first Piola–Kirchhoff (nominal) traction vector

$$\boldsymbol{t}_0 = \lim_{\Delta A_0 \to 0} \frac{\Delta \boldsymbol{f}}{\Delta A_0}. \tag{2.33}$$

It points in the same direction as the Cauchy traction vector $\boldsymbol{t}$ but is measured in force per unit undeformed surface area (Holzapfel, 2000).

Cauchy's stress theorem. The multitude of all possible cuts through a material point of the body defines the stress state at this material point. It can be shown that three perpendicular cuts suffice for a complete description of the stress state. The nine coordinates of the corresponding traction vectors constitute the stress tensor in the material point (Altenbach, 2015). According to Cauchy's stress theorem, there exist unique second-order stress tensors $\boldsymbol{\sigma}$ and $\boldsymbol{P}$ so that

$$\boldsymbol{t} = \boldsymbol{\sigma}^{\top} \boldsymbol{n}, \tag{2.34a}$$

$$\boldsymbol{t}_0 = \boldsymbol{P}^{\top} \boldsymbol{n}_0, \tag{2.34b}$$

where $\boldsymbol{\sigma}$ denotes the symmetric spatial Cauchy stress tensor and $\boldsymbol{P}$ is the first Piola–Kirchhoff stress tensor. The Cauchy stress tensor is symmetric ($\boldsymbol{\sigma} = \boldsymbol{\sigma}^{\top}$) and has six

independent components. A proof is provided in Section 2.1.3. The first Piola–Kirchhoff stress tensor $\boldsymbol{P}$ is a two-point tensor like $\boldsymbol{F}$ and can be expressed by

$$\boldsymbol{P} = J\boldsymbol{\sigma}\boldsymbol{F}^{-\top}. \tag{2.35}$$

Equation (2.35) is known as the Piola transformation and implies $\boldsymbol{P}\boldsymbol{F}^{\top} = \boldsymbol{F}\boldsymbol{P}^{\top}$. Hence, $\boldsymbol{P}$ is, in general, not symmetric and has nine independent components (Holzapfel, 2000).

Alternative stress tensors. The so-called Kirchhoff stress tensor $\boldsymbol{\tau}$ differs from the Cauchy stress tensor $\boldsymbol{\sigma}$ by the volume ratio J, i.e.,

$$\boldsymbol{\tau} = J\boldsymbol{\sigma}. \tag{2.36}$$

It is a contravariant spatial tensor in spatial coordinates. The second Piola–Kirchhoff stress tensor

$$\boldsymbol{S} = \boldsymbol{F}^{-1}\boldsymbol{P}, \tag{2.37}$$

is a symmetric material tensor in material coordinates and, hence, does not admit a physical interpretation in terms of surface tractions. However, it is a useful quantity in computational mechanics. It is obtained by the *pull back* operation on the contravariant spatial tensor $\boldsymbol{\tau}$, i.e.,

$$\boldsymbol{S} = \boldsymbol{F}^{-1}\boldsymbol{\tau}\boldsymbol{F}^{-\top}. \tag{2.38}$$

Accordingly, the spatial Kirchhoff stress tensor is the *push forward* of the contravariant material tensor $\boldsymbol{S}$, i.e.,

$$\boldsymbol{\tau} = \boldsymbol{F}\boldsymbol{S}\boldsymbol{F}^{\top}. \tag{2.39}$$

Other contravariant tensors, which transform according to Eqs. (2.38) and (2.39), are the left Cauchy–Green strain tensor $\boldsymbol{B}$ and the inverse of the right Cauchy–Green strain tensor $\boldsymbol{C}^{-1}$ (Holzapfel, 2000).

Normal and shear stresses. The Cauchy traction vector (2.32) can be expressed by the sum of a vector along the plane normal $\boldsymbol{n}$ and a vector perpendicular to $\boldsymbol{n}$, i.e.,

$$\boldsymbol{t} = \boldsymbol{t}_{\parallel} + \boldsymbol{t}_{\perp}. \tag{2.40}$$

The length of $\boldsymbol{t}_{\parallel}$ is called normal stress $\sigma = |\boldsymbol{t}_{\parallel}| = \boldsymbol{t} \cdot \boldsymbol{n}$, the length of $\boldsymbol{t}_{\perp}$ is denoted shear stress $\tau = |\boldsymbol{t}_{\perp}| = \sqrt{\boldsymbol{t} \cdot \boldsymbol{t} - \sigma^2}$.

Extreme values. Directions $\boldsymbol{n}$, in which normal stresses σ assume maximum and minimum values are denoted principal axes of $\boldsymbol{\sigma}$. They are obtained from the condition

$$\boldsymbol{t} = \sigma \boldsymbol{n}, \tag{2.41}$$

considering symmetry of the Cauchy stress tensor and using Eq. (2.34a), which yields the eigenvalue problem

$$(\boldsymbol{\sigma} - \sigma \boldsymbol{I})\boldsymbol{n} = \boldsymbol{0}. \tag{2.42}$$

The eigenvalues σ are identified from the characteristic polynomial of $\boldsymbol{\sigma}$, i.e.,

$$\sigma^3 - I_{\boldsymbol{\sigma}}\sigma^2 + II_{\boldsymbol{\sigma}}\sigma - III_{\boldsymbol{\sigma}} = 0, \tag{2.43}$$

where $I_{\boldsymbol{\sigma}}$, $II_{\boldsymbol{\sigma}}$ and $III_{\boldsymbol{\sigma}}$ are the principal invariants of $\boldsymbol{\sigma}$. The principal scalar invariants of a tensor $\boldsymbol{Y}$ are given by

$$I_{\boldsymbol{Y}} = \operatorname{tr} \boldsymbol{Y}, \tag{2.44a}$$

$$II_{\boldsymbol{Y}} = \frac{1}{2}\left[(\operatorname{tr} \boldsymbol{Y})^2 - \operatorname{tr}\left(\boldsymbol{Y}^2\right)\right], \tag{2.44b}$$

$$III_{\boldsymbol{Y}} = \det \boldsymbol{Y}. \tag{2.44c}$$

The characteristic equation (2.43) has three real-valued solutions $\sigma_{\mathrm{I}} > \sigma_{\mathrm{II}} > \sigma_{\mathrm{III}}$ called principal normal stresses. The corresponding three eigenvectors $\boldsymbol{n}_i$ are determined from Eq. (2.42) and are called the principal directions of $\boldsymbol{\sigma}$ (Altenbach, 2015).

Spherical–deviatoric split. The Cauchy stress tensor can be decomposed additively into its spherical and deviatoric parts according to

$$\boldsymbol{\sigma} = \boldsymbol{\sigma}_{\mathrm{sph}} + \boldsymbol{\sigma}_{\mathrm{dev}}. \tag{2.45}$$

The spherical part is represented by a diagonal matrix with the average normal stress as components. This corresponds to the hydrostatic pressure p and we obtain

$$\boldsymbol{\sigma}_{\mathrm{sph}} = p\boldsymbol{I}, \qquad p = \frac{1}{3}\operatorname{tr} \boldsymbol{\sigma}, \tag{2.46}$$

where p is defined as positive for hydrostatic tension. The deviatoric part describes the deviation from a pure hydrostatic stress state. It reads

$$\boldsymbol{\sigma}_{\mathrm{dev}} = \boldsymbol{\sigma} - \frac{\operatorname{tr} \boldsymbol{\sigma}}{3}\boldsymbol{I}. \tag{2.47}$$

Principal scalar invariants of the deviatoric part $\boldsymbol{Y}_{\mathrm{dev}}$ of a tensor are indicated by a prime symbol and given by

$$I'_{\boldsymbol{Y}} = \operatorname{tr} \boldsymbol{Y}_{\mathrm{dev}} = 0, \tag{2.48a}$$

$$II'_{\boldsymbol{Y}} = \frac{1}{2}\left[(\operatorname{tr} \boldsymbol{Y}_{\mathrm{dev}})^2 - \operatorname{tr}\left(\boldsymbol{Y}^2_{\mathrm{dev}}\right)\right], \tag{2.48b}$$

$$III'_{\boldsymbol{Y}} = \det \boldsymbol{Y}_{\mathrm{dev}}. \tag{2.48c}$$

2.1.3 Balance principles

Balance equations are fundamental laws of continuum mechanics expressing the relationship between certain quantities characterizing the material body (continuum) and the external influences on the body. They are generally given as global statements in integral form for the whole body. For sufficiently smooth fields of the considered quantities, local formulations in the form of differential equations that refer to any small part of the body can be given. Fundamental balance principles of continuum mechanics are conservation of mass, balance of linear and angular momentum and the first and second laws of thermodynamics. They hold for all times and all materials.

Conservation of mass. Mass cannot be produced or destroyed. A closed system can change in volume but it has a fixed amount of mass m. No mass, only energy in the form of work or heat, can cross its boundary. Considering a closed system, the total mass of a body in the reference configuration must stay the same during a motion, i.e.,

$$m = \int_{V_0} \rho_0 \mathrm{d}V_0 = \int_V \rho \mathrm{d}V, \tag{2.49}$$

where the index 0 denotes quantities in the reference configuration, ρ is the volumetric mass density and V the body's volume (Altenbach, 2015). Considering an infinitesimal mass element, yields the differential form

$$\mathrm{d}m = \rho_0 \mathrm{d}V_0 = \rho \mathrm{d}V. \tag{2.50}$$

With $J = \mathrm{d}V/\mathrm{d}V_0$ (2.7), we obtain a relation between the spatial mass density ρ and the reference mass density ρ_0, i.e.,

$$\rho_0 = J\rho. \tag{2.51}$$

Note that the reference mass density ρ_0 is time-independent and intrinsically associated with the reference configuration (Parisch, 2003).

Balance of linear momentum. According to Newton's second law of motion, the rate of change of the total linear momentum during the deformation of a body equals the sum of all surface and volume forces acting on the body. The vector of linear momentum links the velocity and mass distributions of a body. It is given by

$$\boldsymbol{p} = \int_V \boldsymbol{v}\, \rho \mathrm{d}V, \tag{2.52}$$

where $\boldsymbol{v}$ (2.2) is the spatial velocity vector. Expressing surface forces using the Cauchy traction vector $\boldsymbol{t}$ (2.32) and introducing the spatial body force vector field $\boldsymbol{f}$ defined per unit deformed volume, the global form of balance of linear momentum is given by

$$\frac{\mathrm{d}}{\mathrm{d}t} \int_V \boldsymbol{v}\, \rho \mathrm{d}V = \int_A \boldsymbol{t}\, \mathrm{d}A + \int_V \boldsymbol{f}\, \mathrm{d}V, \tag{2.53}$$

where A is the deformed surface area of the body. On the left-hand side in Eq. (2.53) both the velocity $\boldsymbol{v}$ and the density ρ are functions of time. In order to derive the local form of the balance of linear momentum, we make use of Eq. (2.50) to switch to the reference configuration, take the time derivative of the vector of linear momentum $\boldsymbol{p}$ and return to the current configuration (Parisch, 2003). Converting the surface integral in Eq. (2.53) into a volume integral using the divergence theorem, then allows for gathering all terms of Eq. (2.53) in one integral

$$\int_V (\operatorname{div} \boldsymbol{\sigma} + \boldsymbol{f} - \rho \dot{\boldsymbol{v}}) \, \mathrm{d}V = \boldsymbol{0}. \tag{2.54}$$

Equation (2.54) is referred to as the global form of Cauchy's first equation of motion. Because it must hold for any volume V, we can deduce the local form of Cauchy's first equation of motion

$$\operatorname{div} \boldsymbol{\sigma} + \boldsymbol{f} = \rho \dot{\boldsymbol{v}}, \tag{2.55}$$

which serves as the basis for the formulation of boundary value problems. For this purpose, the surface of the body ∂V is split into two subsurfaces $\partial V = \partial V_\mathrm{t} \cup \partial V_\mathrm{u}$. On ∂V_t we prescribe tractions $\tilde{\boldsymbol{t}}$ and on ∂V_u displacements $\tilde{\boldsymbol{u}}$. If the acceleration $\dot{\boldsymbol{v}}$ is zero in all points of the body, the boundary value problem of elastostatics follows as

$$\operatorname{div} \boldsymbol{\sigma} + \boldsymbol{f} = \boldsymbol{0} \quad \text{on} \quad V, \tag{2.56a}$$

$$\boldsymbol{\sigma} \boldsymbol{n} = \tilde{\boldsymbol{t}} \quad \text{on} \quad \partial V_\mathrm{t}, \tag{2.56b}$$

$$\boldsymbol{u} = \tilde{\boldsymbol{u}} \quad \text{on} \quad \partial V_\mathrm{u}, \tag{2.56c}$$

where Eq. (2.56a) is often referred to as Cauchy's equation of equilibrium (Holzapfel, 2000).

Balance of angular momentum. As the rotational equivalent to linear momentum, we postulate that the total angular momentum of a closed system relative to a fixed point remains constant during the deformation of a body. Relative to the coordinate origin, the vector of angular momentum is given by

$$\boldsymbol{l} = \int_V (\boldsymbol{x} \times \boldsymbol{v}) \, \rho \mathrm{d}V. \tag{2.57}$$

Its rate of change equals the resultant moment of all external forces acting on the body, which yields the global form of balance of angular momentum

$$\frac{\mathrm{d}}{\mathrm{d}t} \int_V (\boldsymbol{x} \times \boldsymbol{v}) \, \rho \mathrm{d}V = \int_A (\boldsymbol{x} \times \boldsymbol{t}) \, \mathrm{d}A + \int_V (\boldsymbol{x} \times \boldsymbol{f}) \, \mathrm{d}V. \tag{2.58}$$

Equation (2.58) provides no new information for the solution of the boundary value problem (2.56) because it only corresponds to Eq. (2.53) vector-multiplied by the location

vector $\boldsymbol{x}$ (Parisch, 2003). However, it requires symmetry of the Cauchy stress tensor $\boldsymbol{\sigma}$. Following similar arguments as for the balance of linear momentum, using Cauchy's stress theorem (2.32) and converting the surface integral into a volume integral using the divergence theorem yields

$$\int_V \boldsymbol{x} \times (\rho \dot{\boldsymbol{v}} - \boldsymbol{f} - \operatorname{div} \boldsymbol{\sigma}) \, \mathrm{d}V = \int_V \boldsymbol{\mathcal{E}} : \boldsymbol{\sigma}^\top \, \mathrm{d}V, \tag{2.59}$$

where $\boldsymbol{\mathcal{E}} = \varepsilon_{ijk} \boldsymbol{e}_i \otimes \boldsymbol{e}_j \otimes \boldsymbol{e}_k$ is the third-order permutation tensor. On account of Cauchy's first equation of motion (2.55) and the fact that the considered volume V is arbitrary, we conclude

$$\boldsymbol{\mathcal{E}} : \boldsymbol{\sigma}^\top = \boldsymbol{0}, \tag{2.60}$$

which yields $\sigma_{32} = \sigma_{23}$, $\sigma_{13} = \sigma_{31}$ and $\sigma_{21} = \sigma_{12}$. These relations are satisfied if and only if the Cauchy stress tensor is symmetric, i.e,

$$\boldsymbol{\sigma} = \boldsymbol{\sigma}^\top, \tag{2.61}$$

which is often referred to as Cauchy's second law of motion (Holzapfel, 2000).

Balance of mechanical energy. Multiplying Cauchy's equation of motion (2.55) by $\boldsymbol{v}$, applying product rule and integrating over the whole body yields

$$\underbrace{\frac{\mathrm{d}}{\mathrm{d}t} \int_V \frac{1}{2} \boldsymbol{v} \cdot \boldsymbol{v} \, \rho \mathrm{d}V}_{\dot{\mathcal{K}}} + \underbrace{\int_V \boldsymbol{\sigma} : \boldsymbol{D} \, \mathrm{d}V}_{\mathcal{P}_{\mathrm{int}}} = \underbrace{\int_A \boldsymbol{t} \cdot \boldsymbol{v} \, \mathrm{d}A + \int_V \boldsymbol{f} \cdot \boldsymbol{v} \, \mathrm{d}V}_{\mathcal{P}_{\mathrm{ext}}}, \tag{2.62}$$

where the rate of deformation tensor $\boldsymbol{D}$ (2.31a) is the symmetric part of the spatial velocity gradient $\boldsymbol{L}$ (Altenbach, 2015). With the rate of change of kinetic energy $\dot{\mathcal{K}}$, internal mechanical power $\mathcal{P}_{\mathrm{int}}$ and external mechanical power $\mathcal{P}_{\mathrm{ext}}$, we conclude that the rate of change of the mechanical energy of a body equals the power of all external forces

$$\dot{\mathcal{K}} + \mathcal{P}_{\mathrm{int}} = \mathcal{P}_{\mathrm{ext}}. \tag{2.63}$$

For conservative systems, mechanical power can be given by time derivatives of scalar-valued functions (Altenbach, 2015), i.e.,

$$\mathcal{P}_{\mathrm{int}} = \frac{\mathrm{d}\Pi_{\mathrm{int}}}{\mathrm{d}t}, \qquad \mathcal{P}_{\mathrm{ext}} = -\frac{\mathrm{d}\Pi_{\mathrm{ext}}}{\mathrm{d}t}, \tag{2.64}$$

where Π_{ext} is the potential energy of external forces and Π_{int} strain energy. Hence, for conservative systems we obtain

$$\frac{\mathrm{d}}{\mathrm{d}t} \left(\mathcal{K} + \Pi_{\mathrm{int}} + \Pi_{\mathrm{ext}} \right) = 0, \qquad \mathcal{K} + \Pi_{\mathrm{int}} + \Pi_{\mathrm{ext}} = \text{const.} \tag{2.65}$$

implying that the total mechanical energy $\Pi = \Pi_{\mathrm{int}} + \Pi_{\mathrm{ext}}$ of a body is conserved during a motion. Balance of mechanical energy is not an additional statement but a consequence of the balance of linear momentum (Altenbach, 2015).

First law of thermodynamics. The first law of thermodynamics is a fundamental axiom in mechanics and postulates the conservation of energy. It states that the rate of change of the total energy of a thermodynamic system equals the rate at which external mechanical and thermal work is done on the system:

$$\dot{\mathcal{K}} + \dot{\mathcal{U}} = \mathcal{P}_{\text{ext}} + \mathcal{Q}. \tag{2.66}$$

The total energy of the system is composed of kinetic energy $\mathcal{K}$ and internal energy $\mathcal{U}$. External mechanical work is done by surface tractions and body forces. Its rate is the external mechanical power $\mathcal{P}_{\text{ext}}$ (2.62). Thermal power $\mathcal{Q}$ is the rate of thermal work done by heat flux per unit surface area $\boldsymbol{q}$ and a heat source per unit volume r, i.e.,

$$\mathcal{Q} = -\int_A \boldsymbol{q} \cdot \boldsymbol{n} \, \mathrm{d}A + \int_V r \, \rho \mathrm{d}V. \tag{2.67}$$

The sign of the heat flux vector $\boldsymbol{q}$ is chosen so that a positive heat flux corresponds to heat entering the body. The total internal energy is obtained from the specific internal energy per unit mass u according to

$$\mathcal{U} = \int_V u \, \rho \mathrm{d}V. \tag{2.68}$$

Subtracting the mechanical energy balance (2.63) from Eq. (2.66) and applying the divergence theorem to Eq. (2.67) yields a reduced global form of the first law of thermodynamics

$$\int_V \dot{u} \, \rho \mathrm{d}V = \int_V \left(\boldsymbol{\sigma} : \boldsymbol{D} - \operatorname{div} \boldsymbol{q} + r\rho \right) \mathrm{d}V. \tag{2.69}$$

Again the choice of reference volume V is arbitrary and for sufficiently smooth tensor fields we obtain the local form of the first law of thermodynamics

$$\rho \dot{u} = \boldsymbol{\sigma} : \boldsymbol{D} - \operatorname{div} \boldsymbol{q} + r\rho. \tag{2.70}$$

For purely mechanical, adiabatic processes with $\boldsymbol{q} = \boldsymbol{0}$ and $r = 0$, the rate of specific internal energy equals the stress power, i.e., the rate of strain energy (Parisch, 2003). It may be expressed using different work conjugate pairs of stress and rate of deformation tensors

$$\rho_0 \dot{u} = J \boldsymbol{\sigma} : \boldsymbol{D} = \boldsymbol{P} : \dot{\boldsymbol{F}} = \boldsymbol{S} : \dot{\boldsymbol{E}}. \tag{2.71}$$

The double contraction of work conjugate pairs describes real physical power in dynamic processes (Holzapfel, 2000).

Second law of thermodynamics. The first law of thermodynamics governs energy transfer within a thermodynamic process independent of its direction. The second law of thermodynamics supplements the direction of the energy transfer. It postulates that the total production of entropy[2] per unit time is never negative, i.e.,

$$\frac{\mathrm{d}}{\mathrm{d}t}\int_V s\,\rho \mathrm{d}V \geq \int_V \frac{r}{T}\,\rho \mathrm{d}V - \int_A \frac{1}{T}\,\boldsymbol{q}\cdot\boldsymbol{n}\,\mathrm{d}A, \tag{2.72}$$

where s is specific entropy per unit mass and T the absolute temperature. The right-hand side of Eq. (2.72) describes the rate of entropy input into a certain region V of a continuum body. It consists of entropy transferred across its boundary A and entropy generated (or destroyed) inside that region. Equation (2.72) is known as the global form of the Clausius–Duhem inequality (Coleman and Noll, 1963). It states that the rate of entropy increase of a system must be equal or greater than the rate of entropy introduced into the system by external sources. Equality holds only for reversible processes (Altenbach, 2015). Converting the surface integral in Eq. (2.72) to a volume integral using the divergence theorem, applying the product rule and exploiting arbitrariness of the volume V yields the local form of the Clausius–Duhem inequality

$$\rho T\dot{s} + \operatorname{div}\boldsymbol{q} - r\rho - \frac{1}{T}\,\boldsymbol{q}\cdot\operatorname{grad} T \geq 0. \tag{2.73}$$

On account of the first law of thermodynamics (2.70), we can express the heat terms $\operatorname{div}\boldsymbol{q} - r\rho$ through internal mechanical power and internal energy, i.e.,

$$\mathcal{D} := \underbrace{\boldsymbol{\sigma}:\boldsymbol{D} - \rho\,(\dot{u} - T\dot{s})}_{\mathcal{D}_{\mathrm{int}}} \underbrace{-\frac{1}{T}\,\boldsymbol{q}\cdot\operatorname{grad} T}_{\mathcal{D}_{\mathrm{con}}} \geq 0, \tag{2.74}$$

defining the rate of dissipation $\mathcal{D}$, which quantifies the rate of generated entropy per unit volume. It is composed of the entropy rate generated within the continuum body $\mathcal{D}_{\mathrm{int}}$ and entropy increase through heat conduction or temperature compensation $\mathcal{D}_{\mathrm{con}}$. Not only the sum $\mathcal{D} = \mathcal{D}_{\mathrm{int}} + \mathcal{D}_{\mathrm{con}}$ but both individual constituents are nonnegative (Truesdell and Noll, 2004). The heat conduction inequality $\mathcal{D}_{\mathrm{con}} \geq 0$ expresses that heat flows against a temperature gradient. The Clausius–Planck inequality

$$\mathcal{D}_{\mathrm{int}} = \boldsymbol{\sigma}:\boldsymbol{D} - \rho(\dot{u} - T\dot{s}) \geq 0, \tag{2.75}$$

represents an alternative, stronger form of the second law of thermodynamics. For isothermal processes (T = const.), it provides a particularly important statement

$$\mathcal{D}_{\mathrm{int}} = \boldsymbol{\sigma}:\boldsymbol{D} - \rho\dot{\Psi} \geq 0, \tag{2.76}$$

[2] Entropy is a made-up expression derived from the Greek words ἐν and τρόπος meaning *in* and *direction*, respectively. It can be viewed as the quantitative measure of microscopic disorder (Holzapfel, 2000).

where we introduced the free Helmholtz energy $\Psi = u - Ts$ as the part of the specific internal energy, which is associated with reversible deformations. If the thermodynamic process is reversible, no entropy is generated and the internal dissipation is zero, $\mathcal{D}_{\text{int}} = 0$. Then, on account of Eq. (2.71), the rate of internal mechanical work $\dot{u}$ equals the rate of change of the Helmholtz free energy $\dot{\Psi}$ (Parisch, 2003).

2.1.4 Hyperelasticity

The fundamental relations introduced in Sections 2.1.1 to 2.1.3 characterize kinematics, stresses and balance principles and hold for any continuum body for all times. However, they do not distinguish one material from another. In order to determine the material response, additional equations, namely appropriate constitutive laws, are required. Constitutive laws describe the behavior, i.e., stresses as functions of other field functions such as strain or temperature, of an ideal material. They can be considered as models for the physical behavior of a real material (Holzapfel, 2000).

Elasticity. A material is denoted simple elastic or Cauchy-elastic if the current stress state is determined exclusively by the current state of deformation. Despite path-independence of the stress tensor, the work done by stresses in Cauchy-elastic materials may depend on the deformation path. Hence, such materials are generally not conservative and stresses cannot be derived from a scalar potential function (Ogden, 1997). Several authors argue that the laws of thermodynamics require all Cauchy-elastic materials to be Green-elastic (Coleman and Noll, 1963; Casey, 2005).

Hyperelasticity. Materials for which elastic deformations are reversible and whose stress state can be derived from a potential are called hyperelastic or Green-elastic. In contrast to Cauchy-elastic materials, they are conservative (Parisch, 2003). The potential is given by the reversible part of the specific internal energy u known as Helmholtz free energy

$$\Psi = u - Ts, \tag{2.77}$$

where T is the absolute temperature and s specific entropy, cf. Eq. (2.76). In general, the internal energy u and thus the Helmholtz free energy Ψ are functions of both deformation and temperature. Differentiating Ψ with respect to kinematic state variables at constant temperature yields internal forces (i.e., stresses) defined per unit mass. Entropy is obtained by differentiating Ψ with respect to the state variable temperature when stresses are constant (Ziegler, 1983).

Strain energy density function. Let us restrict our consideration to isothermal processes[3] (T = const.), where free energy is a function of deformation alone. To obtain stresses per unit volume, we introduce the so-called strain energy density function (also known as stored energy function) defined per unit undeformed volume

$$\mathcal{W} = \rho_0 \Psi, \tag{2.78}$$

where ρ_0 denotes the material's density in the reference configuration. In general, strain energy density $\mathcal{W} = \mathcal{W}(\boldsymbol{X}, \boldsymbol{F})$ is a function of the deformation gradient $\boldsymbol{F}$ (2.4) and the position $\boldsymbol{X}$ of a point in the medium. For homogeneous materials with uniform distribution of their internal constituents on the continuum scale and identical material properties in every material point, the position vector $\boldsymbol{X}$ can be dropped as an argument (Parisch, 2003).

Normalization and growth conditions. In the undeformed reference configuration, i.e., where $\boldsymbol{F} = \boldsymbol{I}$, the so-called normalization condition (Holzapfel, 2000) requires strain energy density to vanish

$$\mathcal{W}(\boldsymbol{I}) = 0. \tag{2.79}$$

From physical observation the strain energy function $\mathcal{W}$ must increase with deformation and we additionally require

$$\mathcal{W}(\boldsymbol{F}) \geq 0, \tag{2.80}$$

which restricts ranges of admissible functions used in expressions for the strain energy. The so-called growth conditions (Holzapfel, 2000) imply that $\mathcal{W}$ tends to infinity if the volume ratio J (2.6) approaches either infinity or zero, i.e.,

$$\begin{aligned} \mathcal{W}(\boldsymbol{F}) &\to \infty \quad \text{as} \quad J \to \infty, \\ \mathcal{W}(\boldsymbol{F}) &\to \infty \quad \text{as} \quad J \to 0^+. \end{aligned} \tag{2.81}$$

Physically, this means that expanding a continuum body to infinity or compressing it to a point with singular volume requires an infinite amount of strain energy. Equations (2.79) and (2.80) ensure that the reference configuration is stress-free (Ogden, 1997).

[3] Processes may be considered isothermal if deformations are sufficiently slow and the vicinity of an elastic solid is maintained at constant temperature. Then, heat exchange inside the body and with its surroundings yields temperatures inside the body that practically equal the outside temperature. If, on the other hand, deformations are sufficiently fast, there is no time for considerable heat exchange and the process will be practically adiabatic (Ziegler, 1983).

Polyconvexity. A strain energy function is called polyconvex if it can be expressed as a convex function of the deformation gradient $\boldsymbol{F}$, its cofactor $\operatorname{cof}\boldsymbol{F} = \det(\boldsymbol{F})\boldsymbol{F}^{-\top}$ and its determinant $\det\boldsymbol{F}$ (Ball, 1976), i.e.,

$$\mathcal{W}(\boldsymbol{F}) = \mathcal{W}(\boldsymbol{F}, \operatorname{cof}\boldsymbol{F}, \det\boldsymbol{F}). \tag{2.82}$$

Note that here and in the following we use the same symbol $\mathcal{W}$ for different strain energy density functions in order to keep the notation simple. Polyconvexity of the strain energy density function is required for the proof of existence and uniqueness of the solution and ensures ellipticity of the problem (Marsden and Hughes, 1983). The loss of ellipticity causes material instabilities resulting in negative tangent moduli and hyperbolic partial differential equations (Belytschko et al., 2013).

Objectivity. The strain energy density function must be objective, i.e., the strain energy generated by a certain deformation of an elastic body must be independent of a rotation or translation in space of the deformed body. Hence, the strain energy $\mathcal{W}(\boldsymbol{F})$ must be equal to the strain energy $\mathcal{W}(\boldsymbol{Q}\boldsymbol{F})$ generated by the same motion superimposed with a rigid body motion expressed by the orthogonal tensor $\boldsymbol{Q}$. With the special choice of $\boldsymbol{Q} = \boldsymbol{R}^{\top}$ as the transpose of the proper orthogonal rotation tensor $\boldsymbol{R}$ and using the right polar decomposition (2.8a), we find that the strain energy density function $\mathcal{W}(\boldsymbol{F}) = \mathcal{W}(\boldsymbol{R}^{\top}\boldsymbol{R}\boldsymbol{U}) = \mathcal{W}(\boldsymbol{U})$ is independent of the rotational part of the deformation gradient $\boldsymbol{F} = \boldsymbol{R}\boldsymbol{U}$ (Becker and Bürger, 1975; Holzapfel, 2000). The response of a hyperelastic material depends only on the stretching part of $\boldsymbol{F}$, i.e., the right stretch tensor $\boldsymbol{U}$. The relation

$$\mathcal{W}(\boldsymbol{F}) = \mathcal{W}(\boldsymbol{U}), \tag{2.83}$$

is the necessary and sufficient condition for objectivity of the strain energy when rigid body motions are superimposed (Holzapfel, 2000). Using Eqs. (2.10a) and (2.14) we can express the right Cauchy–Green strain tensor and the Green–Lagrange strain tensor by $\boldsymbol{C} = \boldsymbol{U}^2$ and $\boldsymbol{E} = (\boldsymbol{U}^2 - \boldsymbol{I})/2$, respectively. Hence, on account of Eq. (2.83), an objective strain energy function can also be expressed as a function of the six components of the symmetric material tensors $\boldsymbol{C}$ and $\boldsymbol{E}$, i.e.,

$$\mathcal{W} = \mathcal{W}(\boldsymbol{C}) \quad \text{or} \quad \mathcal{W} = \mathcal{W}(\boldsymbol{E}). \tag{2.84}$$

Isotropy. A hyperelastic material is called isotropic if the strain energy generated by the deformation of a body is independent of the original location and orientation of the body. Hence, the strain energy $\mathcal{W}(\boldsymbol{F})$ generated by a certain motion must equal the strain energy $\mathcal{W}(\boldsymbol{F}\boldsymbol{Q}^{\top})$ generated by the same motion superimposed on an arbitrarily translated and rotated reference configuration whose motion is expressed by the orthogonal tensor $\boldsymbol{Q}$. Now, with the special choice of $\boldsymbol{Q} = \boldsymbol{R}$ and using the left

polar decomposition (2.8b) we obtain $\mathcal{W}(\boldsymbol{F}) = \mathcal{W}(\boldsymbol{V}\boldsymbol{R}\boldsymbol{R}^{\mathsf{T}}) = \mathcal{W}(\boldsymbol{V})$ as the condition for isotropy (Ogden, 1997; Truesdell and Noll, 2004). The condition for isotropy

$$\mathcal{W}(\boldsymbol{F}) = \mathcal{W}(\boldsymbol{V}), \tag{2.85}$$

is fundamentally distinct from the requirement of objectivity (2.83). Objectivity demands observer-independence of the strain energy during rigid body motions, which is a fundamental physical requirement and must hold for all materials. The condition for isotropy (2.85) holds only for a certain class of materials (Holzapfel, 2000). For isotropic materials, to which we will restrict further considerations, strain energy may also be expressed as a function of the six components of the symmetric left Cauchy–Green strain tensor $\boldsymbol{B}$. From Eqs. (2.8a), (2.8b), (2.10a) and (2.10b) we obtain $\boldsymbol{B} = \boldsymbol{V}^2 = \boldsymbol{R}\boldsymbol{U}^2\boldsymbol{R}^{\mathsf{T}} = \boldsymbol{R}\boldsymbol{C}\boldsymbol{R}^{\mathsf{T}}$. Isotropy requires $\mathcal{W}(\boldsymbol{C}) = \mathcal{W}(\boldsymbol{F}^{\mathsf{T}}\boldsymbol{F}) = \mathcal{W}(\boldsymbol{Q}\boldsymbol{F}^{\mathsf{T}}\boldsymbol{F}\boldsymbol{Q}^{\mathsf{T}}) = \mathcal{W}(\boldsymbol{Q}\boldsymbol{C}\boldsymbol{Q}^{\mathsf{T}})$ and substituting $\boldsymbol{R}$ for $\boldsymbol{Q}$ finally yields $\mathcal{W}(\boldsymbol{C}) = \mathcal{W}(\boldsymbol{R}\boldsymbol{C}\boldsymbol{R}^{\mathsf{T}}) = \mathcal{W}(\boldsymbol{B})$. Hence, objective strain energy density functions of isotropic materials can also be formulated using the symmetric spatial tensor $\boldsymbol{B}$, i.e.,

$$\mathcal{W} = \mathcal{W}(\boldsymbol{B}). \tag{2.86}$$

If the requirement of isotropy (2.85) holds, $\mathcal{W}$ is a scalar-valued isotropic tensor function of one variable, e.g., $\boldsymbol{C}$ or $\boldsymbol{B}$. It is then also an invariant of the respective variable $\boldsymbol{C}$ or $\boldsymbol{B}$ (Holzapfel, 2000).

Representation in terms of invariants. According to the representation theorem for invariants (Gurtin, 1981; Truesdell and Noll, 2004), a scalar-valued tensor function that is invariant under rotation may be expressed in terms of the principal invariants of its argument, e.g., $\boldsymbol{C}$ or $\boldsymbol{B}$. The right and left Cauchy–Green stretch tensors $\boldsymbol{C}$ and $\boldsymbol{B}$ have the same eigenvalues, namely the squares of the principal stretches λ_1^2, λ_2^2 and λ_3^2, and the same principal invariants given by Eqs. (2.44a) to (2.44c). Hence, a strain energy density function can also be expressed through

$$\mathcal{W} = \mathcal{W}(I_{\boldsymbol{C}}, II_{\boldsymbol{C}}, III_{\boldsymbol{C}}) = \mathcal{W}(I_{\boldsymbol{B}}, II_{\boldsymbol{B}}, III_{\boldsymbol{B}}), \tag{2.87}$$

which is exclusively valid for isotropic hyperelastic materials (Ogden, 1997; Holzapfel, 2000).

Constitutive equations. By definition, the internal dissipation of hyperelastic materials is zero ($\mathcal{D}_{\text{int}} = 0$). For this class of materials, constitutive equations are derived directly from the Clausius–Planck form (2.76) of the second law of thermodynamics, which degenerates to an equality (Truesdell and Noll, 2004). Considering Eq. (2.71), the Clausius–Planck inequality (2.76) can be expressed using different work conjugate pairs

of stress and rate of deformation tensors. Suppose $\mathcal{W} = \mathcal{W}(\boldsymbol{F})$, then with Eqs. (2.51) and (2.78) we obtain

$$\mathcal{D}_{\text{int}} = \boldsymbol{P} : \dot{\boldsymbol{F}} - \dot{\mathcal{W}} = \left(\boldsymbol{P} - \frac{\partial \mathcal{W}}{\partial \boldsymbol{F}} \right) : \dot{\boldsymbol{F}} = 0, \tag{2.88}$$

where we made use of $\dot{\mathcal{W}} = \partial \mathcal{W}(\boldsymbol{F}) / \partial \boldsymbol{F} : \dot{\boldsymbol{F}}$. Because Eq. (2.88) must hold for all times at every point of the continuum body and for any $\boldsymbol{F}$ and, hence, any $\dot{\boldsymbol{F}}$, the expression in parentheses must vanish (Coleman and Noll, 1963). This yields

$$\boldsymbol{P} = \frac{\partial \mathcal{W}}{\partial \boldsymbol{F}}, \tag{2.89}$$

for the two-point tensors $\boldsymbol{F}$ (2.4) and $\boldsymbol{P}$ (2.34b). For work conjugate pairs of the reference configuration, i.e., the material tensors $\boldsymbol{S}$ (2.37) and $\boldsymbol{E}$ (2.14) or $\boldsymbol{C}$ (2.10a) and with $\dot{\boldsymbol{C}} = 2\dot{\boldsymbol{E}}$ we obtain

$$\boldsymbol{S} = \frac{\partial \mathcal{W}}{\partial \boldsymbol{E}} = 2 \frac{\partial \mathcal{W}}{\partial \boldsymbol{C}}. \tag{2.90}$$

Finally, the constitutive equation for the spatial tensors $\boldsymbol{\sigma}$ (2.34a) and $\boldsymbol{B}$ (2.10b) of the current configuration is given by

$$\boldsymbol{\sigma} = \frac{2}{J} \frac{\partial \mathcal{W}}{\partial \boldsymbol{B}} \boldsymbol{B}. \tag{2.91}$$

Using the invariant representation (2.87) of the strain energy density function $\mathcal{W}(\boldsymbol{C}) = \mathcal{W}(I_C, II_C, III_C)$, applying chain rule, and expressing derivatives with respect to the principal invariants through

$$\frac{\partial I_C}{\partial \boldsymbol{C}} = \boldsymbol{I}, \quad \frac{\partial II_C}{\partial \boldsymbol{C}} = I_C \boldsymbol{I} - \boldsymbol{C}, \quad \frac{\partial III_C}{\partial \boldsymbol{C}} = III_C \boldsymbol{C}^{-1}, \tag{2.92}$$

yields the most general form of a stress relation in material coordinates in terms of the three strain invariants

$$\boldsymbol{S} = 2 \left[\left(\frac{\partial \mathcal{W}}{\partial I_C} + I_C \frac{\partial \mathcal{W}}{\partial II_C} \right) \boldsymbol{I} - \frac{\partial \mathcal{W}}{\partial II_C} \boldsymbol{C} + III_C \frac{\partial \mathcal{W}}{\partial III_C} \boldsymbol{C}^{-1} \right]. \tag{2.93}$$

Similar arguments lead to the spatial counterpart of Eq. (2.93) in the current configuration given by

$$\boldsymbol{\sigma} = \frac{2}{J} \left[III_B \frac{\partial \mathcal{W}}{\partial III_B} \boldsymbol{I} + \left(\frac{\partial \mathcal{W}}{\partial I_B} + I_B \frac{\partial \mathcal{W}}{\partial II_B} \right) \boldsymbol{B} - \frac{\partial \mathcal{W}}{\partial II_B} \boldsymbol{B}^2 \right]. \tag{2.94}$$

Elasticity tensors. Differentiating Eq. (2.90) again with respect to $\boldsymbol{C}$ yields the fourth-order material elasticity tensor

$$\mathbb{C}_0 = 2\frac{\partial \boldsymbol{S}}{\partial \boldsymbol{C}} = 4\frac{\partial^2 \mathcal{W}}{\partial \boldsymbol{C}\partial \boldsymbol{C}}, \tag{2.95}$$

which characterizes the gradient of the second Piola–Kirchhoff stress tensor $\boldsymbol{S}$. It measures the change in stress resulting from a change in strain (Holzapfel, 2000). The first equality in Eq. (2.95) implies the minor symmetries

$$C^0_{ijkl} = C^0_{jilk} = C^0_{ijlk}, \tag{2.96}$$

where C^0_{ijlk} are components of the material elasticity tensor $\mathbb{C}_0$. The second equality in Eq. (2.95) requires the existence of a scalar-valued strain energy function $\mathcal{W}$ and implies the major symmetries

$$C^0_{ijlk} = C^0_{klij}, \tag{2.97}$$

representing a necessary and sufficient condition for hyperelasticity. Hence, major symmetry is equivalent to the existence of a strain energy function (Holzapfel, 2000). Because of the minor symmetries (2.96), only 36 of the 81 components of the fourth-order tensor $\mathbb{C}_0$ are independent. If a strain energy function exists, only 21 independent components remain owing to the major symmetries (2.97). The spatial elasticity tensor is given by

$$\mathbb{C} = 2\frac{\partial \boldsymbol{\sigma}}{\partial \boldsymbol{B}} = \frac{4}{J}\boldsymbol{B}\frac{\partial^2 \mathcal{W}}{\partial \boldsymbol{B}\partial \boldsymbol{B}}\boldsymbol{B}, \tag{2.98}$$

and possesses the same minor and major symmetries as its material counterpart (Marsden and Hughes, 1983; Miehe and Stein, 1992).

Isochoric–volumetric split. Based on the kinematic assumption (2.19), i.e., the multiplicative volumetric–isochoric decomposition of the deformation gradient, we postulate a unique decoupled representation of the strain energy density function of the form

$$\mathcal{W} = \mathcal{W}_{\text{iso}}(I_{\overline{C}}, II_{\overline{C}}) + \mathcal{W}_{\text{vol}}(J) = \mathcal{W}_{\text{iso}}(I_{\overline{B}}, II_{\overline{B}}) + \mathcal{W}_{\text{vol}}(J), \tag{2.99}$$

using the representation theorem for invariants (2.87). In Eq. (2.99), the volumetric potential $\mathcal{W}_{\text{vol}}$ is a strictly convex function with a unique minimum at $J = 1$. The isochoric (distortional) potential $\mathcal{W}_{\text{iso}}$ is a function of the first two strain invariants $I_{\overline{C}} = I_{\overline{B}}$ and $II_{\overline{C}} = II_{\overline{B}}$ of the modified Cauchy–Green strain tensors $\overline{\boldsymbol{C}}$ and $\overline{\boldsymbol{B}}$ (2.23) given by Eq. (2.44) or the relations

$$I_{\overline{C}} = J^{-2/3} I_{\boldsymbol{C}}, \qquad II_{\overline{C}} = J^{-4/3} II_{\boldsymbol{C}}, \qquad III_{\overline{C}} = 1, \tag{2.100a}$$

$$I_{\overline{B}} = J^{-2/3} I_{\boldsymbol{B}}, \qquad II_{\overline{B}} = J^{-4/3} II_{\boldsymbol{B}}, \qquad III_{\overline{B}} = 1. \tag{2.100b}$$

They are known as modified strain invariants and equal the strain invariants of $\boldsymbol{C}$ and $\boldsymbol{B}$ in the limit case of full incompressibility (Penn, 1970; Holzapfel, 2000).

A vast number of constitutive equations of the form (2.99) have been proposed in literature and providing a comprehensive overview is nearly impossible. In the following, selected material models that have proven practical and successful in the fields of civil engineering, mechanical engineering and biomechanics are discussed. The discussion is divided into isochoric and volumetric models and distinguishes phenomenological and physically motivated approaches. The former are mainly concerned with fitting mathematical expressions to experimental data without reference to the mechanism of deformation or the underlying physical structure of the material. The latter consider polymer chain networks on the microscopic scale and employ statistical methods to obtain mathematical formulations on the macroscopic level. Network models provide different strain energy functions depending on the microscopic phenomena accounted for.

First invariant based models. First invariant based models characterize the distortional behavior of hyperelastic materials using the first principal invariant of a strain tensor (2.44a) only. They omit the second principal invariant (2.44b) as an argument of the isochoric strain energy function. This simplification is based on observations that $\partial\mathcal{W}/\partial I\!I$ is often much smaller than $\partial\mathcal{W}/\partial I$. It is not identically zero but $\partial\mathcal{W}/\partial I\!I \ll \partial\mathcal{W}/\partial I$ justifies the approximation $\partial\mathcal{W}/\partial I\!I \approx 0$ (Yeoh and Fleming, 1997). Usually, but not exclusively, the first principal invariant of the modified Cauchy–Green strain tensors $I = I_{\bar{\boldsymbol{C}}} = I_{\bar{\boldsymbol{B}}}$ is used. A particularly simple expression is given by the phenomenological form of the Neo-Hookean model

$$\mathcal{W}_{\text{iso}} = c_1(I-3), \tag{2.101}$$

where the material constant $c_1 = \mu/2$ is directly linked to the shear modulus μ. Despite its simplicity, the Neo-Hookean model (2.101) includes typical effects known from nonlinear elasticity within the small strain domain. It will be shown later that Eq. (2.101) may also be motivated from statistical theory (Treloar, 1943a,b).

In technical applications, elastomers are often reinforced with filler particles, such as carbon black in natural rubber vulcanizates or silica in silicones. These fillers cause a stiffening effect in the large strain domain. The Yeoh model

$$\mathcal{W}_{\text{iso}} = c_1(I-3) + c_2(I-3)^2 + c_3(I-3)^3, \tag{2.102}$$

with the material constants c_1, c_2 and c_3 accounts for this effect by incorporating higher order terms of the first strain invariant (Yeoh, 1990).

Material parameters such as c_1, c_2 and c_3 in Eqs. (2.101) and (2.102) are typically determined by curve fitting to test data. Assuming a dependence of the strain energy

density on the first strain invariant only, the Marlow (2003) model identifies the material response without curve fitting from a single test. The derivation of the model is particularly instructive assuming incompressibility. Compressibility can be included but is not shown here. In uniaxial tension of an incompressible material, the first invariant of the left Cauchy–Green strain tensor is given by

$$I_{\boldsymbol{B}}^{\mathrm{T}} = \lambda_{\mathrm{T}}^2 + 2\lambda_{\mathrm{T}}^{-1}, \tag{2.103}$$

where λ_{T} is the stretch in axial direction. For a general deformation characterized by a certain value of $I_{\boldsymbol{B}}$, we can always find a unique equivalent uniaxial stretch, say λ_{T}, which generates the same value of $I_{\boldsymbol{B}} = I_{\boldsymbol{B}}^{\mathrm{T}}$ because Eq. (2.103) has one root that is greater than one. The strain energy density corresponding to this value of $I_{\boldsymbol{B}}$ is obtained from the integration of the uniaxial stress-strain curve up to the nominal uniaxial strain $\lambda_{\mathrm{T}} - 1$, i.e.,

$$\mathcal{W}_{\mathrm{iso}} = \int_0^{\lambda_{\mathrm{T}}(I_{\boldsymbol{B}})-1} \sigma_0(\varepsilon_0)\,\mathrm{d}\varepsilon_0, \tag{2.104}$$

where ε_0 and σ_0 correspond to the nominal uniaxial strain and the nominal uniaxial traction measured experimentally. Hence, Eq. (2.104) defines the isochoric strain energy density function directly from experimentally measured data.

More recent first invariant based models were proposed by Elías-Zúñiga and Beatty (2002), Beatty (2008), Lopez-Pamies (2010), and Khajehsaeid et al. (2013), among others.

Two invariant based models. Two invariant based models express the isochoric strain energy function in terms of the first two principal invariants of a strain tensor (2.44a) and (2.44b). The first phenomenological model of this kind was presented by Mooney (1940). He assumed an isotropic hyperelastic material that obeys Hooke's law in simple shear and obtained

$$\mathcal{W}_{\mathrm{iso}} = c_1(I - 3) + c_2(II - 3), \tag{2.105}$$

where the proportionality between shear stress and shear strain is expressed by the constant shear modulus $\mu = 2(c_1 + c_2)$. Equation (2.105) became known as the Mooney–Rivlin equation. Rivlin (1948) expressed the isochoric strain energy function as an infinite power series

$$\mathcal{W}_{\mathrm{iso}} = \sum_{i+j=1}^{\infty} c_{ij}(I - 3)^i (II - 3)^j, \tag{2.106}$$

which is typically truncated after a certain number of terms. It contains the Neo-Hooke (2.101), Mooney–Rivlin (2.105) and Yeoh (2.102) models as special cases. Attempts to emphasize the impact of the second invariant such as the Gent and Thomas (1958) model

$$\mathcal{W}_{\mathrm{iso}} = c_1(I - 3) + c_2 \ln \frac{II}{3}, \tag{2.107}$$

did not prove more efficient than the Mooney–Rivlin model (2.105). A large number of two invariant models is available in literature. The interested reader is referred to, e.g., Isihara et al. (1951), Rivlin and Saunders (1951), Hart-Smith (1966), Alexander (1968), James et al. (1975), Haines and Wilson (1979), Kilian (1981), Lambert-Diani and Rey (1999), Pucci and Saccomandi (2002), Attard and Hunt (2004), Amin et al. (2006), Horgan and Saccomandi (2006), Beda (2007), and Carroll (2011).

Principal stretches based models. Valanis and Landel (1967) suggested that the contributions of the strain invariants I and II to the strain energy may be very complex and not easy to determine experimentally. Therefore, they proposed to express $\mathcal{W}_{\text{iso}}$ in terms of the principal stretches λ_1, λ_2 and λ_3 directly. They postulated an additive decomposition of the strain energy into three separate functions

$$\mathcal{W}_{\text{iso}} = \omega(\lambda_1) + \omega(\lambda_2) + \omega(\lambda_3), \tag{2.108}$$

which is known as the Valandis–Landel hypothesis. A computationally simple model obeying this hypothesis was proposed by Ogden (1972a). He used the power series

$$\mathcal{W}_{\text{iso}} = \sum_{i=1}^{N} \frac{\mu_i}{\alpha_i}\left(\lambda_1^{\alpha_i} + \lambda_2^{\alpha_i} + \lambda_3^{\alpha_i} - 3\right), \tag{2.109}$$

where N is a positive integer determining the number of terms. The classical shear modulus can be expressed through

$$\mu = \frac{1}{2}\sum_{i=1}^{N} \mu_i \alpha_i, \tag{2.110}$$

where all terms $\mu_i \alpha_i$ must be larger than zero. The Ogden model (2.109) contains the Neo-Hooke (2.101) and the Mooney–Rivlin (2.105) models as special cases.

Based on the Valandis-Landel hypothesis (2.108), further stretch based models were proposed by Klüppel and Schramm (2000), Shariff (2000), Meissner and Matějka (2003), Drozdov (2007), Horgan and Murphy (2007), as well as Mansouri and Darijani (2014), among others.

True strain based models. The use of constitutive equations based on logarithmic (true) strains is motivated by the assumption of an additive superposition of stresses. If coaxial stretches decompose multiplicatively, an additive composition of the corresponding stresses is provided by the logarithm. The Hencky strain energy function

$$\mathcal{W} = \mathcal{W}_{\text{iso}} + \mathcal{W}_{\text{vol}} = \mu \operatorname{tr}\left(\boldsymbol{\varepsilon}^2\right) + \frac{\Lambda}{2}\left(\operatorname{tr}\boldsymbol{\varepsilon}\right)^2, \tag{2.111}$$

where μ and Λ are the Lamé elastic constants, is often attributed to Hencky (1928, 1931, 1933) but was already proposed in a similar form by Becker (1893). The corresponding finite stress–strain relation[4] is given by

$$\boldsymbol{\tau} = J\boldsymbol{\sigma} = \frac{\partial \mathcal{W}}{\partial \boldsymbol{\varepsilon}} = 2\mu\boldsymbol{\varepsilon} + \Lambda(\ln J)\boldsymbol{I}, \tag{2.112}$$

which is a generalization of Hooke's law

$$\boldsymbol{\sigma} = 2\mu\boldsymbol{\varepsilon}_0 + \Lambda(\operatorname{tr}\boldsymbol{\varepsilon}_0)\boldsymbol{I}, \tag{2.113}$$

by the replacement of the infinitesimal strain tensor $\boldsymbol{\varepsilon}_0$ by the Hencky strain tensor $\boldsymbol{\varepsilon}$ (Bruhns et al., 2001). Anand (1979) showed that this simple strain energy function with the two classical Lamé constants is in good agreement with a wide class of materials for moderately large deformations. Other forms of true strain based constitutive equations are provided by Anand (1986), Criscione et al. (2000), Xiao (2012), and Neff et al. (2015), among others.

Network models. Amorphous polymers are composed of bundles of highly flexible long-chain molecules. The polymer chains are cross-linked to form a network. Constitutive equations for the network can be derived from statistical theory and the physical properties of individual chain segments between tie points (Guth and Mark, 1934; Kuhn, 1938, 1946). The contour length of such a segment is denoted L and the distance between its two tie points is called end-to-end distance r. The distance r characterizes the molecular conformation (different shapes or arrangements) of a chain molecule. If the end-to-end distance equals the chain length ($r = L$), only one possible conformation exists. The smaller the end-to-end distance, the larger the number of possible conformations of the polymer chain. The entropy of a single chain is related to the probability of thermodynamic states, i.e., molecular conformations. According to Boltzmann's principle, it is proportional to the logarithm of the probability of a certain end-to-end distance r. Stretching a polymer network increases the end-to-end distance, reduces the number of possible conformations and, hence, reduces entropy. Reactive forces of ideal rubbers are determined purely by changes in entropy. Therefore, they are denoted entropic elastic materials[5].

The polymer chain itself is assembled from a number of monomers, i.e., chemically identical units. This structure is modeled as a chain of n rigid beam segments[6] of

[4] In general, $\boldsymbol{\varepsilon}$ and $\boldsymbol{\tau}$ do not constitute a pair of work conjugate variables as introduced in Section 2.1.3. For the particular case of isotropy, however, Bruhns et al. (2000) have shown that $\boldsymbol{\varepsilon}$ and $\boldsymbol{\tau}$ are a conjugate pair.

[5] In contrast, elasticity of energetic elastic materials such as metals, glasses, ceramics or crystals arises from the removal of atoms from their equilibrium positions. This causes rapid changes in internal energy but no change in entropy (Hill, 1975).

[6] Often denoted Kuhn segments.

length l, which can rotate freely with respect to each other. The contour length of the chain is given by $L = nl$. Statistical considerations (random walk) yield the end-to-end distance $r_0 = \sqrt{n}l$ of a stress-free undeformed chain (Kuhn, 1934). This motivates the introduction of a chain stretch $\lambda^* = r/r_0$.

For small strains, i.e., $r \ll L$, the probability of a certain end-to-end distance r of a single chain can be described by a Gaussian distribution. Since the internal energy (2.68) of an ideal incompressible rubber does not change with deformation, the change of the free Helmholtz energy (2.77) is determined by the change of entropy alone and the stored energy of a single (Gaussian) chain is given by

$$\mathcal{W}_{\mathrm{G}}^* = \frac{3}{2}\mathrm{k_B}T\left(\lambda^*\right)^2 + \mathcal{W}_0, \tag{2.114}$$

where $\mathrm{k_B}$ is the Boltzmann constant, T the absolute temperature, $\lambda^* = r/r_0$ the chain stretch and $\mathcal{W}_0$ a constant. At large deformations (approximately $r/L \geq 0.4$), the observed stress–stretch behavior departs significantly from that predicted by the Gaussian model and so-called non-Gaussian effects, i.e., finite chain extensibility must be accounted for. Kuhn and Grün (1942) used Langevin chain statistics to account for the effect of the relative chain length r/L on configurations available to the chain. The resulting stored energy of a single (Langevin) chain with n monomers is given by

$$\mathcal{W}_{\mathrm{L}}^* = \mathrm{k_B}Tn\left[\frac{\lambda^*}{\sqrt{n}}\beta + \ln\left(\frac{\beta}{\sinh\beta}\right)\right] + \mathcal{W}_0, \qquad \beta = \mathcal{L}^{-1}\left(\frac{\lambda^*}{\sqrt{n}}\right), \tag{2.115}$$

where $\mathcal{L}^{-1}$ denotes the inverse of the Langevin function $\mathcal{L}(x) = \coth(x) - x^{-1}$. Macroscopic constitutive models are derived by averaging the energies of an ensemble of m chains, i.e.,

$$\mathcal{W}_{\mathrm{iso}} = N\langle\mathcal{W}^*\rangle \approx \frac{N}{m}\sum_{i=1}^{m}\mathcal{W}^*(\lambda_i^*), \tag{2.116}$$

where N is the chain density per unit volume and $\langle\,\cdot\,\rangle$ denotes the arithmetic mean. The accuracy of the macroscopic model depends on how realistically the ensemble represents the true polymer network.

Considering three chains oriented along the principal axes and accounting for Eq. (2.79), Eqs. (2.114) and (2.116) yield the Neo-Hookean material model in the form

$$\mathcal{W}_{\mathrm{iso}} = \frac{1}{2}N\mathrm{k_B}T(I_{\boldsymbol{B}} - 3), \tag{2.117}$$

which relies on the assumption $r \ll L$ and, hence, is valid for small strains only (Treloar, 1943a,b). Comparison with Eq. (2.101) yields $\mu = N\mathrm{k_B}T$ for the shear modulus. Considering Langevin chains and Eqs. (2.115) and (2.116), many network models have been

proposed for large deformations. Among others, these are the three-chain, the four-chain, the eight-chain and full network models. The three-chain model by James and Guth (1943) and Wang and Guth (1952) considers chains oriented in the principal directions of deformation. Chain deformations are assumed affine. That is, it is assumed that all chains deform in accordance with the entire network. The four-chain model of Flory and Rehner (1943) and Treloar (1946) represents the polymer network by four chains connected to the corners of a tetrahedron. The tetrahedron deforms in accordance with the macroscopic deformation. However, the displacement of the central junction point is determined by an equilibrium condition. Hence, chain deformations are non-affine (see also Flory, 1944). The eight-chain model by Arruda and Boyce (1993) results in a single non-affine network stretch representative for all chains (see also Beatty, 2003). Instead of considering certain chain arrangements, full network models assume randomly oriented chains. Treloar (1954) and Treloar and Riding (1979) proposed affine full network models for uniaxial and biaxial deformations, respectively. Wu and van der Giessen (1992) provided a three-dimensional formulation, which was extended to non-affine deformations by Wu and van der Giessen (1993). Boyce and Arruda (2000) argue that non-affine models provide more realistic results than affine models even when considering simplified chain arrangements.

The above micro-mechanical models allow for free motions of all chains. Hence, no molecular interactions are considered and polymer chains may freely penetrate each other. In real networks, single chain movements are subjected to certain topological constraints. Among others, Ronca and Allegra (1975) and Flory (1977) impose topological constraints at chain junctions (constrained junction theory). The so-called tube model approach by Edwards and Vilgis (1986) and Heinrich and Kaliske (1997) applies constraints along the chain contour (constrained segment theory). The idea of tube-like topology constraints is reported to agree well with small-angle neutron scattering experiments by Straube et al. (1994, 1995). In their extended tube model, Kaliske and Heinrich (1999) replace the Gaussian chain assumption of Heinrich and Kaliske (1997) by a non-Gaussian distribution of the end-to-end distance to account for finite extensibility. Miehe et al. (2004) provide a non-affine full network model with tube-like constraints considering randomly oriented Langevin chains (2.115) and employing a numerical integration scheme to average their contributions to the macroscopic strain energy. Further refinements of the above theories are given by Diani and Gilormini (2005), Bechir et al. (2010), Itskov et al. (2010), Kroon (2011), and Davidson and Goulbourne (2013).

Comparisons of the vast number of constitutive models are given by Boyce and Arruda (2000), Seibert and Schöche (2000), Marckmann and Verron (2006), Steinmann et al. (2012), and Beda (2014). For unfilled rubbers, the experimental data sets of Treloar (1944) and Kawabata et al. (1981) are often used as benchmarks. For this class of materials, Marckmann and Verron (2006) recommend the Ogden model (Ogden, 1972a), the

extended-tube model (Kaliske and Heinrich, 1999), the Shariff model (Shariff, 2000), and the tube-like microsphere model (Miehe et al., 2004) as they prove capable of capturing stress-strain relations of unfilled rubbers in several different states of deformation. Comparisons of constitutive models for silicones are given by Staudt et al. (2014), Dias et al. (2014), and Dispersyn et al. (2017), who report difficulties in reproducing the stress–strain response of several different experiments with the same set of model parameters.

Volumetric models. In Eq. (2.99) we postulated a unique volumetric strain energy function $\mathcal{W}_{\text{vol}} = \mathcal{W}_{\text{vol}}(J)$ as a function of the volume ratio $J = \det \boldsymbol{F}$ alone. In order to satisfy the normalization condition (2.79), the volumetric strain energy function must take on its unique minimum $\mathcal{W}_{\text{vol}} = 0$ in the undeformed state ($J = 1$). To fulfill the growth conditions (2.81) it must become infinite for indefinite expansion ($J \to \infty$) and total compression ($J \to 0$). For the undeformed state to be free of hydrostatic stresses, the derivative

$$p = \frac{\mathrm{d}\mathcal{W}_{\text{vol}}}{\mathrm{d}J}, \tag{2.118}$$

where p is the hydrostatic pressure, must vanish at $J = 1$. Further, hydrostatic stresses must generate an infinite resistance against total compression ($\mathcal{W}'_{\text{vol}} \to -\infty$ as $J \to 0$) and against indefinite expansion ($\mathcal{W}'_{\text{vol}} \to +\infty$ as $J \to \infty$). Convexity requires $\mathcal{W}''_{\text{vol}} \geq 0$ so that hydrostatic stresses always increase with J. Note that for nearly incompressible materials the scalar function p is specified by a constitutive equation (2.118). Here, the hydrostatic pressure is defined as positive so that p and J are work conjugate scalars (Holzapfel, 2000; Parisch, 2003).

A simple volumetric model that is often used in finite element implementations is given by

$$\mathcal{W}_{\text{vol}} = \frac{K}{2}(J-1)^2, \tag{2.119}$$

where K is the bulk modulus. It describes a linear relation between volume change and hydrostatic pressure and provides unphysical finite hydrostatic stresses as $J \to 0$. Boyce and Arruda (2000) report a nonlinear relationship between pressure and volume change for $0.75 < J < 1$ contradicting the linear prediction of Eq. (2.119). Extending Eq. (2.119) by the natural logarithm according to

$$\mathcal{W}_{\text{vol}} = \frac{K}{4}\left((J-1)^2 + (\ln J)^2\right), \tag{2.120}$$

as suggested by Simo and Taylor (1982), corrects this characteristic. Using the correction term only

$$\mathcal{W}_{\text{vol}} = \frac{K}{2}(\ln J)^2, \tag{2.121}$$

as done by Simo et al. (1985) for plasticity, violates convexity and yields decreasing hydrostatic stresses, i.e., $\mathcal{W}''_{\text{vol}} < 0$ for $J > \text{e}$, where e is Euler's number. Ogden (1972b) proposed a general volumetric model

$$\mathcal{W}_{\text{vol}} = \frac{K}{\beta^2}\left(\frac{1}{J^\beta} - 1 + \beta \ln J\right), \tag{2.122}$$

that satisfies all of the above requirements. His formulation was applied by Simo and Taylor (1991) with $\beta = -2$, and by Miehe (1994) with $\beta = -1$, among others. Hartmann and Neff (2003) suggest new convex volumetric models and provide a comprehensive overview of existing formulations.

In practical applications of nearly incompressible materials, volumetric deformations often remain small ($0.9 < J < 1.1$). In this domain, the differences between the above models (2.119) to (2.122) are minor and even Eq. (2.119), which violates basic physical principles, yields good results. However, when volumetric deformations become large, rubber-like materials are prone to cavitation. The formation of cavities changes the material response considerably but is not necessarily associated to catastrophic failure. Drass et al. (2018c) propose a general volumetric strain energy function in the form

$$\mathcal{W}_{\text{vol}} = \int_J \frac{J-1}{\sum_{i=0}^{m} d_i (J-1)^i}\,\mathrm{d}J, \tag{2.123}$$

where m is a positive integer, in order to account for stress softening after the onset of cavitation. The bulk modulus is obtained as $K = 1/d_0$. With appropriate choices of the parameters d_i, Eq. (2.123) reproduces the material responses of Eqs. (2.119) to (2.122).

2.2 Bulk material failure

An evaluation of the strength or maximum extensibility of materials in uniaxial tension or compression is relatively simple and widely investigated. Determining critical states under multiaxial loading is more involved and requires extensive experimental programs. Because not all possible stress or strain states can be examined experimentally (for both practical and economical reasons), the generation, interpretation and use of failure criteria goes back to the origins of the overall field of mechanics (see, e.g., Coulomb, 1773). A compelling reason for this is that the safe and efficient use of materials requires an understanding of limits of their integrity in any situation (Christensen, 1997b).

Failure criteria can be formulated in one of two ways: they can be derived from the microstructure or simply provided as mathematical expression that interpolate between experimental data. The well-known Gurson (1977) criterion, for instance, was developed

using the former approach. The following sections introduce the main aspects of the formulation of the latter (phenomenological) failure criteria for isotropic materials. The discussion is based on the comprehensive monographs by Chen and Zhang (1991), Christensen (2013), and Kolupaev (2018).

Failure surface. A safe region, where a material can sustain multiaxial loads indefinitely, can be described in either stress, strain or stretch space. Accordingly, a region where the material will fail exists in either space. Both regions are separated by a failure surface. A function representing all points on this surface is called failure criterion or yield[7] function.

Equivalent stress. The three eigenvalues $(\sigma_{\mathrm{I}}, \sigma_{\mathrm{II}}, \sigma_{\mathrm{III}})$ of the Cauchy stress tensor (2.34a) are denoted principal stresses. They are invariants of the stress tensor and their direction vectors are its principal directions (eigenvectors). The so-called Haigh–Westergaard space (also known as principal stress space) is spanned by the principal stresses as coordinate axes. A hypersurface Φ in principal stress space constitutes a failure condition according to

$$\Phi(\boldsymbol{\sigma}) = 0, \tag{2.124}$$

where $\boldsymbol{\sigma}$ is the Cauchy stress tensor (2.34a). The material can sustain loads for which $\Phi(\boldsymbol{\sigma}) < 0$. Stress states associated to failure are given by $\Phi(\boldsymbol{\sigma}) \geq 0$. In order to formulate a failure criterion, we introduce an equivalent stress function $\sigma_{\mathrm{eq}}(\boldsymbol{\sigma})$ that transforms the tensor-valued input $\boldsymbol{\sigma}$ into a scalar quantity. Failure occurs when the equivalent stress assumes its critical value σ_{c}. This provides a description of the failure surface and, hence, a failure criterion according to

$$\Phi(\boldsymbol{\sigma}) = \sigma_{\mathrm{eq}}(\boldsymbol{\sigma}) - \sigma_{\mathrm{c}} = 0. \tag{2.125}$$

The equivalent stress allows for comparing multiaxial stress states. They coincide with the failure surface when

$$\frac{\sigma_{\mathrm{eq}}(\boldsymbol{\sigma})}{\sigma_{\mathrm{c}}} = 1. \tag{2.126}$$

Accounting for different failure modes, sometimes requires the use of different equivalent stress functions and different corresponding thresholds for each failure mode. This will be addressed in the end of this section. Note that in the following we use the same symbol σ_{eq} for different equivalent stress functions in order to keep the notation simple.

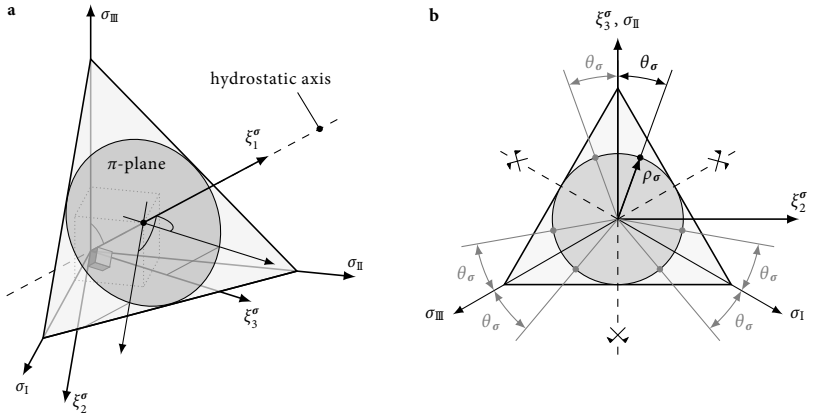

Fig. 2.1 Deviatoric plane (π-plane): **a** in Haigh–Westergaard space $(\sigma_I, \sigma_{II}, \sigma_{III})$ with $(\xi_1^\sigma, \xi_2^\sigma, \xi_3^\sigma)$-coordinate system, **b** with Haigh–Westergaard coordinates $(\xi_1^\sigma, \rho_\sigma, \theta_\sigma)$ and projection of principal axes $(\sigma_I, \sigma_{II}, \sigma_{III})$.

Deviatoric plane. Stress states on the hydrostatic axis ($\sigma_I = \sigma_{II} = \sigma_{III}$) are characterized by vanishing deviatoric stresses and, hence, correspond to pure hydrostatic tension or pressure. Cuts perpendicular to this axis are denoted deviatoric plane, octahedral plane or π-plane (Chen and Zhang, 1991). Points in the π-plane describe deviatoric stress states at constant hydrostatic tension or pressure. The deviatoric plane through the coordinate origin is denoted π_0-plane and corresponds to vanishing hydrostatic pressure. It is spanned by the axes

$$\xi_2^\sigma = \frac{1}{\sqrt{2}}(\sigma_I - \sigma_{III}), \tag{2.127a}$$

$$\xi_3^\sigma = \frac{1}{\sqrt{6}}(-\sigma_I + 2\sigma_{II} - \sigma_{III}). \tag{2.127b}$$

Together with the hydrostatic axis they constitute an orthogonal right-handed coordinate system (Fig. 2.1a). The coordinate transformation is expressed by

$$\begin{bmatrix} \sigma_I \\ \sigma_{II} \\ \sigma_{III} \end{bmatrix} = \frac{1}{\sqrt{6}} \begin{bmatrix} \sqrt{2} & \sqrt{3} & -1 \\ \sqrt{2} & 0 & 2 \\ \sqrt{2} & -\sqrt{3} & -1 \end{bmatrix} \begin{bmatrix} \xi_1^\sigma \\ \xi_2^\sigma \\ \xi_3^\sigma \end{bmatrix}. \tag{2.128}$$

[7] For historical reasons, theoretical works on multiaxial failure often use the denomination yield function even when damage or brittle failure is considered. Bigoni and Piccolroaz (2004) argue that in phenomenological approaches there is no need to distinguish between these situations because all are based on the same concept, i.e., a permissible stress or strain range, bounded by a hypersurface defined in stress or strain space.

A similar representation is provided by the cylindrical Haigh–Westergaard[8] or Lode coordinates (Haigh, 1920; Westergaard, 1920; Lode, 1926), given by

$$\xi_1^\sigma = \frac{1}{\sqrt{3}} I_\sigma, \tag{2.129a}$$

$$\rho_\sigma = \sqrt{2 I\!I'_\sigma}, \tag{2.129b}$$

$$\theta_\sigma = \frac{1}{3} \arccos\left(\frac{3\sqrt{3}}{2} \frac{I\!I\!I'_\sigma}{(I\!I'_\sigma)^{3/2}} \right). \tag{2.129c}$$

where ξ_1^σ corresponds to the hydrostatic axis, ρ_σ represents the radial distance from the hydrostatic axis and θ_σ is called meridian angle or Lode angle. Owing to isotropy and arbitrariness of ordering eigenvalues of the Cauchy stress tensor, the meridian angle $\theta_\sigma \in [0, \pi/3]$ corresponds to six different points in the π-plane (Fig. 2.1b). As a result, cross sections of Φ are symmetric about projections of the principal axes σ_{I}, σ_{II} and σ_{III} onto the π-plane. The meridian angle (2.129c) may be replaced by

$$\varphi_\sigma = \frac{1}{3} \arcsin\left(-\frac{3\sqrt{3}}{2} \frac{I\!I\!I'_\sigma}{(I\!I'_\sigma)^{3/2}} \right). \tag{2.130}$$

Meridian plane. The deviatoric plane (Fig. 2.1b) shows the Lode-dependence of a failure criterion, i.e., the dependence of the radius of cross sections of the failure surface Φ on the meridian angle θ. The meridian plane adds information on the pressure-sensitivity of the criterion, i.e., on the dependence on the first invariant of the stress tensor. It is also know as Burzyński plane and uses the second invariant of the stress deviator $I\!I'_\sigma$ and the first invariant of the stress tensor I_σ as coordinate axes. The invariants are often scaled and normalized so that the von Mises criterion appears as a parallel to the abscissa at unit value (Fig. 2.2). For $I\!I\!I'_\sigma$-sensitive criteria, different meridians with $\theta_\sigma = \text{const.}$ can be displayed.

Failure modes. Isotropic materials may exhibit two modes of failure, each associated to a particular safe region and failure surface (Cuntze, 1996; Christensen, 1997b). The intersection of all safe regions constitutes the safe region of the material. Its surface is the material failure surface. Nearly incompressible elastomers possess a dilatational and a distortional failure mode (Blatz, 1963; Lindsey, 1967). Historically, distortional failure criteria were developed mainly for metals. Dilatational failure criteria are often formulated specifically for nearly incompressible elastomers.

[8] Note the difference between Haigh–Westergaard space $(\sigma_{\mathrm{I}}, \sigma_{\mathrm{II}}, \sigma_{\mathrm{III}})$ and Haigh–Westergaard coordinates $(\xi_1^\sigma, \rho_\sigma, \theta_\sigma)$ (Chen and Zhang, 1991).

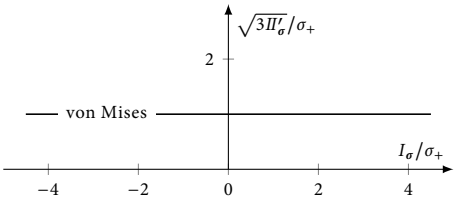

Fig. 2.2 Meridian plane (Burzyński plane) scaled so that the von Mises criterion appears at a value of one as a parallel to the abscissa, where σ_+ corresponds to the uniaxial tensile strength.

Distortional failure criteria. Distortional failure denotes failure owing to deviatoric stress at vanishing or constant subcritical hydrostatic stress. The respective failure surface is coaxial with the hydrostatic axis. However, its π-plane cross section is not necessarily constant along the hydrostatic axis. This property is known as pressure-sensitivity of the material. The first distortional failure hypothesis was formulated by Coulomb (1773) and elaborated by Tresca (1868). Their criterion postulates failure when the maximum shear stress reaches a critical value. In terms of principal stresses this is expressed by

$$\sigma_{\mathrm{eq}}(\boldsymbol{\sigma}) = \max\{\sigma_{\mathrm{I}}, \sigma_{\mathrm{II}}, \sigma_{\mathrm{III}}\} - \min\{\sigma_{\mathrm{I}}, \sigma_{\mathrm{II}}, \sigma_{\mathrm{III}}\} = \sigma_{\mathrm{I}} - \sigma_{\mathrm{III}}. \tag{2.131}$$

Equation (2.131) is known as Tresca criterion and typically applies to ductile metals (Altenbach et al., 1995). Rankine (1876) postulated brittle failure at a critical value of the maximum principal stress, i.e.,

$$\sigma_{\mathrm{eq}}(\boldsymbol{\sigma}) = \max\{\sigma_{\mathrm{I}}, \sigma_{\mathrm{II}}, \sigma_{\mathrm{III}}\} = \sigma_{\mathrm{I}}. \tag{2.132}$$

The Rankine criterion (2.132) describes pressure-sensitive material behavior. That is, its π-plane cross section changes with the first stress invariant I_σ. Assuming a critical value of the distortional part of the strain energy density, von Mises (1913) proposed a failure criterion of the form

$$\sigma_{\mathrm{eq}}(\boldsymbol{\sigma}) = \sqrt{3II'_\sigma}, \tag{2.133}$$

which allows for direct comparison with the uniaxial tensile strength σ_+. The von Mises criterion (2.133) was developed as a yield criterion for ductile materials (Altenbach et al., 1995). However, owing to its simplicity, it has become one of the most widely used criteria for many classes of materials in the fields of mechanical and civil engineering. A pressure-insensitive version of the Rankine criterion (2.132) is given by the so-called Mariotte[9] criterion of maximum deviatoric stress

$$\sigma_{\mathrm{eq}}(\boldsymbol{\sigma}) = \frac{3}{2}\left(\sigma_{\mathrm{I}} - \frac{1}{3}I_\sigma\right), \tag{2.134}$$

[9] Attributed to Edme Mariotte (Altenbach et al., 1995).

where σ_{I} is the maximum principal stress. Conversely, Ivlev (1959) proposed a threshold of the mean deviatoric stress according to

$$\sigma_{\mathrm{eq}}(\boldsymbol{\sigma}) = I_{\boldsymbol{\sigma}} - 3\sigma_{\mathrm{III}}, \tag{2.135}$$

where σ_{III} is the minimum principal stress. All of the above criteria as so-called zero-parameter criteria. They are based on certain physical assumptions and contain no shape parameter.

Because zero-parameter criteria are often too primitive to capture the complex Lode-dependence of experimental data, in particular for polymers, many generalizations of these criteria with one or more shape parameters were proposed. An overview of shapes of zero-parameter criteria and generalized criteria in the π-plane is given in Fig. 2.3. Among these generalized criteria there are

- the Mohr–Coulomb criterion (Mohr, 1900), which is a linear combination of the Rankine criterion (2.132) and the Tresca criterion (2.131),
- the Burzyński–Yagn criterion (Burzyński, 1928; Yagn, 1931), a second-order polynomial of the principal stresses,
- the Drucker–Prager criterion (Drucker and Prager, 1952), a pressure-sensitive generalization of the von Mises criterion (2.133),
- the Mariotte–St. Venant criterion (Filonenko-Boroditsch, 1963) assuming failure at a maximum principal strain threshold,
- the Pisarenko–Lebedev criterion (Pisarenko and Lebedev, 1968), which is a linear combination of the Rankine criterion (2.132) and the von Mises criterion (2.133),
- the criteria of Haythornthwaite (1960) and Capurso (1967), which are sixth-order polynomials of the deviatoric stress invariants,
- the Sayir criterion (Sayir and Ziegler, 1969; Sayir, 1970), a linear combination of the Mariotte (2.134) and Ivlev (2.135) criteria,
- and the criteria of hexagonal symmetry of Sokolovsky (1969) and Ishlinsky and Ivlev (2003), which are twelfth-order polynomials of the deviatoric stress invariants.

Particularly useful generalizations are given by the modified Altenbach–Zolochevsky criterion introduced by Kolupaev (2017) and the Podgórski (1985) criterion. The former is an extension of the criterion presented by Altenbach et al. (1995). Normalized with

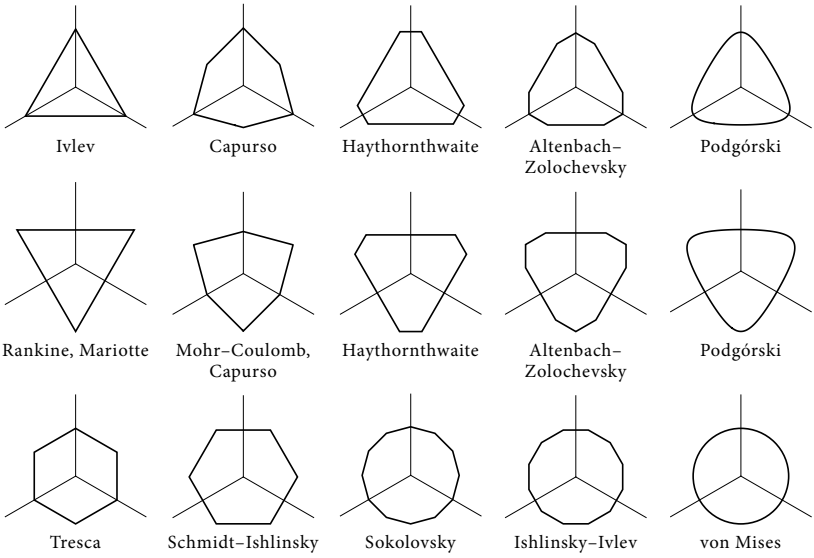

Fig. 2.3 Classical and generalized failure criteria in the π-plane with projections of the principal stress coordinate axes as symmetry axes.

respect to the uniaxial tensile strength it reads

$$\sigma_{\mathrm{eq}}(\boldsymbol{\sigma}) = \sqrt{\frac{3}{2}}\,\rho_\sigma \left[\left(\frac{1}{\alpha} - 1 \right) \sin\varphi_\sigma + \frac{1 + \alpha - 2\alpha\beta}{\sqrt{3}\alpha} \cos\varphi_\sigma + \beta \sin\left(\frac{\pi}{6} + \arcsin(\cos\varphi_\sigma) \right) \right], \tag{2.136}$$

where α and β are shape parameters and ρ_σ and φ_σ are π-plane coordinates introduced in Eqs. (2.129b) and (2.130). The criterion is convex for

$$0 \le \beta \le \begin{cases} 2 - \frac{1}{\alpha}, & \alpha \in \left[\frac{1}{2}, 1\right], \\ \frac{2}{\alpha} - 1, & \alpha \in [1, 2]. \end{cases} \tag{2.137}$$

Within these parameter ranges, it comprises several classical criteria and certain generalizations, e.g.,

- the Tresca criterion ($\alpha = 0.5, \beta = 0$),
- the Ivlev criterion ($\alpha = 1, \beta = 0$),

- the Mariotte criterion $(\alpha = 2, \beta = 0)$,
- the Schmidt–Ishlinsky criterion $(\alpha = 1, \beta = 1)$,
- the Sokolovsky criterion $(\alpha = 1, \beta = 0.5)$,
- and the Capurso criterion $(\alpha \in [0.5, 2], \beta = 0)$.

However, it is only $\mathcal{C}^0$-continuous and only describes some of the π-plane shapes shown in Fig. 2.3. For instance, the von Mises criterion or the Haythornthwaite criterion are not included. The Podgórski (1985) criterion can describe $\mathcal{C}^1$-continuous yield or failure surfaces. In the notation of the present work and normalized to uniaxial tensile strength, it is given by

$$\sigma_{\mathrm{eq}}(\boldsymbol{\sigma}) = \sqrt{\frac{3}{2}}\,\rho_\sigma \frac{\cos\left(\frac{1}{3}\left(\pi\beta - \arccos\left(\alpha\cos\left(3\theta_\sigma\right)\right)\right)\right)}{\cos\left(\frac{1}{3}\left(\pi\beta - \arccos\alpha\right)\right)}, \tag{2.138}$$

where $\alpha \in [0,1]$ and $\beta \in [0,1]$ are shape parameters and ρ_σ and θ_σ are π-plane coordinates according to Eqs. (2.129b) and (2.129c). The Pogórski criterion (2.138) comprises

- the Mariotte criterion $(\alpha = 1, \beta = 0)$,
- the Tresca criterion $(\alpha = 1, \beta = 0.5)$,
- the Ivlev criterion $(\alpha = 1, \beta = 1)$,
- the Capurso criterion $(\alpha = 1, \beta \in [0,1])$,
- the Sayir criterion $(\alpha \in [0,1], \beta \in \{0,1\})$,
- the von Mises criterion $(\alpha = 0, \beta \in [0,1])$,

and is $\mathcal{C}^1$-continuous for $\alpha < 1$. However, it cannot assume the shape of the Haythornthwaite (1960) criterion nor describe yield surfaces of hexagonal symmetry such as the Schmidt–Ishlinsky, Sokolovsky or Ishlinsky–Ivlev criteria (Fig. 2.3). Nonetheless, Kolupaev (2017, 2018) recommends the modified Altenbach–Zolochevsky criterion (2.136) and the Podgórski criterion (2.138) as the best available criteria for application because they describe a single convex surface without additional outer contours and because of their adaptability.

Dilatational failure criteria. Dilatational failure of nearly incompressible elastomers, i.e., failure due to hydrostatic stress, corresponds to the formation of cavities. The phenomenon was first noticed by Busse (1938) and Yerzley (1939) and engages researchers to the present day (Drass et al., 2018c; Santarsiero et al., 2018; Nelson, 2019). Cavitation is typically treated as a problem of elastic instability (Fond, 2001). Green and Zerna (1954) showed that a hollow sphere of Neo-Hookean material under hydrostatic stress will inflate indefinitely once the applied stress reaches a certain threshold. For a spherical

cavity in an incompressible infinite Neo-Hookean solid, this elastic stability limit is given by

$$p_c = \frac{5}{2}\mu, \tag{2.139}$$

where p_c is the critical hydrostatic stress (2.46) corresponding to infinite inflation and μ the material's shear modulus (Green and Zerna, 1954). Gent and Lindley (1959) were able to associate p_c with the onset of cavitation and confirmed the proportionality to μ in Eq. (2.139) experimentally. In his mathematical analysis of stability conditions for spherical cavities under hydrostatic loading, Ball (1982) coined the denomination of a bifurcated solution, which differs from the solution without cavities. The above studies implicitly presume the presence of microcavities, e.g., in the form of gas bubbles dissolved during material processing (Lindsey, 1967).

On account of Eq. (2.139), an invariant-based failure criterion in the form (2.125) may be formulated as

$$\sigma_{eq}(\boldsymbol{\sigma}) = \frac{I_{\boldsymbol{\sigma}}}{3}, \tag{2.140}$$

where the corresponding threshold $\sigma_c = 5\mu/2$ is known from Eq. (2.139). The first invariant of the Cauchy stress tensor $I_{\boldsymbol{\sigma}}$ can become large even under volume-preserving deformations. Failure (cavitation) predictions by Eq. (2.140) do not agree with observations in, e.g., uniaxial or biaxial tensile tests. Hence, it is only applicable to states of homogeneous triaxial tension. In order to resolve this issue, Hou and Abeyaratne (1992) use variational arguments to propose a void growth criterion for arbitrary triaxial stress states that yields the equivalent stress

$$\sigma_{eq}(\boldsymbol{\sigma}) = \left(\frac{8}{27}I_{\boldsymbol{\sigma}}^3 - \frac{50}{3}I_{\boldsymbol{\sigma}}II'_{\boldsymbol{\sigma}} + 125III'_{\boldsymbol{\sigma}}\right)^{\frac{1}{3}}, \tag{2.141}$$

where, for consistency with Eq. (2.139), the threshold is given by $\sigma_c = 5\mu$. Chang et al. (1993) determine the bifurcation point of a single void under complex loads numerically and obtain similar results. Lopez-Pamies et al. (2011a) compute instabilities of randomly distributed, disconnected, zero-volume cavities under arbitrary triaxial stress in finite element analyses. From this study, Lopez-Pamies et al. (2011b) derive an approximate closed-form cavitation criterion that reads

$$\sigma_{eq}(\boldsymbol{\sigma}) = \left[8\left(\frac{I_{\boldsymbol{\sigma}}^3}{9} - \frac{I_{\boldsymbol{\sigma}}II'_{\boldsymbol{\sigma}}}{3} + III'_{\boldsymbol{\sigma}}\right) - 12\mu\left(\frac{I_{\boldsymbol{\sigma}}^2}{3} - II'_{\boldsymbol{\sigma}}\right) + 18\mu^2 I_{\boldsymbol{\sigma}}\right]^{\frac{1}{3}}. \tag{2.142}$$

With $\sigma_c = \sqrt[3]{35}\mu$, they recover the result of Eq. (2.139) for homogeneous hydrostatic tension. Considering multiple voids, Eq. (2.142) is considerably more conservative than Eq. (2.141) for inhomogeneous hydrostatic tensile stress.

Although the above criteria only account for the growth of existing cavities and not for the formation of new surfaces, i.e., cracking, instable void growth is an important phenomenon. Expanded cavities may grow further, coalesce and eventually form macroscopic cracks (Creton et al., 2001; Creton and Ciccotti, 2016).

Pressure sensitivity Materials are denoted pressure-sensitive when hydrostatic stresses affect distortional failure, i.e., when their π-plane cross sections depend on $I_{\boldsymbol{\sigma}}$ and change along the hydrostatic axis. Ductile metals are typically pressure-insensitive (at least for $I_{\boldsymbol{\sigma}} < 0$) and their failure surface is described by a prism centered around the hydrostatic axis. Rock or concrete are often much stronger when hydrostatic compression is superimposed. They are pressure-sensitive and the corresponding failure surface is conical or parabolic.

Arguments of deviatoric yield functions such as Eqs. (2.131), (2.133) to (2.136) and (2.138) are typically only the π-plane coordinates $\rho_{\boldsymbol{\sigma}}$ and $\theta_{\boldsymbol{\sigma}}$. They describe failure within the π_0-plane and make no statement about pressure sensitivity. The latter is accounted for by substituting the equivalent stress through

$$\sigma_{\mathrm{eq}}(\boldsymbol{\sigma}) \to \left[\left(\frac{\sigma_{\mathrm{eq}}(\boldsymbol{\sigma}) - \eta_1 I_{\boldsymbol{\sigma}}}{1-\eta_1} \right)^i \left(\frac{\sigma_{\mathrm{eq}}(\boldsymbol{\sigma}) - \eta_2 I_{\boldsymbol{\sigma}}}{1-\eta_2} \right)^j \sigma_{\mathrm{eq}}(\boldsymbol{\sigma})^k \right]^{\frac{1}{i+j+k}}, \tag{2.143}$$

where the exponents i, j and k are positive integers and the reciprocals of $\eta_1 \in [0,1)$ and $\eta_2 \in (-\infty, 0]$ describe the locations of the tensile and compressive hydrostatic nodes, i.e., the intersections of the failure surface with the hydrostatic axis (Altenbach et al., 2014). Fig. 2.4 shows meridians of pressure sensitive generalizations of the von Mises criterion obtained using Eq. (2.143). Choosing $i = j = 0$ and $k = 1$ yields the original pressure-insensitive von Mises criterion. The linear substitution $i = 1$ and $j = k = 0$ provides conical failure surfaces such as the Drucker–Prager criterion

$$\frac{\sigma_{\mathrm{eq}}(\boldsymbol{\sigma}) - \eta_1 I_{\boldsymbol{\sigma}}}{1-\eta_1} = \sqrt{3 II_{\boldsymbol{\sigma}}}. \tag{2.144}$$

This pressure-sensitive generalization of the von Mises hypothesis is shown in Fig. 2.4 for $\eta_1 = 1/3$. Higher order substitutions ($i + j \geq 2$) yield parabolic meridians for $\eta_2 = 0$ and elliptic meridians for $\eta_2 < 0$ (Fig. 2.4). Note how, on account of their normalization, all failure surfaces contain the point $(1,1)$ in the Burzyński plane (Kolupaev, 2018).

Replacing the equivalent stress according to Eq. (2.143) scales the π_0-plane along the hydrostatic axis, but it leaves its geometry unchanged. In particular for concrete (Argyris et al., 1974; Hsieh et al., 1982; Ottosen, 1977) and soil (Lade and Kim, 1995; Lade, 1997; Bigoni and Piccolroaz, 2004) several authors proposed pressure-sensitive failure criteria with variable π-plane cross sections. Hsieh et al. (1982) suggest a linear combination of

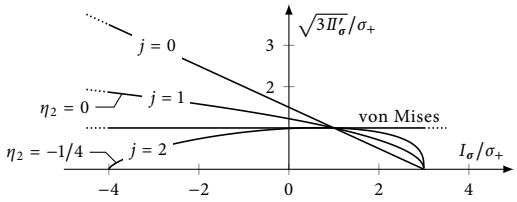

Fig. 2.4 Pressure-sensitive generalization of the von Mises hypothesis using Eq. (2.143) with $i = 1$, $k = 0$ and $\eta_1 = 1/3$ in the Burzyński plane.

the Rankine (2.132) and von Mises (2.133) criteria. With the normalization and notation of the present work, this pressure-sensitive criterion reads

$$\sigma_{\mathrm{eq}}(\boldsymbol{\sigma}) = A\,\frac{\xi_\sigma}{\sqrt{3}} + \frac{3}{2}\,B\,\frac{\rho_\sigma^2}{\sigma_{\mathrm{c}}} + \sqrt{\frac{3}{2}}\,C\,\rho_\sigma + D\,\sigma_{\mathrm{I}}, \tag{2.145}$$

where A, B, C and D are constants and σ_{I} denotes the maximum principal stress. Ottosen (1977) extends this approach using more general shape functions similar to the Podgórski criterion (2.138), i.e,

$$\sigma_{\mathrm{eq}}(\boldsymbol{\sigma}) = A\,\frac{\xi_\sigma}{\sqrt{3}} + \frac{3}{2}\,B\,\frac{\rho_\sigma^2}{\sigma_{\mathrm{c}}} + \sqrt{\frac{3}{2}}\,C\,\rho_\sigma \cos\left(\frac{1}{3}\arccos\left(\alpha\cos(3\theta_\sigma)\right)\right), \tag{2.146}$$

where A, B, C and α are constants and ξ_σ, ρ_σ and θ_σ Lode coordinates (2.129). It will be shown later that replacing the cosine-term in Eq. (2.146) by even more general shape functions, allows for further generalization of this criterion.

Failure mode concept. Instead of developing sophisticated mathematical formulations to represent all possible failure states with a single function, Cuntze (1996, 1999) suggests considering different failure modes individually and describing each by a separate failure surface. Combining the safe regions of all failure modes then yields the complete failure surface of the material. The interaction of different failure modes is localized around their transition region and can be adjusted by a parameter. The approach is known as failure mode concept (FMC).

Blatz (1963) and Lindsey (1967) postulate one dilatational and one distortional failure mode as the two failure modes of nearly incompressible elastomers. A generic formulation of the failure mode concept with these two failure modes is given by

$$\sigma_{\mathrm{eq}}(\boldsymbol{\sigma}) = \left[\left(\frac{\sigma_{\mathrm{eq}}^{\mathrm{vol}}(\xi_\sigma)}{\sigma_{\mathrm{c}}^{\mathrm{vol}}}\right)^m + \left(\frac{\sigma_{\mathrm{eq}}^{\mathrm{iso}}(\rho_\sigma,\theta_\sigma)}{\sigma_{\mathrm{c}}^{\mathrm{iso}}}\right)^m\right]^{\frac{1}{m}} = 1, \tag{2.147}$$

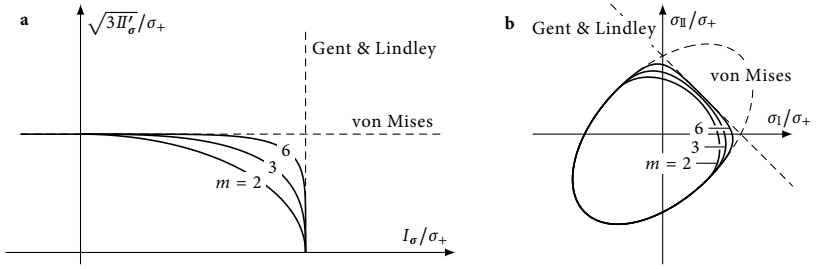

Fig. 2.5 Failure mode concept using the cavitation criterion of Gent and Lindley (2.140) and the distortional von Mises hypothesis (2.133) with different interaction exponents m. **a** In the Burzyński plane, **b** in the σ_I-σ_{II}-plane under plane stress conditions.

where $m \geq 1$ characterizes the interaction of both failure modes. The first term in Eq. (2.147) describes the dilatational failure surface. The corresponding equivalent stress σ_{eq}^{vol} is a function of the position on the hydrostatic axis ξ_σ (2.129a). Its threshold is defined by σ_c^{vol}. The second term with the equivalent stress σ_{eq}^{iso} captures distortional failure. It is a function of the deviatoric invariants ρ_σ (2.129b) and θ_σ (2.129c) and has the threshold σ_c^{iso}.

Using the von Mises hypothesis (2.133) and the cavitation criterion of Gent and Lindley (2.140) as exemplary distorional and dilatational failure criteria, yields

$$\sigma_{eq}(\boldsymbol{\sigma}) = \left[\left(\frac{2I_\sigma}{15\mu}\right)^m + \left(\frac{\sqrt{3II_\sigma}}{\sigma_+}\right)^m\right]^{\frac{1}{m}} = 1, \tag{2.148}$$

for the material's failure surface according to Eq. (2.147). This interaction law is sketched in the Burzyński plane and in the σ_I-σ_{II}-plane under plane stress conditions[10] in Fig. 2.5. Typically, $1 \leq m \leq 4$ yields satisfactory approximations of failure data. The FMC may be formulated without interaction of the individual failure modes. In this case, the failure modes are considered individually or the interaction parameter set to $m \to \infty$. A major advantage of the failure mode concept is its generalizability to more than two failure modes when anisotropic materials are considered (see, e.g., Puck and Schürmann, 1998, 2002, 2004; Cuntze and Freund, 2004; Cuntze, 2004, 2006).

[10] Note that cavitation may never occur in plane stress conditions. This particular stress state is chosen simply because the corresponding elliptic shape of the von Mises criterion in the σ_I-σ_{II}-plane is well-known.

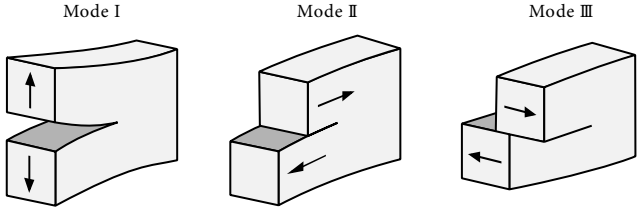

Fig. 2.6 Crack opening modes.

2.3 Fracture mechanics

Fracture mechanics, as a branch of continuum mechanics, is concerned with the quantitative description of the mechanical behavior of bodies containing one or multiple cracks, in particular regarding the resistance to crack growth. It is based on the concept that the crack as an entity itself behaves according to a law of mechanics expressed in terms of a relationship between crack driving force and motion (Freund, 1990).

We distinguish three different crack opening modes (Fig. 2.6). Mode I denotes cleavage, i.e., normal separation of the crack faces. Modes II and III correspond to crack sliding and crack tearing, i.e., in-plane and out-of-plane shear deformations of the crack faces.

Energy balance during crack growth. The work of Griffith (1921) is commonly viewed as the origin of fracture mechanics as a quantitative science. He considered an ideally brittle elastic body containing a crack and recognized that the total potential energy of the system varies with the size of the crack. He then postulated that a certain amount of energy per unit crack surface area is required at the microscopic level to create the new surface during crack extension and included this work as an additional potential energy Γ of the system (Freund, 1990). The first law of thermodynamics (2.66) then reads

$$\dot{\mathcal{K}} + \dot{\mathcal{U}} = \mathcal{P}_{\text{ext}} + \mathcal{Q} - \dot{\Gamma}, \tag{2.149}$$

where $\dot{\Gamma} \geq 0$ represents the rate of energy dissipation due to crack growth. Owing to its dissipative character, it appears on the right hand side of the equation[11]. Considering quasi-static ($\dot{\mathcal{K}} = 0$) and adiabatic ($\mathcal{Q} = 0$) fracture processes and using Eqs. (2.62), (2.64) and (2.71) we obtain

$$\frac{\mathrm{d}}{\mathrm{d}t}\left(\Pi_{\text{int}} + \Pi_{\text{ext}} + \Gamma\right) = 0, \tag{2.150}$$

[11] Griffith (1921) introduced Γ as a surface energy and, hence, formally considered the fracture processes reversible.

where $\Pi = \Pi_{\text{int}} + \Pi_{\text{ext}}$ is the total potential energy of the system. For the considered case, all changes with respect to time are caused by a change in crack size. Applying chain rule yields

$$\frac{\mathrm{d}\bigcirc}{\mathrm{d}t} = \frac{\mathrm{d}\bigcirc}{\mathrm{d}A}\frac{\mathrm{d}A}{\mathrm{d}t} = \frac{\mathrm{d}\bigcirc}{\mathrm{d}A}\dot{A}, \tag{2.151}$$

where $\bigcirc$ serves as a placeholder. This implies that the sum of the total potential energy Π and the fracture energy Γ remains constant upon crack advance:

$$\frac{\mathrm{d}\Pi_{\text{int}}}{\mathrm{d}A} + \frac{\mathrm{d}\Pi_{\text{ext}}}{\mathrm{d}A} + \frac{\mathrm{d}\Gamma}{\mathrm{d}A} = 0. \tag{2.152}$$

Given Griffith's postulate that the energy required to form a unit of new crack surface is constant, we can formulate a crack growth condition

$$\mathcal{G} = \mathcal{G}_{\mathrm{c}}, \tag{2.153}$$

where $\mathcal{G} = -\mathrm{d}\Pi/\mathrm{d}A$ is denoted energy release rate and $\mathcal{G}_{\mathrm{c}} = \mathrm{d}\Gamma/\mathrm{d}A$ is a material constant, the so-called fracture toughness. A particular advantage of Griffith's fracture condition (2.153) is that the actual fracture process at the crack tip does not have to be examined in detail (Gdoutos, 1990).

Linear elastic fracture mechanics. The actual process of bond separation takes place in a region very close to the crack front. This so-called process zone can usually not be described by means of classical continuum mechanics. However, it is often highly localized and sufficiently small that continuum mechanics can be applied to the entire body. A special case is linear elastic fracture mechanics, which considers the body as linear elastic. This typically applies to particularly brittle materials and is used to describe brittle fracture.

Stresses and deformations in the immediate vicinity of the crack tip, the so-called crack tip field, are of particular importance. For a crack in an infinite, two-dimensional body of homogeneous, isotropic, linear elastic material, the crack tip field can be obtained using asymptotic methods. With respect to a polar coordinate system (r, φ) located at the crack tip, it is given by

$$\begin{aligned} \boldsymbol{u} - \boldsymbol{u}_0 &= r^{1/2}\hat{\boldsymbol{u}}^{(1)}(\varphi) + r\hat{\boldsymbol{u}}^{(2)}(\varphi) + r^{3/2}\hat{\boldsymbol{u}}^{(3)}(\varphi) + \dots, \\ \boldsymbol{\sigma} &= r^{-1/2}\hat{\boldsymbol{\sigma}}^{(1)}(\varphi) + \hat{\boldsymbol{\sigma}}^{(2)}(\varphi) + r^{1/2}\hat{\boldsymbol{\sigma}}^{(3)}(\varphi) + \dots, \end{aligned} \tag{2.154}$$

where $\boldsymbol{u}_0$ are rigid body motions and $\hat{\boldsymbol{u}}^{(i)}$ and $\hat{\boldsymbol{\sigma}}^{(i)}$ are functions of the angle φ that are determined with the exception of a multiplicative constant. The immediate vicinity of the crack tip ($r \to 0$) is dominated by singular terms of the stress field. The singular behavior in this domain is characterized by the so-called singularity order, i.e., the

exponents of the displacement field that are smaller than one which, hence, lead to singular stresses. The singularity order of a crack in a homogeneous, isotropic, linear elastic body is 1/2 and stresses decay according to $1/\sqrt{r}$. It is convenient to split the crack tip fields into symmetric and antisymmetric parts, which correspond to the crack opening modes I and II, respectively. The symmetric part (mode I) of the stress near-field reads

$$\begin{bmatrix} \sigma_{xx} \\ \sigma_{yy} \\ \tau_{xy} \end{bmatrix} = \frac{K_\mathrm{I}}{\sqrt{2\pi r}} \cos\frac{\varphi}{2} \begin{bmatrix} 1 - \sin\frac{\varphi}{2} \sin\frac{3\varphi}{2} \\ 1 + \sin\frac{\varphi}{2} \sin\frac{3\varphi}{2} \\ \sin\frac{\varphi}{2} \cos\frac{3\varphi}{2} \end{bmatrix}, \tag{2.155}$$

where K_I is the so-called stress intensity factor. It characterizes local crack tip loading and depends on geometry and global loading. Similarly, stress intensity factors K_II and K_III can be introduced for the crack opening modes II and III. The stress intensity factor K_I of a crack of length $2a$ in an infinite plate subjected to uniaxial tensile stress σ reads

$$K_\mathrm{I} = \sigma\sqrt{\pi a}. \tag{2.156}$$

Stress intensity factors can be given as closed-form analytical expressions for a number of structural situations (Gross and Seelig, 2016). Many other cases have been analyzed using numerical methods and corresponding approximate solutions are listed in stress intensity factor handbooks (Tada et al., 2000; Pilkey and Pilkey, 2008).

In addition to cracks, there are many singular problems in which singularity orders deviating from 1/2 occur. An important class of such problems are sharp notches (Fig. 2.7). The stress and displacements fields in the vicinity of the notch tip

$$\begin{aligned} \boldsymbol{u} - \boldsymbol{u}_0 &= r^{\lambda_1} \hat{\boldsymbol{u}}^{(1)}(\varphi) + r^{\lambda_2} \hat{\boldsymbol{u}}^{(2)}(\varphi) + \dots, \\ \boldsymbol{\sigma} &= r^{\lambda_1 - 1} \hat{\boldsymbol{\sigma}}^{(1)}(\varphi) + r^{\lambda_2 - 1} \hat{\boldsymbol{\sigma}}^{(2)}(\varphi) + \dots, \end{aligned} \tag{2.157}$$

can be obtained from an asymptotic analysis. The singularity orders λ_1 and λ_2 correspond to modes I and II, respectively, and depend on the notch opening angle θ (Fig. 2.7a). The limit case of a crack with $\lambda_1 = \lambda_2 = 1/2$ is recovered for $\theta = 0$. Between $0 \leq \theta < 102.5°$ both modes I and II are singular. For larger notch opening angles $\theta \geq 102.5°$, only the mode I stress field is singular.

Singularity orders of bi-material notches (Fig. 2.7b) depend on both the notch opening angle and the elastic contrast, i.e., the ratio of the Young's moduli of both materials E_1/E_2 (Bogy, 1971). For instance, rectangular bi-material notches feature singularity orders between 1/2 and 1 for $E_1/E_2 \leq 1$, i.e., when material 1 is softer than material 2 (Sator and Becker, 2012; Weißgraeber, 2014). Singularities orders between 1/2 and 1 are denoted weak singularities. Stress singularities that are stronger than the crack tip singularity ($\lambda < 1/2$) are denoted strong singularities or hypersingularities (Sator, 2010; Mayland, 2012; Hell and Becker, 2015). A limit for singularity exponents results from

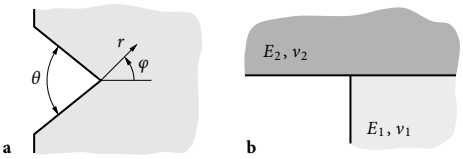

Fig. 2.7 Structures with weak singularities: **a** sharp V-notch, **b** bi-material notch.

the requirement of boundedness of the strain energy. Therefore, the singularity order cannot become smaller than 0 in two-dimensional problems and not smaller than 1/2 in three-dimensional situations.

When a crack propagates in the interface between two dissimilar materials, stresses decay with $1/\sqrt{r}$. However, the singularity exponent $\lambda = 1/2 + \gamma i$ becomes complex and the singular stresses oscillate according to

$$\begin{aligned} \boldsymbol{u} - \boldsymbol{u}_0 &= r^{1/2} \cos(\gamma \ln r)\, \hat{\boldsymbol{u}}^{(1)}(\varphi) + \dots , \\ \boldsymbol{\sigma} &= r^{-1/2} \cos(\gamma \ln r)\, \hat{\boldsymbol{\sigma}}^{(1)}(\varphi) + \dots , \end{aligned} \tag{2.158}$$

where γ is the so-called bi-material constant defined as

$$\gamma = \frac{1}{2\pi} \ln \frac{\mu_2 \kappa_1 + \mu_1}{\mu_1 \kappa_2 + \mu_2}, \qquad \mu_i = \frac{E_i}{2(1+\nu_i)}, \qquad \kappa_i = 3 - 4\nu_i. \tag{2.159}$$

In the case of linear elasticity, the energy release rate $\mathcal{G}$ can be expressed through stress intensity factors. The relationship is derived from so-called virtual crack closure integrals that account for the work required to virtually close a crack (Gross and Seelig, 2016). For general mixed-mode loading we obtain

$$\mathcal{G} = \frac{1}{E^*} \left(K_{\mathrm{I}}^2 + K_{\mathrm{II}}^2 \right) + \frac{1}{2\mu} K_{\mathrm{III}}^2, \tag{2.160}$$

per unit length, where μ is the shear modulus and E^* an effective Young's modulus defined as

$$E^* = \begin{cases} E & \text{in plane stress,} \\ E/(1-\nu^2) & \text{in plane strain.} \end{cases} \tag{2.161}$$

Presuming that conditions at the crack tip are comprehensively defined by stress intensity factors, Irwin (1957) proposed crack growth conditions based on these so-called K-factors. With reference to Griffith's condition for crack growth (2.153) and Eq. (2.160) he postulated

$$K_{\mathrm{I}} = K_{\mathrm{Ic}}, \qquad K_{\mathrm{II}} = K_{\mathrm{IIc}}, \qquad K_{\mathrm{III}} = K_{\mathrm{IIIc}}, \tag{2.162}$$

for pure mode I, II and III loading, respectively. Like $\mathcal{G}_c$, the threshold values K_{Ic}, K_{IIc} and K_{IIIc} are called fracture toughnesses. Equation (2.162) is known as Irwin criterion and is well-established for practical applications. A crack growth condition for mixed-mode loading must account for the interaction of individual crack opening modes. A general expression in terms of K-factors can be formulated as

$$f(K_I, K_{II}, K_{III}) = K_c, \tag{2.163}$$

where f denotes a function of the stress intensity factors of all three crack opening modes.

Elastic–plastic fracture mechanics. Arguments of linear elastic fracture mechanics apply to ideally brittle materials whose process zone can be neglected altogether. Irwin (1960, 1962) showed that the above concepts are still valid for elastic–plastic materials when the plastic zone that develops around the crack tip remains small. The situation is known as small-scale yielding (Rice, 1968). Irwin (1960, 1962) derived the extent of the plastic zone along the crack axis from equilibrium conditions at critical loading. For an elastic–perfectly plastic material it reads

$$r_p = \frac{1}{2n\pi}\left(\frac{K_{Ic}}{\sigma_y}\right)^2, \tag{2.164}$$

where σ_y is the uniaxial yield strength and $n = 1$ or $n = 3$ a constant accounting for plane stress or plane strain conditions (Irwin, 1960, 1962). Outside the plastic zone, we recover the crack tip near-field shifted by the size of the plastic zone r_p and, hence, obtain an effective crack length $a + r_p$. According to Eqs. (2.156) and (2.162), the uniaxial failure stress of a crack of length $2a$ in an infinite plate is given by

$$\sigma_f = \frac{K_{Ic}}{\sqrt{\pi a}} \frac{1}{\sqrt{1 + \frac{r_p}{a}}}. \tag{2.165}$$

The size of the plastic zone characterized by r_p (2.164) is an indicator for brittleness. Structures are called ideally brittle when they break without plastic deformations. In this case, Irwin's approach coincides with linear elastic fracture mechanics ($r_p/a \to 0$). When r_p/a assumes large values, other concepts of elastic–plastic fracture mechanics must be used. From Eq. (2.165) it is evident that brittleness is not a material parameter but depends on a structural dimension, e.g., the crack length a.

The Dugdale (1960) model considers long but narrow plastic zones that mainly develop along the crack axis. It virtually extends the crack by the length of the plastic zone and loads the crack faces of the extension with the material's yield stress. This reduces the problem to a linear elastic boundary value problem. The length of the plastic zone is

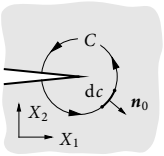

Fig. 2.8 Integration path enclosing a crack tip in the reference configuration.

obtained from the requirement of a vanishing stress intensity factor at the end of the virtually extended crack. A crack growth condition can then be formulated assuming a critical value of the crack tip opening displacement at the physical crack tip.

Similarly, cohesive zone models (CZM), first proposed by Barenblatt (1959) and Leonov and Panasyuk (1959), consider a strip-like process zone in which a separation-dependent interaction of the potential crack faces is assumed. Different traction–separation laws allow for considering different fracture phenomena such as ductile and brittle fracture.

Path-independent integrals. Materials and structures feature inhomogeneities on different scales. While continuum mechanics disregards microscopic imperfections such as dislocations or point defects in crystal lattices, macroscopic departures from uniformity such as interfaces, cavities or cracks are all considered defects of some sort. All these entities can change their configuration. Interfaces may move, cavities can change their shape, and cracks can expand. The configuration of defects can be described by a number of parameters. The rate of decrease of the total energy of the system with respect to one parameter can be interpreted as a generalized force acting on that parameter, or, in simple cases, on the defect itself. The force is called configurational force and can be determined using the path-independent J-integral (Eshelby, 1951, 1999).

Consider a body of homogeneous, elastic but arbitrarily nonlinear and anisotropic material with the strain energy density $\mathcal{W}$. In the absence of body forces, the J-integral vector is defined as

$$\boldsymbol{J} = \int_{\partial V} \left(\mathcal{W}\boldsymbol{I} - \boldsymbol{P}\frac{\partial \boldsymbol{u}}{\partial \boldsymbol{X}} \right) \boldsymbol{n}_0 \, \mathrm{d}A, \tag{2.166}$$

where ∂V is a closed surface with the unit outward normal vector $\boldsymbol{n}_0$ in the reference configuration, $\boldsymbol{I}$ is the identity matrix, $\boldsymbol{P}$ the first Piola-Kirchhoff stress tensor (2.34b), $\boldsymbol{u}$ the displacement vector (2.1) and $\boldsymbol{X}$ are Lagrangian coordinates. It represents a generalized force in units N. Using the divergence theorem, it can be shown that the J-integral vector (2.166) vanishes for any surface ∂V that encloses only defect-free material and no singularities of the integrand (Gross and Seelig, 2016).

When discontinuities such as crack tips are enclosed, the J-integral generally assumes finite values. In particular, applied to a crack with load-free crack faces in a two-dimensional homogeneous elastic body, J_1 and J_2 can be interpreted as the change in total potential energy of the system upon motion of the crack tip in X_1 and X_2-direction, respectively (Fig. 2.8). In this case, the surface integral reduces to a contour integral along a closed contour C. With X_1 aligned with the crack axis, J_1 has significance as a fracture parameter as it describes the energy release rate of crack extension per unit width in two-dimensional problems (Cherepanov, 1967; Rice, 1968). In this case, the index 1 is frequently omitted and we write

$$J = -\frac{\mathrm{d}\Pi}{\mathrm{d}a}. \tag{2.167}$$

Accounting for the out-of-plane width w this provides the energy release rate per unit crack surface area

$$\mathcal{G} = \frac{J}{w} = \int_C \left(\mathcal{W}\,\mathrm{d}X_2 - \boldsymbol{t}_0 \frac{\partial \boldsymbol{u}}{\partial X_1}\mathrm{d}c \right), \tag{2.168}$$

where $\boldsymbol{t}_0$ is the nominal traction vector (2.33). On account of Eqs. (2.153) and (2.167), we may formulate a crack growth condition as

$$J = J_\mathrm{c}. \tag{2.169}$$

In the linear elastic case, J, $\mathcal{G}$ and K can be used equivalently to formulate crack growth conditions. However, the J-integral is not restricted to linear elasticity. In fact, for monotonically increasing loading, it is even applicable to inelastic material behavior. Owing to its path-independence, the J-integral can provide means to determine the energy release rate without knowledge of the crack tip field, also in the context of large deformations (Gross and Seelig, 2016).

Crack opening integral. Intact material transfers load, i.e., stresses, through any material point. When a crack is present, the load can no longer be transmitted and stresses are zero[12]. Hence, introducing a crack increment ΔA can be understood as the quasi-static reduction of the stresses on ΔA to zero. Reducing the stresses gradually separates the crack faces and finally yields the fully open crack. The work ΔW done by the stresses during this process corresponds to the change in total potential energy $\Delta\Pi$ owing to a crack extension of ΔA. It can be split into contributions of the normal, sliding and tearing crack opening modes, i.e.,

$$\Delta\Pi = \Delta W_\mathrm{I} + \Delta W_\mathrm{II} + \Delta W_\mathrm{III}. \tag{2.170}$$

For this purpose, we introduce local normal coordinates u_n and local tangential coordinates u_s and u_t on the crack faces. The corresponding normal and shear stress

[12] We do not consider compression and neglect friction of crack faces.

components of the Cauchy stress tensor (2.34a) are denoted σ_n, τ_ns and τ_nt. Opposing crack faces are distinguished by + and −. For nonlinear elastic material behavior and large deformations, the work of the individual stress components for a crack increment ΔA is given by

$$\Delta W_\mathrm{I} = -\int_{\Delta A}\left(\int_{u_\mathrm{n}^0}^{u_\mathrm{n}^+}\sigma_\mathrm{n}^+(u_\mathrm{n})\,\mathrm{d}u_\mathrm{n} - \int_{u_\mathrm{n}^0}^{u_\mathrm{n}^-}\sigma_\mathrm{n}^-(u_\mathrm{n})\,\mathrm{d}u_\mathrm{n}\right)\mathrm{d}A, \tag{2.171a}$$

$$\Delta W_\mathrm{II} = -\int_{\Delta A}\left(\int_{u_\mathrm{s}^0}^{u_\mathrm{s}^+}\tau_\mathrm{ns}^+(u_\mathrm{s})\,\mathrm{d}u_\mathrm{s} - \int_{u_\mathrm{s}^0}^{u_\mathrm{s}^-}\tau_\mathrm{ns}^-(u_\mathrm{s})\,\mathrm{d}u_\mathrm{s}\right)\mathrm{d}A, \tag{2.171b}$$

$$\Delta W_\mathrm{III} = -\int_{\Delta A}\left(\int_{u_\mathrm{t}^0}^{u_\mathrm{t}^+}\tau_\mathrm{nt}^+(u_\mathrm{t})\,\mathrm{d}u_\mathrm{t} - \int_{u_\mathrm{t}^0}^{u_\mathrm{t}^-}\tau_\mathrm{nt}^-(u_\mathrm{t})\,\mathrm{d}u_\mathrm{t}\right)\mathrm{d}A, \tag{2.171c}$$

where the subscript 0 denotes the uncracked state (Talmon l'Armée et al., 2017; Talmon l'Armée, 2019). In the case of linear elasticity, Eq. (2.171) simplifies significantly. Denoting the normal distance between the open crack faces Δu_n and the corresponding tangential distances Δu_s and Δu_t, we obtain

$$\Delta\Pi = -\frac{1}{2}\int_{\Delta A}\left(\sigma_\mathrm{n}\,\Delta u_\mathrm{n} + \tau_\mathrm{ns}\,\Delta u_\mathrm{s} + \tau_\mathrm{nt}\,\Delta u_\mathrm{t}\right)\mathrm{d}A. \tag{2.172}$$

The crack opening integral is particularly useful in combination with the finite element method (FEM), where it can be formulated using nodal forces and nodal displacements. Assuming self-similar crack growth, it allows for determining mode-separated energy release rates from a single analysis without the need for considering actual crack advance (Irwin, 1958; Rybicki and Kanninen, 1977).

2.4 Finite fracture mechanics

The concepts and models introduced in the previous sections allow for the characterization of bulk material failure, i.e., failure of materials subjected to homogeneous stresses that is often catastrophic, and for the description of crack extension and the resistance of materials against crack growth. However, both concepts have difficulties in predicting crack nucleation at locations of strong stress gradients. Assuming the instantaneous formation of finite sized cracks, finite fracture mechanics provides a physically sound model for crack initiation events in such situations. It bridges the gap between bulk failure mechanisms and crack growth phenomena. The ideas and concepts of this nonlocal failure criterion are introduced and discussed in the following sections.

History of nonlocal failure criteria. Presumably, the first account of nonlocal approaches to failure was given by Wieghardt (1907). He considered a semi-infinite crack in an infinite sheet loaded by a single force at one crack face. He determined the exact solution of the singular crack tip field and recognized that the local evaluation of stress-based criteria cannot predict failure in the presence of cracks. Therefore, he introduced a length parameter and concluded that fracture does not occur on account of a critical local stress but rather when the stress level in a certain area becomes critical. Although Griffith's energy balance may provide a better model for real cracks, the nonlocal consideration of stresses is an essential concept.

Unaware of Wieghardt's suggestion, Neuber (1936) examined the singular stress field of sharp notches and came to similar conclusions. He assumed a geometry-dependent supporting effect of the surrounding material and considered stresses averaged over a certain distance from the notch tip to predict failure. The concept is known as line method (LM). It has been refined over the years (Neuber, 1958, 2001) and has been incorporated into industrial standards (DIN Standard 743-2, 2012). Novozhilov (1969) proposed a similar stress-averaged failure criterion for elliptical holes considering the atomic diameter as the characteristic length scale.

Instead of averaging stresses over a characteristic distance, Peterson (1938) and later Whitney and Nuismer (1974) evaluated stresses in a point-wise manner in a certain distance from stress concentrations. This allowed the latter to describe the size effect of open-holes. Size effects describe the experimentally observed dependence of the effective strength of self-similar structures on structural dimensions, such as the hole diameter, although stress fields and stress concentrations are unaffected by self-similar scaling (Bažant, 1984, 1999). The point-wise stress evaluation motivates the denomination point method (PM).

Again in order to account for open-hole size effects, Waddoups et al. (1971) treat *intense energy regions* around stress concentrations as imaginary initial cracks in order to apply the Irwin criterion (2.162). Similarly, El Haddad et al. (1980) assume pre-existing cracks at rounded notches and evaluate the crack growth condition of Eq. (2.169). The concept is known as imaginary crack method (ICM).

Strain energy density methods (SED) substitute the material's strength by a strain energy density threshold. In analogy to LM and PM above, several authors either evaluate SED along rays from the crack tip (Sih, 1974) or averaged in a finite sized domain (Lazzarin and Zambardi, 2001).

Hashin (1996) notes that when crack formation is considered instead of crack extension, new microcracks may appear and accumulate to a macrocrack within very short time. He concludes that resolving this time scale is not of interest and considers the formation of new cracks as fracture events. This implies that crack nucleation creates a new finite

crack surface associated to a certain change in total potential energy that can be assessed using a Griffith-like energy criterion. Hashin (1996) suggests calling this approach finite fracture mechanics (FFM).

Recent theories of fracture. Classical concepts require the addition of a length parameter in order to capture failure emerging from stress concentrations and, in fact, also many modern theories of fracture involve a material length scale, i.e., a parameter with the dimensions of a length. Some models use physically motivated lengths, for instance derived from the microstructure or the length of a crack increment. Others involve length scales implicitly, for instance as the size of fracture process zones. Models using length scales explicitly are known under the common name *theory of critical distances* (TCD) and comprise the concepts discussed above (Taylor et al., 2004; Taylor, 2007, 2008).

Phase-field models for brittle fracture include a regularization length, which is often interpreted as a material parameter. Based on Griffith's idea of competition between elastic and fracture energy and its variational formulation by Francfort and Marigo (1998), phase-field models are able to predict propagation of existing cracks, crack branching and crack paths, also in hyperelastic materials (Schänzel et al., 2013; Miehe and Schänzel, 2014). However, critical loads depend on the regularization parameter. Recent works by Tanné et al. (2018) and Wu and Nguyen (2018) suggest that fracture processes are governed by stress and energy simultaneously. Tanné et al. (2018) identify the regularization length of their phase-field approach from the material's strength. Wu and Nguyen (2018) use a phase-field regularized cohesive zone model and derive the regularization length from the traction-separation law, i.e., dependent on both strength and toughness. Considering strength and toughness simultaneously, both works are capable of modeling not only crack propagation but also initiation using the phase-field approach. In process zone models such as cohesive zone models (CZM) the size of the process zone appears as an implicit length scale (Ortiz and Pandolfi, 1999; Gasser and Holzapfel, 2005). In CZMs, traction–separation laws relate crack opening displacements to stresses acting on the crack surface. Peak tractions are associated with the material's strength. The work done by tractions during the material softening process in the cohesive zone corresponds to the fracture toughness. Using finite element analyses (FEA) in order to locally evaluate stress criteria introduces the element size as a characteristic length scale. That is, in order to predict failure, both the material's strength and the FEA discretization must be calibrated with experiments.

Physics of nonlocal fracture. The above models introduce length scales as convenient ways to describe experimental observations. While predictions of nonlocal failure criteria are often accurate and useful in practice, the length parameter involved in all of the above approaches is not known a priori and lacks definite physical meaning. Whitney

and Nuismer (1974), Pipes et al. (1979), Awerbuch and Madhukar (1985), Tan (1987) and Clark and McGregor (1993), for instance, find a dependence of the critical distance on geometrical features which, hence, cannot be regarded a material constant.

Moreover, evidence of the nonlocal nature of the underlying physical mechanisms is scarce. An important hint is given by all-atom molecular dynamics simulations: Brochard et al. (2018, 2019) investigate pre-cracked and notched graphene at the athermal limit (0 K). At this limit, failure corresponds to an instability of the atomic system. It occurs when one of the eigenvalues of the Hessian matrix of the energy becomes negative. The associated eigenvectors provide the movement of atoms at the time of failure. These eigenvectors strongly depend on the stress concentration and indicate the nucleation of a deformation band whose length increases as the stress concentration weakens. This implies that failure actually involves a length scale and demands the application of nonlocal failure criteria. Note that at finite temperature, failure in all-atom simulations is no longer deterministic and requires a probabilistic description.

Strength or toughness? Given fracture processes involve a length scale, both stress and energy may be used in nonlocal failure criteria. While strength captures failure of a flawless material subjected to homogeneous stress, fracture toughness measures resistance against the extension of existing cracks. Both concepts represent well-understood limit cases and, yet, yield contradictory and unphysical predictions in certain situations when applied exclusively. Let us illustrate this using two examples.

Consider a homogeneous isotropic bar subjected to a critical strain $\hat{\varepsilon}$ at which it fails. The critical strain is associated to a critical stress $\hat{\sigma}$. After rupture the broken bar is of course stress and strain-free. It stores no elastic energy. Hence, the energy released during the fracture process is the entire energy, which was stored in the bar prior to fracture

$$\Delta\Pi = -\frac{1}{2} A l \hat{\sigma}\hat{\varepsilon} = -\frac{1}{2} A l \frac{\hat{\sigma}^2}{E}, \tag{2.173}$$

where A is the cross section of the bar, l is its length and E its Young's modulus. According to Hashin's energy criterion for crack formation $-\Delta\Pi/A = \mathcal{G}_c$ (Hashin, 1996), we obtain

$$\frac{1}{2} A l \frac{\hat{\sigma}^2}{E} = \mathcal{G}_c A. \tag{2.174}$$

It would be wrong to assume that Eq. (2.174) allows for computing the critical stress at which the bar will break according to

$$\hat{\sigma} = \sqrt{2\frac{E\mathcal{G}_c}{l}}, \tag{2.175}$$

if the fracture toughness $\mathcal{G}_c$ is a known material constant. Equation (2.175) implies that the bar will fail at arbitrarily small loads provided it is sufficiently long, which obviously

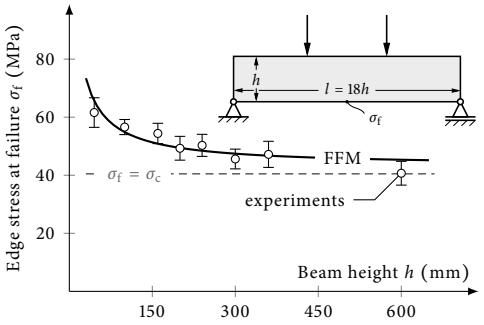

Fig. 2.9 Size effect of wood beams in 299 self-similar four-point bending experiments. Experimental results reported by Fonselius (1997) are given as mean and standard deviation. The out-of-plane depth of the beams is always $b = 45$ mm.

contradicts observations. It draws an incorrect conclusion because the problem is not governed by energy exclusively, but certain stress conditions must be satisfied, too (Leguillon, 2002).

As a second example, consider the problem of edge crack nucleation in four-point bending tests. Fig. 2.9 shows the results of 299 such experiments on rectangular homogeneous wooden beams reported by Fonselius (1997). Depicted are maximum tensile edge stresses at failure computed from the critical loading at failure. Self-similar specimens of different size but constant length-to-height-ratio are tested in this size-effect study. According to strength-of-materials, failure occurs when the maximum stress within the beam reaches the material's strength

$$\sigma_f = \sigma_c. \tag{2.176}$$

However, this simple expression is valid only for sufficiently large beams. The experiments in Fig. 2.9 show that small specimens fail at considerably larger loads than predicted by Eq. (2.176). In structures with localized stress concentrations, the initiation of cracks is observed at loads causing stresses that locally exceed the material's strength. This size effect originates from an insufficient energy release for crack formation.[13]

The contradictions in the above examples can be resolved assuming the sudden formation of crack of finite size (as proposed by Hashin) when both a stress and an energy condition are satisfied simultaneously. This so-called coupled stress and energy failure criterion in the framework of finite fracture mechanics was proposed by Leguillon

[13] Leguillon et al. (2015a) showed that size effects are often a combination of energetic and statistical effects.

(2002). It states that a finite crack can only nucleate when its energy release is larger than the fracture toughness and when the material's strength is exceeded on the entire potential crack length. The coupled criterion is capable of predicting the effective flexural strength of all 299 four-point bending experiments shown in Fig. 2.9 using only two fundamental material properties: the uniaxial tensile strength and the mode I fracture toughness.

The above examples show that fracture processes are governed not by one exclusive but by two conditions simultaneously even if one often hides the other (Leguillon, 2002). Finite fracture mechanics introduces a length scale with clear physical meaning – the finite size of the initiated crack. The length is not a material constant but a result of the failure model and depends on the structural situation.

Coupled stress and energy criterion. The coupled stress and energy criterion reconciles strength and toughness. It requires the simultaneous satisfaction of both a strength criterion and an energy criterion. Both individual criteria are necessary conditions. Their simultaneous satisfaction provides a sufficient condition for crack nucleation.

In the framework of finite fracture mechanics, we assume the instantaneous formation of finite sized cracks as suggested by Hashin (1996). On account of Eq. (2.152), the energy balance of quasi-static, adiabatic finite crack extension reads

$$\frac{\Delta\Pi_{\text{int}}}{\Delta A} + \frac{\Delta\Pi_{\text{ext}}}{\Delta A} + \frac{\Delta\Gamma}{\Delta A} = 0, \tag{2.177}$$

where ΔA is the change in crack surface area. The sum $\Delta\Pi = \Delta\Pi_{\text{int}} + \Delta\Pi_{\text{ext}}$ corresponds to the change in total potential energy due to the crack increment ΔA. Again, the energy required to create a finite unit of new crack surface $\mathcal{G}_{\text{c}} = \Delta\Gamma/\Delta A$ is the fracture toughness. The change in total potential energy owing to a crack increment ΔA is called *incremental* energy release rate $\overline{\mathcal{G}}$. It corresponds to the average *differential* energy release rate on finite crack surface

$$\overline{\mathcal{G}} = -\frac{\Delta\Pi}{\Delta A} = \frac{1}{\Delta A}\int_{\Delta A} \mathcal{G}(A)\,\mathrm{d}A. \tag{2.178}$$

With reference to Griffith's criterion (2.153), the necessary energetic condition for the nucleation of finite sized cracks is given by

$$\overline{\mathcal{G}} \geq \mathcal{G}_{\text{c}}. \tag{2.179}$$

Restricting the consideration to two-dimensional problems with out-of-plane width w, we may substitute $\Delta A = w\Delta a$ in the above equations, where Δa denotes the finite crack length. On account of Eq. (2.178), the differential energy release rate at the tip of a crack

of length Δa can by calculated from its incremental energy release rate using product rule, i.e.,

$$\mathcal{G}(\Delta a) = \overline{\mathcal{G}}(\Delta a) + \Delta a \frac{\partial \overline{\mathcal{G}}(\Delta a)}{\partial \Delta a}. \tag{2.180}$$

The energy balance of finite sized cracks introduces a new unknown: the size of the finite crack. That is, the critical loading that causes the initiation of a finite crack and the size of the nucleating crack are not known a priori. For this reason, Leguillon (2002) introduces a second necessary condition and, hence, a second equation to determine both unknowns. This stress criterion requires the material to be overloaded in terms of stress on the entire potential crack surface. In general form, this is expressed by a certain equivalent stress function σ_{eq} that exceeds its threshold σ_{c}

$$\sigma_{\mathrm{eq}}(\boldsymbol{\sigma}(\boldsymbol{x})) \geq \sigma_{\mathrm{c}} \;\forall\; \boldsymbol{x} \in \Gamma_{\mathrm{c}}(\Delta A), \tag{2.181}$$

where $\Gamma_{\mathrm{c}}(\Delta A)$ denotes the surface of the potential finite crack of size ΔA. Any of the equivalent stress functions introduced in Section 2.2 that describe bulk material failure accurately may be used. Cornetti et al. (2006) propose an alternative form of the stress criterion averaging the equivalent stress on the potential crack surface:

$$\overline{\sigma}_{\mathrm{eq}}(\Delta A) = \frac{1}{\Delta A} \int_{\Delta A} \sigma_{\mathrm{eq}}(\boldsymbol{\sigma}(\boldsymbol{x}))\, \mathrm{d}A \geq \sigma_{\mathrm{c}}. \tag{2.182}$$

In analogy to theory of critical distances, Eqs. (2.181) and (2.182) are called point method and line method, respectively.

In order to formulate a sufficient condition for crack nucleation, both the stress and the energy condition must be satisfied simultaneously. Using point method, this yields the coupled stress and energy criterion for crack nucleation

$$\sigma_{\mathrm{eq}}(\boldsymbol{\sigma}(\boldsymbol{x})) \geq \sigma_{\mathrm{c}} \;\forall\; \boldsymbol{x} \in \Gamma_{\mathrm{c}}(\Delta A) \quad \wedge \quad \overline{\mathcal{G}}(\Delta A) \geq \mathcal{G}_{\mathrm{c}}, \tag{2.183}$$

proposed by Leguillon (2002). Equation (2.183) is sometimes also referred to as hybrid criterion (Hebel et al., 2010; Sun et al., 2015; Gross and Seelig, 2016). Using line method, we obtain

$$\overline{\sigma}_{\mathrm{eq}}(\Delta A) \geq \sigma_{\mathrm{c}} \quad \wedge \quad \overline{\mathcal{G}}(\Delta A) \geq \mathcal{G}_{\mathrm{c}}. \tag{2.184}$$

Solving the coupled criterion (2.183) results in a constrained optimization problem: The smallest load P satisfying both the energy and the stress condition, Eqs. (2.179) and (2.181), for any kinematically admissible crack ΔA is to be found. Using point method this yields

$$\begin{aligned} P_{\mathrm{f}} = \min_{P,\Delta A} \big\{ P \,|\, P > 0, \exists \Delta A > 0 : \\ \sigma_{\mathrm{eq}}(\boldsymbol{\sigma}(P, \boldsymbol{x})) \geq \sigma_{\mathrm{c}} \;\forall\; \boldsymbol{x} \in \Gamma_{\mathrm{c}}(\Delta A) \;\wedge\; \overline{\mathcal{G}}(P, \Delta A) \geq \mathcal{G}_{\mathrm{c}} \big\}. \end{aligned} \tag{2.185}$$

Again, the point method stress criterion may be substituted by line method and we obtain

$$P_\mathrm{f} = \min_{P,\Delta A} \left\{ P \mid P > 0, \exists \Delta A > 0 : \ \overline{\sigma}_\mathrm{eq}(P, \Delta A) \geq \sigma_\mathrm{c} \ \ \wedge \ \ \overline{\mathcal{G}}(P, \Delta A) \geq \mathcal{G}_\mathrm{c} \right\}. \tag{2.186}$$

It is to note that the surface area ΔA of new cracks is not restricted to a single connected crack. It may also describe the surface area of a crack pattern composed of multiple disjoint cracks (Leguillon et al., 2014; Weißgraeber et al., 2015a; Rosendahl et al., 2017d).

Chapter 3

Samples and finite element models

The present work makes use of a large set of different specimens and experiments in order to identify elastic and fracture material properties and in order to verify and validate proposed models and theories. The following sections detail dimensions and manufacturing procedures for all specimens. They also present particulars of numerical models of the corresponding experiments such as boundary conditions, discretization and element types. We will refer to this chapter throughout this work.

3.1 Unnotched specimens

Unnotched specimens are used to identify the constitutive behavior and bulk material fracture properties. Two hyperelastic materials, the structural silicone sealant DOWSIL™ 993 and the transparent structural sealant adhesive DOWSIL™ TSSA are examined. The materials are characterized using different specimens because their semi-finished products differ.

3.1.1 Dumbbell specimens

Dumbbell specimens for uniaxial tensile tests of DOWSIL™ 993 (Fig. 3.1a) are manufactured by pouring a sheet of DOWSIL™ 993 of 2 mm nominal thickness onto a polyethylene (PE) foil. The sheets are stored at ambient conditions for 14 days before specimens are punched and tested at 23 °C and 50 % relative humidity. The specimen geometry is chosen according to ASTM Standard D412 (2016), which details test methods for vulcanized rubbers and thermoplastic elastomers that have similar material properties as the silicones considered in the present work. Five samples were tested at a loading rate of 6 mm/min using a 500 N load cell. Deformations are recorded optically and evaluated using digital image correlation (DIC). The tensile tests were performed and reported by Staudt et al. (2014, 2018) and Staudt (2017).

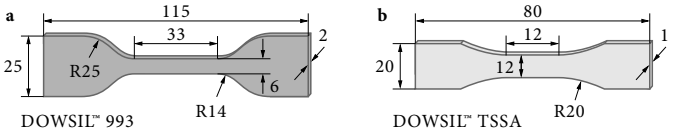

Fig. 3.1 Dumbbell shaped specimen. **a** DOWSIL™ 993 specimen according to ASTM Standard D412 (2016) **b** DOWSIL™ TSSA specimen according to Becker (2009). Dimensions in mm.

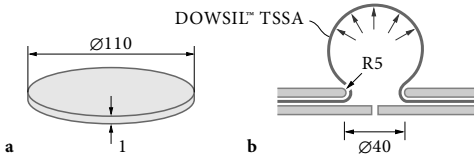

Fig. 3.2 Bulge test: **a** DOWSIL™ TSSA specimen, **b** rig with clamped and inflated membrane. Dimensions in mm.

For DOWSIL™ TSSA, modified dumbbell specimens according to Becker (2009) are used (Fig. 3.1b). The modified geometry features a wider central section allowing for optical measurements of lateral strains in order to determine the Poisson's ratio. DOWSIL™ TSSA is provided as sheets of 1 mm nominal thickness. Ten samples were punched from sheets after 1 h of curing at 130 °C and tested at a loading rate of 5 mm/min at ambient conditions. The tests were performed by Drass et al. (2018e).

3.1.2 Bulge specimens

The inflation of a thin membrane through hydraulic or pneumatic pressure is called bulge test. The test allows for the investigation of biaxial deformation and stress states at the pole of the inflated membranes (Sasso et al., 2008; Machado et al., 2012; Selvadurai and Shi, 2012). It avoids edge effects and is remarkably simple. Using elliptical holes different biaxiality ratios can be configured (Hamdi et al., 2006a,b, 2007a). However, the test setup is not standardized. For the present analysis, circular discs of 110 mm diameter are cut from sheets of DOWSIL™ TSSA that were cured for 1 h at 130 °C (Fig. 3.2a). The discs are provided with a speckle pattern and clamped to a base plate using an anchor plate with a circular center hole of 40 mm diameter (Fig. 3.2b). The anchor plate's edges are rounded off to a radius of 5 mm to avoid strong stress concentrations. DIC pole strain measurements at failure could only be obtained for six out of 15 tested specimens as the speckle pattern flaked off several specimens at large strains. The bulge tests were performed by Drass et al. (2018e).

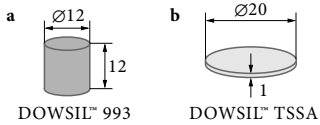

Fig. 3.3 Uniaxial compression specimens. **a** DOWSIL™ 993, **b** DOWSIL™ TSSA. Dimensions in mm.

3.1.3 Uniaxial compression specimens

Uniaxial compression specimens of DOWSIL™ 993 (Fig. 3.3a) are manufactured according to ISO Standard 7743 (2017) in a polytetrafluoroethylene (PTFE) mold and cured for seven days at ambient conditions. The tests are performed at a loading rate of 1.44 mm/min at ambient conditions using a hydraulic press with polished plates and a 10 kN load cell. Displacements are recorded using linear inductive displacement transducers. Lubricants did not reduce friction satisfactorily. Hence, they were omitted in order to avoid additional impacts on the material. The compression tests were performed and reported by Staudt (2017) and Staudt et al. (2018).

The fixed thickness of 1 mm of the semi-finished product does not allow for manufacturing DOWSIL™ TSSA compression samples according to ISO Standard 7743 (2017). The small thickness-to-diameter ratio of the specimens used in the present analysis (Fig. 3.3b) renders lubrication important. Therefore, contact plates were lubricated using Würth HSS® adhesive lubricant 5000. The tests were performed at a loading rate of 0.174 mm/min at ambient conditions by Drass et al. (2018e).

3.1.4 Tubular lap shear specimens

Tubular lap shear specimens are composed of two steel cylinders of different diameters that are bonded by a thick layer of DOWSIL™ 993 and rotated against each other during testing (Fig. 3.4). This setup attempts to avoid stress concentrations at bi-material corners. The steel adherends are carefully cleaned using DOWSIL™ R-40 solvent and DOWSIL™ 1200 OS primer is applied prior to pouring the adhesive. Silicone mixing and pouring is performed using a professional static mixing and dispense pump. The quality of the adhesive is monitored using the two plates test detailed by the Dow Corning Corporation (2011). Five samples are manufactured and stored at ambient conditions for 15 days before they are tested. The tests are performed at 20 °C and 50 % relative humidity at a loading rate of 1.5 °/min using a tension–torsion machine. The torsional moment is measured using a 4 kNm load cell. Rotation and axial displacement are recorded using displacement transducers mounted to the steel cylinders. Axial forces

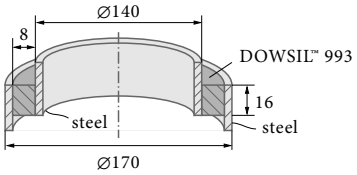

Fig. 3.4 DOWSIL™ 993 tubular lap joint specimen. Dimensions in mm.

are controlled to vanish. The lap shear tests were performed and reported by Staudt (2017) and Staudt et al. (2018).

3.2 Notched specimens

Notched samples are used for the characterization of fracture properties and for the verification and validation of failure models. Cantilever beam specimens with manufactured pre-cracks provide mode I and mode III fracture toughnesses. H-shaped specimens, notched tubular lap joints and pancake specimens are employed for validation purposes. The sample preparation and corresponding finite element models are detailed in the following sections.

3.2.1 H-shaped specimens

H-shaped specimens composed of two steel plates bonded by DOWSIL™ 993 (Fig. 3.5) are manufactured according to the European Technical Approval Guideline for Structural Sealant Glazing Systems (EOTA, 2012) with an out-of-plane width of $w = 12$ mm. They are used in simple shear and pull-off tests. Adhesive thicknesses of $t = 6$ mm, 12 mm and 24 mm, and bond lengths of $l = 50$ mm, 100 mm and 200 mm are manufactured. The steel adherends are sandblasted, ground, carefully cleaned with DOWSIL™ R-40 solvent and primed with DOWSIL™ 1200 OS primer. They are separated using a PE mold and fixed using screws for silicone pouring. Silicone mixing and pouring is performed using a professional static mixing and dispense pump. The specimens are cured for four weeks at ambient conditions.

Simple shear tests in longitudinal direction are performed at ambient conditions using a 5 kN load cell. Displacements are measured using displacement transducers. Displacement-controlled loading with a constant nominal shear rate is prescribed. That is, samples with $t = 6$ mm adhesive thickness are tested at 1 mm/min, $t = 12$ mm specimens at 2 mm/min and $t = 24$ mm specimens at 4 mm/min. Several simple shear

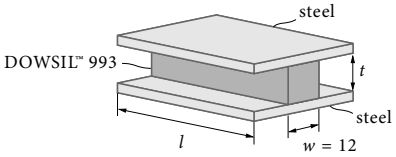

Fig. 3.5 H-shaped specimen of length l and adhesive thickness t. Dimensions in mm.

tests are video recorded. Pull-off specimens are loaded with a displacement rate of 5 mm/min. The tests were performed and reported by Staudt (2017).

Quantities required for the evaluation of failure criteria proposed in the present work are computed using the commercial finite element analysis software Abaqus® (2018). H-shaped specimens are represented by two-dimensional finite element models (Fig. 3.6). Because of the strong elastic contrast between the silicone adhesive with an initial Young's modulus at the order of 1 MPa and steel adherends with a Young's modulus at the order of 200 GPa, the adherends are modeled rigidly. Cracks Δa are introduced by locally removing displacement constraints from the adhesive boundary (Fig. 3.6a). This is expressed by the following boundary-value problem

$$\begin{cases} -\operatorname{div}\boldsymbol{\sigma} = 0 & \text{in} \quad \Omega, \\ \boldsymbol{u} = 0 & \text{along} \quad \Gamma_0, \\ \boldsymbol{u} = \tilde{\boldsymbol{u}} & \text{along} \quad \Gamma_u, \\ \boldsymbol{\sigma}\boldsymbol{n} = 0 & \text{along} \quad \Gamma_t^- \cup \Gamma_t^+ \cup \Gamma_c, \end{cases} \tag{3.1}$$

where $\boldsymbol{\sigma}$ is the Cauchy stress tensor (2.34a), $\boldsymbol{u}$ the displacement vector field (2.1), $\boldsymbol{n}$ the unit outward normal vector and $\partial\Omega = \Gamma_c \cup \Gamma_0 \cup \Gamma_t^+ \cup \Gamma_u \cup \Gamma_t^-$ the boundary of the problem domain Ω (Fig. 3.6a). We prescribe stress-free boundary conditions along Γ_t^- and Γ_t^+, vanishing displacements along Γ_0 and constant displacements $\tilde{\boldsymbol{u}}$ along Γ_u. Cracks are represented by the stress-free boundary Γ_c. In experiments, we observe cohesive cracks that nucleate from the singular bi-material notch and grow close to the interface within the adhesive. Using bulk adhesive fracture properties for the failure criterion, cohesive failure can be examined despite modeling cracks geometrically within the adherend-adhesive interface. Introducing cracks within or close to the interface has a negligible impact on failure load predictions as shown by Hell et al. (2014).

The hyperelastic adhesive is modeled using the Marlow (2003) material model (cf. Section 2.1.4) detailed and characterized in Section 4.2. It is assumed fully incompressible and no volumetric strain energy potential is specified. Four-noded Abaqus® (2018) plane-strain hybrid elements with selective reduced pressure integration are used. Specimens are loaded by prescribed displacements. Converged discretizations structured as

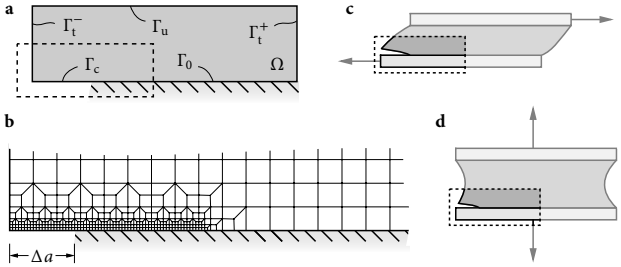

Fig. 3.6 Plane strain finite element model of H-shaped specimens. **a** Problem domain with boundaries and **b** magnification of the discretization of **c** simple shear and **d** pull-off tests.

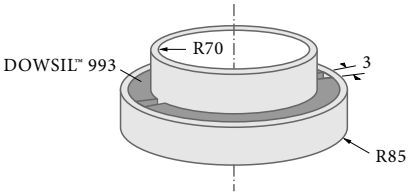

Fig. 3.7 Notched tubular lap joint specimen of DOWSIL™ 993. Manufactured inserting two opposing 3 mm wide PTFE spacers into tubular lap joints (Fig. 3.4) during curing. Dimensions in mm.

shown in (Fig. 3.6b) have less than 10 000 degrees of freedom. Solving a single nonlinear boundary value problem requires less than 30 s on a standard desktop computer. The adhesive is loaded by prescribed horizontal or vertical displacements as shown in Figs. 3.6c and d, respectively. In order to provide all outputs of the nonlinear solution in adequate resolution, the load is applied in at least 20 increments and cracks are resolved in 32 to 96 increments depending on their estimated maximum length.

3.2.2 Notched tubular lap joints

Notched tubular lap shear specimens (Fig. 3.7) are manufactured and tested as their unnotched counterparts described in Section 3.1.4. Notches are manufactured by inserting two 3 mm wide PTFE spacers at opposing sides into the mold prior to pouring. The notch width is chosen so that opposing silicone faces do not touch during testing. Four notched tubular lap shear specimens were tested and reported by Staudt (2017) and Staudt et al. (2018).

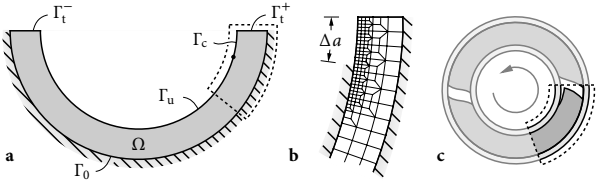

Fig. 3.8 Plane strain finite element model of notched tubular lap joints. **a** Problem domain with boundaries, **b** magnification of the crack tip discretization, and **c** angular displacement loading.

The finite element model of the notched tubular lap joint (Fig. 3.8) differs from the H-specimen model only in its curved boundaries and its angular displacement loading. The same boundary value problem (3.1) is solved (Fig. 3.8a) and the same mesh structuring technique is used (Fig. 3.8b). The number of degrees of freedom and computational cost are similar. The nonlinear adhesive is loaded by a prescribed angular displacement (Fig. 3.8c) in at least 20 increments and cracks are resolved in 32 steps.

3.2.3 Pancake specimens

Pancake tests (also known as poker chip tests) are typical experiments conducted on nearly incompressible hyperelastic elastomers. The name refers to the thin, flat, and round shape of the tested material. In the present case, specimens are composed of two steel cylinders that are bonded by a thin layer of DOWSIL™ TSSA (Fig. 3.9). Under axial loading, the volumetric constraint imposed by the stiff adherends in combination with the large bulk modulus of the silicone causes high volumetric stresses in the specimen center, allowing for the investigation of dilatational failure.

Specimens of $d = 20\,\text{mm}, 40\,\text{mm}$ and $50\,\text{mm}$ diameter are cured in an autoclave according to the specifications of Sitte et al. (2011). Because only small displacements are expected, the samples are tested at a loading rate of $0.1\,\text{mm/min}$ at ambient conditions. Deformations are obtained from DIC measurements. For this purpose, the specimens are coated with a white primer and provided with a black speckle pattern. The tests were performed and reported by Drass et al. (2018c).

The pancake specimens are analyzed computationally using an axisymmetric finite element model (Fig. 3.10). The FE model uses the same discretization strategy as the H-specimen model (Fig. 3.10b) and employs eight-noded axisymmetric elements. Again, displacements are fixed along Γ_0 and prescribed along Γ_u, Γ_t and Γ_c are stress-free, and symmetry boundary conditions, i.e., fixed radial displacements, are applied along Γ_s (Fig. 3.10a). DOWSIL™ TSSA is compressible. Hence, its constitutive behavior is composed of both an isochoric and a volumetric strain energy density function. The

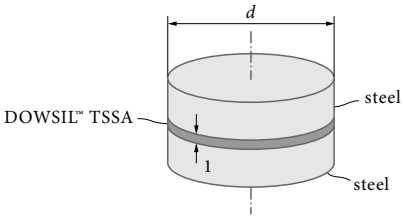

Fig. 3.9 Pancake specimen of DOWSIL™ TSSA with diameter d. Dimensions in mm.

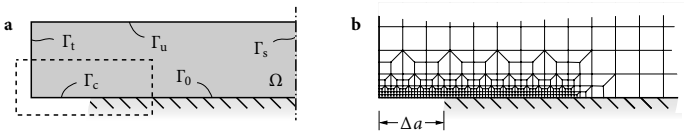

Fig. 3.10 Axisymmetric finite element model of pancake specimens. **a** Problem domain with boundaries and **b** magnification of the crack tip discretization.

isochoric part is modeled using a Neo-Hookean potential (2.101). The volumetric part is represented by a four-term volumetric potential (2.123) suggested by Drass et al. (2018c). Details on the material model are given in Section 4.2.

3.2.4 Cleavage double cantilever beam specimens

Double cantilever beam (DCB) specimens are used for the measurement of mode I fracture toughnesses of DOWSIL™ 993 and DOWSIL™ TSSA. The silicones have different typical forms of application and different semi-finished products, which requires different DCB specimen geometries (Fig. 3.11). DOWSIL™ TSSA is supplied in sheets of 1 mm thickness, while DOWSIL™ 993 can be cast into any shape and is typically applied as a thick layer with rectangular cross section.

DOWSIL™ 993 specimens (Fig. 3.11a) are manufactured from high strength aluminum EN AW 7075 with two different adhesive thicknesses t = 6 mm and 12 mm. The bond thicknesses correspond to the lower bound and the standard adhesive thickness in component tests specified in the European Technical Approval Guideline for Structural Sealant Glazing Systems (EOTA, 2012), respectively. A 3 mm pre-crack is cut at mid-height of the adhesive using a razor blade. The test samples are manufactured on a polyethylene plate. PE blocks serve as adherend spacers and adhesive molds, simultaneously. All components are secured against movement using screw clamps. The adherends are carefully cleaned using DOWSIL™ R-40 solvent and DOWSIL™ 1200

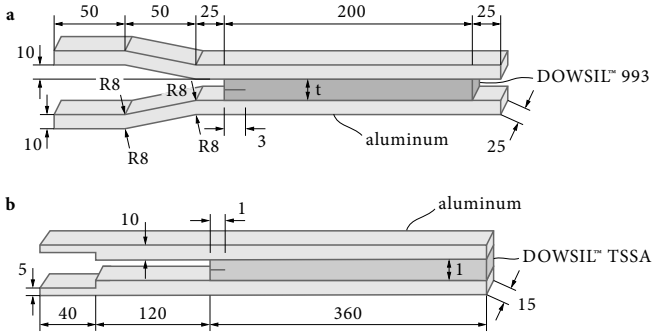

Fig. 3.11 Geometry of cleavage double cantilever beam specimens for **a** DOWSIL™ 993 and **b** DOWSIL™ TSSA. Dimensions in mm.

OS primer is applied prior to pouring the adhesive. Silicone mixing and pouring is performed at the facilities of a local facade manufacturer using a professional static mixing and dispense pump. The quality of the adhesive is monitored using the two plates test detailed by the Dow Corning Corporation (2011). The specimens are stored at the manufacturer for 15 days before demolding and are tested earliest after one month of curing time.

For testing, samples are clamped at the extremities of their cantilever arms. Inclinometers record the rotation of the load points. The crack tip opening displacement is measured using video-extensometry based on a 3D digital image correlation system tracking speckle patterns applied on the adherends above and below the crack tip. All tests are performed at ambient conditions and under quasi-static loading. Specimens of 6 mm adhesive layer thickness are tested at a loading rate of 1.5 mm/min. Specimens with 12 mm adhesive thickness are loaded at 3 mm/min. Although DOWSIL™ 993 is not expected to exhibit viscoelastic effects, this ensures approximately equivalent crack tip strain rates. The tests were performed and reported by Rosendahl et al. (2019c).

DOWSIL™ TSSA specimens (Fig. 3.11b) are composed of two EN AW 6082 aluminum adherends and an adhesive layer of 1 mm nominal thickness. They are cured in an autoclave as specified by Sitte et al. (2011). A pre-crack of 1 mm nominal length is cut using a razor blade. The DOWSIL™ TSSA samples are tested at ambient conditions at a loading rate of 6 mm/min. The load point rotation is recorded using inclinometers. The crack tip opening displacement is measured using line sensors. For this purpose, white flags are attached to the substrates above and below the pre-crack tip. The sensors detect the contrast between the white flags and a black background. The optical sensor system is oriented along the specimen's longitudinal axis avoiding impacts of rigid body

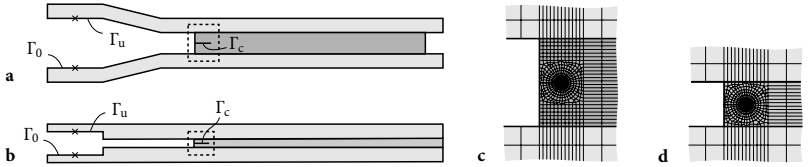

Fig. 3.12 Plane strain finite element models of double cantilever beam specimens. DOWSIL™ 993 and DOWSIL™ TSSA specimen boundaries (**a** and **b**) and magnification of the corresponding discretizations (**c** and **d**).

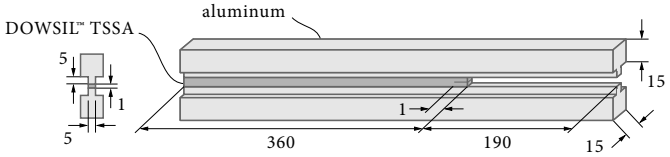

Fig. 3.13 Out-of-plane shear double cantilever beam specimen of DOWSIL™ TSSA. Dimensions in mm.

movements during loading.

For an assessment of the quality of fracture toughness measurements, the DCB samples are investigated in plane-strain FEAs (Fig. 3.12). Manufactured pre-cracks are represented by stress-free boundaries Γ_c (Figs. 3.12a and b). No crack growth is considered. Displacements are prescribed in such a way that the boundaries Γ_0 and Γ_u move like rigid bodies pivoted at the indicated reference point ($\times$). All other boundaries that are not labeled are stress-free. Refined radial meshes of eight-noded plane strain elements are provided around the crack tip (Figs. 3.12c and d) to allow for an accurate evaluation of the *J*-integral (2.166). DOWSIL™ 993 is modeled as described in Section 3.2.1. The constitutive behavior of DOWSIL™ TSSA is described by a Neo-Hookean strain energy density function (2.101) with a shear modulus of $\mu = 2.67$ MPa and the simple volumetric model given by Eq. (2.119) with a bulk modulus of $K = 2.5$ GPa.

3.2.5 Out-of-plane shear double cantilever beam specimens

Out-of-plane double cantilever beam (ODCB) specimens are used for the determination of the mode III fracture toughness of DOWSIL™ TSSA (Fig. 3.13). The samples are manufactured from two EN AW 6082 aluminum substrates bonded by a layer of DOWSIL™ TSSA of 1 mm nominal thickness. The special geometry of the adherends allows for simple clamping and keeps the out-of-plane width of the adhesive layer small. The latter is important to obtain failure loads of a desired magnitude. The samples are

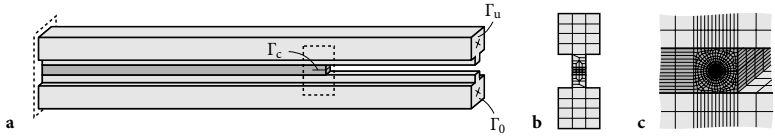

Fig. 3.14 Three-dimensional finite element model of the out-of-plane shear double cantilever beam specimen. **a** Boundaries, **b** out-of-plane discretization and **c** in-plane and crack tip discretization.

cured in an autoclave as specified by Sitte et al. (2011) and a pre-crack of 1 mm nominal length is cut using a razor blade.

We use a biaxial tension–torsion test machine with a 200 Nm load cell at ambient conditions. The out-of-plane shear loading is imposed by a rotation on the free beam ends around the vertical axis at 3.6 °/min. Vertical forces are controlled to vanish. In-plane and out-of-plane forces are avoided using linear slides. Crack tip opening displacements are measured using a 3D stereo camera system and speckled adherends. Strain gauges record deformations of the cantilever arms on their bending tension side.

The samples are investigated computationally using a three-dimensional finite element model (Fig. 3.14). The stress-free boundary Γ_c represents the manufactured pre-crack (Fig. 3.14a). Displacements are prescribed on Γ_0 and Γ_u in such a way that the cantilever arm faces move like rigid bodies pivoted at the marked reference points ($\times$). Boundaries that are not labeled are stress-free. The adherends are discretized coarsely using eight-noded volume elements (Fig. 3.14b). The crack tip is enclosed in a refined radial mesh (Fig. 3.14c). DOWSIL™ TSSA is modeled using a Neo-Hookean constitutive law (2.101) with the volumetric potential given by Eq. (2.119) using shear and bulk moduli of $\mu = 2.67$ MPa and $K = 2.5$ GPa, respectively.

Chapter 4

Experimental material characterization

Modeling fracture of nearly incompressible hyperelastic media is challenging for several reasons: i) different failure modes such as dilatational and distortional failure may occur, ii) notches induce weak singularities with infinite stresses but vanishing energy release rates, iii) the onset of interface cracks is a mixed-mode fracture problem and iv) the nonlinear elastic constitutive behavior must be accounted for. In order to address all of the above points, let us consider two exemplary nonlinear elastic silicones: DOWSIL™ 993 Structural Glazing Sealant (Dow Chemical Company, 2018) and DOWSIL™ Transparent Structural Silicone Adhesive (TSSA, Dow Chemical Company, 2019).

DOWSIL™ 993 (previously known as Dow Corning® 993) is a nearly incompressible, hyperelastic, two-component, room temperature curing silicone. Despite large deformations prior to failure, no significant zone of inelastic deformations develops. Fracture surfaces of a fully fractured sample align perfectly because only the formation of the fracture surface dissipates energy. The specimen will take its original shape when put back together because no inelastic processes occur. Hence, fracture of DOWSIL™ 993 is associated with a sudden drop in loading and can be considered brittle. It is typically applied in a thick but comparatively narrow bead, allowing for lateral contractions. Its prevailing mode of failure in practical applications is distortional.

DOWSIL™ TSSA is a nearly incompressible, hyperelastic, transparent, one-part, heat curing silicone film adhesive for glass–metal connections. While it is slightly stiffer than DOWSIL™ 993, it has similar mechanical properties. However, DOWSIL™ TSSA is supplied in sheets of 1 mm nominal thickness. Hence, its large bulk modulus is prone to cause large hydrostatic stresses and, thus, dilatational failure in volumetrically constrained applications. Both DOWSIL™ 993 and DOWSIL™ TSSA are virtually free of viscous effects.

The following sections use the specimens introduced in Chapter 3 to characterize the constitutive behavior, mixed-mode bulk failure properties and fracture properties of DOWSIL™ 993 and DOWSIL™ TSSA. The main results discussed in this chapter are published in peer-reviewed journals and conference proceedings (Rosendahl et al., 2018, 2019a,c,e,d).

4.1 State of the art

Several experimental methods for the characterization of the constitutive behavior are standardized. Many standards for linear elastic materials can be readily applied to hyperelastic media, as well (ASTM Standard D4762, 2018). Often dedicated hyperelastic test methods are available (ASTM Standard D624, 2000; ASTM Standard D6976, 2013; ASTM Standard D3492, 2016). This also holds for the characterization of bulk material failure. For instance, uniaxial tensile tests can be performed equivalently for linear elastic (ASTM Standard D638, 2014) and hyperleastic materials (ASTM Standard D412, 2016). Biaxial tests such as the bulge test (ASTM Standard E2712, 2015) can be adapted to hyperelastic media. Tubular lap shear tests (Adams and Peppiatt, 1977) are again applicable to both classes of materials. Certain tweaks have been suggested to better the handling of large deformations. Becker (2009), for instance, proposes a wider uniaxial tension specimen to improve the optical tracking of lateral contractions.

Major differences are present when testing for fracture properties, in particular for the fracture toughness. Here, more complex models are required to calculate properties of interest from experimentally accessible quantities. Classical models often rely on the assumption of linear elasticity and cannot be readily transferred to hyperelastic media. Several standardized methods to determine the fracture toughness are available. Linear elastic bulk material can be tested using compact tension (CT) or three-point bending (3PB) specimens as detailed in ASTM Standard E399 (2017). The standard exploits known stress intensity factors of manufactured pre-cracks. Employing beam theory, ASTM Standard D5528 (2013) describes fracture toughness measurements using bulk material double cantilever beam (DCB) specimens. Both standards require the manufacturing of bulk specimens, which may not be feasible or possible for all adhesives. Hence, ASTM Standard D3433 (2012) and BS Standard 7991 (2001) detail tests using adhesively bonded DCB or tapered double cantilever beam (TDCB) specimens. Using the Irwin–Kies equation (Irwin and Kies, 1954), also known as compliance method, the energy release rate can be determined measuring applied loads only. Here, the change of compliance with crack growth is constant and can be determined either analytically using beam theory or experimentally in separate tests. The so-called work-area method uses periodic loading and unloading of DCB or TDCB specimens to trigger incremental crack advances. It is used for instance by Hashemi et al. (1990), Blackman et al. (1991), and Marzi et al. (2009a). The fracture toughness can be obtained from the slope of a linear regression of per cycle changes in potential energy and per cycle crack growth. The results of a round-robin test reported by Blackman et al. (2003) show similar results of the above methods for DCB or TDCB tests. The rigid DCB (RDCB) test proposed by Khayer Dastjerdi et al. (2013) exploits rigidity of very stiff adherends. Assuming rigidity, the fracture toughness can be determined from a directly measured traction–separation law. Except for the RDCB test, which is limited to thin adhesive layers, all of the above

methods require the assumption of linearity for the adhesive and are thus not suitable for thick hyperelastic silicones.

Evaluating the above fracture tests using the path independent J-integral (2.166) requires no assumption of linearity. The integral is applicable when the material is elastic or no unloading from inelastically deformed states occurs (Eshelby, 1999). Nonlinearity is explicitly permitted. The J-integral provides an expression for the energy release rate that only depends on readily measurable quantities. In particular, the expression is independent of the crack length. Li and Ward (1989) use the J-integral approach for CT and 3PB specimens and obtain results that agree well with the standardized evaluation methods detailed in ASTM Standard E399 (2017). Sørensen (2002), Andersson and Stigh (2004), Andersson and Biel (2006), Marzi et al. (2014), and Biel and Stigh (2017) use the J-integral to test adhesively bonded DCB specimens with both linear and nonlinear adhesives. Comparing different methods for evaluating such DCB specimens, Marzi et al. (2011) report a good agreement between Irwin–Kies equation, work-area method and J-integral approach for thin linear elastic adhesives. Banea et al. (2010) and Schmandt and Marzi (2018a,b) apply the J-integral model to mode I DCB tests of hyperelastic adhesives. Loh and Marzi (2018a) develop a J-integral based mode III DCB specimen and perform mixed-mode I+III fracture toughness tests on hyperelastic adhesives (Loh and Marzi, 2018b,c, 2019). Banea et al. (2015) and Campilho et al. (2015) use the J-integral approach for ductile adhesive DCB specimens. However, all of the above studies rely on small deformation assumptions or neglect the adhesive in their derivation altogether.

In the following, we use standard methods in order to characterize the constitutive behavior and bulk material fracture properties of DOWSIL™ 993 and DOWSIL™ TSSA. Then, a finite deformation J-integral model for adhesively bonded DCB specimens is derived to determine the mode I and mode III fracture toughnesses of thick-layered hyperelastic structural sealants.

4.2 Characterization of the constitutive behavior

A comprehensive assessment of the vast number of available constitutive laws, regarding their suitability for a particular hyperelastic material, is nearly impossible. Moreover, only some of the models are available in commercial finite element software. In order to determine constitutive models for DOWSIL™ 993 and TSSA, we review the literature on suitable constitutive laws and use own experiments to identify model parameters.

DOWSIL™ 993. Staudt et al. (2014), Dias et al. (2014), and Dispersyn et al. (2017) evaluate different common strain energy density functions regarding their applicability

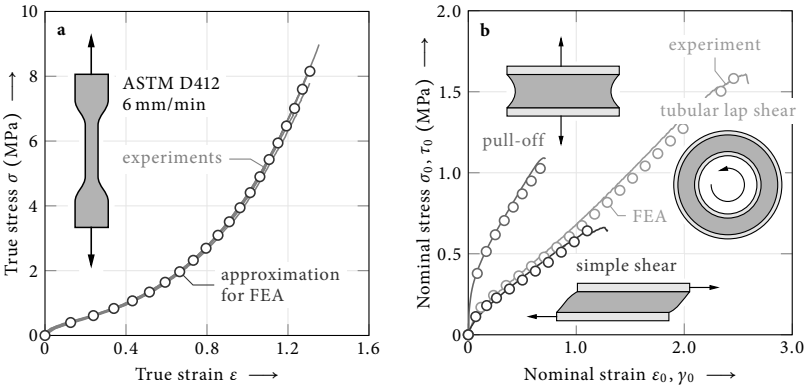

Fig. 4.1 Characterization of the constitutive behavior of DOWSIL™ 993. **a** Uniaxial tension test according to ASTM Standard D412 (2016) used as tabular input for a Marlow-type material model. **b** Numerical reproduction of different adhesive joint geometries using the Marlow (2003) material model in finite element analyses (FEA).

to hyperelastic adhesives. Dispersyn et al. (2017) perform several different tests on the hyperelastic adhesive sealant Soudaseal 207 HS and compare Neo-Hooke (2.101), Yeoh (2.102), Mooney–Rivlin (2.105), and Ogden (2.109) strain energy density functions, as well as the models of Arruda and Boyce (1993), Gent and Thomas (1958), and Yeoh and Fleming (1997), among others. In this study none of the considered constitutive models provides a satisfactory description of all experiments using a single set of parameters. Nonetheless, Dispersyn et al. (2017) recommend the Ogden model (2.109). Dias et al. (2014) test DOWSIL™ 993 in uniaxial tension, unaxial compression and simple shear, and deem the Neo-Hooke (2.101), Yeoh (2.102), and Mooney–Rivlin (2.105) models inadequate and, hence, propose a new constitutive equation. Staudt et al. (2014) examine the Neo-Hooke (2.101), Yeoh (2.102), Mooney–Rivlin (2.105), Ogden (2.109), and Marlow (2.104) constitutive laws, as well as the extended tube model (Kaliske and Heinrich, 1999), and the model of Gent and Thomas (1958), regarding their suitability for DOWSIL™ 993 in uniaxial tension and simple shear tests of different bond thicknesses. They report good results only for the Marlow (2003) model. Extending the validation to pull-off and tubular lap shear tests, this conclusion is confirmed in the present work.

For the present analysis, the constitutive law for DOWSIL™ 993 is determined in uniaxial tensile tests according to ASTM Standard D412 (2016) (Section 3.1.1). True strains are obtained from DIC measurements. True stresses are computed from the force signal considering the change of the cross section during loading. Figure 4.1a shows measurements of five specimens reported by Staudt et al. (2014, 2018). Assuming incompressibility,

the smoothed mean of all five measurements is used as tabular input for a Marlow material model (2.104). This material model requires no parameter identification but uses uniaxial tension data as input directly (Section 2.1.4). Using the tabular data of Fig. 4.1a, simple shear and pull-off tests using H-shaped specimens (Section 3.2.1), and a shear test using tubular lap joints (Section 3.1.4) are reproduced using FEA in Fig. 4.1b. The Marlow (2003) material model provides an excellent description of the constitutive behavior of DOWSIL™ 993 in all tested configurations.

DOWSIL™ TSSA. Using transmission electron images, Drass et al. (2018c) show that TSSA is a porous material with micro cavities of the order of 30 nm in diameter. Such voids have an elastic stability limit as discussed in Section 2.2. The (instable) expansion of cavities is observed as whitening of the initially transparent silicone in experiments (Drass et al., 2018c,d). Pore growth is typically not associated with ultimate failure but causes softening of the macroscopic bulk material response and, hence, must be accounted for in the volumetric part $\mathcal{W}_{\text{vol}}$ of constitutive models, cf. Eq. (2.99). Because DOWSIL™ TSSA is not fully incompressible, and owing to the particular formulation of Eq. (2.123), volumetric deformations may also cause a reduction of $\mathcal{W}_{\text{vol}}$ in, e.g., uniaxial and biaxial load cases where softening is not observed experimentally. Hence, in order to use Eq. (2.123), the strain energy density function

$$\mathcal{W} = \mathcal{W}_{\text{iso}} + \mathcal{W}_{\text{vol}} + \mathcal{W}_{\text{coup}}, \tag{4.1}$$

incorporates a coupling term $\mathcal{W}_{\text{coup}}$ that tracks the geometric evolution of cavities and corrects for the loss of volumetric strain energy in distortion-dominated situations.

Drass et al. (2018e) report uniaxial tension, uniaxial compression, bulge, and shear tests of DOWSIL™ TSSA (Fig. 4.2a). In a consecutive numerical analysis of these experiments, the authors investigate different isochoric strain energy density functions regarding their suitability for the material (Drass et al., 2018f). The best results are obtained with a newly proposed strain energy function. However, the Neo-Hookean potential (2.101) yields an excellent representation of all four experiments with the same set of parameters, despite its simplicity. The performance of models developed for filled rubbers such as the extended tube model (Kaliske and Heinrich, 1999) is slightly worse. Hence, we model the isochoric part of the strain energy $\mathcal{W}_{\text{iso}}$ of DOWSIL™ TSSA using a Neo-Hookean potential (2.101).

The volumetric part is represented by the softening model (2.123) proposed by Drass et al. (2018c) using four terms. This yields

$$\mathcal{W} = \frac{\mu}{2}(I_{\bar{\boldsymbol{B}}} - 3) + \int_J \frac{J-1}{d_0 + d_1(J-1) + d_2(J-1)^2 + d_3(J-1)^3}\,\mathrm{d}J + \mathcal{W}_{\text{coup}}(J, \chi). \tag{4.2}$$

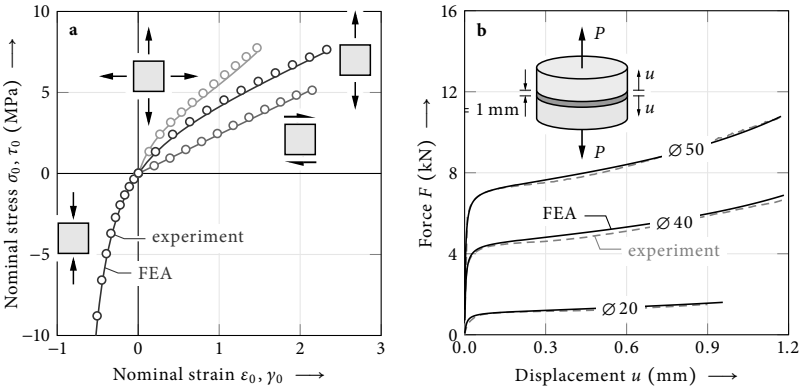

Fig. 4.2 Characterization of the constitutive behavior of DOWSIL™ TSSA. **a** Fit of the isochoric part of the strain energy density function (4.2) to uniaxial tension (Section 3.1.1), bulge (Section 3.1.2), uniaxial compression (Section 3.1.3), and shear tests (Section 3.2.3) that yields $\mu = 2.67$ MPa. **b** Fit of the volumetric part of the strain energy density function (4.2) to pancake tests of ∅50 mm diameter yielding $K = 1/d_0 = 2.5$ GPa as well as $d_1 = 0.271\,\text{MPa}^{-1}$, $d_2 = 0.260\,\text{MPa}^{-1}$, and $d_3 = -0.194\,\text{MPa}^{-1}$, and validation of the identified parameters using specimens of ∅40 mm and ∅20 mm diameter (Section 3.2.3).

The coupling term $\mathcal{W}_{\text{coup}}$ is defined as specified by Drass (2020). It is a function of the volume ratio J (2.6) and an internal variable $\chi \in [0,1]$ expressing the geometric shape of voids. The use of internal variables to capture softening effects is known as pseudo-elasticity (Lazopoulos and Ogden, 1998; Ogden and Roxburgh, 1999).

The simultaneous fit of the isochoric Neo-Hookean potential to uniaxial tension, uniaxial compression, bulge and simple shear tests (Fig. 4.2a) yields a shear modulus of $\mu = 2.67$ MPa. The parameters d_i of the volumetric part of the strain energy density function (4.2) are identified from pancake tests (Fig. 4.2b). Using the isochoric potential with $\mu = 2.67$ MPa, FE calculations are fitted to pancake specimens of ∅50 mm diameter (Fig. 4.2b). This yields a bulk modulus of $K = 1/d_0 = 2.5$ GPa as well as $d_1 = 0.271\,\text{MPa}^{-1}$, $d_2 = 0.260\,\text{MPa}^{-1}$, and $d_3 = -0.194\,\text{MPa}^{-1}$. The accuracy of this fit is evaluated using specimens of ∅40 mm and ∅20 mm diameter (Fig. 4.2b). The parameters d_i characterize the volumetric (pressure–volume change) response of DOWSIL™ TSSA, which governs the structural (force–displacement) response of pancake specimens. The bulk modulus $K = 1/d_0$ determines the initial slope of the volumetric material response, d_1 the onset of elastic instabilities, d_2 subsequent softening and d_3 the pressure-response at large volume ratios. Note that volumetric parameters identified and used in the present work are different from the ones reported by Drass et al. (2018c) and Drass (2020) because instead of a relatively coarsely discretized three-dimensional model an

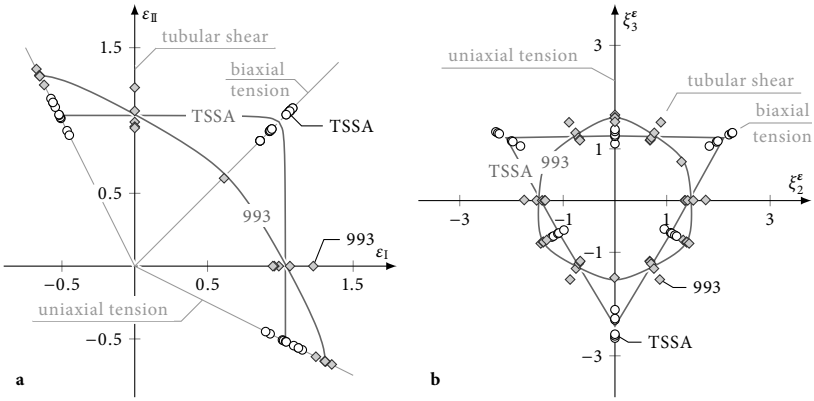

Fig. 4.3 Ultimate true strains (markers) in **a** ε_I-ε_{II}-plane and **b** deviatoric strain plane with corresponding deviatoric failure criteria (lines) given by Eq. (5.21) for DOWSIL™ TSSA ($\beta = 0.02$, $\gamma = 0.98$, $\varepsilon_c = 1.24 \pm 0.10$) and DOWSIL™ 993 ($\beta = 0.56$, $\gamma = 0.66$, $\varepsilon_c = 1.47 \pm 0.11$).

axisymmetric FE model of high mesh resolution is used (Section 3.2.3).

4.3 Bulk material extensibility

In a wide temperature range, elastomers are soft materials that undergo large deformations prior to failure. Tracking cross sectional changes in multiaxial fracture tests in order to compute true failure stresses is challenging. Measuring in-plane surface displacements, in particular using modern optical digital image correlation technology, proves considerably easier. Hence, much of the studies of multiaxial elastomer fracture available in literature report critical deformations only. Moreover, considering their micro structure, strains or stretches seem appropriate measures of the failure of soft polymers. The extensibility of chain segments of cross-linked macro molecules is limited (Wang and Guth, 1952). Although, macroscopic and chain deformations cannot be assumed equal (Kaliske and Heinrich, 1999), finite chain extensibility can be attributed to stiffening at large deformations and finally to rupture (Yeoh and Fleming, 1997).

In computational applications, calculated stresses and, thus, stress-based failure criteria depend on the specific choice of strain energy density function. For instance, while Nakamura and Lopez-Pamies (2012) obtain convex cavitational failure surfaces in principal stress space using a Neo-Hookean material model, they find nonconvex failure surfaces using an Ogden material model. Moreover, when computational tools are used

Table 4.1
Ultimate principal true strains of DOWSIL™ TSSA.

Test setup	$\varepsilon_{\mathrm{I}}^{\times}$	$\varepsilon_{\mathrm{II}}^{\times}$	$\varepsilon_{\mathrm{III}}^{\times}$
Uniaxial tension	0.930	−0.465	−0.465
	1.015	−0.507	−0.507
	1.120	−0.560	−0.560
	1.022	−0.511	−0.511
	1.037	−0.518	−0.518
	1.040	−0.520	−0.520
	1.151	−0.575	−0.575
	1.092	−0.546	−0.546
	1.124	−0.562	−0.562
	0.899	−0.449	−0.449
Equibiaxial tension	1.067	1.067	−2.135
	1.071	1.071	−2.142
	1.054	1.054	−2.109
	0.938	0.938	−1.876
	0.926	0.926	−1.852
	0.861	0.861	−1.721
	1.085	1.085	−2.170
	1.064	1.064	−2.129
	1.040	1.040	−2.080
	0.931	0.931	−1.861
	0.941	0.941	−1.883
	0.861	0.861	−1.722

to determine limit states of components, stresses and strains may exceed experimentally tested regimes, in particular in multiaxial loading settings. If the chosen strain energy density function is not strictly polyconvex, computed stresses may decrease unphysically with increasing strain outside the domain where material parameters were fitted to experimental data. Thus, stress-based failure criteria may never be satisfied in such cases and deformation-based criteria are preferred for hyperelastic media. While stretches (2.25) are fundamental quantities of local deformation in continuum mechanics, the mathematical description of failure surfaces and their physical interpretation is more convenient using strains (2.27).

Experiments on DOWSIL™ 993 and DOWSIL™ TSSA are reported by Staudt et al. (2018) and Drass et al. (2018e) in terms of stresses and are re-evaluated by Rosendahl et al. (2019a,d) in terms of ultimate extensibility. The data sets comprise uniaxial tension (Section 3.1.1), tubular lap shear (Section 3.1.4) and uniaxial compression (Section 3.1.3) tests for DOWSIL™ 993 and uniaxial (Section 3.1.1) and equibiaxial tension (Section 3.1.2) tests for DOWSIL™ TSSA. Corresponding ultimate principal true strains at failure are shown in Fig. 4.3 and given in Table 4.1 for DOWSIL™ TSSA and in Table 4.2 for DOWSIL™ 993.

Figure 4.3a shows the failure data in the ε_{I}-$\varepsilon_{\mathrm{II}}$-plane. For the incompressible silicone

Table 4.2
Ultimate principal true strains of DOWSIL™ 993.

Test setup	$\varepsilon_{\mathrm{I}}^{\times}$	$\varepsilon_{\mathrm{II}}^{\times}$	$\varepsilon_{\mathrm{III}}^{\times}$
Uniaxial tension	1.353	−0.675	−0.675
	1.304	−0.652	−0.652
	1.311	−0.655	−0.655
	1.307	−0.654	−0.654
	1.244	−0.622	−0.622
Tubular lap shear	1.066	0.0	−1.076
	1.226	0.0	−1.255
	0.949	0.0	−0.958
	0.990	0.0	−0.999
	0.958	0.0	−0.967
Uniaxial compression	0.614	0.603	−1.217

DOWSIL™ 993, the strain state under uniaxial compression corresponds to biaxial extension. While DOWSIL™ TSSA is rather insensitive to biaxial tension, the ultimate extensibility of DOWSIL™ 993 is considerably smaller in the biaxial case than in the uniaxial case. A strain failure criterion capable of describing the behavior of both materials will be introduced in Section 5.3. The criterion is shown alongside the test data in Fig. 4.3. Applying the π-plane coordinate transformation (2.128) to principal strains instead of principal stresses, we obtain a deviatoric plane that comprises deviatoric strain states at constant (zero) volumetric strain. This deviatoric strain plane is spanned by the coordinates ξ_2^{ε} and ξ_3^{ε}. Ultimate strains in the deviatoric plane are shown in Fig. 4.3b.

4.4 Fracture toughness

As for stresses, measuring fracture toughness in the context of large deformations is challenging. For this reason, the present work derives and uses a finite deformation *J*-integral model for adhesively bonded DCB specimens to determine the mode I and mode III fracture toughness of thick-layered hyperelastic structural sealants. The methodology is applied to cleavage DCB specimens (Section 3.2.4) bonded using DOWSIL™ 993 and DOWSIL™ TSSA and to out-of-plane shear DCB specimens (Section 3.2.5) of DOWSIL™ TSSA. The novelty of the present approach lies in the determination of the fracture toughness as a material property in the context of large deformations. By neglecting nonlinear deformations of the adhesive, previous studies aimed at characterizing an effective cohesive fracture toughness as a structural property of the entire adhesive layer rather than a material property of the adhesive.

4.4.1 Cleavage tests

Path independence of the *J*-integral (2.168) in elastic processes allows for the derivation of an approximate expression of J that only depends on experimentally accessible quantities. The accuracy of this approximation of the energy release rate of cleavage double cantilever beam specimens is quantified using FEA. The results of 13 DOWSIL™ 993 specimens and 11 DOWSIL™ TSSA specimens are reported.

Energy release rate of cleavage DCB specimens. Given that the energy release rate of a specimen is known, the fracture toughness can be determined experimentally as its critical value. For linear elastic bulk material DCB specimens, the energy release rate can be calculated using the Irwin–Kies equation

$$\mathcal{G}_{\mathrm{I}} = \frac{F^2}{2w}\frac{\mathrm{d}C}{\mathrm{d}a}, \tag{4.3}$$

where F is the applied end load, w the out-of-plane specimen width, C the compliance and a the crack length. The change of compliance with change of crack length $\mathrm{d}C/\mathrm{d}a$ is either calculated using beam theory or determined in separate experiments. However, analytical expressions for $\mathrm{d}C/\mathrm{d}a$ always rely on certain assumptions and can only be derived for linear elastic materials. Determining $\mathrm{d}C/\mathrm{d}a$ experimentally requires tracking the crack tip, which is a challenging task.

For a linear elastic bulk material DCB specimen, Paris and Paris (1988) derive an expression for the energy release rate

$$\mathcal{G}_{\mathrm{I}} = \frac{2F\theta}{w}, \tag{4.4}$$

using the *J*-integral and Eq. (2.167). Here, F is the applied load, θ the rotation of the load point and w the out-of-plane specimen width (Fig. 4.4). Compared to Eq. (4.3), Eq. (4.4) contains only readily measurable quantities. Olsson and Stigh (1989) obtain Eq. (4.4) for an adhesively bonded DCB specimen using Euler–Bernoulli beam theory and a weak-interface model assuming a simplified linear elastic continuum for the adhesive layer. Hence, either one of two assumptions, neglecting the adhesive or treating it as a simplified continuum, yields Eq. (4.4). Both hold for thin adhesive layers. As discussed in Section 4.1, several authors apply Eq. (4.4) to bonded mode I DCB specimens with linear and nonlinear adhesives under these assumptions.

Without linear elastic assumptions or neglecting the adhesive altogether, it may be shown that Eq. (4.4) represents a very good approximation for thick hyperelastic adhesives. To this end, consider the *J*-integral for crack extension in X_1-direction at finite deformation and nonlinear elasticity, Eq. (2.168). Exploiting its path independence, the *J*-integral is

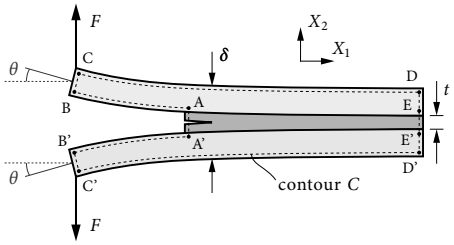

Fig. 4.4 Integration path along the outer contour of a bonded cleavage DCB specimen for the evaluation of the *J*-integral.

evaluated along the outer contour C of the DCB specimen depicted in Fig. 4.4, fully enclosing the crack tip. Given that the specimen is sufficiently long, the vertical edges $\overline{\text{BC}}$, $\overline{\text{B'C'}}$ and $\overline{\text{DD'}}$ are traction-free and their contribution to J vanishes. Similarly, the J-integral contribution vanishes along $\overline{\text{AA'}}$, provided the initial crack is sufficiently long. Along horizontal edges ($\overline{\text{AB}}$, $\overline{\text{A'B'}}$, $\overline{\text{CD}}$, $\overline{\text{C'D'}}$) and interfaces ($\overline{\text{AE}}$ and $\overline{\text{A'E'}}$), the first term in Eq. (2.168) vanishes because the edges are oriented along the X_1-axis. Further, $\overline{\text{AB}}$ and $\overline{\text{A'B'}}$ are traction-free so that all contributions to the J-integral are zero except at the load points. Exploiting the symmetry of the specimen (identical adherends), Eq. (2.168) simplifies to

$$J_{\text{I}} = 2 \int_{\text{C}}^{\text{D}} t_2^0 \frac{\partial u_2}{\partial X_1} \, \mathrm{d}c = \mathcal{G}_{\text{I}}, \tag{4.5}$$

where the index I indicates mode I crack opening, u_2 is the vertical displacement and t_2^0, the second component of the nominal traction vector (2.33), is zero everywhere except at the load point. Assuming Kirchhoff kinematics, $\partial u_2 / \partial X_1$ is given by $\tan\theta$ (Fig. 4.4) at this point. Despite present finite deformations, measured angles θ stay below 5° (cf. Fig. 4.8b) so that small angle approximation is admissible. The energy release rate of cleavage DCB specimens with thick hyperelastic adhesives is well approximated by

$$J_{\text{I}} = \frac{2F\theta}{w} = \mathcal{G}_{\text{I}}. \tag{4.6}$$

Equation (4.6) represents an approximation because the strain energy density $\mathcal{W}$ in Eq. (2.168) does not vanish completely on $\overline{\text{AA'}}$ for finite crack lengths. Thus, a small contribution to the J-integral is not accounted for and Eq. (4.6) overestimates the actual energy release rate. Rosendahl et al. (2019c) show that the error is below 13 % for DOWSIL™ 993 specimens and below 3 % for DOWSIL™ TSSA specimens (cf. Fig. 4.5).

Applying a cohesive zone concept as done by Nilsson (2005), the energy release rate can be calculated from the cohesive traction per unit area in the reference configuration

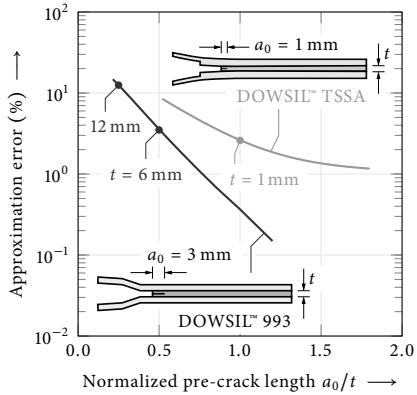

Fig. 4.5 Difference between mode I energy release rates determined in a finite element model from crack tip contour J-integrals and from Eq. (4.6). For DOWSIL™ 993 the relative deviation between both methods is below 4 % at t = 6 mm and below 13 % at t = 12 mm. For DOWSIL™ TSSA it is below 3 % at t = 1 mm.

according to

$$\mathcal{G}_\mathrm{I} = \int_0^\delta P_{22}(\tilde{\delta})\,\mathrm{d}\tilde{\delta}, \tag{4.7}$$

where δ is the crack tip opening displacement (Fig. 4.4). Equating Eqs. (4.6) and (4.7) and differentiating with respect to δ allows for determining the first Piola–Kirchhoff stress (2.34b) component

$$P_{22} = \frac{\mathrm{d}\mathcal{G}_\mathrm{I}}{\mathrm{d}\delta} = \frac{2}{w}\frac{\mathrm{d}(F\theta)}{\mathrm{d}\delta}. \tag{4.8}$$

Details of these derivations in the reference configuration are reported by Ortiz and Pandolfi (1999). Gasser and Holzapfel (2005) show that similar arguments yield expressions in the current configuration. However, as pointed out by Nilsson (2005), operating in the current configuration requires additional knowledge of the crack tip stretches λ_1 and λ_3 that are challenging to determine experimentally but may be assessed using a digital twin model (Budzik et al., 2011; Jumel et al., 2015; Cabello et al., 2016). Using Eq. (4.8) allows for identifying a peak nominal stress in the P_{22}–δ traction–separation curve. Deriving a peak true (Cauchy) stress would require detailed information about local deformation that is not readily available for the present study.

Quality of the approximation. Displacement-controlled DCB tests are designed to exhibit a domain of stable crack growth that manifests in a plateau of the energy release rate $\mathcal{G}_\mathrm{I}$ corresponding to the mode I fracture toughness $\mathcal{G}_\mathrm{Ic}$. That is, the fracture

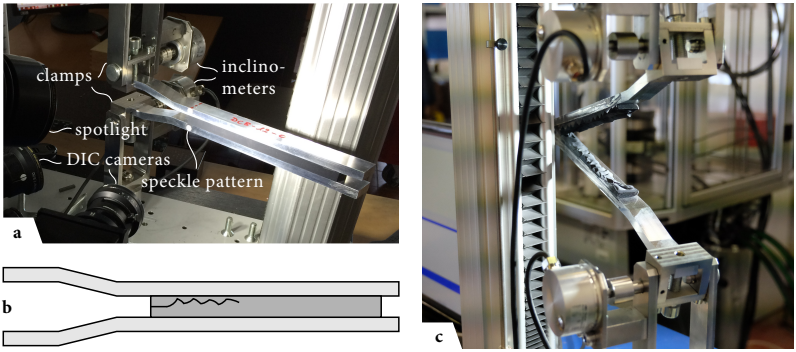

Fig. 4.6 DOWSIL™ 993 cleavage DCB experiments. **a** Test setup, **b** characteristic sawtooth crack pattern in thick layers of 993 and **c** representative failed specimen.

toughness is determined for long cracks, for which the contribution of the strain energy density $\mathcal{W}$ on $\overline{\mathrm{AA'}}$ (Fig. 4.4) to the J-integral (2.168) is negligible and Eq. (4.6) holds. However, in particular DOWSIL™ 993 DCB specimens tested in the present work do not enter this steady state. Hence, only the first instance of crack growth is considered for measurements of the fracture toughness and the accuracy of the approximation (4.6) for relatively short manufactured pre-cracks must be examined. For this purpose, we use the finite element models presented in Section 3.2.4 to compare the J-integral evaluated along contours closely around the crack tip with Eq. (4.6). FE crack tip opening displacements are determined as in the experiments as the vertical displacement difference of the adherends.

The analysis shows that Eq. (4.6) consistently overestimates the energy release rate. Computed relative deviations between crack tip contour J-integral and Eq. (4.6) are shown in Fig. 4.5. For tested DOWSIL™ 993 specimens with a pre-crack length of $a_0 = 3\,\mathrm{mm}$, the model error is smaller than 13 % at $t = 12\,\mathrm{mm}$ and smaller than 4 % at $t = 6\,\mathrm{mm}$. DOWSIL™ TSSA specimens with a pre-crack length of $a_0 = 1\,\mathrm{mm}$ exhibit a relative error below 3 % at the tested adhesive thickness of $t = 1\,\mathrm{mm}$. Although an error of 13 % is considerable, the model error is smaller than the standard deviation of the test series in all cases. The approximation is considered sufficiently accurate for the purpose of the present work. Based on Fig. 4.5, a normalized pre-crack length of $a_0/t > 0.5$, i.e., a manufactured crack of at least half the adhesive thickness, is recommended to ensure a model error below 10 %.

Evaluation of test data. Force, inclination and displacement signals of cleavage DCB tests (Fig. 4.6) are sampled at a rate of 50 Hz yielding noisy data. In order to evaluate

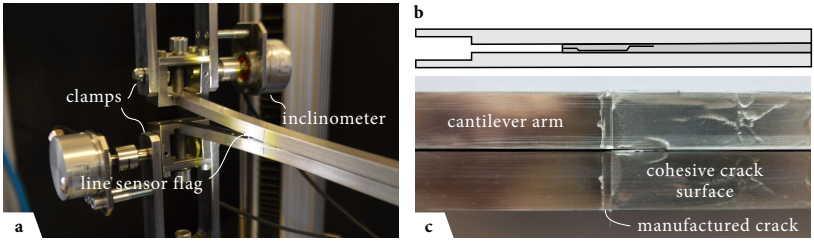

Fig. 4.7 DOWSIL™ TSSA cleavage DCB experiments. **a** Test setup, **b** characteristic crack pattern in thin layers of TSSA and **c** representative failed specimen.

the up to 45 min long individual tests, the signals are resampled at 1 Hz, which provides reasonable smoothing and adequate resolution. Typically, DCB specimens exhibit stable crack growth associated with a constant energy release rate, i.e., a plateau of the *J*-integral. However, as shown in Figs. 4.6b and c, DOWSIL™ 993 develops a sawtooth shaped crack surface. The effect is assumed to be related to the presence of fillers in the silicone sealant and is observed in many different experiments (Staudt, 2017; Staudt et al., 2018). That is, the crack does not propagate parallel to the adherends but instead grows towards one adherend where it is deflected back towards the other adherend. Deflecting the crack consumes additional energy and requires additional loading, which is reflected in a larger energy release rate, i.e., a further increasing *J*-integral. Additionally, once the crack propagates, the measured δ-signal does not correspond to the crack tip opening displacement anymore.

A similar behavior is observed for DOWSIL™ TSSA, which is filled with silica particles (Fig. 4.7). Instead of developing a sawtooth pattern, cracks in the thin DOWSIL™ TSSA layer are initially unstable and propagate as cohesive cracks close to one interface before they arrest. Crack propagation is associated with load reduction. Subsequent load increase is accompanied by stable crack growth where cracks may grow across the adhesive layer (Fig. 4.7b). At the initial critical load level another unstable crack event is observed. As in the initial propagation phase, the unstable crack arrests after a certain load drop.

In both cases, first crack growth can be identified unambiguously from distinct sudden drops in the force signal (Fig. 4.8a). Peak identification can be performed using signal processing toolboxes of, e.g., MathWorks MATLAB or Wolfram Mathematica allowing for automated data processing. The load point inclination signal (Fig. 4.8b) is affected much less by the onset of crack growth. Nonetheless, a slight sudden increase is observed.

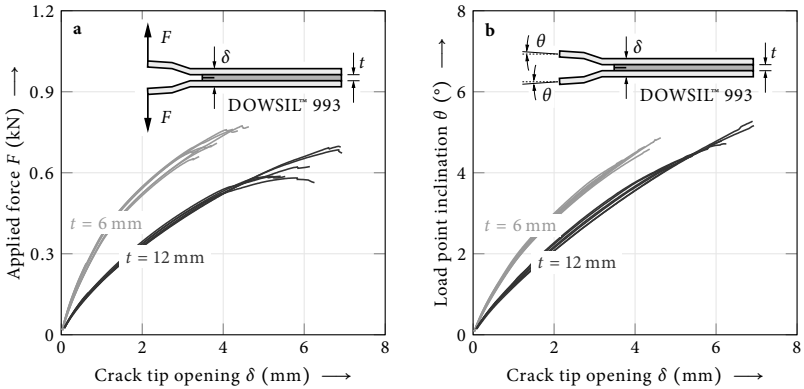

Fig. 4.8 Signals measured for DOWSIL™ 993 DCB specimens of t = 6 mm and 12 mm adhesive thickness. **a** Applied force and **b** load point inclination versus crack tip opening displacement. Signals are capped shortly after the first distinct drop in transferred force corresponding to the first instance of crack propagation.

Table 4.3
Summary of DOWSIL™ 993 mode I DCB test results: Fracture toughness $\mathcal{G}_{Ic}$, peak nominal traction P_{22}^c and critical crack tip opening displacement δ_c of specimens of adhesive thickness t.

	t = 6 mm			t = 12 mm		
Specimen	$\mathcal{G}_{Ic}$ (N/mm)	P_{22}^c (MPa)	δ_c (mm)	$\mathcal{G}_{Ic}$ (N/mm)	P_{22}^c (MPa)	δ_c (mm)
01	3.59	1.26	3.26	3.73	0.88	5.83
02	4.73	1.32	4.20	3.57	0.90	5.24
03	3.74	1.35	3.22	4.02	0.90	5.85
04	4.18	1.49	3.70	3.49	0.88	5.11
05	4.82	1.35	4.08	4.88	0.91	6.85
06	5.15	1.39	4.47	4.94	0.93	6.62
07	4.08	1.35	3.54	–	–	–
Mean	4.33	1.36	3.78	4.11	0.90	5.92
Std. dev.	0.58	0.07	0.48	0.65	0.02	0.71

Mode I fracture toughness and critical nominal stress. Figure 4.9a shows J-integral curves determined using Eq. (4.6) for 7 DOWSIL™ 993 specimens of 6 mm adhesive thickness and 6 specimens of 12 mm adhesive thickness. The curves are capped at the identified first drop of the load signal corresponding to crack propagation. The maxima in Fig. 4.9a represent critical values of $\mathcal{G}_I$, i.e., fracture toughnesses. Table 4.3 summarizes the fracture toughnesses determined for the DOWSIL™ 993 cleavage DCB specimens tested in the present work. Overall, mean and standard deviation of the mode I fracture toughness of DOWSIL™ 993 are $\mathcal{G}_{Ic} = 4.22 \pm 0.60$ N/mm.

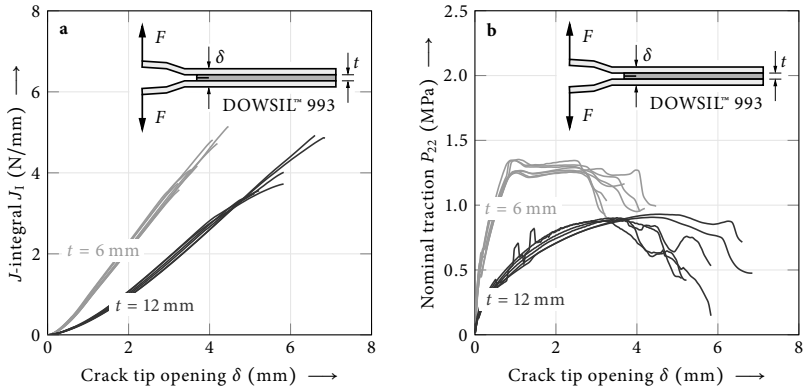

Fig. 4.9 Quantities of interest in DOWSIL™ 993 DCB tests. **a** *J*-integral according to Eq. (4.6) and **b** first Piola–Kirchhoff stress versus crack tip opening displacement capped at identified first crack propagation.

Determining the fracture toughness using DCB specimens is known to depend on the adhesive thickness up to a certain threshold value. For linear elastic adhesives Carlberger and Stigh (2010) and Marzi et al. (2011) identify an adhesive thickness threshold of about 1 mm. Schmandt and Marzi (2018a) report a threshold of 6 mm for DCB tests of a soft hyperelastic adhesive, above which measured fracture toughnesses are constant with respect to the adhesive thickness. Present tested thicknesses lie above this threshold and obtained fracture toughnesses are independent of adhesive thickness (Table 4.3). Hence, it can be assumed that the bulk material mode I fracture toughness of DOWSIL™ 993 is measured.

Figure 4.9b shows nominal traction versus crack tip opening displacement for 7 specimens of 6 mm adhesive thickness and 6 specimens of 12 mm adhesive thickness. In cohesive zone modeling, these curves are known as traction–separation laws. They are the result of a differentiation of the curves in Fig. 4.9a with respect to δ according to Eq. (4.8) and can be used to model cohesive crack propagation numerically as shown by Ortiz and Pandolfi (1999). Meaningful parameters are maximum traction P_{22}^{c} and maximum crack tip opening displacement δ_c. The peak traction in terms of true (Cauchy) stress can be assumed to represent a material property. However, as discussed above, without knowledge of 3D local crack tip deformations, only the first Piola–Kirchhoff stress (2.34b), i.e., the nominal traction can be deduced. Because the 6 mm adhesive layer cannot contract as much as the thicker adhesive layer, its load transferring cross section is larger. Therefore, larger nominal stresses can be withstood given that the adhesive's true (Cauchy) peak stress is a material constant. Identified peak

Table 4.4
Summary of DOWSIL™ TSSA mode I DCB test results: Fracture toughness $\mathcal{G}_{\mathrm{Ic}}$, peak nominal traction P_{22}^{c} and critical crack tip opening displacement δ_{c}.

Specimen	$\mathcal{G}_{\mathrm{Ic}}$ (N/mm)	P_{22}^{c} (MPa)	δ_{c} (mm)
01	4.42	6.35	0.95
02	4.71	8.69	1.02
03	4.85	5.97	1.09
04	3.26	5.45	0.82
05	2.25	4.75	0.65
06	3.13	5.66	0.70
07	4.03	5.42	0.92
08	3.91	6.44	0.88
09	3.40	5.84	0.79
10	3.92	6.41	0.89
11	2.12	4.75	0.60
Mean	3.64	5.98	0.85
Std. dev.	0.91	1.08	0.15

nominal tractions P_{22}^{c} and critical crack tip opening displacements δ_c are summarized in Table 4.3.

The mode I fracture toughness of DOWSIL™ TSSA is determined using 11 specimens of 1 mm nominal adhesive thickness (Fig. 4.10). The specimens do not show stable crack propagation but several unstable crack extension events. All crack growth events are associated with a similar magnitude of the *J*-integral. A similar behavior is observed by Loh and Marzi (2018a). Because the specimens are loaded displacement-controlled, crack propagation reduces the loading and causes unstable cracks to arrest after a certain distance. Subsequent load increase allows for further crack propagation once critical loading is recovered. Considering the first instance of crack growth of each of the 11 DOWSIL™ TSSA cleavage DCB specimens, yields a mode I fracture toughness of $\mathcal{G}_{\mathrm{Ic}} = 3.64 \pm 0.91\,\mathrm{N/mm}$ (Table 4.4). Accounting for all crack extension events (Fig. 4.10), we obtain $\mathcal{G}_{\mathrm{Ic}} = 3.75 \pm 0.76\,\mathrm{N/mm}$, i.e., a similar magnitude but better statistics. The small deviation between the evaluation of first instances or all instances of crack growth, emphasizes the accuracy of Eq. (4.6) even for short cracks in agreement with Fig. 4.5. Peak identification is performed using the same algorithm as for DOWSIL™ 993.

The signal-to-noise ratio of the J_{I}-signal obtained for DOWSIL™ TSSA specimens does not permit the computation of smooth derivatives, even after resampling. Therefore, the J_{I} curves are approximated until first crack propagation using the regression function

$$J_{\mathrm{I}}(\delta) = \sum_{i=1}^{n} \alpha_i \left(1 - \mathrm{e}^{-\delta/i}\right), \tag{4.9}$$

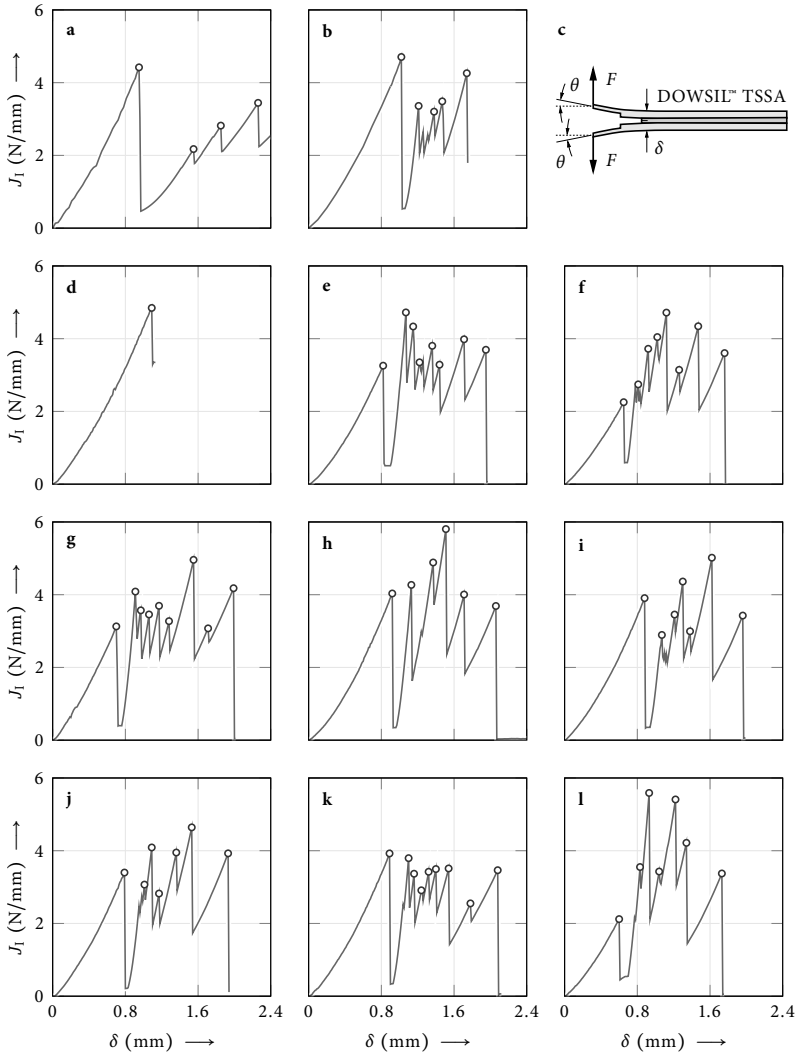

Fig. 4.10 Mode I *J*-integral (J_I) measurements using DOWSIL™ TSSA cleavage DCB tests (lines) with algorithmically identified instances of crack growth (circles).

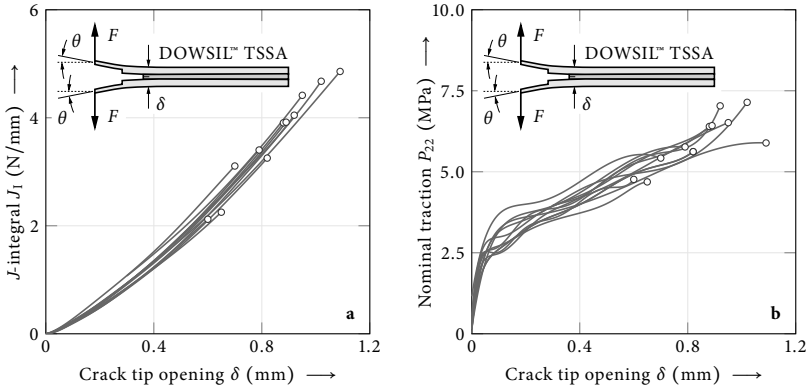

Fig. 4.11 Quantities of interest in 11 DOWSIL™ TSSA DCB tests. **a** *J*-integral according to Eq. (4.6) fitted using Eq. (4.9) and **b** first Piola–Kirchhoff stress versus crack tip opening displacement until first crack propagation.

where δ is the crack tip opening displacement and α_i parameters determined using the least-squares method. In the present case $n = 8$ suffices. Equation (4.9) provides an excellent representation of the *J*-integral signals (Fig. 4.11a) and can be readily differentiated with respect to δ to derive nominal traction–separation laws according to Eq. (4.8). Obtained traction–separation laws of the 11 DOWSIL™ TSSA specimens are shown in Fig. 4.11b. The curves are capped at the first instance of crack propagation after which δ is not measured at the location of the crack tip anymore. Maximum Piola–Kirchhoff stresses P_{22}^{c} and critical crack tip openings δ_c are listed in Table 4.4.

4.4.2 Out-of-plane shear tests

Crack nucleation in adhesive joints is a mixed-mode problem because the crack is confined in the adhesive layer. Relevant crack opening modes are cleavage (mode I) and in-plane sliding (mode II). For classical tests that determine the mode II fracture toughness such as the end-notched flexure (ENF) test (Barrett and Foschi, 1977; Chai and Mall, 1988) or the end-loaded shear joint (ELSJ) test (Marzi et al., 2009b), the silicones considered in the present work are too compliant. However, applying the *J*-integral to out-of-plane loaded DCB specimens provides an approximate expression for the tearing (mode III) fracture toughness that only depends on experimentally accessible quantities. Because the present structural silicones cannot be tested in in-plane shear tests, we examine out-of-plane shear in order to characterize the shear

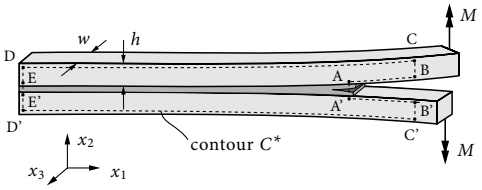

Fig. 4.12 Integration path for the evaluation of the *J*-integral in out-of-plane shear DCB specimens.

fracture behavior of DOWSIL™ TSSA. Indeed, several studies measure similar fracture toughnesses in mode II and III using different test setups for the same adhesive (Marzi et al., 2011; Stamoulis et al., 2014, 2016; Loh and Marzi, 2018a). The accuracy of the model is quantified using FEA. The results of 5 DOWSIL™ TSSA out-of-plane DCB (ODCB) specimens are reported.

Energy release rate of out-of-plane DCB specimens. Consider the ODCB specimen loaded by moments M at the ends of its cantilever arms shown in Fig. 4.12. The rotation of the lever arms causes an out-of-plane shear loading of the adhesive layer. Although the vicinity of the crack tip is loaded by a mix of peel, in-plane shear and out-of-plane shear stresses, and the energy release rate does not correspond to pure mode III, the out-of-plane energy release dominates crack propagation within this specimen. Preliminary FEA results provide out-of-plane shear stresses and out-of-plane crack tip opening displacements that are both at least on order of magnitude larger than all other stress components and displacements. Under the bending moment loading, the *J*-integral (2.168) for crack extension in x_1-direction depends on the x_3-position of the contour C^* (Gross and Seelig, 2016). As for the mode I DCB specimen (Section 4.4.1) contributions to the *J*-integral along C^* vanish on the stress-free vertical edges $\overline{\text{AA'}}$ and $\overline{\text{DD'}}$ given the initial crack and the specimen are sufficiently long, respectively. Along horizontal edges ($\overline{\text{AB}}$, $\overline{\text{A'B'}}$, $\overline{\text{CD}}$, $\overline{\text{C'D'}}$) and interfaces ($\overline{\text{AE}}$ and $\overline{\text{A'E'}}$) the first term in Eq. (2.168) vanishes because the edges are oriented along the X_1-axis. Further, $\overline{\text{AB}}$ and $\overline{\text{A'B'}}$ are traction-free so that the only contributions to the *J*-integral originate from $\overline{\text{BC}}$ and $\overline{\text{B'C'}}$.

Both segments are found within the linear elastic adherends whose strain energy density is given by $\mathcal{W} = \sigma_{ij}\,\varepsilon_{ij}/2$. Along $\overline{\text{BC}}$ and $\overline{\text{B'C'}}$ the material is loaded by normal stresses $\sigma_{11} = x_3\,M/I_y$ only, where $I_y = hw^3/12$ denotes the adherends' moment of inertia with respect to the x_2-axis. With identical adherends of height h and out-of-plane width w, the *J*-integral per unit width corresponding to a contour C^* considering crack extension in negative x_1-direction is expressed by

$$J^*_{\text{III}}(x_3) = -2\int_{\text{B}}^{\text{C}} \left(\mathcal{W} - t_1 \frac{\partial u_1}{\partial x_1}\right) \mathrm{d}x_2 = -2h\left(\frac{\sigma_{11}^2}{2E} - \frac{\sigma_{11}^2}{E}\right) = \frac{hM^2}{EI_y^2}x_3^2, \tag{4.10}$$

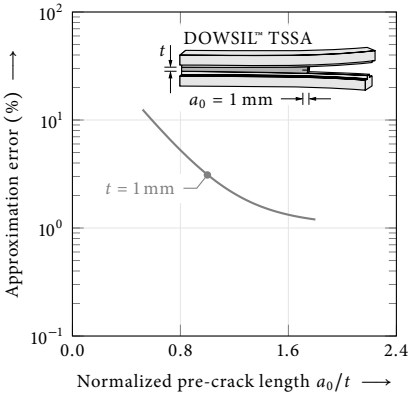

Fig. 4.13 Difference between mode III energy release rates determined in finite element models from crack tip contour *J*-integral s and from Eq. (4.12). The deviation between both methods is approximately 3 % at $t = 1\,\mathrm{mm}$ nominal adhesive thickness.

where the index III indicates mode III loading, and where we made use of $\partial u_1/\partial x_1 = \varepsilon_{11}$ and Hooke's law $\sigma_{11} = E\varepsilon_{11}$ with the adherends' Young's modulus E. The total 3D *J*-integral of the crack front is obtained by integrating Eq. (4.10) over the specimen width, i.e.,

$$J_{\mathrm{III}} = \int_{-w/2}^{w/2} J_{\mathrm{III}}^{*}(x_3)\,\mathrm{d}x_3. \tag{4.11}$$

Manufactured pre-cracks in ODCB specimens are cut with a razor blade, i.e., initially straight. To the extent it is visually assessable, the crack front stays straight as initially cut during crack propagation. With reference to Eq. (2.168), the energy released upon crack extension with straight crack front in ODCB specimens is given by

$$\mathcal{G}_{\mathrm{III}} = \frac{J_{\mathrm{III}}}{w} = \frac{1}{w}\frac{M^2}{EI_y}. \tag{4.12}$$

Again, Eq. (4.12) represents an approximation because the contribution to the *J*-integral on $\overline{\mathrm{AA'}}$ due to $\mathcal{W}$ is not accounted for.

Quality of the approximation. In order to assess the accuracy of Eq. (4.12) for short cracks, where the contribution of the strain energy density $\mathcal{W}$ may not vanish completely on $\overline{\mathrm{AA'}}$ (Fig. 4.12), we use the finite element model presented in Section 3.2.5 to compare the *J*-integral evaluated along contours closely around the crack tip with Eq. (4.12). The approximation (4.12) overestimates the actual energy release rate. The relative error

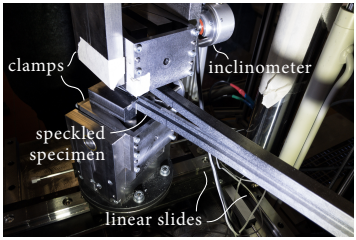

Fig. 4.14 DOWSIL™ TSSA out-of-plane shear DCB test setup.

Table 4.5
DOWSIL™ TSSA fracture toughness $\mathcal{G}_{\text{IIIc}}$ from ODCB tests.

Specimen	$\mathcal{G}_{\text{IIIc}}$ (N/mm)
01	7.08
02	6.36
03	6.38
04	8.63
05	6.70
Mean	7.03
Std. dev.	0.94

decreases quickly with increasing length of the manufactured pre-crack (Fig. 4.13). At the tested 1 mm nominal adhesive thickness, it is approximately 3 %, i.e., smaller than the experimental scatter. It can be assumed that the mode III fracture toughness $\mathcal{G}_{\text{IIIc}}$ of DOWSIL™ TSSA is reliably determined in the present out-of-plane shear DCB test.

Evaluation of test data. The generic ODCB geometry considered for the model derivation (Fig. 4.12) differs slightly from the tested specimen geometry shown in Section 3.2.5. However, derived equations are not affected by the differences. Recorded signals are sampled and evaluated at a rate of 10 Hz. As in mode I tests, DOWSIL™ TSSA fails in several unstable crack increments. Again, sudden load signal drops are identified algorithmically and used for the determination of the mode III fracture toughness.

Mode III fracture toughness. Five ODCB specimens of 1 mm nominal thickness are tested for the determination of the mode III fracture toughness of DOWSIL™ TSSA (Fig. 4.15). Because considering all instances of crack growth yields a significant standard deviation, only the first instances of crack propagation are evaluated. Corresponding mode III fracture toughnesses are listed in Table 4.5. We obtain a mean mode III fracture toughness of DOWSIL™ TSSA of $\mathcal{G}_{\text{IIIc}} = 7.03 \pm 0.94\,\text{N/mm}$, which is approximately two times the mode I fracture toughness of DOWSIL™ TSSA, $\mathcal{G}_{\text{IIIc}} \approx 2\mathcal{G}_{\text{Ic}}$.

As for mode I experiments, noisy J_{III}-signals are approximated using Eq. (4.9) for the derivation of traction–separation laws. Here, we use six terms, i.e., $n = 6$. Although the regression function provides an excellent representation of the recorded signals, out-of-plane crack tip opening displacement measurements δ yield inconsistent results (Fig. 4.16a). Hence, derivatives of $\mathcal{G}_{\text{III}}$ with respect to δ do not provide reliable information about the nominal traction (Fig. 4.16b). Crack tip opening measurements in ODCB tests are challenging because both adherends rotate out of the camera sensor plane. Hence, local rotating reference systems must be reconstructed from stereo images. This typically robust process failed for the tests reported here and no assessment of critical crack tip opening displacements or nominal tractions can be given.

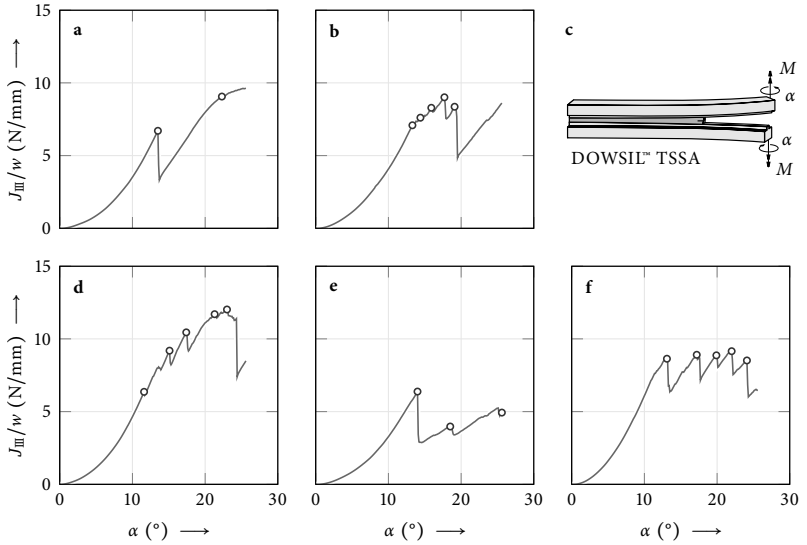

Fig. 4.15 Measured J-integral signals J_{III}/w in DOWSIL™ TSSA out-of-plane shear DCB tests (solid) with algorithmically identified instances of crack growth (circles).

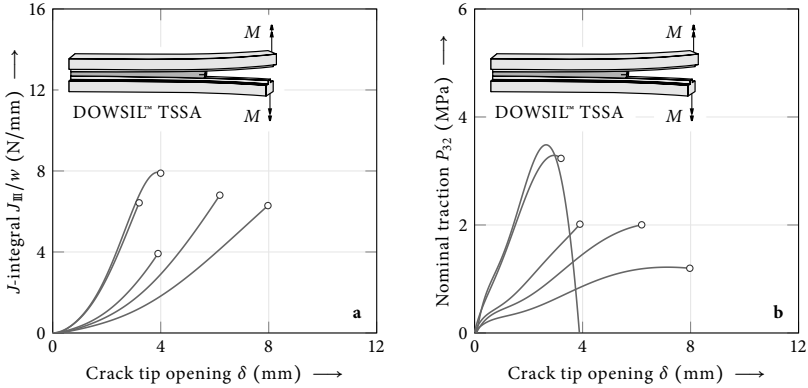

Fig. 4.16 Quantities of interest in DOWSIL™ TSSA out-of-plane shear DCB tests with respect to the out-of-plane crack tip opening displacement δ. **a** J-integral (J_{III}/w) according to Eq. (4.6) fitted using Eq. (4.9) and **b** first Piola–Kirchhoff stress versus crack tip opening displacement until first crack propagation.

Chapter 5

Bulk material failure

Bulk material failure is observed when solids are subjected to homogeneous (multiaxial) loads. It describes critical states of materials such as the onset of yielding, damage or brittle fracture in the absence of structural features that affect the stress state and, hence, failure. Stress concentrators comprise, for instance, open-holes, inclusions, notches or cracks. Although failure originating from strong stress concentrations is governed by other mechanisms, the identification and description of bulk material failure is important as it applies to large parts of structures that are subjected to homogeneous loads or mild stress gradients.

The following sections present a universal, generally applicable, phenomenological failure criterion that describes a single, smooth, and convex hypersurface in principal stress space. Exploiting properties of the proposed generalized failure criterion, a strain-based description of the bulk material failure of nearly incompressible hyperelastic elastomers is derived. The main results discussed in this chapter are published in peer-reviewed journals and conference proceedings (Altenbach et al., 2018; Drass et al., 2018a, 2020; Rosendahl et al., 2019a,b,e).

5.1 State of the art

Phenomenological failure criteria provide simple means to describe the onset of yielding, damage or brittle failure without consideration of the microstructure. The critical state of materials is described solely by the stresses at which the respective limit is reached. This set of stress states constitutes a hypersurface in principal stress space and is denoted limit or failure surface. A failure criterion is the mathematical description of all points on this limit surface.

Selecting a specific criterion for a particular material requires certain knowledge of the material behavior and its failure characteristics, such as sensitivity to biaxial loading or to superimposed hydrostatic pressure. For instance, classical failure criteria for isotropic materials such as the von Mises, Tresca, and Schmidt–Ishlinski hypotheses are

applicable to ductile materials whereas the Rankine criterion (normal stress hypothesis) is used for brittle materials (Section 2.2).

Classical criteria are often too primitive to accurately describe experimental data and to capture, e.g., the complex Lode-dependence of materials. Hence, many generalizations of these criteria have been proposed. For instance, the Mohr–Coulomb criterion (Mohr, 1900), the Burzyński–Yagn criterion (Burzyński, 1928; Yagn, 1931), the Mariotte–St. Venant criterion (Filonenko-Boroditsch, 1963), and the Pisarenko–Lebedev criterion (Pisarenko and Lebedev, 1968) comprise one or two of the classical criteria and are found in many practical applications. However, applying new materials in critical components and structures procedures requires more comprehensive criteria. Even though several sophisticated generalized yield and strength criteria were formulated (Podgórski, 1985; Altenbach et al., 1995; Bigoni and Piccolroaz, 2004; Kolupaev, 2018; Yu, 2018), choosing an appropriate criterion for a particular material remains challenging. Data sets are often incomplete and scattering of available data renders fitting the multitude of different existing criteria time-consuming. More importantly, trying different criteria does not guarantee the optimal result.

Early studies on the distortional fracture of multiaxially loaded rubber-like polymers (Sharma and Lim, 1965; Jones and Kruse, 1966; Sharma, 1966; Knauss, 1967; Dickie and Smith, 1969; Smith and Rinde, 1969; Tschoegl, 1971; Kawabata, 1973) tried to describe distortional failure surfaces using stress-based failure criteria developed for metals. However, these approaches fell short of providing an accurate description of experimental data. More recent works fit polynomial (Hamdi et al., 2006a,b, 2007b) or exponential functions (Hamdi and Mahjoubi, 2015) to test data in principal stretch space and obtain a more satisfactory representation of their experiments, in particular in the latter case. Staudt et al. (2018) find a description of their test data in principal strain space. All of the above studies are restricted to one or few elastomers.

Dilatational failure of nearly incompressible hyperelastic materials, i.e., the formation of cavities, was first described for the single stress state of pure hydrostatic tension (Green and Zerna, 1954; Gent and Lindley, 1959; Ball, 1982). This stress-based concept has been extended to multiaxial loading conditions (Hou and Abeyaratne, 1992; Lopez-Pamies et al., 2011b). Importantly, dilatational failure criteria typically only aim at capturing the elastic instability point, at which existing cavities expand rapidly. This phenomenon is not necessarily associated to the formation of new surfaces, i.e., cracking. Yet, expanded cavities may grow further, coalesce and eventually form macroscopic cracks (Creton et al., 2001; Creton and Ciccotti, 2016).

In contrast to the stress, strain or stretch-based description of failure surfaces, approaches such as the network alteration theory by Marckmann et al. (2002), the domain transition theory by Qi and Boyce (2004), or energy delimiter theory by Dal and Kaliske

(2009) or Volokh (2010) incorporate failure directly into the description of the constitutive behavior of hyperelastic materials. That is, such concepts assume energy-driven material failure. They can be applied to both distortional and dilatational failure (Nelson, 2019). Mars and Fatemi (2002, 2005, 2006) investigate the fatigue life of rubber-like materials under multiaxial loading and use classical equivalent strain concepts to describe initial damage onset.

Since the pioneering papers on multiaxial elastomer fracture, considerable progress in the mathematical description of failure surfaces was made. In the following, we make use of these recent advances to formulate a universal function describing deviatoric failure in principal stress space with a single, smooth and convex surface. This universal deviatoric function is then transferred to the principal strain space and combined with a dilatational failure criterion to provide a comprehensive description of elastomer failure under complex loads. While most present contributions are restricted to a few different materials, the present work considers six different elastomers.

5.2 Generalized deviatoric function

Beyond the obvious interest in generalization, a specific motivation for describing failure of different materials using a single criterion is drawn from the fact that failure surfaces may evolve from one shape to another under increasing loading. For instance, granular materials, and in particular metal powders, initially behave like true granular materials but become porous metals during compaction. A yield function reflecting this behavior must evolve from the typical triangular deviatoric shape of granular media to the circular deviatoric shape of a porous metal (Bigoni and Piccolroaz, 2004). Conversely, the failure process of rock-like materials or glass is characterized by the decomposition from a solid into a granular material (Molnár et al., 2016). A failure criterion that describes all conceivable deviatoric shapes as a single function is capable of describing the above transitions using load-dependent shape parameters.

Requirements. In order to formulate such a universal criterion, we assume a phenomenological point of view and restrict the consideration to isotropic materials. The following general properties of failure criteria are of interest (Christensen, 1997a; Bigoni and Piccolroaz, 2004; Kolupaev, 2018):

$\mathcal{P}_1$: maximum generality,
$\mathcal{P}_2$: mathematical simplicity,
$\mathcal{P}_3$: minimum number of parameters,
$\mathcal{P}_4$: independence and uniqueness of the parameters,
$\mathcal{P}_5$: convexity,

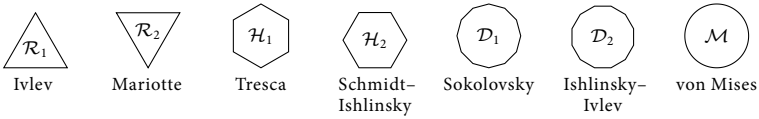

Fig. 5.1 Nomenclature for deviatoric shapes of classical failure criteria.

$\mathcal{P}_6$: continuous differentiability ($\mathcal{C}^1$-continuity),
$\mathcal{P}_7$: single surface with no intersections or outer contours,
$\mathcal{P}_8$: reduction to known criteria in limit cases, and
$\mathcal{P}_9$: provision of an explicit expression for the equivalent stress σ_{eq}.

None of the above features are essential, in the sense that limit states of materials may be described without all of the above, but all are desirable for the development of models and in particular for finite element implementations.

Continuous differentiability ($\mathcal{P}_6$) is a broadly employed concept for quasibrittle and frictional materials as evidence supporting corner formation in the yield function is weak (Bigoni and Piccolroaz, 2004). Although theoretical considerations suggest that corners should be expected for single crystals and polycrystals (Hill, 1967), experiments are inconclusive in this regard (Naghdi et al., 1958; Paul, 1968; Philipps, 1974). Hence, differentiability of the failure surface may be considered a mere simplification.

Unlike differentiability, convexity of the failure surface ($\mathcal{P}_5$) is supported by experiments on large numbers of materials (Bigoni and Piccolroaz, 2004). It is a useful mathematical property with fundamental importance for variational inequalities in plasticity theory (Duvaut and Lions, 1976). For polycrystals it is a result of Schmid's law of single crystals (Schmid and Boas, 1935; Bishop and Hill, 1951; Mandel, 1966). Hence, in the absence of specific reasons it is not sensible to employ nonconvex failure criteria.

Present concepts. Let us consider deviatoric functions and introduce a nomenclature for deviatoric shapes of classical failure criteria (Fig. 5.1). Maximum generality ($\mathcal{P}_1$) requires the description of arbitrary deviatoric shapes between the upper and lower convexity limits (Fig. 5.2a), represented by the criteria of Mariotte (2.134), $\mathcal{R}_2$, and Ivlev (2.135), $\mathcal{R}_1$, respectively (Fig. 5.1). Between these limits, a criterion must be capable of describing both isogonal (equiangular) and isotoxal (equilateral) polygons as limit situations (Fig. 5.2b). Polynomial formulations of these polygons are given by the criteria of Capurso (1967) (isotoxal hexagons) and Haythornthwaite (1960) (isogonal hexagons). However, both correspond only to the polygonal limit cases and, hence, violate $\mathcal{P}_6$. Since polynomial criteria assemble the failure surface from the intersection of individual contours, they always violate $\mathcal{P}_7$ and their application is involved.

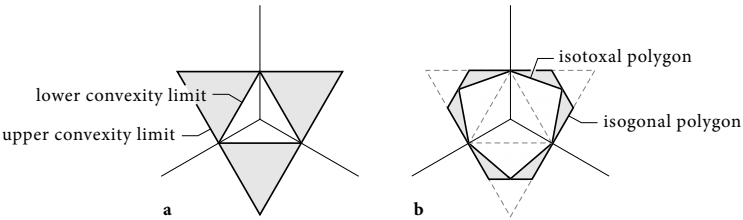

Fig. 5.2 Limit cases of deviatoric shape functions in the π-plane normalized with respect to the uniaxial tensile strength. **a** Upper and lower convexity limits, **b** isogonal (equiangular) and isotoxal (equilateral) polygons.

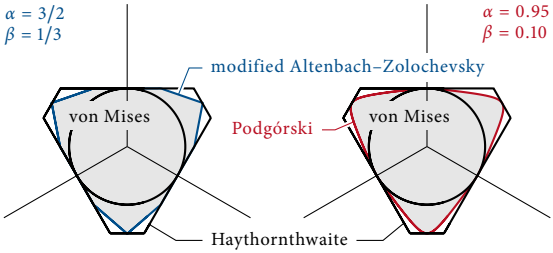

Fig. 5.3 Deviatoric functions of the modified Altenbach–Zolochevsky criterion (2.136) with $\alpha = 3/2$ and $\beta = 1/3$, and the Podgórski criterion (2.138) with $\alpha = 0.95$ and $\beta = 0.1$ in comparison to isotoxal hexagons of the Haythornthwaite (1960) criterion and the circle of the von Mises (1913) criterion.

Deviatoric functions that comprise most intermediate shapes between the convexity limits and that comply best with the requirements $\mathcal{P}_1$–$\mathcal{P}_9$ are the modified Altenbach–Zolochevsky (2.136) and the Podgórski (2.138) shape functions. The former comprises $\mathcal{R}_1$, $\mathcal{R}_2$, $\mathcal{H}_1$, $\mathcal{H}_2$, and $\mathcal{D}_1$ and can describe the isotoxal (equilateral) $\mathcal{R}_1$–$\mathcal{H}_1$–$\mathcal{R}_2$ transition covered by the Capurso (1967) criterion (Fig. 2.3). However, it is not differentiable and although it contains $\mathcal{H}_2$, it cannot describe the isogonal (equilangular) $\mathcal{R}_1$–$\mathcal{H}_2$–$\mathcal{R}_2$ transition captured by the Haythornthwaite (1960) criterion, nor collapse onto the von Mises circle $\mathcal{M}$ (Fig. 5.3).

The Podgórski criterion is $\mathcal{C}^1$-continuous except in polygonal limit cases. It comprises $\mathcal{M}$ and can describe the isotoxal $\mathcal{R}_1$–$\mathcal{H}_1$–$\mathcal{R}_2$ transition. It covers $\mathcal{R}_1$, $\mathcal{R}_2$, and $\mathcal{H}_1$ and describes isotoxal polygons and their corresponding differentiable representations but not the isogonal (equilangular) $\mathcal{R}_1$–$\mathcal{H}_2$–$\mathcal{R}_2$ transition (Fig. 5.3). A deviatoric function that comprises all classical deviatoric shapes (Fig. 5.1) and that can describe the isogonal $\mathcal{R}_1$–$\mathcal{H}_2$–$\mathcal{R}_2$ transition as a single function is unknown.

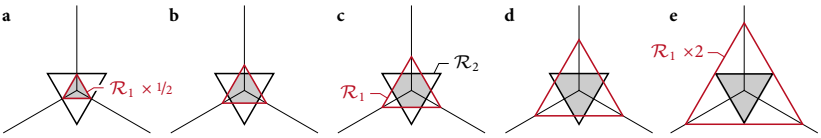

Fig. 5.4 Isogonal (equiangular) hexagons (gray) obtained from the intersection of the bodies of two equilateral triangles, $\mathcal{R}_1$ and $\mathcal{R}_2$.

Novel deviatoric function. The Podgórski shape function (2.138) has many desirable characteristics that we may exploit to provide a more general deviatoric function. Isogonal hexagons can be obtained from the intersection of the bodies of the two equilateral triangles $\mathcal{R}_1$ and $\mathcal{R}_2$. Different polygons are constructed by scaling one of the two triangles (Fig. 5.4). Expressing the triangles using Podgórski-like shape functions then allows for describing not only equiangular hexagons but arbitrarily many differentiable deviatoric shapes between the convexity limits. The approach is not restricted to triangles and hexagons but can be transferred to m-gons with $m \geq 3$, which is relevant for the generalization of yield surfaces of hexagonal symmetry.

Following this approach, the description of equiangular hexagons is obtained from the minimum of the shape functions of $\mathcal{R}_1$ and $\mathcal{R}_2$, ω_n^- and ω_n^+, respectively. This is expressed by

$$\Xi_n(\theta_\sigma) = \frac{1}{2}\left(\omega_n^+(\theta_\sigma) + \zeta_n\omega_n^-(\theta_\sigma) + \sqrt{\left[\omega_n^+(\theta_\sigma) - \zeta_n\omega_n^-(\theta_\sigma)\right]^2}\right), \tag{5.1}$$

where ζ_n scales $\mathcal{R}_1$ as sketched in Fig. 5.4 and θ_σ is the meridian angle (2.129c). Shape functions of the form

$$\omega_n^\pm(\theta_\sigma;\,\beta,\gamma) = \cos\left[\frac{1}{3n}\left(\pi\beta - \arccos\left[\pm\sin\left(\gamma\frac{\pi}{2}\right)\cos\left(3n\,\theta_\sigma\right)\right]\right)\right], \tag{5.2}$$

where $n \in \mathbb{N}^+$, $\beta \in [0,1]$ and $\gamma \in [0,1]$, provide not only the triangles $\mathcal{R}_1$ and $\mathcal{R}_2$ but arbitrary isogonal and isotoxal m-gons with $m = 3n$ edges. For instance, ω_1^+ corresponds to a slightly tweaked version of the Podgórski shape function (2.138). The original Podgórski (1985) function is exceptionally sensitive to deviations of the parameter in the arccos term from unity. Introducing this parameter as $\sin(\gamma\pi/2)$ in Eq. (5.2) improves the robustness of the shape function considerably. With the unit scaling parameter $\alpha \in [0,1]$, the scaling functions read

$$\zeta_n(\alpha) = \left[\alpha + (1-\alpha)\cos\left(\frac{\pi}{3n}\right)\right]. \tag{5.3}$$

Normalizing with respect to the uniaxial tensile strength $\sigma_{\mathrm{eq}} = \sigma_+$ at $\theta_{\boldsymbol{\sigma}} = 0$ then yields the novel equivalent stress function

$$\sigma_{\mathrm{eq}}(\boldsymbol{\sigma}) = \frac{\sqrt{3}\,\Xi_n(\theta_{\boldsymbol{\sigma}};\,\alpha,\beta,\gamma)}{\sqrt{2}\,\Xi_n(0;\,\alpha,\beta,\gamma)}\rho_{\boldsymbol{\sigma}}, \tag{5.4}$$

describing a multitude of convex deviatoric shapes, where $\rho_{\boldsymbol{\sigma}}$ is the radial distance from the hydrostatic axis, and $\theta_{\boldsymbol{\sigma}}$ meridian angle (2.129). Note that all shape parameters are normalized to the unit interval, i.e.,

$$\alpha \in [0,1], \qquad \beta \in [0,1], \qquad \gamma \in [0,1]. \tag{5.5}$$

In the following we will refer to the right-hand side of Eq. (5.4) as robust deviatoric function RDF_n, where the index denotes the value of the parameter n.

Trigonal symmetry. RDF_1 constructs deviatoric shapes from the intersection of triangles as fundamental shapes and, hence, provides deviatoric functions of trigonal symmetry. It comprises

- the Ivlev criterion $(\alpha = 0, \beta = 1, \gamma = 1)$,
- the Mariotte criterion $(\alpha = 0, \beta = 0, \gamma = 1)$,
- the Tresca criterion $(\alpha \in [0,1], \beta = 0.5, \gamma = 1)$,
- the Schmidt–Ishlinsky criterion $(\alpha = 1, \beta \in [0,1], \gamma = 1)$,
- the Sokolovsky criterion $(\alpha = 1, \beta \in \{0.25, 0.75\}, \gamma = 1)$,
- the von Mises criterion $(\alpha \in [0,1], \beta \in [0,1], \gamma = 0)$,
- the Capurso criterion $(\alpha = 0, \beta \in [0,1], \gamma = 1)$,
- the Sayir criterion $(\alpha = 0, \beta \in \{0,1\}, \gamma \in [0,1])$,
- the Haythornthwaite criterion $(\alpha \in [0,1], \beta \in \{0,1\}, \gamma = 1)$, and
- the Podgórski criterion $(\alpha = 0, \beta \in [0,1], \gamma \in \{0,1\})$.

Eq. (5.4) recovers the Podgórski criterion (2.138) because for $n = 1$ and $\alpha = 0$ the shape function ω_n^- is scaled so that it does not intersect with ω_n^+ anymore (Fig. 5.4a).

On account of α, RDF_1 describes the isogonal Haythornthwaite $\mathcal{R}_1$–$\mathcal{H}_2$–$\mathcal{R}_2$ transition not covered by other generalized criteria in the literature in a single equation (Fig. 5.5a). The isotoxal Capurso $\mathcal{R}_1$–$\mathcal{H}_1$–$\mathcal{R}_2$ transition is captured by β (Fig. 5.5c). Differentiability is provided by $\gamma < 1$ for all α, β, and n. Hence, the parameter describes the $\mathcal{R}_1$–$\mathcal{M}$–$\mathcal{R}_2$ Sayir transition (Fig. 5.5e). Combinations of the three fundamental cases shown in the left column of Fig. 5.5 provide exceptionally adaptable $(\mathcal{P}_1)$ convex $(\mathcal{P}_5)$ deviatoric shapes described by a single equation $(\mathcal{P}_7)$ that is differentiable $(\mathcal{P}_6)$ in all cases except limit cases $(\mathcal{P}_8)$.

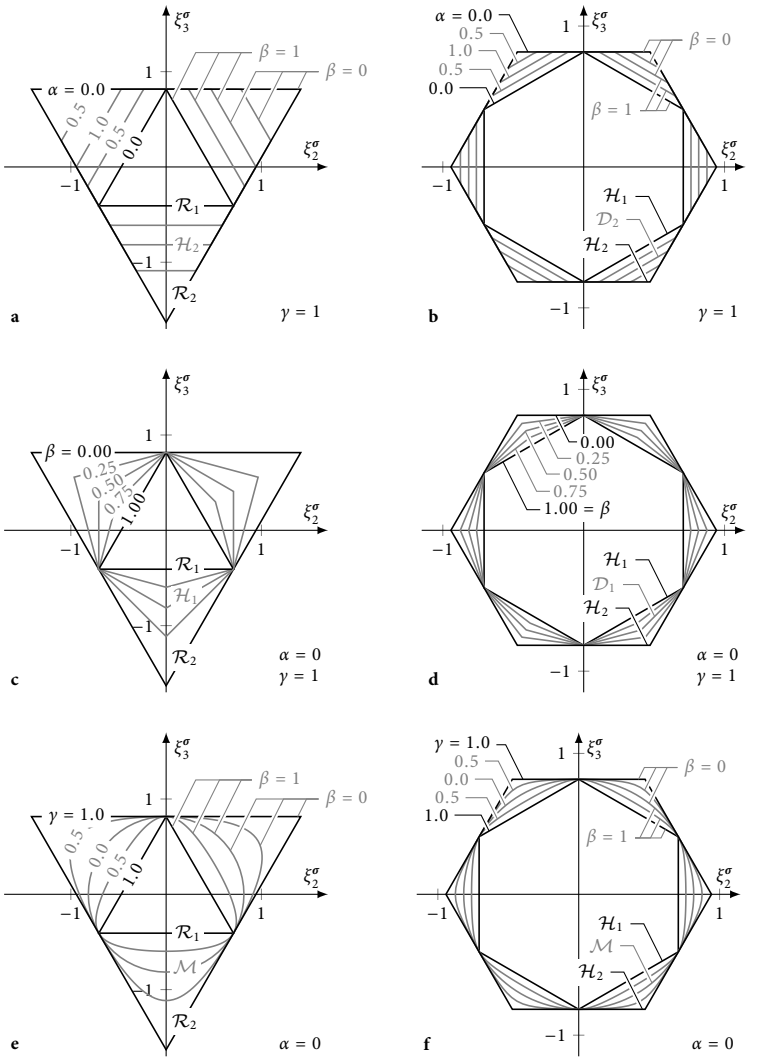

Fig. 5.5 Shape transitions of the robust deviatoric functions RDF_1 (left column, $n = 1$) and RDF_2 (right column, $n = 2$). Isogonal transition captured by α (**a** and **b**), isotoxal transition modeled by β (**c** and **d**), and circular transition given by γ (**e** and **f**).

Hexagonal symmetry. RDF_2 uses hexagons as fundamental shapes to assemble more complex polygons and, hence, constitutes a deviatoric function of hexagonal symmetry. It comprises

- the Tresca criterion ($\alpha = 0, \beta = 1, \gamma = 1$),
- the Schmidt–Ishlinsky criterion ($\alpha = 0, \beta = 0, \gamma = 1$),
- the Sokolovsky criterion ($\alpha \in [0,1], \beta = 0.5, \gamma = 1$),
- the Ishlinsky–Ivlev criterion ($\alpha = 1, \beta \in \{0,1\}, \gamma = 1$),
- the von Mises criterion ($\alpha \in [0,1], \beta \in [0,1], \gamma = 0$),
- the unified yield criterion of Yu (2004) ($\alpha = 1, \beta \in [0,1], \gamma = 1$),
- the multiplicative ansatz criterion of Kolupaev and Altenbach (2010) ($\alpha \in [0,1], \beta \in \{0,1\}, \gamma = 1$), and
- the bicubic criterion of Bolchoun et al. (2011) ($\alpha = 0, \beta \in \{0,1\}, \gamma \in [0,1]$).

In analogy to RDF_1, RDF_2 describes the isogonal $\mathcal{H}_1$–$\mathcal{D}_2$–$\mathcal{H}_2$ transition (Kolupaev and Altenbach, 2010) using α (Fig. 5.5b). The isotoxal $\mathcal{H}_1$–$\mathcal{D}_1$–$\mathcal{H}_2$ transition (Yu, 2004) is captured by β (Fig. 5.5d) and γ represents the $\mathcal{H}_1$–$\mathcal{M}$–$\mathcal{H}_2$ transition (Bolchoun et al., 2011) (Fig. 5.5f). Higher orders ($n \geq 3$) follow the same rules but are not useful because associated polygons can hardly be distinguished from the von Mises circle $\mathcal{M}$. RDF_1 represents the most relevant generalization.

Particular forms. RDF_n comprises two interesting simpler cases. For $\alpha = 0$, ω_n^- is scaled so that it does not intersect with ω_n^+ anymore. Sacrificing the shape transition captured by α (Fig. 5.5a and b), equivalent stress functions can be formulated using ω_n^+ only, i.e.,

$$\sigma_{\mathrm{eq}}(\boldsymbol{\sigma}) = \frac{\sqrt{3}\,\omega_n^+(\theta_\sigma;\,\beta,\gamma)}{\sqrt{2}\,\omega_n^+(0;\,\beta,\gamma)}\rho_\sigma. \tag{5.6}$$

Using $n = 1$, yields a shape function of trigonal symmetry similar to the one proposed by Podgórski (1985), i.e.,

$$\omega_1^+(\theta_\sigma;\,\beta,\gamma) = \cos\left[\frac{1}{3}\left(\pi\beta - \arccos\left[\sin\left(\gamma\frac{\pi}{2}\right)\cos\left(3\theta_\sigma\right)\right]\right)\right]. \tag{5.7}$$

It covers the shape transitions shown in Fig. 5.5c and e. With $n = 2$, we obtain a failure criterion with similar properties but of hexagonal symmetry (Fig. 5.5d and f), i.e.,

$$\omega_2^+(\theta_\sigma;\,\beta,\gamma) = \cos\left[\frac{1}{6}\left(\pi\beta - \arccos\left[\sin\left(\gamma\frac{\pi}{2}\right)\cos\left(6\theta_\sigma\right)\right]\right)\right]. \tag{5.8}$$

A comparable shape function of hexagonal symmetry was recently proposed by Szwed (2000) and Jemioło and Szwed (2013). Their deviatoric function corresponds to Eq. (5.8) with $\beta = 0$.

Table 5.1
Data of plane stress experiments ($\sigma_{\text{III}} = 0$) on three different types of concrete provided by Kupfer (1972). All quantities are normalized with respect to the material's uniaxial tensile strength σ_+, where $\boldsymbol{\sigma}^+ = \boldsymbol{\sigma}/\sigma_+$ denotes the normalized Cauchy stress tensor.

σ_+	$\sigma_{\text{I}}/\sigma_+$	$\sigma_{\text{II}}/\sigma_+$	I_{σ^+}	II'_{σ^+}	III'_{σ^+}	θ_{σ^+}	$\cos(3\theta_{\sigma^+})$	$\sqrt{3/2}\,\rho_{\sigma^+}$
1.96	−11.25	−11.25	−22.50	42.19	105.47	0.0	0.98	11.25
MPa	−12.10	−6.29	−18.39	36.62	5.90	28.7	0.07	10.48
	−11.90	−2.62	−14.52	39.10	−75.90	47.9	−0.81	10.83
	−9.55	0.00	−9.55	30.40	−64.52	60.0	−0.98	9.55
	−9.00	0.47	−8.53	28.48	−57.99	57.5	−0.99	9.24
	−8.25	0.58	−7.67	24.39	−45.64	56.7	−0.98	8.55
	−6.95	0.72	−6.23	17.93	−28.29	55.2	−0.97	7.33
	−4.15	0.84	−3.31	7.13	−6.53	51.0	−0.89	4.63
	−2.86	0.88	−1.98	3.82	−2.23	47.0	−0.78	3.38
	0.00	0.98	0.98	0.33	0.07	0.0	1.01	0.98
	0.25	1.07	1.32	0.31	0.05	12.7	0.79	0.97
	0.58	1.07	1.65	0.29	−0.01	32.7	−0.14	0.93
	0.98	0.98	2.00	0.33	−0.07	60.0	−0.98	0.98
2.79	−12.57	−12.57	−25.14	52.67	147.13	0.0	0.98	12.57
MPa	−13.34	−11.04	−24.38	50.82	123.37	9.3	0.88	12.35
	−13.56	−7.05	−20.61	45.97	8.30	28.7	0.07	11.74
	−13.03	−2.87	−15.89	46.87	−99.60	47.9	−0.81	11.86
	−10.95	0.00	−10.95	39.97	−97.27	60.0	−0.98	10.95
	−9.33	0.49	−8.85	30.61	−64.62	57.5	−0.99	9.58
	−8.45	0.59	−7.86	25.59	−49.05	56.6	−0.98	8.76
	−6.76	0.70	−6.06	16.97	−26.03	55.2	−0.97	7.13
	−4.01	0.81	−3.20	6.68	−5.91	51.0	−0.89	4.47
	−2.84	0.85	−1.99	3.74	−2.19	47.3	−0.79	3.35
	0.00	0.98	0.98	0.33	0.07	0.0	0.98	0.98
	0.25	1.07	1.32	0.32	0.05	12.7	0.79	0.97
	0.56	1.03	1.59	0.27	−0.01	32.6	−0.14	0.89
	0.98	0.98	2.00	0.33	−0.07	60.0	−0.98	0.98
5.12	−13.05	−13.05	−26.09	56.73	164.47	0.0	0.98	13.05
MPa	−14.66	−7.62	−22.28	53.72	10.49	28.7	0.07	12.70
	−14.04	−3.09	−17.13	54.45	−124.71	47.9	−0.81	12.78
	−11.38	0.00	−11.38	43.16	−109.15	60.0	−0.98	11.38
	−8.45	0.44	−8.01	25.09	−47.96	57.5	−0.99	8.68
	−6.82	0.48	−6.34	16.67	−25.78	56.6	−0.98	7.07
	−4.94	0.51	−4.43	9.07	−10.17	55.2	−0.97	5.22
	−3.30	0.67	−2.63	4.50	−3.27	51.0	−0.89	3.67
	−2.02	0.65	−1.37	1.94	−0.79	46.5	−0.76	2.41
	0.00	0.98	0.98	0.33	0.07	0.0	0.98	0.98
	0.22	0.97	1.19	0.26	0.04	12.7	0.79	0.88
	0.48	0.89	1.37	0.20	−0.00	32.6	−0.14	0.77
	0.93	0.93	1.86	0.29	−0.06	60.0	−0.98	0.93

Table 5.2
Best fit parameter sets for the three types of concrete examined by (Kupfer, 1972).

	σ_+	α	β	γ	η_1
Conical robust deviatoric function (RDF_1)	1.96 MPa	0.17	0.06	0.92	0.31
	2.79 MPa	0.15	0.06	0.94	0.31
	5.12 MPa	0.01	0.04	0.95	0.31
Conical modified Altenbach–Zolochevsky (MAZ)	1.96 MPa	1.70	0.08	–	0.31
	2.79 MPa	1.74	0.12	–	0.31
	5.12 MPa	1.75	0.08	–	0.31

Application to concrete. In order to benchmark the capabilities of the proposed deviatoric function, let us consider the comprehensive experimental data set on three different types of concrete provided by Kupfer (1972) studied in a series of publications (Kupfer et al., 1969; Kupfer and Zelger, 1973; Kupfer and Gerstle, 1973) and listed in Table 5.1. Concrete has a complex pressure-sensitive failure behavior. The simplest way of accounting for pressure-sensitivity is the linear substitution of the equivalent stress in Eq. (5.4) through Eq. (2.143) using $i = 1$ and $j = k = 0$. Solving

$$\frac{\sigma_{\mathrm{eq}}(\boldsymbol{\sigma}) - \eta_1 I_{\boldsymbol{\sigma}}}{1 - \eta_1} = \frac{\sqrt{3}\,\Xi_n(\theta_{\boldsymbol{\sigma}};\,\alpha,\beta,\gamma)}{\sqrt{2}\,\Xi_n(0;\,\alpha,\beta,\gamma)}\,\rho_{\boldsymbol{\sigma}}, \tag{5.9}$$

for $\sigma_{\mathrm{eq}}(\boldsymbol{\sigma})$ yields the conical RDF_n. In the same way, we obtain a conical expression of the modified Altenbach–Zolochevsky criterion (2.136). Fig. 5.6 shows least-squares approximations of the experimental data by both conical criteria computed requiring the interpolation of uniaxial tension, uniaxial compression and equibiaxial compression data points. Details on the fitting procedure are given by Rosendahl et al. (2019b). Identified best fit parameter sets are given in Table 5.2. The plane stress test data are symmetric about the angle bisector of the σ_{I}-σ_{II}-plane. Hence, the left column of Fig. 5.6 plots one criterion on each side of the bisector. The pressure-insensitive von Mises hypothesis is shown for reference. The right column of Fig. 5.6 shows the conical RDF_1 in the π-plane. Deviatoric cross sections are shown for particular values of the first invariants $I_{\boldsymbol{\sigma}}$ of the Cauchy stress tensor: $I_{\boldsymbol{\sigma}} = \sigma_+$ corresponds to uniaxial tension, $I_{\boldsymbol{\sigma}} = \sigma_-$ uniaxial compression and $I_{\boldsymbol{\sigma}} = 0$ represents the cross section of the π_0-plane through the coordinate origin.

Even with simple linear meridians, RDF_1 provides a good agreement for all three experimental data sets (Fig. 5.6). An improvement over the modified Altenbach–Zolochevsky deviatoric function is evident at moderate biaxiality ratios in compression. Improvements over the deviatoric function of the Podgórski criterion manifest in considerable magnitudes of the α-parameter of RDF_1 (Table 5.2), which allows for isogonal corner formation in the limit $\gamma = 1$, not possible with the Podgórski shape function. Even more accurate results can be obtained substituting the deviatoric function in Ottosen's ansatz

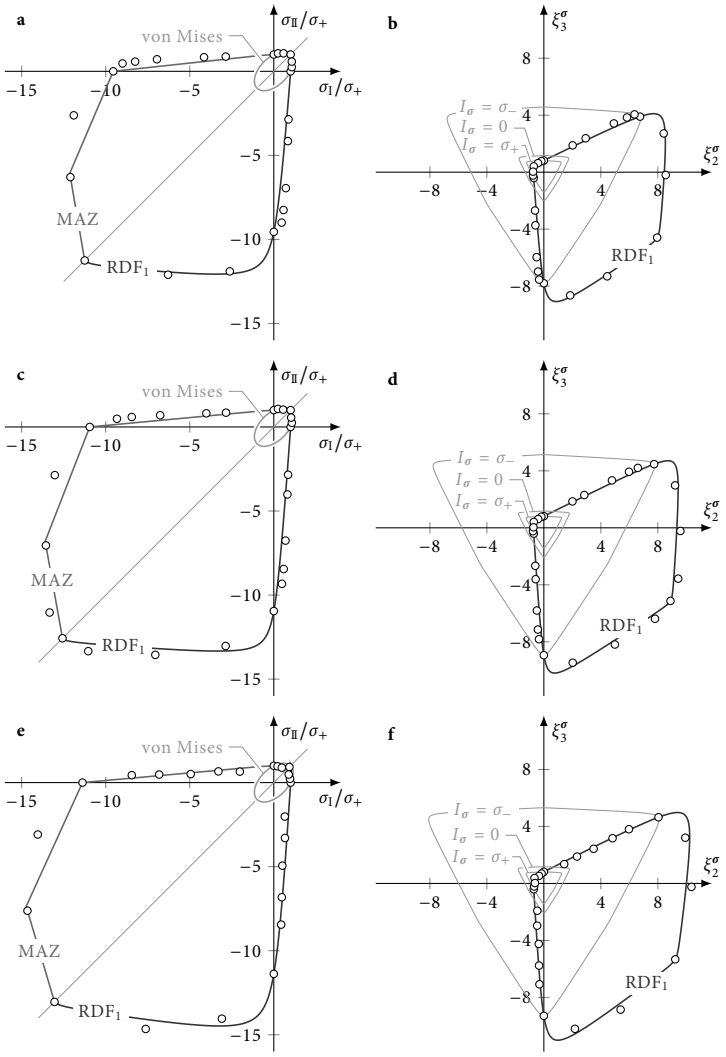

Fig. 5.6 Plane stress experiments (dots) on three different types of concrete (rows) provided by Kupfer (1972). Fits of the von Mises criterion, the conical modified Altenbach–Zolochevsky criterion (MAZ), and the conical robust deviatoric function (RDF_1) in the σ_I-σ_II-plane (left column) and RDF_1 with representative cross sections in the π-plane (right column). The test data are symmetric about the angle bisector. Hence, in the σ_I-σ_II-plane one criterion is shown on each side of the bisector.

(2.146) for RDF_1 (Rosendahl et al., 2019b). This allows for cross section changes along the hydrostatic axis. Alternatively, we may consider individual failure criteria for different failure modes such as tension, shear and compression according to the failure mode concept (2.147) proposed by Cuntze (1996, 1999). However, pressure sensitivity is not the subject of the present work. On the contrary, the above analysis is merely presented as an illustrative example of how modeling of failure can benefit from a generalized deviatoric function.

5.3 Equivalent strain failure criterion for hyperelastic media

Several reasons mandate the characterization of failure of soft hyperelastic elastomers in terms of strain instead of stress (see Section 4.3). The mathematical concepts used above for the stress-based assessment of deviatoric failure can be readily employed for the description of failure surfaces in principal true strain space ($\varepsilon_\mathrm{I}, \varepsilon_\mathrm{II}, \varepsilon_\mathrm{III}$). In the following, we use comprehensive literature data sets of isochoric experiments to determine suitable deviatoric functions for hyperelastic materials and provide a functional description of the deviatoric failure surfaces of DOWSIL™ 993 and DOWSIL™ TSSA.

Comprehensive experimental data sets on the deviatoric failure of rubber-like materials are given by Kawabata (1973) and Hamdi et al. (2006a, 2007b). Their test data are shown in the deviatoric plane in Fig. 5.7, where $\xi_2^{\boldsymbol{\varepsilon}}$ (2.127a) and $\xi_3^{\boldsymbol{\varepsilon}}$ (2.127b) denote the coordinates of the strain deviatoric plane. Both studies investigate multiaxial failure of a styrene–butadiene rubber (SBR). While Kawabata's experiments are concerned with unfilled SBR, Hamdi et al. examine SBR filled with carbon black. Both data sets comprise uniaxial and biaxial tension tests of different biaxiality ratios. The latter are obtained inflating a thin membrane through circular or elliptical holes. In this setup, fracture emanates from the pole of the inflated bodies. In addition to this bulge test, Kawabata (1973) designed an apparatus clamping membranes mechanically in order to apply biaxial loading. Hamdi et al. (2007b) additionally modify a planar tension test to measure fracture data in so-called pure shear deformation. Here, a thin rectangular polymer sheet is clamped along its long edges. Together with incompressibility of the material the clamps prevent lateral in-plane contraction causing an in-plane stress state corresponding to pure shear. While Hamdi et al. (2006a, 2007b) indicate individual data points, Kawabata (1973) provides mean and standard deviation only.

The two data sets (Fig. 5.7) are used to assess the general suitability of various failure criteria. Appropriate criteria are then analyzed in detail using additional test data by Kawabata (1973) and Hamdi et al. (2006a, 2007b) who investigated unfilled and carbon black filled natural rubber (NR) in the same test conditions described above and by own data on DOWSIL™ 993 and DOWSIL™ TSSA presented in Section 4.3.

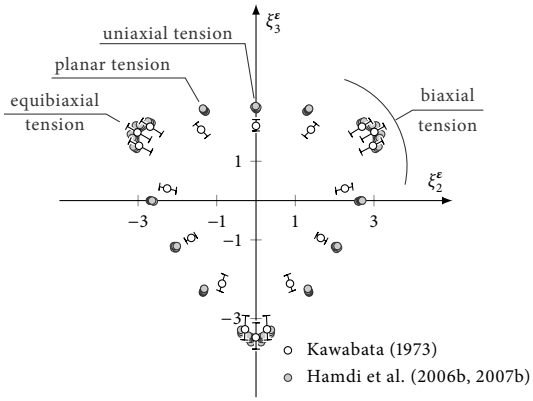

Fig. 5.7 Ultimate true strains of unfilled (Kawabata, 1973) and carbon black filled (Hamdi et al., 2006a, 2007b) styrene–butadiene rubber under different loading conditions in the deviatoric plane.

Classical criteria in strain space. Mainly developed for metals, classical criteria describe failure in principal stress space. However, their mathematical formulations and, hence, the shapes they represent in the deviatoric plane may also be used for strain-based description of failure. For this purpose, we substitute principal stresses for principal true strains in the respective expressions and append a suffix, e.g., Rankine-*like*, to distinguish the original stress criterion from its strain-based counterpart. As a result we, obtain the deviatoric shapes that classical criteria describe in principal stress space in strain space.

The Rankine criterion (2.132) assumes failure when the maximum principal stress approaches the material's tensile strength. Kawabata (1973) proposed a similar maximum principal stretch concept for elastomers:

$$\lambda_{\mathrm{eq}}(\boldsymbol{F}) = \max\{\lambda_{\mathrm{I}}, \lambda_{\mathrm{II}}, \lambda_{\mathrm{III}}\} = \lambda_{\mathrm{I}}, \tag{5.10}$$

where λ_{eq} is the equivalent stretch function and $\boldsymbol{F}$ the deformation gradient. Instead of Kawabata's simple replacement of principal stresses by principal stretches, we may as well substitute stresses for principal strains, which yields the Rankine-like strain criterion

$$\varepsilon_{\mathrm{eq}}(\boldsymbol{\varepsilon}) = \max\{\varepsilon_{\mathrm{I}}, \varepsilon_{\mathrm{II}}, \varepsilon_{\mathrm{III}}\} = \varepsilon_{\mathrm{I}}, \tag{5.11}$$

where $\boldsymbol{\varepsilon}$ is the Hencky strain tensor (2.18). The Tresca criterion (2.131) suggests a shear stress limit. A Tresca-like maximum shear strain criterion

$$\varepsilon_{\mathrm{eq}}(\boldsymbol{\varepsilon}) = \varepsilon_{\mathrm{I}} - \varepsilon_{\mathrm{III}}, \tag{5.12}$$

can be formulated denoting the largest and smallest principal strain as ε_{I} and $\varepsilon_{\mathrm{III}}$, respectively. Owing to its simplicity, the von Mises yield criterion, originally developed for ductile metals, enjoys great popularity for different classes of materials. It predicts failure at a critical value of the second stress deviator invariant. Accordingly,

$$\varepsilon_{\mathrm{eq}}(\boldsymbol{\varepsilon}) = \sqrt{3 I\!I'_{\boldsymbol{\varepsilon}}}, \tag{5.13}$$

constitutes a von Mises-like strain criterion where $I\!I'_{\boldsymbol{\varepsilon}}$ denotes the second invariant of the deviatoric part $\boldsymbol{\varepsilon}_{\mathrm{dev}}$ of the spatial Hencky strain tensor (2.18). Applying the assumption of maximum deviatoric stress of the Mariotte criterion (2.134) to principal strains yields a Mariotte-like strain criterion

$$\varepsilon_{\mathrm{eq}}(\boldsymbol{\varepsilon}) = \frac{3}{2}\left(\varepsilon_{\mathrm{I}} - \frac{1}{3} I_{\boldsymbol{\varepsilon}}\right), \tag{5.14}$$

where ε_{I} denotes the maximum principal true strain (5.11) and $I_{\boldsymbol{\varepsilon}}$ the first invariant of the spatial Hencky strain tensor. Conversely, the Ivlev criterion supposes a threshold of the mean deviatoric stress. The corresponding Ivlev-like strain criterion reads

$$\varepsilon_{\mathrm{eq}}(\boldsymbol{\varepsilon}) = I_{\boldsymbol{\varepsilon}} - 3\varepsilon_{\mathrm{III}}, \tag{5.15}$$

where, $\varepsilon_{\mathrm{III}}$ denotes the minimum principal strain. Interestingly, the Ivlev criterion represents a pressure-insensitive formulation of the criterion of Ko (1963) developed for a hyperelastic polyurethane foam.

The above principal strain formulations of classical failure criteria are compared to experimental data in the deviatoric plane in Fig. 5.8. The top row presents test data of unfilled SBR reported by Kawabata (1973). The bottom row shows test data of carbon black filled SBR given by Hamdi et al. (2006a, 2007b). The Rankine-like strain criterion (5.11) provides a fairly good representation of Kawabata's test data (Fig. 5.8a). A similar observation can be made considering stretches, which led Kawabata (1973) to propose his maximum principal stretch criterion. However, the criterion describes biaxial tension data of Hamdi et al. (2006a, 2007b) poorly. A Rankine-like strain criterion is intrinsically pressure-sensitive. It implies that hydrostatic tensile failure ($\varepsilon_{\mathrm{I}} = \varepsilon_{\mathrm{II}} = \varepsilon_{\mathrm{III}}$) can be described using the same critical strain ε_{c} as distortional failure data. However, dilatational failure strains are much smaller than those corresponding to distortional failure (Drass et al., 2018e). Hence, the Rankine-like criterion cannot represent a meaningful failure surface for both failure modes. Instead, a combination of two individual failure surfaces, a distortional and a dilatational surface, according to the failure mode concept (2.147) is sensible. The pressure-insensitive Tresca-like (5.12) and von Mises-like (5.13) criteria capture biaxial test data well but cannot describe uniaxial and planar tension data simultaneously (Fig. 5.8b and c). The Mariotte-like criterion (5.14), describes the same shape as the Rankine-like criterion (Fig. 5.8a). It represents the upper convexity

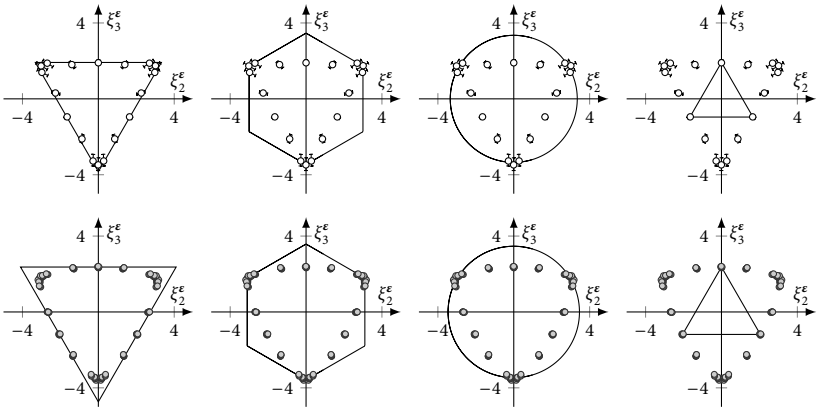

a Rankine-like Eq. (5.11) | **b** Tresca-like Eq. (5.12) | **c** von Mises-like Eq. (5.13) | **d** Ivlev-like Eq. (5.15)

Fig. 5.8 Strain-based formulations of classical failure criteria in the deviatoric strain plane with test data of unfilled (top) and carbon black filled (bottom) SBR of Kawabata (1973) and Hamdi et al. (2006a, 2007b), respectively.

limit. The Ivlev-like criterion (5.15) provides the lower convexity limit. However, it cannot describe the present test data (Fig. 5.8d).

None of the classical criteria presented above is capable of describing failure surfaces of both SBRs. The data sets shown in Fig. 5.8 demonstrate that a universally applicable failure criterion for elastomers must allow for a shape modification of the deviatoric cross section of the failure surface. Classical criteria do not provide this feature.

Dedicated criteria for rubber-like materials. Besides attempts to fit classical failure criteria to elastomers, dedicated criteria for hyperelastic media were developed. Because of the challenges in determining true stress at large deformations discussed above, recent failure criteria for hyperelastic materials are commonly formulated in principal stretches. Ayatollahi et al. (2016) (uniaxial loading) and Heydari-Meybodi et al. (2017) (multiaxial loading) consider a representative volume element of the 8-chain network model (Arruda and Boyce, 1993) to derive an equivalent stretch function. The 8-chain model assumes a cubic representative volume element with eight identical molecular chains connected to the cube's corners and a central junction. In this model, each chain is stretched equally. Hence, the chain stretch

$$\lambda_{\mathrm{eq}}(\boldsymbol{F}) = \sqrt{\frac{\lambda_{\mathrm{I}}^2 + \lambda_{\mathrm{II}}^2 + \lambda_{\mathrm{III}}^2}{3}}, \tag{5.16}$$

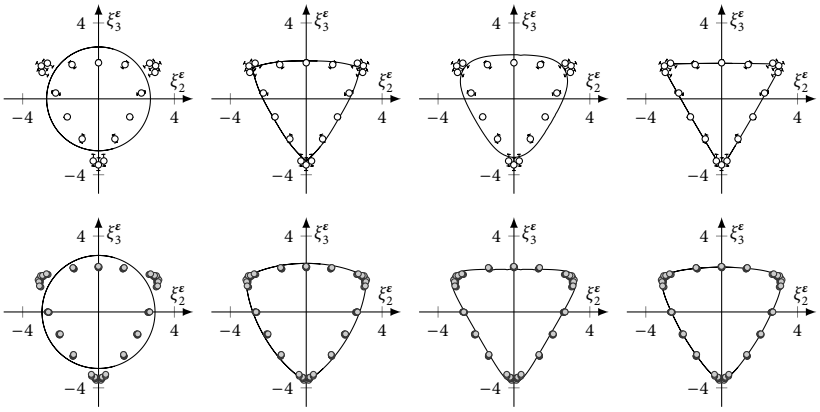

a Average true strain Eq. (5.17) | **b** Hamdi–Mahjoubi Eq. (5.19) | **c** Strain energy density Eq. (5.20) | **d** Present Eq. (5.21)

Fig. 5.9 Best fits of recent strain failure criteria in the deviatoric strain plane to test data of unfilled (top) and carbon black filled (bottom) SBR of Kawabata (1973) and Hamdi et al. (2006a, 2007b), respectively.

with the principal macroscopic stretches λ_I, λ_II and λ_III, is used as an equivalent stretch function. Khiêm and Itskov (2016) show that the same effective stretch is obtained from a 4-chain (Wang and Guth, 1952) network model or a full-network model. In full-network models Eq. (5.16) is obtained averaging stretches of randomly oriented chains using a surface integral (Kearsley, 1989). Since fillers and crystallization may magnify stretches on the micro scale, Eq. (5.16) is referred to as average macro stretch criterion. It implies that elastomers break when the average stretch of network chains exceeds a certain threshold. Based on their test data, Staudt et al. (2018) propose a failure criterion for DOWSIL™ 993 of similar form, yet using true strains, i.e.,

$$\varepsilon_\mathrm{eq}(\boldsymbol{\varepsilon}) = \sqrt{\varepsilon_\mathrm{I}^2 + \varepsilon_\mathrm{II}^2 + \varepsilon_\mathrm{III}^2}. \tag{5.17}$$

Here, ε_I, ε_II and ε_III are principal true strains and Eq. (5.17) is referred to as average true strain criterion. Hamdi et al. (2006a) develop a strain-based criterion implicitly using the Hencky strain tensor without mentioning it explicitly. In the notation of the present work, their criterion can be expressed as

$$\varepsilon_\mathrm{eq}(\boldsymbol{\varepsilon}) = \sqrt{6 I\!I'_{\boldsymbol{\varepsilon}}}, \tag{5.18}$$

where $I\!I'_{\boldsymbol{\varepsilon}}$ is the second invariant of the deviatoric part $\boldsymbol{\varepsilon}_\mathrm{dev}$ of the spatial Hencky strain tensor (2.18). Equation (5.18) represents a scaled von Mises-like strain criterion. Restricting the analysis to incompressible media, both Eq. (5.17) and Eq. (5.18) represent circular failure surfaces in the deviatoric strain plane (Fig. 5.9a and Fig. 5.8c).

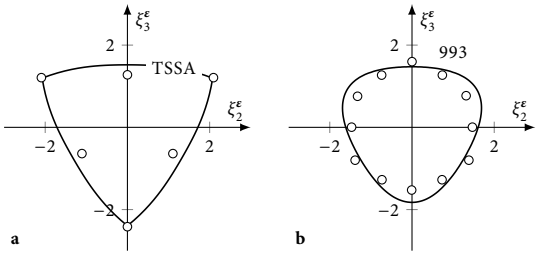

Fig. 5.10 Limitations of **a** the Hamdi–Mahjoubi criterion (5.19) and **b** the strain energy density criterion (5.20) describing the materials examined in the present work.

In a later work, Hamdi and Mahjoubi (2015) propose a new stretch-based criterion using the same set of test data. Although using a different coordinate transformation than the present work, they exploit the deviatoric plane representation of their data to develop a distortional failure criterion. Transferred to principal strains and adjusted to the present notation, their equivalent stretch function may be expressed as

$$\varepsilon_{\mathrm{eq}}(\boldsymbol{\varepsilon}) = \frac{\rho_{\boldsymbol{\varepsilon}}}{1 + \cosh\left(\alpha\theta_{\boldsymbol{\varepsilon}}\right)}, \tag{5.19}$$

where $\rho_{\boldsymbol{\varepsilon}}$ is the distance from the hydrostatic axis ($\varepsilon_{\mathrm{I}} = \varepsilon_{\mathrm{II}} = \varepsilon_{\mathrm{III}}$) and $\theta_{\boldsymbol{\varepsilon}}$ the meridian angle. The parameter $\alpha > 0$ allows for a certain shape adaption. Nelson (2019) employs the energy delimiter theory of Volokh (2010) and considers a threshold of the isochoric strain energy density to describe deviatoric failure. This can be expressed as

$$\mathcal{W}_{\mathrm{eq}}(\boldsymbol{F}) = \mathcal{W}_{\mathrm{iso}}(\boldsymbol{F}) = \mathcal{W}_{\mathrm{c}}, \tag{5.20}$$

which mandates an accurate representation of the material's constitutive behavior by the isochoric strain energy density function $\mathcal{W}_{\mathrm{iso}}$. Hamdi et al. (2006a) model NR using the Yeoh model (2.102) and SBR using a second-order Ogden model (2.109). Identified and reported material parameters provide a good description of the constitutive behavior. Kawabata (1973) uses the Mooney–Rivlin model (2.105) for both NR and SBR. Constitutive models for DOWSIL™ 993 and DOWSIL™ TSSA are given in Section 4.2.

The advantages of RDF_1, formulated in stress space in Section 5.2, can be exploited in principal strain space. Capturing failure of the hyperelastic materials studied in the present work does not require all features of RDF_1. Using the shape function ω_1^+ (5.2) suffices and we obtain the equivalent strain criterion

$$\varepsilon_{\mathrm{eq}}^{\mathrm{iso}}(\boldsymbol{\varepsilon}) = \rho_{\boldsymbol{\varepsilon}} \cos\left(\beta\frac{\pi}{3} - \frac{1}{3}\arccos\left[\sin\left(\gamma\frac{\pi}{2}\right)\cos(3\theta_{\boldsymbol{\varepsilon}})\right]\right), \tag{5.21}$$

Table 5.3
Mean critical strain ε_c and relative standard deviation (SD) of different failure criteria for unfilled (Kawabata, 1973) and carbon black filled (Hamdi et al., 2006a, 2007b) styrene–butadiene rubber.

	Unfilled SBR$^\circ$		Filled SBR$^\bullet$	
Criterion	Mean	SD (%)	Mean	SD (%)
Rankine-like	1.50	3.9	1.73	11.0
Tresca-like	3.50	26.4	3.85	15.7
von Mises-like	3.35	28.0	3.65	16.9
Mariotte-like	2.24	3.9	2.60	11.0
Ivlev-like	6.01	47.6	6.36	36.6
Average true strain	2.74	28.0	2.98	16.9
Hamdi et al.	4.74	28.0	5.16	16.9
Hamdi–Mahjoubi	1.61	3.7	1.69	2.5
Present ε_{eq}^{iso} (5.21)	1.87	2.4	2.35	1.4

with the shape parameters $\beta \in [0,1]$ and $\gamma \in [0,1]$. In Eq. (5.21) we omit the normalization used in Eq. (5.4), which is less meaningful in principal strain space, and add the superscript iso to emphasize the deviatoric (isochoric) character of this equivalent strain function.

The suitability of the above strain failure criteria for hyperelastic materials is assessed in Fig. 5.9. It shows least squares approximations of the experimental data of Kawabata (1973) and Hamdi et al. (2006a, 2007b) in the deviatoric plane. The circular cross sections of the average true strain criterion and the criterion of Hamdi et al. (Fig. 5.9a) provide poor representations of test data. The average true strain criterion (5.17) describes a sphere in principal strain space. Hence, it implies that not just distortional but also dilatational failure is captured. As mentioned above, hydrostatic failure strains are much smaller than those corresponding to distortional failure (Drass et al., 2018e) and the description of both distortional and hydrostatic failure by this criterion is unjustified. Fig. 5.9 depicts the deviatoric plane corresponding to incompressible deformation states. The strain energy density criterion approximates the failure data of Hamdi et al. (2006a, 2007b) well but deviates from the data of Kawabata (1973) (Fig. 5.9c). The Hamdi–Mahjoubi criterion and the present criterion (5.21) offer a good qualitative description of the SBRs (Figs. 5.9b and d). However, neither the Hamdi–Mahjoubi criterion nor the strain energy density criterion provide satisfactory descriptions of the materials considered in the present work (Fig. 5.10). The deviatoric shape of the strain energy density criterion (5.20) is prescribed by the isochoric strain energy density function, and cannot adjust to different shapes of failure surfaces (Fig. 5.10b). Similarly, the Hamdi–Mahjoubi criterion (5.19) is limited to a certain deviatoric shape and does not capture failure of DOWSIL™ TSSA well (Fig. 5.10a).

A quantitative measure for the quality of data representation is given by the relative

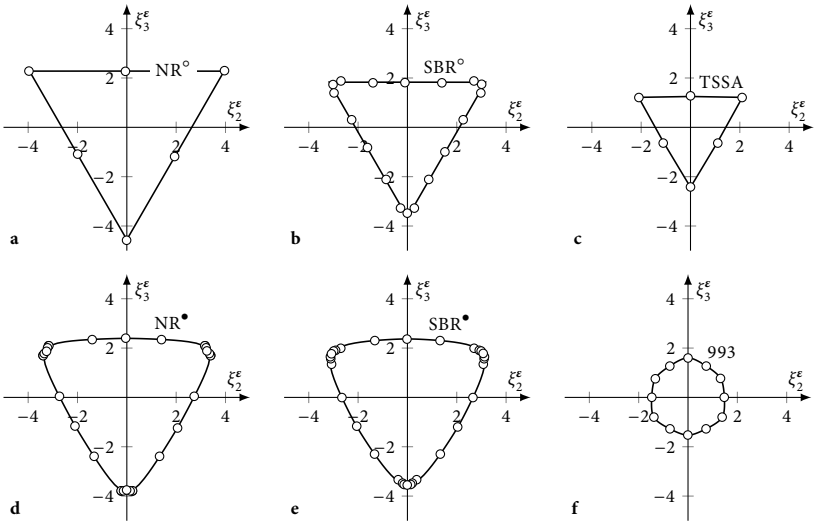

Fig. 5.11 Least squares approximation of multiaxial test data using the deviatoric strain function (5.21) of **a** unfilled natural (NR°) and **b** styrene–butadiene (SBR°) rubber (Kawabata, 1973), **c** DOWSIL™ TSSA, **d** carbon black filled natural (NR•) and **e** styrene–butadiene (SBR•) rubber (Hamdi et al., 2006a, 2007b), and **f** DOWSIL™ 993 in the deviatoric plane.

standard deviation in percent of the mean critical strain ε_c. Table 5.3 lists mean and standard deviation for best fits of all criteria and both data sets shown in Figs. 5.8 and 5.9. Note that listed mean critical strains differ considerably in magnitude because of the different formulations of different criteria. Except the Hamdi–Mahjoubi criterion (5.19) and the present strain criterion (5.21), all other criteria display double-digit relative standard deviations. That is, only criteria that allow for a certain change in shape are capable of describing failure surfaces of different elastomers.

A detailed assessment of the proposed deviatoric function for soft hyperelastic elastomers (5.21) is given in Fig. 5.11 in the deviatoric plane and Fig. 5.12 in the ε_I-ε_{II}-plane. The shape parameters for each material are identified using the method of least squares and reported in Table 5.4. The present criterion provides an excellent representation of all materials considered in the present analysis and proves qualified for the description of distortional failure surfaces of incompressible hyperelastic elastomers. Figure 5.12 further suggests that two of the most important experiments for the characterization of multiaxial failure of elastomers are uniaxial and equibiaxial tension tests. Such tests can be performed using classical dumbbell shaped specimens and bulge tests inflating thin

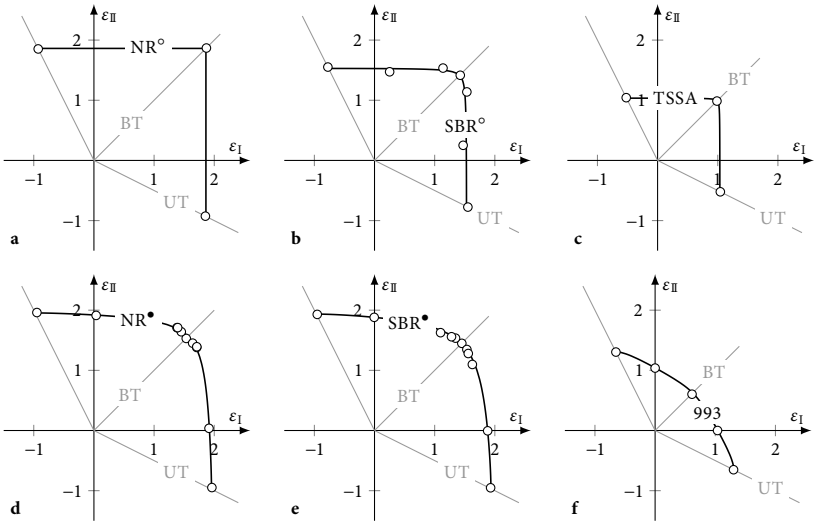

Fig. 5.12 Least squares approximation of multiaxial test data using the deviatoric strain function (5.21) of **a** unfilled natural (NR°) and **b** styrene–butadiene (SBR°) rubber (Kawabata, 1973), **c** DOWSIL™ TSSA, **d** carbon black filled natural (NR•) and **e** styrene–butadiene (SBR•) rubber (Hamdi et al., 2006a, 2007b), and **f** DOWSIL™ 993 in the ε_I-ε_{II}-plane with uniaxial tension (UT) and equibiaxial tension (BT) load paths.

Table 5.4
Best fit parameters of the proposed deviatoric strain failure criterion (5.21) for different materials.

Material	β	γ	ε_c^{iso}
Unfilled NR°	0.00	0.98	2.28 ± 0.06
Unfilled SBR°	0.01	0.94	1.87 ± 0.04
DOWSIL™ TSSA	0.02	0.98	1.24 ± 0.10
Filled NR•	0.02	0.76	2.38 ± 0.04
Filled SBR•	0.04	0.68	2.35 ± 0.03
DOWSIL™ 993	0.56	0.66	1.47 ± 0.11

membranes. Additional experiments of different biaxiality ratios further particularize the shape of the failure surface. However, they do not alter the primary characteristics established by uniaxial and equibiaxial tension failure points.

Rupture of a thin hyperelastic membrane. In order to demonstrate the application of the proposed strain criterion and to verify its implementation, let us investigate the inflation of a thin hyperelastic membrane (Fig. 3.2). Fracture initiates from the

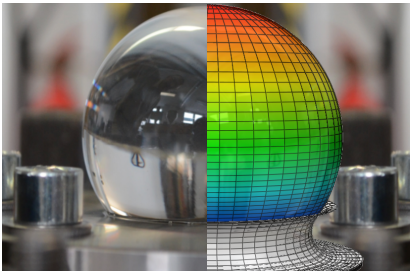

Fig. 5.13 Numerical reproduction of a thin hyperelastic membrane almost inflated to rupture. Color indicates satisfaction of the failure criterion.

equibiaxially loaded pole of the inflated body requiring a multiaxial strength hypothesis. This example showcases the implementation of the present criterion in finite element code (Fig. 5.13).

Specimens are prepared as described in Section 3.1.2. The finite element model of the test setup is shown in Fig. 5.14a. Here, the anchor plates are represented as rigid bodies. DOWSIL™ TSSA is modeled using an incompressible Neo-Hookean strain energy density function (2.101) with a shear modulus of $\mu = 2.67$ MPa. The model exploits the axial symmetry of the geometry and is swept around the center axis for visualization in Fig. 5.14a. Contact between anchor plates and membrane is modeled frictionless. Radial movement of the membrane is restricted at its outer edges representing clamping. The membrane is loaded by bottom side pressure. Because the surface area of the deformed body increases with increasing pressure, the problem becomes unstable at a certain deformation. Here, further increasing the deformation requires pressure reduction to reach equilibrium (Fig. 5.14b). This unstable behavior is representative for the importance of strain measures as opposed to stress measures for the analysis of failure at large deformations. To account for instability, the arc length method (Riks, 1979) is employed. The strain criterion (5.21) is implemented using the Abaqus® (2018) user subroutine `UVARM` (Listing 5.1). The subroutine is called in every integration point in every time step and allows for direct visualization of the criterion. It returns the equivalent strain $\varepsilon_{\mathrm{eq}}^{\mathrm{iso}}$ normalized to the corresponding critical value $\varepsilon_{\mathrm{c}}^{\mathrm{iso}}$ (Fig. 5.14a). The criterion predicts fracture initiating from the pole of the inflated body as observed in experiments.

Experimentally measured pressure–true strain responses of five inflation tests are shown in Fig. 5.14b. The experimental data are shown until the point of rupture. The finite element model captures the pressure–strain behavior well. The decreasing pressure with increasing pole strain illustrates the instability of the test. The experiments yield

Listing 5.1: Implementation of the strain failure criterion as an Abaqus® (2018) user subroutine `uvarm.f`.

```
      SUBROUTINE UVARM(UVAR, DIRECT, T, TIME, DTIME, CMNAME, ORNAME,
     1 NUVARM, NOEL, NPT, LAYER, KSPT, KSTEP, KINC, NDI, NSHR, COORD,
     2 JMAC, JMATYP, MATLAYO, LACCFLA)
      INCLUDE 'ABA_PARAM.INC'

! === VARIABLE DEFINITION ============================================

      DOUBLE PRECISION LEP1, LEP2, LEP3, ECRIT, EEQ, BETA, GAMMA
      DOUBLE PRECISION NUMERATOR, DENOMINATOR, ARCCOS, COSINE, SQRTS
      CHARACTER*80 CMNAME, ORNAME
      CHARACTER*3 FLGRAY(15)
      DIMENSION UVAR(NUVARM), DIRECT(3,3), T(3,3), TIME(2)
      DIMENSION ARRAY(15), JARRAY(15), JMAC(*), JMATYP(*), COORD(*)

! === USER INPUT =====================================================

!     Critical equivalent strain
      ECRIT = 1.24
!     Shape parameters
      BETA = 0.02
      GAMMA = 0.98

! === GET PRINCIPAL LOGARITHMIC STRAINS ==============================

      CALL GETVRM('LEP', ARRAY, JARRAY, FLGRAY, JRCD, JMAC, JMATYP,
     1 MATLAYO, LACCFLA)
!     Write principal strains to variables
      LEP1 = ARRAY(1)
      LEP2 = ARRAY(2)
      LEP3 = ARRAY(3)
!     Compute Pi
      PI = 4.D0*DATAN(1.D0)

! === EVALUATE EQUIVALENT STRAIN FUNCTION ============================

!     Temporary variables
      NUMERATOR = SIN(GAMMA*PI/2.0)*(LEP1 + LEP2 - 2.0*LEP3)
     1 *(2.0*LEP1 - LEP2 - LEP3)*(LEP1 - 2.0*LEP2 + LEP3)
      DENOMINATOR = 2.0*(LEP1**2.0 + LEP2**2.0 - LEP2*LEP3
     1 + LEP3**2.0 - LEP1*(LEP2 + LEP3))**1.5
      ARCCOS = ACOS(NUMERATOR/DENOMINATOR)
      COSINE = COS((BETA*PI - ARCCOS)/3.0)
      SQRTS = SQRT(2.0/3.0)*SQRT(LEP1**2.0 + LEP2**2.0
     1 - LEP2*LEP3 + LEP3**2.0 - LEP1*(LEP2 + LEP3))

!     Evaluate equivalent strain and normalize to its critical value
      EEQ = SQRTS*COSINE/ECRIT

! === OUTPUT =========================================================

!     Return normalized equivalent strain
      UVAR(1) = EEQ

! === CLOSURE ========================================================

      RETURN
      END
```

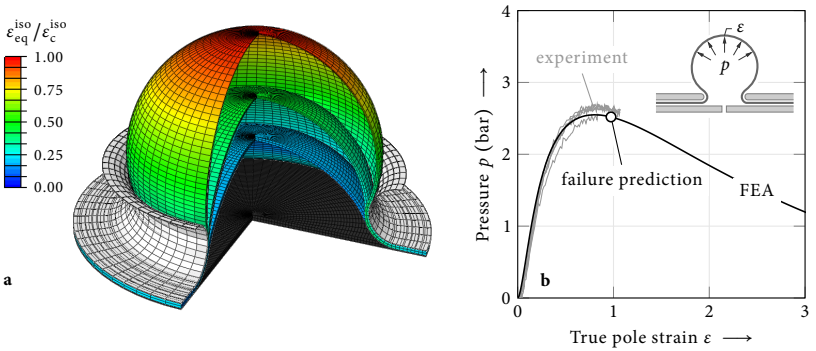

Fig. 5.14 Finite element representation of DOWSIL™ TSSA bulge tests. **a** Inflated membrane at different pressures where the user variable $\varepsilon_{eq}^{iso}/\varepsilon_c^{iso}$ (color bar) indicates the equivalent strain (5.21) normalized with respect to the corresponding critical strain. **b** Measured and computed pressure–true strain curves. Experimental data are shown until point of rupture. The FEA failure prediction using the strain criterion ($\beta = 0.02$, $\gamma = 0.98$ and $\varepsilon_c^{iso} = 1.24$) agrees well with the test data verifying the implementation.

a mean failure true strain of $\varepsilon_{exp}^{\times} = 0.97 \pm 0.09$. The present strain criterion predicts failure at $\varepsilon^{\times} = 0.99$ using the parameters $\beta = 0.02$, $\gamma = 0.98$ and $\varepsilon_c^{iso} = 1.24$, which are also used in Fig. 5.11c. Failure prediction and tests results are in excellent agreement in this structural application verifying the implementation.

5.4 Combined distortional–dilatational failure mode concept

The comprehensive description of failure of nearly incompressible hyperelastic materials requires accounting for both distortional and dilatational failure. The latter manifests in the formation and growth of cavities owing to triaxial tensile loading. It is accompanied by pronounced stress softening (Euchler et al., 2018) and can be examined using so-called pancake or poker chip tests (Section 3.2.3). However, experiments investigating the influence of superimposed dilatation on distortional failure are unavailable. Therefore, we propose a combined distortional–dilatational failure criterion using Cuntze's failure mode concept (Cuntze, 1996, 1999) without explicit definition of the interaction of both failure modes. The failure mode concept (FMC) considers individual failure surfaces for each failure mode and accounts for their interaction only in transition regions. A particular advantage of this concept is that changes to one failure criterion leave all other failure modes unaffected (Section 2.2).

Dilatational failure. While most cavitation failure criteria are formulated in terms of stress (Section 2.2), Drass et al. (2020) propose a stretch-based description. For consistency within the present work, we combine the deviatoric function (5.21) with a strain-based dilatational failure criterion harnessing the advantages of the deformation-based description of failure of the present class of materials (Section 4.3). The cavitation criterion is defined as a critical volume change

$$\varepsilon_{\mathrm{eq}}^{\mathrm{vol}}(\boldsymbol{\varepsilon}) = \langle I_{\boldsymbol{\varepsilon}} \rangle, \tag{5.22}$$

given by the trace of the spatial Hencky strain tensor (2.18), i.e., its first invariant $I_{\boldsymbol{\varepsilon}}$. The latter may be expressed as the natural logarithm of the determinant of the deformation gradient $I_{\boldsymbol{\varepsilon}} = \ln J$. The Maccaulay brackets $\langle \circ \rangle$ express that only volume increase can trigger cavitation failure. The volume change threshold $\varepsilon_{\mathrm{c}}^{\mathrm{vol}}$ depends on the characteristics of the material, e.g., the initial porosity as discussed by Drass et al. (2018b). With increasing porosity, the critical hydrostatic stress causing cavitation decreases and the critical volume change increases. Owing to the lack of experimental data of rubber-like materials subjected to more complex triaxial stress states than hydrostatic tension, the volumetric equivalent strain function (5.22) has no shape parameters.

The critical volumetric strain $\varepsilon_{\mathrm{c}}^{\mathrm{vol}}$ can be determined in pancake tests (Section 3.2.3). Force–displacement responses of such tests show distinct stress softening at the onset of cavitation (Dorfmann et al., 2002). Fitting the pseudo-elastic model of DOWSIL™ TSSA (Section 4.2) to pancake tests, Drass et al. (2019) identify this bifurcation point as a local maximum in plots of the hydrostatic pressure p against the volume change J. Using this methodology, we obtain a critical volumetric strain of $\varepsilon_{\mathrm{c}}^{\mathrm{vol}} = 0.04$ for DOWSIL™ TSSA (Fig. 5.15). Classical cavitation models (Gent and Lindley, 1959; Hou and Abeyaratne, 1992; Lopez-Pamies et al., 2011b) assume the simple relation $p = KJ$, determine the critical hydrostatic pressure from $p_{\mathrm{c}} = 5\mu/2$ and do not account for finite porosity. With a bulk modulus of $K = 2.5\,\mathrm{GPa}$ and a shear modulus of $\mu = 2.67\,\mathrm{MPa}$ they overestimate the pressure at cavitation onset and underestimate the corresponding volumetric strain considerably (Fig. 5.15). Volumetric experiments of DOWSIL™ 993 are unavailable at present.

Combined failure surface. A comprehensive strain-based description of the failure surface of nearly incompressible hyperelastic materials is obtained combining the deviatoric function (5.21) and the volumetric function (5.22) using the failure mode concept (2.147). We postulate an interaction law of the general form

$$\left[\left(\frac{\varepsilon_{\mathrm{eq}}^{\mathrm{iso}}(\boldsymbol{\varepsilon})}{\varepsilon_{\mathrm{c}}^{\mathrm{iso}}} \right)^{m} + \left(\frac{\varepsilon_{\mathrm{eq}}^{\mathrm{vol}}(\boldsymbol{\varepsilon})}{\varepsilon_{\mathrm{c}}^{\mathrm{vol}}} \right)^{m} \right]^{\frac{1}{m}} = 1, \tag{5.23a}$$

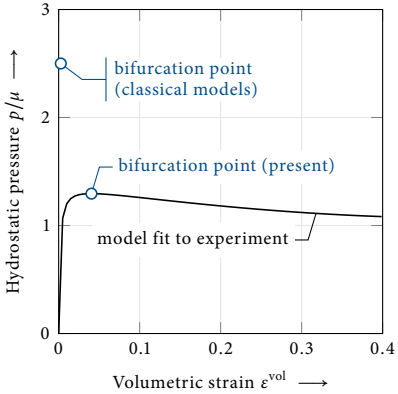

Fig. 5.15 Volumetric response obtained by fitting Eq. (4.2) to pancake tests of DOWSIL™ TSSA. Because DOWSIL™ TSSA is a porous material, classical models (Gent and Lindley, 1959; Hou and Abeyaratne, 1992; Lopez-Pamies et al., 2011b) do not capture cavitation onset (bifurcation point) accurately using $p_c = 5\mu/2$. The present approach yields a critical volumetric strain of $\varepsilon_c^{\mathrm{vol}} = 0.04$.

where

$$\varepsilon_{\mathrm{eq}}^{\mathrm{iso}}(\boldsymbol{\varepsilon}) = \rho_{\boldsymbol{\varepsilon}} \cos\left(\beta\frac{\pi}{3} - \frac{1}{3}\arccos\left[\sin\left(\gamma\frac{\pi}{2}\right)\cos(3\theta_{\boldsymbol{\varepsilon}})\right]\right), \tag{5.23b}$$

and

$$\varepsilon_{\mathrm{eq}}^{\mathrm{vol}}(\boldsymbol{\varepsilon}) = \langle I_{\boldsymbol{\varepsilon}} \rangle. \tag{5.23c}$$

Here, $\langle \circ \rangle$ are Maccaulay brackets, $\boldsymbol{\varepsilon}$ is the spatial Hencky strain tensor (2.18), $I_{\boldsymbol{\varepsilon}}$ is its first invariant (2.44), $\rho_{\boldsymbol{\varepsilon}}$ and $\theta_{\boldsymbol{\varepsilon}}$ are cylindrical Haigh–Westergaard coordinates of the strain deviatoric plane (2.129), $\beta \in [0,1]$ and $\gamma \in [0,1]$ are deviatoric shape parameters, $\varepsilon_c^{\mathrm{iso}}$ and $\varepsilon_c^{\mathrm{vol}}$ are thresholds of the respective individual failure criteria, and $m > 1$ is an interaction parameter characterizing the interaction of both failure modes. The identification of the interaction parameter m requires experiments on distortional failure with superimposed dilatation or volumetric experiments with superimposed distortion, none of which are currently available. Hence, we resort to typical values of $1 \leq m \leq 4$ (Cuntze, 1999). The general effect of the interaction parameter is shown in Fig. 2.5. For $m \to \infty$ both failure modes are independent.

As an example, Fig. 5.16 shows the failure surface of DOWSIL™ TSSA with an interaction parameter $m = 4$. The deviatoric function is plotted using the shape parameters $\beta = 0.02$ and $\gamma = 0.98$, and the threshold $\varepsilon_c^{\mathrm{iso}} = 1.24$ of DOWSIL™ TSSA. The critical volumetric strain is scaled by a factor of 5, i.e., $\varepsilon_c^{\mathrm{vol}} = 5 \times 0.4$, for better visualization. The failure criterion (5.23) is developed and valid for volumetric expansion (blue body in

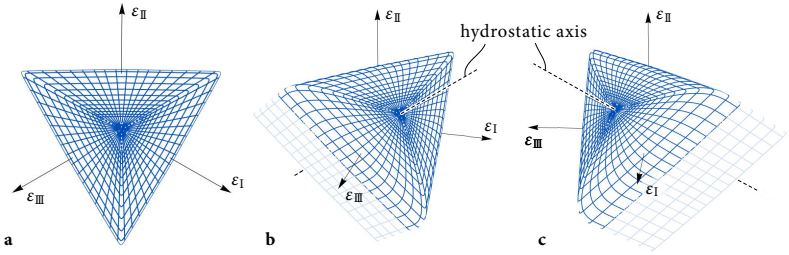

Fig. 5.16 Failure surface of DOWSIL™ TSSA in principal strain space described by the failure mode concept (5.23) using $m = 4$, $\beta = 0.02$, $\gamma = 0.98$, $\varepsilon_c^{iso} = 1.24$, and $\varepsilon_c^{vol} = 5 \times 0.4$. For the purpose of better visualization, the critical volumetric strain is scaled by a factor of 5. The failure criterion is formulated and valid for volumetric expansion (blue body). However, it technically comprises compression (light blue extension), as well.

Fig. 5.16). Since no test data under superimposed volumetric compression are available, no assessment of the pressure-sensitivity of the failure surface can be given. In its present form, the deviatoric function does not distinguish between expansion and compression. However, the criterion cannot be validated and should not be used in the compression region (light blue region in Fig. 5.16).

Chapter 6

Nucleation of finite cracks in hyperelastic materials

Ever since Leguillon (2002) proposed the coupled stress and energy criterion within the framework of finite fracture mechanics for the assessment of crack nucleation, many authors proved its capabilities in a multitude of structural situations. Requiring both stress and energy conditions to be met simultaneously proved key to modeling brittle crack formation at singular and nonsingular stress concentrations. However, only very few studies explore the potential of this so-called coupled stress and energy criterion beyond linear elasticity.

The following sections aim at extending finite fracture mechanics to brittle crack nucleation in hyperelastic media using the example of silicone adhesives. For this purpose, we use the comprehensive constitutive as well as fracture mechanical characterization of DOWSIL™ 993 and DOWSIL™ TSSA (Chapters 4 and 5) to propose a mixed-mode failure model for crack initiation in nonlinear elastic materials.

Characterized in independent experiments (Chapter 4), the model is used to determine critical loads of hyperelastic adhesive bonds of shear, tension and volumetric expansion dominated samples (Chapter 3). For any of the examined adhesive joints the model predicts and explains size effects and agrees well with experimental findings.

Video recordings of the experiments allow for studying stable and unstable crack propagation. It is shown that crack initiation, crack growth and crack arrest are caused by nonmontonic energy release rates and can be predicted. Effects of excess energy available after crack nucleation and initial unstable crack growth are discussed. The main results discussed in this chapter are published in peer-reviewed journals and conference proceedings (Felger et al., 2017a; Rosendahl et al., 2017a, 2018, 2019d,e).

6.1 State of the art

The unique molecular structure of silicones provides mechanical properties that render them excellent structural adhesives. However, at bi-material corners between adherends

and adhesive stress singularities owing to geometrical and material discontinuities are present. In order to capture crack onset at these singularities, classical approaches such as stress-based criteria or fracture mechanics can only be applied using an additional length parameter (Section 2.4).

Different nonlocal approaches were successfully applied to hyperelastic materials. Clift et al. (2014) and Hagl (2016) evaluate stress criteria in relatively coarsely discretized finite element analyses (FEAs) of silicone bonds. Using a fixed discretization in FEAs introduces the element size as a characteristic length scale implicitly. Ayatollahi et al. (2016) and Heydari-Meybodi et al. (2017) are more specific in their use of a critical distance in rubbers. They evaluate an effective stretch criterion in a certain distance from notches and obtain good agreements with experiments. Berto (2015) and Heydari-Meybodi et al. (2018) average strain energy density (SED) in a finite volume around V-notches to predict crack initiation. Schänzel et al. (2013) and Miehe and Schänzel (2014) predict crack initiation in hyperelastic materials using the regularized phase-field approach. The models are able to describe experimental findings on hyperelastic materials adequately. Yet, the length parameter involved in all of the above approaches is not known a priori and lacks definite physical meaning. Awerbuch and Madhukar (1985), Pipes et al. (1979) and Tan (1987) for instance, find a dependence of the critical distance on geometrical features which, hence, cannot be regarded as a material constant.

Assuming the sudden nucleation of a finite sized crack introduces a length scale with clear physical meaning – the finite size of the initiated crack. The concept is known as finite fracture mechanics (FFM) and was suggested by Hashin (1996). In order to determine the finite crack size, Leguillon (2002) proposed requiring the simultaneous satisfaction of both a stress and an energy criterion as necessary and sufficient condition for crack nucleation. This so-called coupled stress and energy criterion involves two equations that allow for computing two unknowns: the critical loading and the size of the initiating crack. The coupled criterion requires only the fundamental material properties strength and fracture toughness as inputs. It provides excellent predictions for the failure of structures with sharp (Yosibash et al., 2006; Carpinteri et al., 2008; Cornetti et al., 2018) and rounded (Carpinteri et al., 2012; Sapora et al., 2015) notches or round and elliptical open-holes (Weißgraeber et al., 2015a, 2016a; Rosendahl et al., 2016a,b; Felger et al., 2017b; Torabi et al., 2017; Doitrand et al., 2019; Sapora and Cornetti, 2018). It can describe mixed-mode failure (Cornetti et al., 2013; Talmon l'Armée et al., 2017; Felger et al., 2017c), cracks through interfaces (Leguillon and Martin, 2013a), adhesive joint failure (Weißgraeber and Becker, 2013; Weißgraeber et al., 2015b; Carrère et al., 2015; Hell et al., 2014; Stein et al., 2015; Felger et al., 2018, 2019b,a), bolted joint tension failure (Catalanotti and Camanho, 2013; Nguyen-Hoang and Becker, 2020), thermo-mechanical problems (Leguillon, 2013; Leguillon et al., 2015b), the formation of crack patterns (Rosendahl et al., 2017d; Li et al., 2018), transverse cracking of cross-ply laminates (García et al., 2016, 2018a,b, 2019), fiber or particle debonding (Mantič,

2009; García et al., 2015), free-edge delamination (Hebel et al., 2010; Martin et al., 2010; Dölling et al., 2020), 3D crack initiation (Doitrand and Leguillon, 2018a,b; Cornetti and Sapora, 2019), fatigue cracks (Sapora et al., 2019), geomechanical crack problems (Rosendahl and Weißgraeber, 2020a,b), and can be linked to micromechanical material properties (Leguillon et al., 2018). A comprehensive review is given by Weißgraeber et al. (2016b).

Common to all of the above FFM studies are the assumptions of brittleness and linear-elastic material behavior. However, the physical background of the coupled criterion allows for a generalization of the method. For instance, Leguillon and Yosibash (2017) develop a theoretical FFM framework for quasi-brittle materials and Doitrand and Sapora (2019) use FFM with a Ramberg–Osgood material law. The present work proposes a formulation of finite fracture mechanics for hyperelastic materials. It uses the example of structural silicone adhesives. Yet, the presented methodology is applicable to crack initiation from stress concentrations in any nonlinear elastic material.

Technologically, a sound understanding of the failure processes of silicone adhesives and corresponding physical failure criteria are needed urgently. Owing to a lack of reliable tools for the assessment of hyperelastic bonds, standards defining requirements for structural sealant glazing applications such as the European Technical Approval Guideline for Structural Sealant Glazing Systems, ETAG 002 (EOTA, 2012), or the ASTM Standard Guide for Evaluating Failure of Structural Sealant Glazing (ASTM Standard C1401, 2014) assume linear elastic material behavior, a simplified load distribution and uniform stresses within the adhesive. They neglect stress concentrations and nonlinearity of the adhesive, which results in significant design factors accounting for all unconsidered effects. Findings of the present failure analysis allow for the derivation of a simple, yet accurate engineering tool for the design of silicone adhesive connections.

6.2 Mixed-mode crack nucleation criterion

Leguillon (2002) showed that fracture processes are governed not by one exclusive but by two conditions simultaneously, even if one often hides the other (Section 2.4). The failure of an isotropic homogeneous bar subjected to tensile loading is dominated by stress or strain. Evaluating a stress or strain criterion provides accurate failure predictions and energy seems irrelevant. The growth of existing cracks is dominated by energy. It can be assessed evaluating the Griffith criterion (2.153). No consideration of stress or strain is required. However, the bi-material notch between adherends and adhesive is a weak singularity (Weißgraeber and Becker, 2013). Stresses and strains are infinite, yet the differential energy release rate vanishes. Evaluating a pure stress or strain criterion locally at the bi-material point would predict failure at any given loading. The

Griffith criterion (2.153) can never be satisfied, i.e., it predicts infinite failure loads. This contradiction is resolved using the coupled criterion in the framework of finite fracture mechanics, i.e., considering both conditions as necessary conditions and only their simultaneous satisfaction as a sufficient condition for crack nucleation. The concept assumes the instantaneous formation of a crack of finite size when both a stress and an energy criterion are satisfied simultaneously. The present work replaces the stress criterion of classical FFM by a strain criterion to accurately describe mixed-mode failure of nonlinear elastic materials (Section 5.3).

Nonlinear elastic finite fracture mechanics. Assuming the instantaneous formation of a finite sized crack at a critical load requires the determination of two unknowns: the failure load $P_\times$ and the size of the nucleating crack ΔA. For this purpose, the coupled criterion requires the simultaneous satisfaction of two necessary conditions: the structure must be overloaded in a finite domain and the energy release of a finite crack must suffice. The energy condition requires the incremental energy release rate to exceed the material's fracture toughness

$$\overline{\mathcal{G}}(\Delta A) \geq \mathcal{G}_\mathrm{c}, \tag{6.1}$$

where the incremental energy release rate $\overline{\mathcal{G}}$ for a crack increment of surface area ΔA is defined as

$$\overline{\mathcal{G}}(\Delta A) = \frac{1}{\Delta A}\int_{\Delta A} \mathcal{G}(A)\,\mathrm{d}A = -\frac{\Delta\Pi}{\Delta A}, \tag{6.2}$$

with the change in total potential energy of the structure $\Delta\Pi$. In the present work, we require the nonlinear elastic adhesive to be overloaded in terms of strain (Section 5.3): an equivalent strain averaged over the entire potential crack surface $\overline{\varepsilon}_\mathrm{eq}(\Delta A)$ must exceed a critical threshold, i.e.,

$$\overline{\varepsilon}_\mathrm{eq}(\Delta A) = \frac{1}{\Delta A}\int_{\Delta A} \varepsilon_\mathrm{eq}\big(\boldsymbol{\varepsilon}(\boldsymbol{x})\big)\,\mathrm{d}A \;\geq\; \varepsilon_\mathrm{c}. \tag{6.3}$$

Instead of averaging the equivalent strain function on the potential crack surface, we may also require it to be exceeded in every point of the crack surface. The former is known as line method (2.182), the latter as point method (2.181). A discussion of their differences is given in Section 6.3.4. The chosen equivalent strain function ε_eq must be capable of describing bulk material failure under complex loads at any given location $\boldsymbol{x}$. It will become evident that ultimate failure of all samples examined in the present work, even ultimate failure of pancake specimens, manifests in crack nucleation owing to deviatoric deformation. Hence, we use the isochoric equivalent strain function (5.21),

$$\varepsilon_\mathrm{eq}\big(\boldsymbol{\varepsilon}(\boldsymbol{x})\big) = \rho_\varepsilon(\boldsymbol{x})\cos\left(\beta\frac{\pi}{3} - \frac{1}{3}\arccos\left[\sin\left(\gamma\frac{\pi}{2}\right)\cos\Big(3\theta_\varepsilon(\boldsymbol{x})\Big)\right]\right), \tag{6.4}$$

where β and γ are shape parameters, and $\rho_{\boldsymbol{\varepsilon}}$ and $\theta_{\boldsymbol{\varepsilon}}$ are cylindrical Haigh–Westergaard coordinates of the strain deviatoric plane (2.129). For plane problems with through-thickness cracks and out-of-plane width w we obtain $\Delta A = w\Delta a$ and the coupled criterion reads

$$\bar{\varepsilon}_{\mathrm{eq}}(\Delta a) \geq \varepsilon_{\mathrm{c}} \quad \wedge \quad \bar{\mathcal{G}}(\Delta a) \geq \mathcal{G}_{\mathrm{c}}. \tag{6.5}$$

Cracks within adhesives, which often constitute the weakest link in complex structures, are forced onto certain paths prescribed by the shape of adherends and adhesive. Hence, crack initiation in adhesive bonds is a mixed-mode problem which is accounted for by the equivalent strain function (6.4). However, concerning mode mixity of the energy criterion, no measurements of the mode II fracture toughness $\mathcal{G}_{\mathrm{IIc}}$ of DOWSIL™ 993 or DOWSIL™ TSSA are available. Therefore, we may assume the equality of $\mathcal{G}_{\mathrm{c}} = \mathcal{G}_{\mathrm{Ic}}$ in Eq. (6.1). Since for most engineering materials the mode II fracture toughness is larger than the mode I fracture toughness, $\mathcal{G}_{\mathrm{IIc}} > \mathcal{G}_{\mathrm{Ic}}$, this is a conservative assumption.

Computation of logarithmic strains and energy release rates. True strains and incremental energy release rates required as inputs for the present failure criterion are computed using the commercial finite element analysis software Abaqus® (2018). Crack nucleation in one DOWSIL™ TSSA and three different DOWSIL™ 993 samples is examined. H-shaped DOWSIL™ 993 specimens (Section 3.2.1) are tested in simple shear (Fig. 3.6c) and tension (Fig. 3.6d) until failure. Additionally, notched tubular shear tests of DOWSIL™ 993 are performed (Section 3.2.2, Fig. 3.8c). DOWSIL™ TSSA is tested using pancake specimens (Section 3.2.3, Fig. 3.9) dominated by volumetric expansion.

The adhesives are loaded by prescribed vertical, horizontal or circular displacements, respectively. External work vanishes and the total potential energy equals the stored strain energy $\Pi = \Pi_{\mathrm{int}}$. Incremental energy release rates are computed from the difference in stored strain energy Π_{int} between cracked and uncracked configurations

$$\bar{\mathcal{G}}(u, \Delta a) = -\frac{\Pi_1^{\mathrm{int}}(u, \Delta a) - \Pi_0^{\mathrm{int}}(u)}{w\Delta a}, \tag{6.6}$$

where the subscripts 0 and 1 correspond to the uncracked and cracked state, respectively. u denotes the prescribed displacement, Δa is the crack length and w the out-of-plane specimen width. For immediate visualization of the mixed-mode strain hypothesis (6.4) the user subroutine of Listing 5.1 can be used.

Optimization problem. Finding the critical displacement $u_\times$ predicted by the coupled criterion (6.5), results in a constrained optimization problem: the smallest displacement u satisfying both the energy (6.1) and the strain (6.3) criterion is to be found for any kinematically admissible crack Δa,

$$u_\times = \min_{u, \Delta a} \{u \mid u > 0, \exists\, \Delta a > 0 : \ \bar{\varepsilon}_{\mathrm{eq}}(u, \Delta a) \geq \varepsilon_{\mathrm{c}} \ \wedge \ \bar{\mathcal{G}}(u, \Delta a) \geq \mathcal{G}_{\mathrm{c}}\}. \tag{6.7}$$

Table 6.1
Mean nominal shear strength $\tau_0^\times$ in MPa and standard deviation of 77 H-shaped DOWSIL™ 993 specimens of nominal width $w = 12$ mm in simple shear tests.

	Adhesive thickness t (# of tested specimens)		
Length l	6 mm	12 mm	24 mm
50 mm	1.002 ± 0.141 (04)	0.855 ± 0.153 (05)	0.610 ± 0.064 (04)
100 mm	0.989 ± 0.117 (18)	0.858 ± 0.132 (21)	0.630 ± 0.110 (15)
200 mm	–	0.830 ± 0.060 (05)	0.570 ± 0.151 (05)

The corresponding critical load at failure $P_\times$ is obtained as the reaction force at $u_\times$ in the uncracked configuration. In the present case, the energy release rate is not monotonic, which is typical for adhesive joints (Weißgraeber et al., 2016a) and requires an online–offline strategy. In the online stage, the equivalent strain function and the energy release rate are evaluated on a grid of feasible crack lengths and loads. In order to provide $\overline{\mathcal{G}}(u, \Delta a)$ in adequate resolution, the load is applied in at least 20 increments and cracks are resolved in 32 to 96 increments depending on their estimated maximum length. In the offline stage, $\varepsilon_{\mathrm{eq}}(u, \Delta a)$ and $\overline{\mathcal{G}}(u, \Delta a)$ are interpolated on the grid using bicubic splines. Critical load and length of the initiating crack are then determined using the sequential least squares programming algorithm of the scientific computing Python library SciPy. Computing the online stage dataset for one particular specimen geometry requires a few minutes on a standard desktop computer. Interpolating the data and solving for failure load and crack length in the offline stage takes less than 100 ms.

6.3 Failure prediction

The failure model introduced in Section 6.2 allows for predicting critical loads as well as lengths of initiating and growing cracks in silicone adhesives. In the following, failure load and crack growth predictions of the model are discussed and compared against experimental observations. The discussion comprises destructive tests of DOWSIL™ 993 H-shaped specimens (Section 3.2.1) under simple shear loading conditions (Fig. 3.6c) and in pull-off (Fig. 3.6d) tests, as well as DOWSIL™ 993 notched tubular lap shear joints (Section 3.2.2) under circular shear loading (Fig. 3.8c) and DOWSIL™ TSSA pancake specimens (Section 3.2.3, Fig. 3.9).

6.3.1 Simple shear test

Consider the results of the simple shear test series of H-shaped DOWSIL™ 993 specimens of adhesive thicknesses $t = 6\,\mathrm{mm}, 12\,\mathrm{mm}$ and 24 mm and specimen lengths

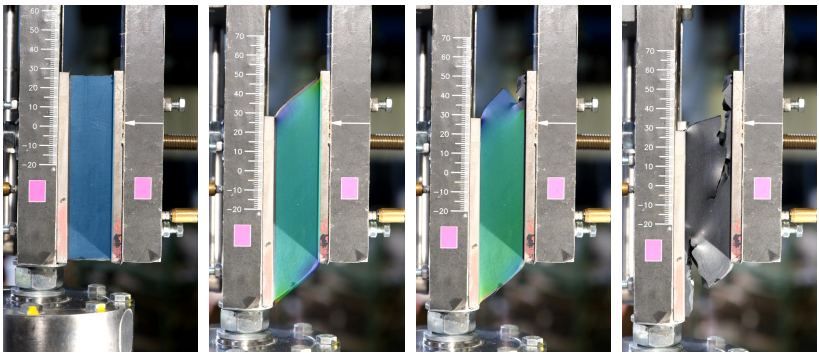

Fig. 6.1 Test setup and numerical reproduction of simple shear test on DOWSIL™ 993 H-shaped specimens with crack initiation and crack growth.

l = 50 mm, 100 mm and 200 mm listed in Table 6.1. The test setup and its numerical reproduction are shown Fig. 6.1. We tested a total number of 77 specimens of nominal width w = 12 mm. Fig. 6.2 compares FFM predictions to measured failure loads. Experimental data are indicated as mean and standard deviation. Nominal experimental strengths $\tau_0^\times$ are calculated from recorded failure loads $P_\times$ using the actual adhesive width and length of individual manufactured specimens. Nominal modeled joint shear strengths $\tau_0^\times$ and initial crack lengths Δa are evaluated using nominal dimensions and mean fracture properties accounting for 13 % overestimation of $\mathcal{G}_c$ (Section 4.4.1). In order to account for the uncertainty of fracture properties, failure load predictions are given with shaded 95 % confidence intervals. Overall, a good agreement between model and experiments is observed despite significant scatter in both experimental data and fracture properties. While failure loads are slightly overestimated, all trends are captured correctly. Confidence intervals of the predictions overlap with experimental standard deviations in any case.

Panels a and b in Fig. 6.2 show the influence of the adhesive thickness t for overlap lengths l = 50 mm and l = 100 mm, respectively. The experiments show the adhesive thickness effect, i.e., a reduction of the effective joint strength with increasing adhesive thickness t. The effect originates from an increasing energy release rate with increasing adhesive thickness, which dominates the crack initiation process. Because the coupled strain and energy criterion accounts for the energy balance, the effect is reproduced well. Several other studies report the adhesive thickness effect for nonlinear adhesives. For instance, Machalická and Eliášová (2017) perform shear and tension tests on nonlinear polyurethane adhesive joints and Wang et al. (2018) examine a two-component structural silicone in simple shear. The thickness effect suggests the use of thinner adhesive

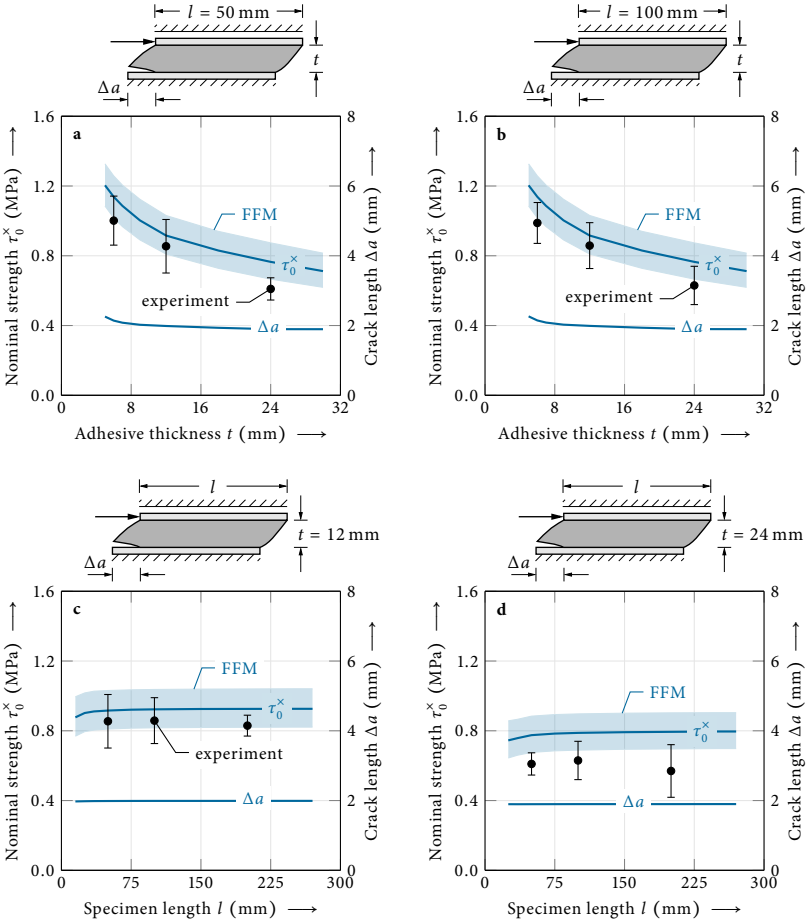

Fig. 6.2 Finite fracture mechanics (FFM) failure load predictions in comparison to DOWSIL™ 993 simple shear experiments. The influence of adhesive thickness is shown for overlap lengths **a** $l = 50$ mm and **b** $l = 100$ mm. The impact of overlap length is shown for adhesive thicknesses **c** $t = 12$ mm and **d** $t = 24$ mm. Experimental data are indicated as mean and standard deviation. Critical nominal failure loads $\tau_0^\times$ are computed using mean fracture properties and are given with shaded 95 % confidence intervals accounting for uncertainty of the fracture properties. Reported finite crack lengths Δa correspond to mean fracture property predictions.

Table 6.2
Mean nominal strength and standard deviation of DOWSIL™ 993 in pull-off and tubular shear tests.

	Pull-off test ($\sigma_0^{\times}$)	Tubular shear test ($\tau_0^{\times}$)
Nominal strength (MPa)	1.150 ± 0.055	1.393 ± 0.162
# of tested specimens	7	4

layers. However, in particular for nearly incompressible hyperelastic adhesives, a general recommendation for the application of thin adhesive layers cannot be given easily as constrained volume effects such as cavitation may occur (Aït Hocine et al., 2011). Panels c and d in Fig. 6.2 show the influence of the overlap length for adhesive thicknesses $t = 12\,\text{mm}$ and $t = 24\,\text{mm}$, respectively. As expected, there is no significant increase of effective joint strength with increasing overlap length l above a certain threshold. All investigated overlap lengths are as long or longer than this threshold. The model indicates threshold lengths of $l^* \approx 30\,\text{mm}$ for $t = 12\,\text{mm}$ and $l^* \approx 50\,\text{mm}$ for $t = 24\,\text{mm}$. As observed before, the effective joint strength of the thicker adhesive is smaller. Figure 6.2 also shows finite crack lengths Δa computed for mean fracture properties. Remarkably, finite crack lengths remain almost constant $\Delta a \approx 2\,\text{mm}$ in all geometrical configurations tested and analyzed. Panels a and b of Fig. 6.2 suggest they only become longer below a certain threshold adhesive thickness $t^* \leq 5\,\text{mm}$. While the strain distribution in adhesive layers is only affected moderately by their thickness, the energy release rate reduces significantly with decreasing thickness. Hence, thin adhesive layers can sustain higher loads and require longer finite cracks to release sufficient energy.

6.3.2 Pull-off and tubular shear tests

Additional structural situations and load cases are examined using 7 H-shaped specimens with adhesive thickness $t = 12\,\text{mm}$, length $l = 50\,\text{mm}$ and width $w = 12\,\text{mm}$ and 4 tubular lap joint specimens with two 3 mm notches, adhesive thickness $t = 8\,\text{mm}$, width $w = 16\,\text{mm}$ and inner diameter ∅140 mm. The results are listed in Table 6.2 and shown in Fig. 6.3. Experiments are shown with mean and standard deviation. Again, FFM predictions are computed using mean fracture properties and are given with shaded 95 % confidence intervals accounting for uncertainty of the fracture parameters. For the pull-off tests (Fig. 6.3a) FFM predictions are slightly conservative. However, as observed in Fig. 6.2, they agree with experimental standard deviations within their confidence intervals. FFM predictions of the circular shear test (Fig. 6.3b) are similar to the simple shear case. While for each test setup only one geometry of the adhesive joint is tested, FFM again predicts the adhesive thickness effect, which is expected to occur in the present test configurations, as well. In both Figs. 6.3a and b, remarkably constant finite crack lengths $\Delta a \approx 1.5\,\text{mm}$ and $\Delta a \approx 2.2\,\text{mm}$ computed with mean fracture properties

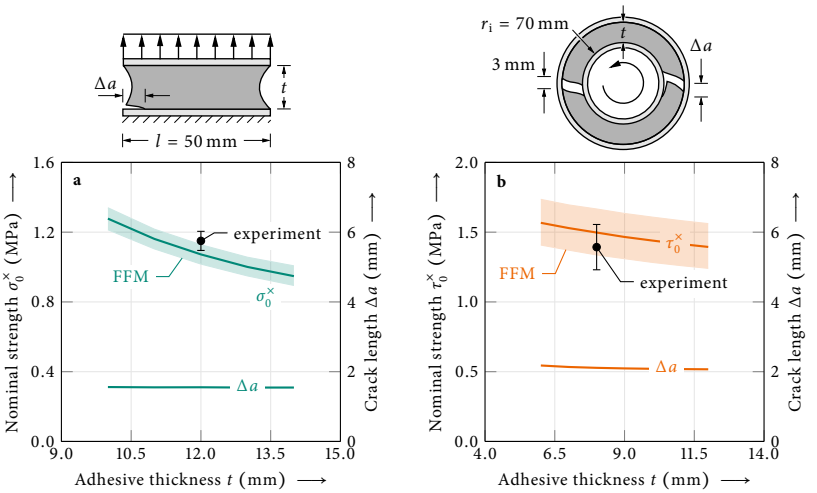

Fig. 6.3 Finite fracture mechanics (FFM) failure load predictions in comparison to **a** pull-off tests of H-shaped DOWSIL™ 993 specimens and **b** circular shear tests of DOWSIL™ 993 notched tubular lap joints. H-shaped specimens of length $l = 50$ mm and width $w = 12$ mm and tubular lap joints with two 3 mm notches as indicated in the pictogram, adhesive width $w = 16$ mm and inner diameter ∅140 mm are examined. Experimental data are shown as mean and standard deviation. FFM predictions are computed using mean fracture properties and shown with shaded 95 % confidence intervals accounting for uncertainty of the fracture properties. Computed finite crack lengths Δa are determined using mean fracture properties.

are observed. It may be assumed that tested and analyzed adhesive thickness are again well above a threshold adhesive thickness, below which the change in finite crack length Δa becomes pronounced.

6.3.3 Pancake test

Pancake tests are designed to cause cavitational failure in nearly incompressible materials in order to study cavitation. However, since cavitation is a phenomenon of elastic instability, it is not necessarily linked to ultimate failure. Indeed, surfaces of fractured DOWSIL™ TSSA specimens have smooth fracture planes and show no signs of bubble formation or coalescence. Instead, fracture appears to originate from the bi-material point where DOWSIL™ TSSA and substrate meet. Therefore, we use the strain energy density function (4.2) accounting for the elastic growth of cavities to simulate DOWSIL™ TSSA pancake tests. The tests are then evaluated using the combined dilatational–

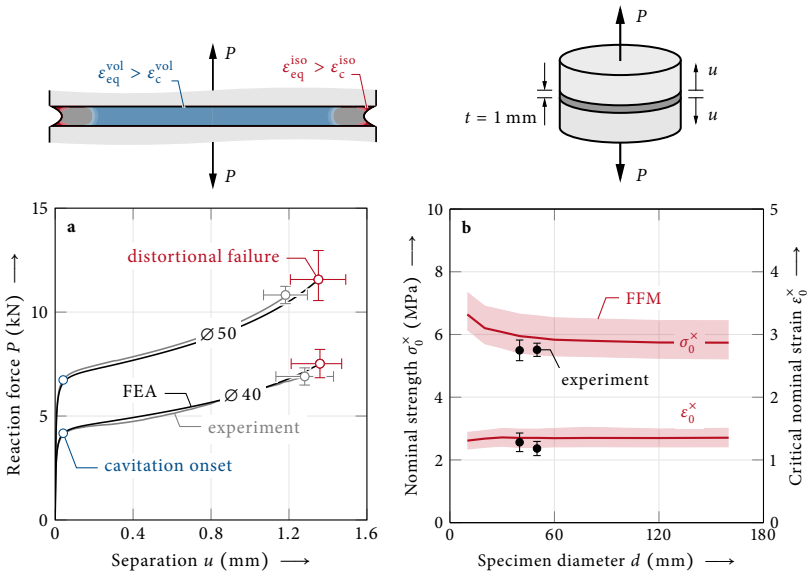

Fig. 6.4 Finite fracture mechanics (FFM) predictions for DOWSIL™ TSSA pancake experiments. **a** Load displacement response with failure modes. Cavitation (blue) occurs early in the specimen center, expands across the specimen with increasing loading, and causes stress softening and load redistribution towards the specimen perimeter. Ultimate failure occurs as crack nucleation owing to distortional deformation (red) from bi-material points. The pictogram illustrates dilatational and distortional overloading shortly before ultimate failure. **b** Influence of specimen diameter on ultimate nominal strength and strain. Experimental data are indicated as mean and standard deviation. Nominal failure loads $\sigma_0^\times$ and critical nominal strain $\varepsilon_0^\times$ are computed using mean fracture properties and are given with shaded 95 % confidence intervals accounting for uncertainty of the fracture properties.

distortional failure criterion (5.23) and we employ the coupled criterion (6.5) to model crack nucleation from the bi-material point. It turns out that, as for DOWSIL™ 993 samples discussed above, the vicinity of the bi-material notch is dominated by distortion. Hence, as for DOWSIL™ 993, the distortional strain criterion (6.4) can be used.

Ultimate nominal stresses and strains of 18 DOWSIL™ TSSA pancake specimens are reported in Table 6.3. The measurements are compared against model predictions of the force–displacement response and predictions of critical loads for crack nucleation from the bi-material point in Fig. 6.4. The material model (4.2) captures the load–displacement response accurately (Fig. 6.4a). Using the fracture parameters of DOWSIL™ TSSA reported in Section 5.4, cavitation onset is predicted at the experimentally observed onset of softening in the force–displacement response. As illustrated

Table 6.3
Mean nominal strength $\sigma_0^{\times}$ and critical nominal strain $\varepsilon_0^{\times}$ of $t = 1$ mm DOWSIL™ TSSA pancake specimens (number of samples in parentheses).

Diameter (mm)	Nominal strength (MPa)	Critical nominal strain (–)
∅40 (12)	5.494 ± 0.330	1.281 ± 0.148
∅50 (06)	5.512 ± 0.211	1.182 ± 0.113

in the pictogram, it first appears in the specimen center and then expands across the adhesive layer with increasing loading. Dilatational failure in the specimen center causes load redistribution towards the specimen perimeter and allows for a significant increase of the substrates' separation. Ultimate loading is associated with crack nucleation from the bi-material point and is predicted well by FFM. The pictogram sketches regions of overloaded material shortly before ultimate failure. The influence of the specimen diameter (Fig. 6.4b) is similar to the effect of overlap length in simple shear specimens (Fig. 6.2). An influence on the nominal ultimate strength $\sigma_0^{\times}$ is only observed for small samples. Above a threshold diameter of approximately ∅60 mm both nominal strength and critical nominal strain are constant, and the force load transferred by point fixtures can be controlled by the specimen diameter. Characterized in independent experiments, FFM model predictions agree with experiments within the given standard deviation intervals. An assessment of the impact of the adhesive thickness is not given because DOWSIL™ TSSA is supplied as sheets of 1 mm thickness and does not permit thicker joint designs.

As observed for experiments on DOWSIL™ 993, the length of initiated finite cracks is constant across all investigated pancake specimens (not shown). For DOWSIL™ TSSA it is approximately $\Delta a \approx 1$ mm. Predicting failure in volumetrically constraint samples like pancake specimens requires a material model that accounts for the growth of cavities and a failure model that captures crack nucleation originating from distortion dominated stress concentrations.

6.3.4 Discussion

A summary of all tested adhesive joint configurations is given in Fig. 6.5. It compares experimental data on the horizontal axis to FFM predictions on the vertical axis. Error bars on the horizontal axis indicate the experimental standard deviation. Error bars on the vertical axis represent predictions obtained using minimum and maximum fracture properties, respectively. Predictions of an ideal model would collapse onto the 1-to-1-line. Predictions by the present FFM failure model are concentrated closely around this diagonal. Considering significant scatter in both the experimental data and

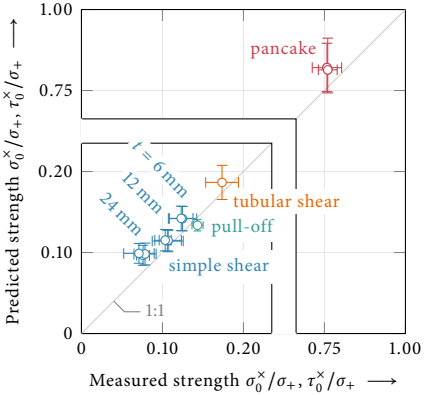

Fig. 6.5 Comparison of predicted and measured nominal strengths $(\sigma_0^\times, \tau_0^\times)$ of all examined adhesive joints normalized to their respective uniaxial tensile strength ($\sigma_+^{993} = 8.0\,\text{MPa}$, $\sigma_+^{\text{TSSA}} = 7.3\,\text{MPa}$). Error bars on the horizontal axis indicate the experimental standard deviation. Error bars on the vertical axis represent predictions from minimum and maximum fracture properties, respectively.

the fracture properties, the present model may be deemed accurate for the examined hyperelastic adhesive.

Instead of using line method (2.182) and averaging the equivalent strain function (6.4) on the potential crack surface, we may use point method (2.181) and require the material to be overloaded on the entire crack surface. In terms of strain this is expressed by

$$\varepsilon_{\text{eq}}\big(\boldsymbol{\varepsilon}(\boldsymbol{x})\big) \geq \varepsilon_{\text{c}} \;\forall\; \boldsymbol{x} \in \Gamma_{\text{c}}(\Delta A), \tag{6.8}$$

where ε_{eq} denotes the isochoric equivalent strain function Eq. (6.4). Accordingly, the coupled criterion reads

$$\varepsilon_{\text{eq}}\big(\boldsymbol{\varepsilon}(x)\big) \geq \varepsilon_{\text{c}} \;\forall\; x \in \Gamma_{\text{c}}(\Delta a) \quad \wedge \quad \overline{\mathcal{G}}(\Delta a) \geq \mathcal{G}_{\text{c}}. \tag{6.9}$$

Again, the critical displacement at failure $u_\times$ is obtained from the constrained optimization problem

$$\begin{aligned} u_\times = \min_{u,\Delta a} \{ u \mid u > 0, \exists\, \Delta a > 0 : \\ \varepsilon_{\text{eq}}\big(\boldsymbol{\varepsilon}(u,x)\big) \geq \varepsilon_{\text{c}} \;\forall\, x \in \Gamma_{\text{c}}(\Delta a) \;\wedge\; \overline{\mathcal{G}}(u,\Delta a) \geq \mathcal{G}_{\text{c}} \}. \end{aligned} \tag{6.10}$$

In both formulations of the coupled criterion – line (6.5) and point method (6.9) – the equivalent strain function ε_{eq} may be replaced by a simpler strength criterion. We could, for instance, use a maximum principal stress criterion (2.132) or a maximum principal

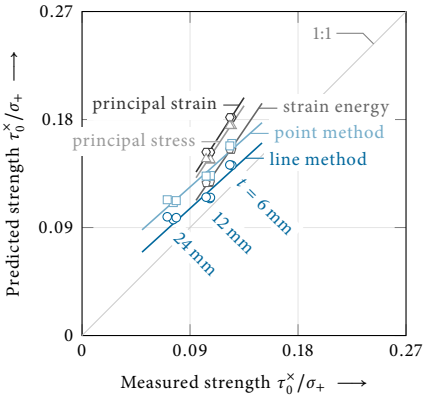

Fig. 6.6 Finite fracture mechanics predictions and corresponding linear regressions for DOWSIL™ 993 simple shear tests using different failure criteria: line method predictions using a maximum principal stress criterion (2.132) (principal stress), a maximum principal strain criterion (5.11) (principal strain), a strain energy density criterion (5.20) (strain energy), and the present isochoric strain energy density function (6.4) (line method), as well as point method predictions using the present isochoric strain energy density function (6.4) (point method).

strain criterion (5.11). Using the example of simple shear tests of H-shaped DOWSIL™ 993 specimens, Fig. 6.6 compares failure predictions using different failure criteria. The figure shows mean predicted nominal shear strengths plotted against mean measured nominal strengths and includes corresponding linear regression functions. The best results are obtained using line method (6.3) and the isochoric equivalent strain function (6.4) proposed in Section 5.3. Although failure loads are slightly overestimated, the model yields consistent results for all specimen dimensions as the regression function is parallel to the one-to-one line. Using the present strain criterion (6.4) with point method yields higher failure loads and, hence, less accurate predictions. However, again, the model results are consistent. Using simpler failure criteria such as maximum principal stress, maximum principal strain or critical strain energy density criteria (with line method), yields even higher failure loads and inconsistent predictions. The corresponding linear regression functions are not parallel to the one-to-one line anymore and no failure load predictions for samples of $t = 24$ mm adhesive thickness can be given. This is because such criteria are too primitive to capture the complex multiaxial bulk failure behavior of DOWSIL™ 993.

While the triangular isochoric failure surface of DOWSIL™ TSSA may be described by a maximum principal strain criterion, the criterion is certainly inaccurate for DOWSIL™ 993. This highlights a particular advantage of the equivalent strain function proposed in

the present work. Identifying a suitable multiaxial bulk failure criterion for a particular material is not necessary. Instead, only the shape parameters β and γ, and the threshold ε_c must be characterized from an adequate set of multiaxial experiments to provide a strain criterion for a crack nucleation model. A possible reason for the general overestimation of failure loads is the simple energy criterion. Since no mode II fracture toughness data are available for the materials of the present, no mixed-mode energy criterion can be used within the coupled criterion.

6.4 Crack nucleation, crack growth and crack arrest

In the present displacement-controlled simple shear test setup of DOWSIL™ 993 H-shaped specimens, characteristic load–displacement curves (center columns of Figs. 6.9 and 6.10) are observed consistently. Initial crack formation is not associated with ultimate failure but to a reduction and subsequent increase of the transferred load with increasing applied displacement. In order to investigate this phenomenon, we prepared video recordings of 12 simple shear specimens of length $l = 100\,\mathrm{mm}$. The recordings show that the phenomenon can be attributed to a nonmonotonic energy release rate, crack growth and crack arrest.

Nonmonotonic energy release rates are not unique to adhesive joints (Moradi et al., 2013; Hell et al., 2014) but are found in many technical applications, often in the presence of strong elastic contrasts. Several authors study this behavior in composite laminates: Wang and Crossman (1980) report it for free-edge delamination, Krueger (2004) for the delamination of reinforcement patches and Martin et al. (2008) for the debonding of fiber and matrix. Müller et al. (2006) find nonmonotonic energy release rates for the debonding of fuel cell stacks, García et al. (2015) for particle debonding in composite materials and Doitrand et al. (2019) for rhombus hole specimens under quasi-static compression. Different characteristics of nonmontonic energy release rates in different structural situations are discussed by Weißgraeber et al. (2016a). Sapora and Cornetti (2018) show that cracks originating from open-holes under biaxial compression may exhibit any of the characteristics discussed by Weißgraeber et al. (2016a) depending on the biaxiality of the loading.

In the present case, the nonmonotonic behavior of the energy release rate is caused by the individual contributions of different crack opening modes to the total energy release rate. In order to separate the total energy release rate into contributions from crack opening and crack sliding modes, we model crack nucleation by the quasi-static reduction and finally removal of tractions that hold crack faces closed. Let us denote the work per unit crack surface done by tractions perpendicular to crack faces during crack opening as $\overline{\mathcal{G}}_{\mathrm{I}}$ and the work per unit crack surface of tangential tractions as $\overline{\mathcal{G}}_{\mathrm{II}}$. This allows for

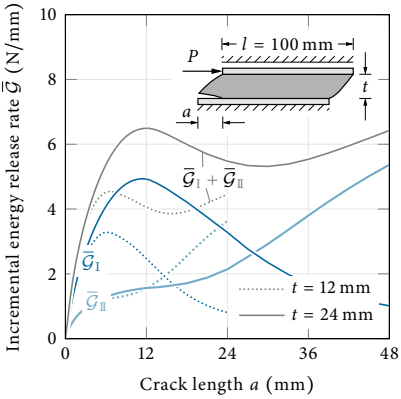

Fig. 6.7 Separation of crack opening mode I and crack sliding mode II contributions to the total incremental energy release rate $\overline{\mathcal{G}} = \overline{\mathcal{G}}_{\mathrm{I}} + \overline{\mathcal{G}}_{\mathrm{II}}$ at initial failure load P = 846 N for DOWSIL™ 993 simple shear specimens of adhesive thickness t = 12 mm and P = 1042 N for adhesive thickness t = 24 mm.

splitting the total incremental energy release rate $\overline{\mathcal{G}} = \overline{\mathcal{G}}_{\mathrm{I}} + \overline{\mathcal{G}}_{\mathrm{II}}$ into mode I and mode II contributions. In contrast to its linear formulation (2.172), the present nonlinear crack opening integral (2.171) requires actual integration of nonlinear tractions over crack face displacements during crack opening. As proposed by Talmon l'Armée et al. (2017), we employ local nodal coordinate systems to compute crack normal and tangential tractions and displacements during crack opening.

The mode separation (Fig. 6.7) reveals that the nonmonotonic behavior of the total energy release rate is caused by crack opening mode I. $\overline{\mathcal{G}}_{\mathrm{II}}$ increases monotonically with crack length while $\overline{\mathcal{G}}_{\mathrm{I}}$ has a distinct maximum at comparatively short crack lengths followed by a reduction to almost zero as the crack length increases. This maximum dominates short cracks and causes the nonmonotonic behavior of the total energy release rate. Hell et al. (2014) reported a similar behavior of linear elastic adhesive joints. Despite the comparison of different load levels in Fig. 6.7, it shall be emphasized that the energy release rate increases with increasing adhesive thickness.

When nonmonotonic energy release rates are present, different scenarios for crack nucleation and for the stability of initiated cracks are possible (Fig. 6.8). Crack nucleation is governed by the incremental energy release rate $\overline{\mathcal{G}}$. Whether subsequent crack propagation is stable or unstable depends on the differential energy release rate $\mathcal{G}$. The latter can be expressed through the former using Eq. (2.180). Equation (2.180) implies that $\mathcal{G}$ is always larger than $\overline{\mathcal{G}}$ where $\overline{\mathcal{G}}$ increases ($\partial\overline{\mathcal{G}}(\Delta a)/\partial\Delta a > 0$), and smaller where $\overline{\mathcal{G}}$ decreases ($\partial\overline{\mathcal{G}}(\Delta a)/\partial\Delta a < 0$). Both energy release rates coincide in local maxima

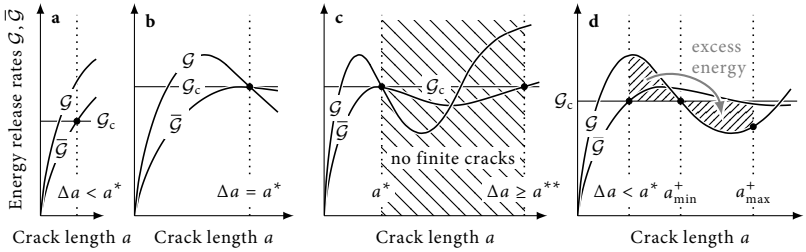

Fig. 6.8 Crack nucleation scenarios for nonmonotonic energy release rates. **a** Finite cracks Δa shorter than a^* are unstable after initiation. **b** Finite cracks $\Delta a = a^*$ are stable and will grow upon further load increase. **c** Given a monotonically decreasing stress or strain criterion, finite fracture mechanics permits only finite cracks shorter than a^* or longer than a^{**}. Finite cracks $\Delta a \geq a^{**}$ are again unstable after initiation. **d** Nucleating cracks $\Delta a < a^*$ are unstable and will grow to a^+_{min}. Because $\mathcal{G} > \mathcal{G}_c$ during crack propagation, excess energy may be available for further crack growth up to a^+_{max}.

or minima of $\overline{\mathcal{G}}$ where $\partial\overline{\mathcal{G}}(\Delta a)/\partial\Delta a = 0$. Let us denote the crack length of the first local maximum of $\overline{\mathcal{G}}$ as a^* (Fig. 6.8c). The crack length at which $\overline{\mathcal{G}}$ subsequently reaches the level of the local maximum again is denoted a^{**}. Initiating finite cracks Δa shorter than a^* (Fig. 6.8a) are initially unstable and grow without further load increase because the differential energy release rate $\mathcal{G}$ exceeds its incremental counterpart $\overline{\mathcal{G}}$ and thus $\mathcal{G}_c$. Finite cracks $\Delta a = a^*$ (Fig. 6.8b) are stable. Here, the incremental and differential energy release rates coincide, yet the gradient of the latter is negative. The initial crack can only grow upon further load increase. Provided stresses or strains decrease monotonically, the coupled criterion (6.5) does not permit finite crack nucleation between a^* and a^{**} (Fig. 6.8c). For any crack $a^* < \Delta a < a^{**}$ we could find a smaller load satisfying the energy criterion (6.1) at $\Delta a = a^*$. Comparing their predictions to experimental data, Hell et al. (2014) observe this jump in finite crack length from a^* to a^{**} with increasing adhesive thickness of linear elastic single-lap joints. Finite cracks longer than a^{**} are again unstable and will propagate without further load increase because they are associated with a differential energy release rate $\mathcal{G}$ that exceeds the fracture toughness $\mathcal{G}_c$.

Given that the local minimum of $\mathcal{G}$ between a^* and a^{**} is smaller than $\mathcal{G}_c$ (Fig. 6.8d), we observe a special situation for initially unstable cracks $\Delta a < a^*$. As they grow, they may reach a length a^+_{min} at which the differential energy release rate $\mathcal{G}$ equals the fracture toughness $\mathcal{G}_c$. During crack propagation from Δa to a^+_{min} more energy than required for crack growth is available ($\mathcal{G} > \mathcal{G}_c$). Depending on the fracture dynamics and the specific structural situation, this excess energy can potentially be available for crack growth beyond a^+_{min} up to a^+_{max}. This is also theorized by Leguillon and Martin (2013a,b) and Doitrand et al. (2019) but experimental evidence is scarce.

Because Hell et al. (2014) observe finite cracks longer than a^{**} only for thin adhesive layers ($t < 0.8\,\mathrm{mm}$), we expect finite cracks $\Delta a \leq a^{*}$ in the present case. Thus, crack initiation and potentially subsequent unstable crack growth are expected to cause a load drop in the present displacement-controlled test setup. The magnitude of the drop depends on the local minimum of the differential energy release rate $\mathcal{G}$ between a^{*} and a^{**}. If it is larger than the fracture toughness $\mathcal{G}_{\mathrm{c}}$, immediate ultimate failure is to be expected. If it is smaller, the initial finite crack may arrest and only a finite drop in loading can be anticipated. Then, this initial load drop would be followed by stable crack growth associated with some load increase prior to ultimate failure. Figures 6.9 and 6.10 show characteristic load–displacement curves for specimens of $t = 24\,\mathrm{mm}$ and $t = 12\,\mathrm{mm}$ adhesive thickness, respectively. Indeed, after an initial load drop (I–II) we observe load increase (II–III) with increasing displacement and finally ultimate failure (IV) as hypothesized above. The local minimum of $\mathcal{G}$ is smaller than $\mathcal{G}_{\mathrm{c}}$ and stable crack growth is observed (right columns of Figs. 6.9 and 6.10). Video recordings (snapshots in left columns of Figs. 6.9 and 6.10) show the sudden formation of a crack from the singular bi-material point at initial failure (I). Soon the crack arrests and stable growth with increasing displacement is observed (II–III), again followed by unstable propagation and the formation of a second crack from the second bi-material singularity (IV).

Figure 6.9 illustrates the successive failure of specimens of adhesive thickness $t = 24\,\mathrm{mm}$. Snapshots and the load–displacement curve of one particular specimen shown in the left and center columns, respectively, are representative for 4 out of 5 recorded specimens of this adhesive thickness. Differential (solid lines) and incremental (dashed lines) energy release rates shown in the right column are normalized to $\mathcal{G}_{\mathrm{c}} = 3.71\,\mathrm{N/mm}$ such that the initial failure load $P = 846\,\mathrm{N}$ (Fig. 6.9a) of this particular specimen is recovered by FFM and experimental scatter is accounted for. Crack nucleation is governed by finite fracture mechanics. At the initial failure load, the FFM energy criterion is satisfied identically ($\overline{\mathcal{G}}/\mathcal{G}_{\mathrm{c}} = 1$ at $a = \Delta a$) and associated with a finite crack length of $\Delta a \approx 3\,\mathrm{mm}$ (Fig. 6.9b). Once a crack is present, the Griffith criterion (2.153) is applicable. At $a = \Delta a$ the differential energy release rate exceeds the fracture toughness, $\mathcal{G} > \mathcal{G}_{\mathrm{c}}$, and the finite crack Δa is unstable while $\mathcal{G}/\mathcal{G}_{\mathrm{c}} > 1$. As discussed above, $\mathcal{G}$ does not increase monotonically but has a distinct local maximum and a local minimum. Depending on the load level, it may intersect with $\mathcal{G}_{\mathrm{c}}$ for $a > \Delta a$. In the present displacement-controlled test, crack growth is associated with load reduction. Hence, crack propagation is limited by $\mathcal{G}/\mathcal{G}_{\mathrm{c}} = 1$ for a loading of $P = 761\,\mathrm{N}$ at point II in the load displacement curve (Fig. 6.9c). According to Fig. 6.9d, this corresponds to a crack length of $a^{+} \approx 16\,\mathrm{mm}$, which agrees well with the experimental observation in frame II at which the initial unstable crack propagation stops. In point II we now find a negative gradient of the differential energy release rate, $\partial\mathcal{G}/\partial a < 0$ at $\mathcal{G}/\mathcal{G}_{\mathrm{c}}$. This allows for the experimentally observed stable crack growth from frame II to frame III with increasing applied displacement accompanied by increased loading (Fig. 6.9e). At a load

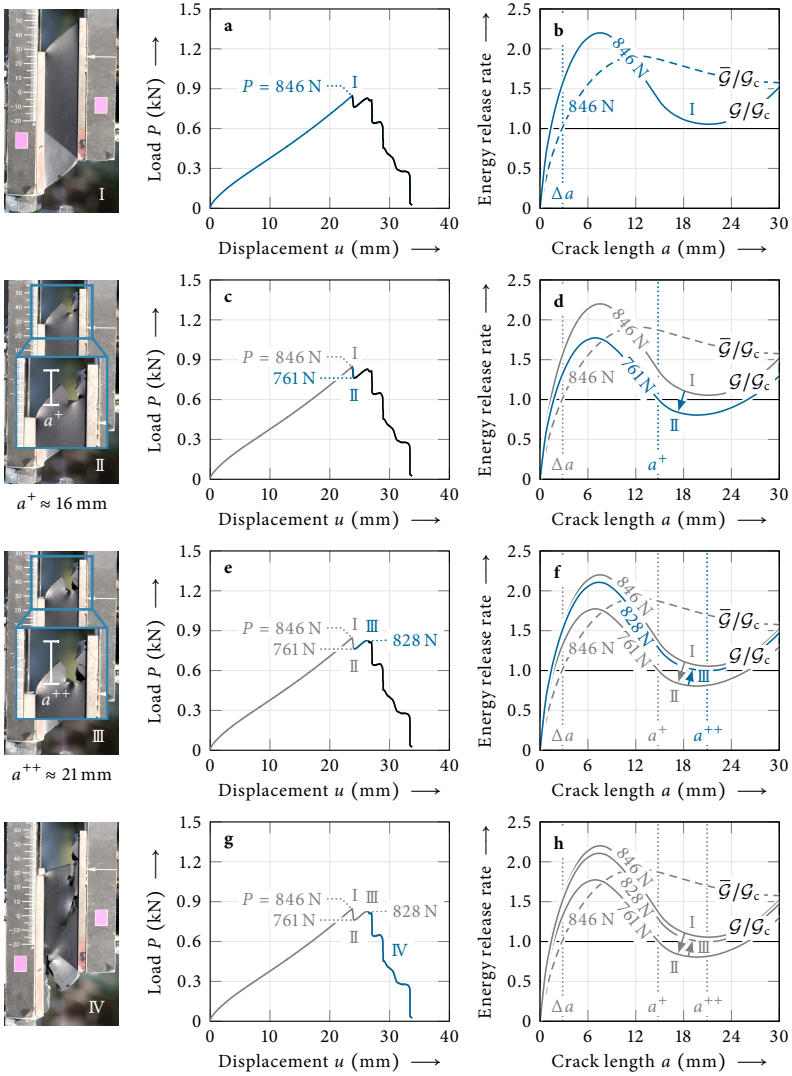

Fig. 6.9 Successive failure of $t = 24$ mm DOWSIL™ 993 simple shear samples: characteristic experimental snapshots (left column) with corresponding load–displacement curves (middle column) and energy release rates (right column). Normalized differential and incremental energy release rates $\mathcal{G}/\mathcal{G}_c$ (solid) and $\overline{\mathcal{G}}/\mathcal{G}_c$ (dashed), respectively, are shown with $\mathcal{G}_c = 3.71\,\mathrm{N/mm}$ accounting for experimental scatter.

of $P = 828\,\mathrm{N}$ at point Ⅲ, ultimate failure and unstable crack growth is observed because, here, $\mathcal{G}/\mathcal{G}_c = 1$ corresponds to the local minimum of the curve and the gradient $\partial\mathcal{G}/\partial a$ becomes positive again. In Fig. 6.9f the local minimum is found at $a^{++} \approx 21\,\mathrm{mm}$ for $P = 828\,\mathrm{N}$. This is in good agreement with the measured crack length prior to ultimate crack propagation in frame Ⅲ. The considerable load increase after initial and prior to ultimate failure is possible because of the nonmonotonic characteristics of the energy release rate in shear-loaded hyperelastic adhesive joints.

Specimens of $t = 24\,\mathrm{mm}$ adhesive thickness exhibit a significant reduction in transferred loading at initial failure but almost recover the initial load level prior to ultimate failure. Thinner specimens with thickness $t = 12\,\mathrm{mm}$ (Fig. 6.10) show only a small initial load drop (Ⅰ–Ⅱ) and are capable of transferring loads that exceed the initial failure load after crack nucleation (Ⅲ). The behavior originates from slightly different energy release rate characteristics. Snapshots and load–displacement curves shown in Fig. 6.10 are representative for 3 out of 4 recorded specimens of adhesive thickness $t = 12\,\mathrm{mm}$. With a fracture toughness of $\mathcal{G}_c = 4.46\,\mathrm{N/mm}$, crack initiation corresponds to $P = 1042\,\mathrm{N}$ and a finite crack length $\Delta a \approx 3\,\mathrm{mm}$ at $\overline{\mathcal{G}}/\mathcal{G}_c = 1$ (Fig. 6.10a and b). Again, the initial crack is unstable while $\mathcal{G}/\mathcal{G}_c > 1$ (Ⅰ–Ⅱ). According to the calculated energy release rates, crack growth stops at $P = 1018\,\mathrm{N}$ and $a^{+} \approx 7.5\,\mathrm{mm}$ because $\mathcal{G}/\mathcal{G}_c = 1$ (Fig. 6.10c and d). This corresponds well to the experimentally observed crack length $a^{+} \approx 8\,\mathrm{mm}$. Owing to the negative gradient $\partial\mathcal{G}/\partial a < 0$, the crack is stable with increasing applied displacement from frame Ⅱ to Ⅲ. At the ultimate load, $P = 1210\,\mathrm{N}$, $\mathcal{G}/\mathcal{G}_c$ corresponds to a local minimum followed by unstable crack propagation (Fig. 6.10e and f). In Fig. 6.10f this local minimum is found at $a^{++} \approx 13.5\,\mathrm{mm}$, which agrees well with the experimental observation of $a^{++} \approx 14\,\mathrm{mm}$. The ultimate load of thin $t = 12\,\mathrm{mm}$ adhesive joints exceeds the initial failure load because their energy release rate after initial failure is significantly smaller than the one of $t = 24\,\mathrm{mm}$ joints despite larger transferred loads. This causes unstable crack propagation to stop at shorter lengths a^{+}. Following unstable propagation, a longer relative increase of the crack length, $(a^{++} - a^{+})/a^{+}$, and larger additional loading is required for the local minimum to coincide with $\mathcal{G}/\mathcal{G}_c = 1$.

The remaining one specimen of adhesive thickness $t = 24\,\mathrm{mm}$ and one specimen of thickness $t = 12\,\mathrm{mm}$ showed the respective other load–displacement characteristics. That is, 1 out of 5 specimens with $t = 24\,\mathrm{mm}$ behaved as shown in Fig. 6.10 and 1 out of 4 specimens with $t = 12\,\mathrm{mm}$ showed a force-displacement curve as depicted in Fig. 6.9. However, the observed crack lengths agree with the patterns discussed above. The thinnest specimens of adhesive thickness $t = 6\,\mathrm{mm}$ did not allow for an analysis as above. Crack initiation could only be hardly identified from the recordings. For all three specimens, initial failure seemed accompanied by the formation of multiple defects along the entire length of the adhesive.

Our experiments consistently show crack arrest at a^{+}_{min} (cf. Fig. 6.8). Excess energy

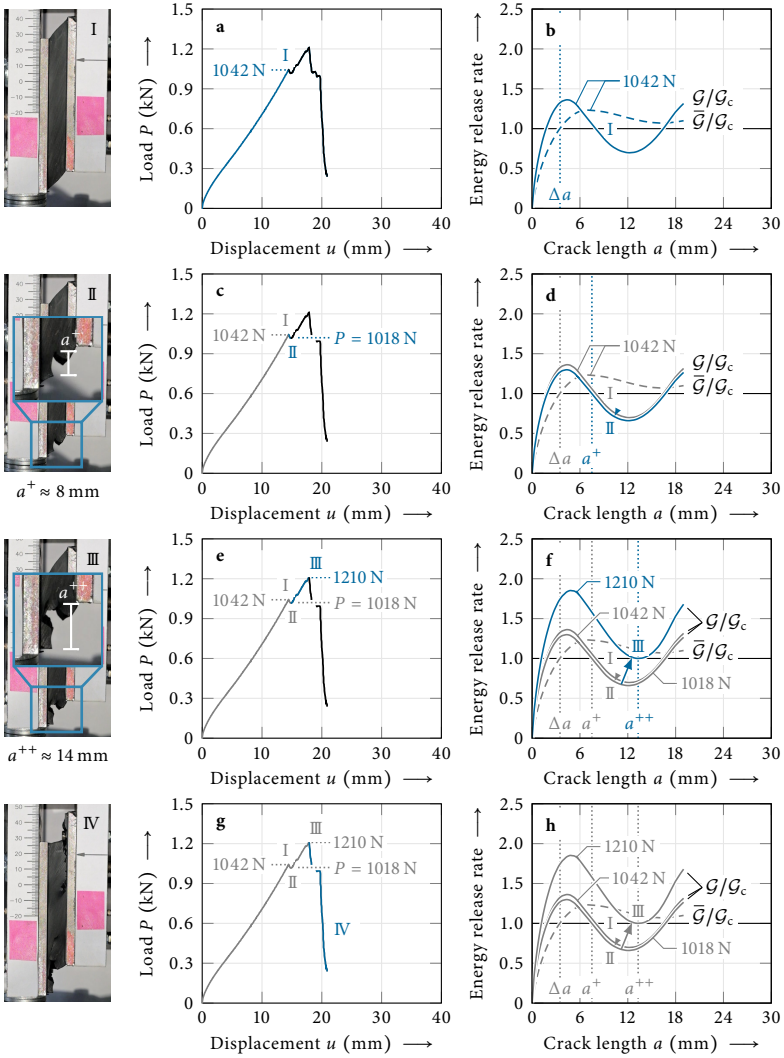

Fig. 6.10 Failure of t = 12 mm DOWSIL™ 993 simple shear samples: characteristic experimental snapshots (left column) with corresponding load–displacement curves (middle column) and energy release rates (right column). Normalized differential and incremental energy release rates $\mathcal{G}/\mathcal{G}_c$ (solid) and $\overline{\mathcal{G}}/\mathcal{G}_c$ (dashed), respectively, are shown with $\mathcal{G}_c$ = 4.46 N/mm accounting for experimental scatter.

does not seem become available for crack growth beyond this crack length. It can be assumed that internal damping dissipates excess energy and does not allow strain waves to propagate through the material.

6.5 Derivation of a simple design tool

Finite fracture mechanics provides a simple model that intuitively reveals the physics of the fracture process: the impact of involved fundamental material properties – strength or strain hypothesis and fracture toughness – is evident and the presence of a length scale is recognized. The model constitutes a comprehensive tool for the design of efficient and safe components. Yet, in practice, fracture mechanical approaches are unpopular because they require knowledge of the energy release rate. Computing energy release rates using conventional finite element analyses involves solving several different boundary values problems – one for each considered crack length – which necessitates a certain computational framework.

The present analysis shows that for practical applications of hyperelastic adhesive joints the design methodology can be simplified considerably. Adhesive thicknesses considered in the present study correspond to typical applications of DOWSIL™ 993 and DOWSIL™ TSSA. At these thicknesses the length scale involved in the fracture process remains almost constant across changes of specimen dimensions but also across different joint designs. With a known constant length scale, the coupled criterion (6.5) can be reduced to a pure evaluation of the averaged mixed-mode equivalent strain function (6.3) at a critical distance a_c. The simplified criterion reads

$$\bar{\varepsilon}_{eq}(a_c) = \frac{1}{a_c}\int_0^{a_c} \rho_\varepsilon(r)\cos\left(\beta\frac{\pi}{3} - \frac{1}{3}\arccos\left[\sin\left(\gamma\frac{\pi}{2}\right)\cos\left(3\theta_\varepsilon(r)\right)\right]\right)\mathrm{d}r = \varepsilon_c, \quad (6.11)$$

where r is the distance from the stress concentration, β and γ are shape parameters, ε_c is the isochoric threshold, and ρ_ε and θ_ε are cylindrical Haigh–Westergaard coordinates of the strain deviatoric plane (2.129). Parameters β, γ and ε_c identified for DOWSIL™ 993 and DOWSIL™ TSSA are given in Table 5.4. The design effort simplifies to the evaluation of one boundary value problem using one sufficiently fine FEA. The approach is known as theory of critical distances (Taylor et al., 2004; Taylor, 2007, 2008). Equation (6.11) can be readily implemented in existing finite element codes (Listing 5.1). Finite crack lengths predicted by FFM in the present analysis are found between approximately 1.5 mm and 2.0 mm for DOWSIL™ 993 and around 1.0 mm for DOWSIL™ TSSA. As strains increase towards the bi-material corner, using a critical distance of a_c = 1.0 mm for DOWSIL™ 993 and 0.5 mm for DOWSIL™ TSSA in Eq. (6.11) will provide conservative predictions of the effective strength of adhesive joints. Figure 6.11 re-evaluates all joint

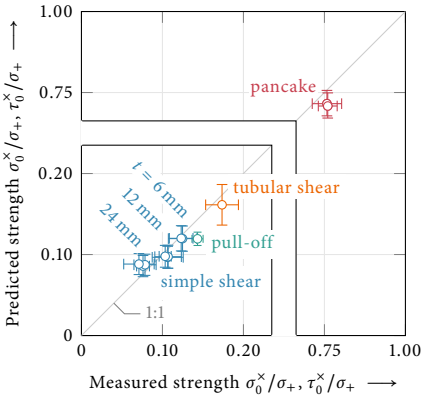

Fig. 6.11 Comparison of predicted and measured nominal strengths ($\sigma_0^{\times}$, $\tau_0^{\times}$) obtained using a critical distance of a_c = 1.0 mm for DOWSIL™ 993 and a_c = 0.5 mm for DOWSIL™ TSSA in Eq. (6.11) normalized to the respective uniaxial tensile strength (σ_+^{993} = 8.0 MPa, σ_+^{TSSA} = 7.3 MPa). Error bars on the horizontal axis indicate the experimental standard deviation. Error bars on the vertical axis correspond to predictions using minimum and maximum fracture properties, respectively.

configurations tested within the present work using Eq. (6.11). The simplified approach provides accurate yet conservative predictions. Note that the critical distance a_c required for the simplified approach may also be determined experimentally from a best fit of Eq. (6.11) to test results.

Chapter 7

Hyperelastic weak interface model

Adhesive joints have similar geometric characteristics and dimensions in many technical applications. Often, flat thin-walled substrates are bonded by thin adhesive layers across comparatively large surfaces. This particular geometry allows for treating the adhesive layer as an interface and, hence, as a simplified continuum. Owing to its compliance, the adhesive constitutes a weak interface allowing for the discontinuity of displacements across the interface. The displacement jump is linked to the traction vector through the interface's constitutive law. The connection can be interpreted as a continuous distribution of nonlinear elastic springs.

While thick-layered applications of DOWSIL™ 993 may often deviate from this rule of thin bonds, DOWSIL™ TSSA is supplied in sheets of 1 mm thickness and, hence, applied as thin layers. Despite today's easy access to commercial finite element software, simple predictive models for stress distributions in adhesive joints are essential in the design process of adhesively bonded structures. In particular, in early design stages or optimization tasks, they can provide substantial savings in time and cost.

The following sections make use of the recurring geometric properties of adhesive joints to develop an efficient predictive stress analysis and failure model for thin hyperelastic adhesive joints. The model is applicable to various joint designs with shear-flexible laminate or isotropic adherends. Adhesives can be described by arbitrary hyperelastic strain energy density functions. The system of governing differential equations is derived analytically using a general sandwich-type model of the overlap domain. Solutions for adhesive shear and peel stresses and strains are obtained solving the system numerically. Stress distributions obtained from the model agree well with detailed finite element analyses.

In order to predict effective joint strengths, a finite fracture mechanics failure model is applied. Using the semi-analytical stress and strain solutions, an iterative solver for the coupled stress and energy criterion of finite fracture mechanics is implemented. A validation of the model against FEA-based finite fracture mechanics evaluations shows that geometric effects are rendered correctly and suggests that the present model

provides reliable failure load predictions. The main results discussed in this chapter are published in peer-reviewed journals and conference proceedings (Rosendahl et al., 2017b,c, 2020).

7.1 State of the art

Owing to the characteristic geometric properties of adhesive joints, classical models such as the single-lap models by Volkersen (1938) or Goland and Reissner (1944), regard the adhesive as smeared linear elastic springs. This assumption served as the basis for many subsequent analyses. While Volkersen (1938) considers shear stresses only, Goland and Reissner (1944) incorporate adherend bending and corresponding peel stresses. Both model adherends as linear elastic beams. Many refinements of the original single-lap models were proposed in the second half of the past century. Hart-Smith (1981) additionally models the unsupported part of the adherends using large bending beam theory. The works of Renton and Vinson (1975) and Tsai et al. (1998) extend the consideration to laminated adherends. Ojalvo and Eidinoff (1978) analyze the effect of the adhesive's thickness. The models of Yang and Pang (1996) and Tsai et al. (1998) consider shear deformations of the adherends and Frostig et al. (1999) present a higher-order theory for single-lap joints with fillets.

An important generalization regarding joint shapes was proposed by Bigwood and Crocombe (1989). Instead of considering a specific joint design, they suggest the analysis of the bonded region only. Applying general loading conditions at the ends of the adherend–adhesive sandwich-type element, allows for the analysis of almost arbitrary joint configurations. Recently, Weißgraeber et al. (2014) and Liu et al. (2014) extended the general sandwich-type approach adding more comprehensive adhesive kinematics and allowing for laminated adherends. Numerous authors are concerned with models for mixed adhesives (das Neves et al., 2009) and functionally graded adhesives (Kumar, 2009; Kumar and Scanlan, 2010; Stein et al., 2016a), also taking advantage of the general sandwich-type formulation (Stein et al., 2016c, 2017a,b). A comprehensive overview of the vast number of linear elastic models is given by da Silva et al. (2009).

The denomination *sandwich* originates from the three-layered adherend–adhesive–adherend geometry. Several authors coined the specific term *anti-sandwich* to distinguish classical sandwich structures with thin skin layers and a thick core layer from the present situation of comparatively thick skin layers and a thin core layer (Altenbach et al., 2015; Aßmus, 2019; Aßmus et al., 2019; Javanbakht et al., 2019). The latter does not only apply to adhesive bonds but also to, e.g., photovoltaic panels (Naumenko and Eremeyev, 2014; Aßmus et al., 2016, 2017). However, the present work omits a strict discrimination between classical sandwich and anti-sandwich.

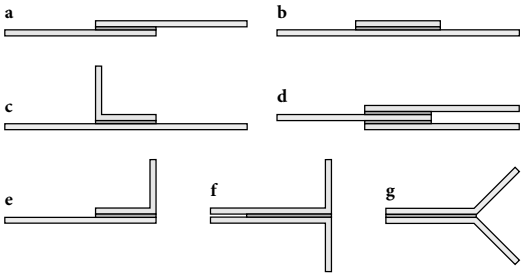

Fig. 7.1 Examples of joint designs covered by the present model: **a** single-lap joint, **b** reinforcement patch, **c** T-joint, **d** double-lap joint, **e** L-joint, **f** peel joint, **g** inclined peel joint.

Despite the vast number of linear elastic analyses, only few predictive models for joints with nonlinear adhesives are available. Most nonlinear analyses can be classified as either elastic–perfectly plastic or deformation theory of plasticity models. The former treat elastic and plastic regions individually and impose continuity conditions in-between (Hart-Smith, 1973a,b,c; Yang et al., 2004; Mardani et al., 2020). Elastic–perfectly plastic approaches commonly consider plasticity of shear stresses only. Peel stresses are assumed to behave linearly. In deformation theory of plasticity, the secant modulus of the stress-strain curve is used to relate total stresses to total strains in both elastic and plastic domains (Bigwood and Crocombe, 1990; Crocombe and Bigwood, 1992; Mortensen and Thomsen, 1997, 2002; Stein et al., 2018). An equivalent stress criterion determines the onset of yielding. Hence, plasticity of both shear and peel stresses is considered.

Analyses of hyperelastic adhesive joints were mostly restricted to finite element analyses (Duncan and Dean, 2003; Loureiro et al., 2010; Lubowiecka et al., 2012; Dias et al., 2014). To our knowledge, the only semi-analytical model for hyperelastic adhesive joints is given by Cabello et al. (2016). The model covers double cantilever beam tests only. It allows for accurate predictions of adherend deformations. However, neither stress distributions nor failure loads are addressed.

In this chapter we propose a general sandwich-type model for adhesive joints similar to the early work of Bigwood and Crocombe (1989) and the recent model by Weißgraeber et al. (2014). It presents an extension regarding the treatment of hyperelastic adhesives.

7.2 Sandwich-type model for nonlinear elastic adhesives

In sandwich-type models, the joint analysis is restricted to the domain where the overlapping adherends are bonded by the adhesive forging a three-layer laminate. General

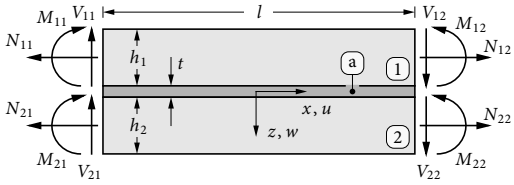

Fig. 7.2 Sandwich-type model of the joint overlap domain under general loading.

section force boundary conditions at the domain boundaries allow for the representation of arbitrary joint configurations such as single-lap joints (SLJ), double-lap joints (DLJ), L-joints, T-joints, peel joints or reinforcement patches (Fig. 7.1). The corresponding section forces and moments at the overlap ends can be computed from linear statics or other suitable methods. For single-lap joints, for instance, a number of authors proposed bending moment factors accounting for off-centered axial loading (Goland and Reissner, 1944; Zhao et al., 2010; Talmon l'Armée et al., 2016).

The following assumptions common for linear elastic sandwich-type models are made for the present nonlinear analysis: i) adhesive shear and peel stresses are constant through the adhesive thickness. This simplified continuum assumption is permissible for sufficiently thin adhesive layers, which will be discussed later. ii) Horizontal normal stresses are neglected owing to a treatment of the adhesive as an interface. iii) Plane strain analysis is applicable. Concerning nonlinearity, iv) nearly incompressible hyperelastic material behavior of the adhesive is presumed and v) joint failure is assumed brittle. These simplifications allow for an efficient analysis of the stress responses of general nonlinear elastic adhesive joints.

Field equations. Consider the model of the joint overlap domain depicted in Fig. 7.2. The overlap is of length l and out-of-plane width b. The adhesive and adherend thicknesses are denoted t, h_1 and h_2, respectively. Here, as well as in the following, the subscripts 1 and 2 correspond to upper and lower adherend. A Cartesian x, z coordinate system with the corresponding displacements u and w is introduced at the center of the adhesive.

The equilibrium equations are deduced from a free body cut of length dx of upper adherend and adhesive (Fig. 7.3). Denoting derivatives with respect to x by $\square'$, they read

$$0 = N_{1x}' + \tau_{xz}, \tag{7.1a}$$

$$0 = V_{1x}' + \sigma_{zz}, \tag{7.1b}$$

$$0 = M_{1x}' - V_{1x} + \frac{h_1 + t}{2}\,\tau_{xz}, \tag{7.1c}$$

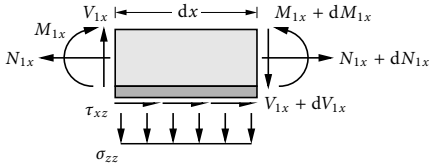

Fig. 7.3 Free body cut of an infinitesimal upper adherend–adhesive element.

where N_{1x}, V_{1x} and M_{1x} are the section forces and moments in the upper adherend at the horizontal position x. Peel and shear stresses in the adhesive are denoted σ_{zz} and τ_{xz}, respectively. Rather than using an equivalent free body cut of the lower adherend, expressions for section forces and moments in the lower adherend are obtained from a vertical free body cut through the entire sandwich (Fig. 7.4), i.e.,

$$N_{2x} = N_{11} + N_{21} - N_{1x}, \tag{7.2a}$$

$$V_{2x} = V_{11} + V_{21} - V_{1x}, \tag{7.2b}$$

$$\begin{aligned} M_{2x} &= M_{11} + M_{21} - M_{1x} \\ &\quad + (V_{11} + V_{21})\left(x + \frac{l}{2}\right) + (N_{1x} - N_{11})\left(t + \frac{h_1 + h_2}{2}\right), \end{aligned} \tag{7.2c}$$

where N_{11}, N_{21}, V_{11}, V_{21}, M_{11} and M_{21} are the section forces and moments at the left end of the overlap region, given as boundary values. The obtained direct relations of upper and lower adherend section forces and moments allow for their elimination in the derivation of the system of differential equations.

The adherend kinematics is formulated using first-order shear deformation theory (FSDT) allowing for the consideration of adherends with low transverse stiffnesses (Reddy, 2003). Introducing additional Cartesian coordinate systems with new vertical locations x, z_i $(i = 1, 2)$ at the respective adherend's center and distinguishing centerline deformations $u_i(x)$ and $w_i(x)$ from the actual displacement fields $u_i^z(x, z)$ and $w_i^z(x, z_i)$ using the superscript z, yields

$$u_i^z(x, z_i) = u_i(x) + z_i \psi_i(x), \tag{7.3a}$$

$$w_i^z(x, z_i) = w_i(x), \tag{7.3b}$$

where ψ denotes an in-plane rotation about the y-axis, and u and w axial and vertical displacements, respectively (Fig. 7.2). Corresponding constitutive equations for laminates

$$\begin{pmatrix} N_{ix} \\ M_{ix} \end{pmatrix} = \begin{pmatrix} A_i^{11} & B_i^{11} \\ B_i^{11} & D_i^{11} \end{pmatrix} \begin{pmatrix} u_i' \\ \psi_i' \end{pmatrix}, \tag{7.4}$$

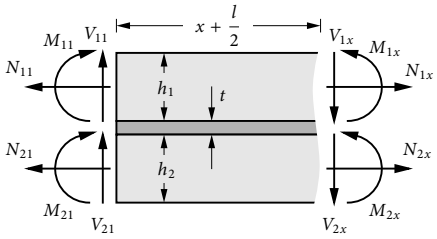

Fig. 7.4 Sandwich segment with equilibrium of left-sided general loading and section forces and moments.

and

$$V_{ix} = k_i A_i^{55}(w_i' + \psi_i), \tag{7.5}$$

with $i = 1, 2$ corresponding to upper and lower adhered can be found in textbooks (Jones, 1998). Recall, A_i^{11} denotes the adherend's extensional stiffness, B_i^{11} the bending–extension coupling stiffness, D_i^{11} the flexural rigidity, A_i^{55} the transverse shear stiffness and k_i the shear correction factor. Inverting the stiffness matrix and introducing the abbreviation $\Delta_i = A_i^{11} D_i^{11} - \left(B_i^{11}\right)^2$, yields the expression in terms of strains and curvature, i.e.,

$$\begin{pmatrix} u_i' \\ \psi_i' \end{pmatrix} = \frac{1}{\Delta_i} \begin{pmatrix} D_i^{11} & -B_i^{11} \\ -B_i^{11} & A_i^{11} \end{pmatrix} \begin{pmatrix} N_{ix} \\ M_{ix} \end{pmatrix}. \tag{7.6}$$

In the present two-dimensional plane strain setting, the adhesive constitutes an interface layer between two elastic bodies, the adherends. Depending on the properties of the elastic bodies and the adhesive, different continuity or discontinuity conditions for tractions and displacements across the interfaces can be modeled (Benveniste and Miloh, 2001). The present soft and thin interface layer allows for a discontinuity of the displacements across the interface. The displacement jump depends on the traction vector according to the interface's constitutive law. This interface condition is known as spring-type interface (Benveniste and Miloh, 2001), weak interface (Geymonat et al., 1999; Lenci, 2001) or imperfect interface (Hashin, 2002). In the present case, it can be understood as a continuous distribution of nonlinear springs in normal and shear direction. Hence, adhesive stresses are constant across the adhesive thickness and adhesive strains depend explicitly on the adherends' displacements. For this assumption to hold, the adhesive layer must be sufficiently thin. This yields the adhesive strain kinematics

$$\varepsilon_{zz} = \frac{w_2 - w_1}{t}, \tag{7.7a}$$

$$\varepsilon_{xx} = \frac{1}{2}\left(u_1^{z\prime}\left(x, \tfrac{h_1}{2}\right) + u_2^{z\prime}\left(x, -\tfrac{h_2}{2}\right)\right) = \frac{1}{2}\left(u_1' + \frac{h_1}{2}\psi_1' + u_2' - \frac{h_2}{2}\psi_2'\right), \tag{7.7b}$$

$$\begin{aligned}\gamma_{xz} &= \frac{1}{t}\left(u_2^z\left(x,-\tfrac{h_2}{2}\right)-u_1^z\left(x,\tfrac{h_1}{2}\right)\right)+\frac{1}{2}\left(w_1^{z\prime}(x)+w_2^{z\prime}(x)\right)\\ &= \frac{1}{t}\left(u_2-\frac{h_2}{2}\psi_2-u_1-\frac{h_1}{2}\psi_1\right)+\frac{1}{2}\left(w_1'+w_2'\right).\end{aligned} \tag{7.7c}$$

Note that u_1^z and u_2^z are expressed in their corresponding adherend coordinate systems x, z_i $(i = 1, 2)$. The out-of-plane strains vanish owing to the plane strain conditions, i.e.,

$$\varepsilon_{yy} = \gamma_{yz} = \gamma_{xy} = 0. \tag{7.8}$$

Constitutive relations for the nonlinear interface springs can be obtained assuming a nearly incompressible hyperelastic adhesive.

Constitutive equations for nearly incompressible hyperelastic adhesives. Hyperelastic materials undergo large deformations and are generally modeled using finite strain theory. However, in the present thin interface setting, deformations are constrained considerably by the linear elastic adherends. Restricting the consideration to distortion dominated deformations, the adhesive kinematics (7.7) can be formulated using linearized strains. It will be shown that while this simplification may cause inaccuracies at large loads, the present model provides good predictions up to failure. Presuming small strains, the deformation gradient can be expressed using adhesive strains according to

$$\boldsymbol{F} = \boldsymbol{I} + \boldsymbol{\varepsilon}_0, \tag{7.9}$$

where $\boldsymbol{I}$ is the identity matrix and $\boldsymbol{\varepsilon}_0$ the infinitesimal adhesive strain tensor under plane strain conditions, i.e.,

$$\boldsymbol{\varepsilon}_0 = \frac{1}{2}\begin{pmatrix} 2\varepsilon_{xx} & 0 & \gamma_{xz} \\ 0 & 0 & 0 \\ \gamma_{xz} & 0 & 2\varepsilon_{zz} \end{pmatrix}. \tag{7.10}$$

The interface constitutive law is obtained by computing the left Cauchy–Green tensor $\boldsymbol{B}$ using Eq. (2.10b) and inserting it into Eq. (2.94). Splitting isochoric and volumetric deformations using the modified left Cauchy–Green tensor $\overline{\boldsymbol{B}}$ (2.23b) and the volume ratio J (2.6) then yields

$$\boldsymbol{\sigma} = \frac{2}{J}\left[\left(\frac{\partial \mathcal{W}}{\partial I_{\overline{\boldsymbol{B}}}} + I_{\overline{\boldsymbol{B}}}\frac{\partial \mathcal{W}}{\partial II_{\overline{\boldsymbol{B}}}}\right)\overline{\boldsymbol{B}} - \frac{\partial \mathcal{W}}{\partial II_{\overline{\boldsymbol{B}}}}\overline{\boldsymbol{B}}^2\right] + \left[\frac{\partial \mathcal{W}}{\partial J} - \frac{2}{3J}\left(I_{\overline{\boldsymbol{B}}}\frac{\partial \mathcal{W}}{\partial I_{\overline{\boldsymbol{B}}}} + 2II_{\overline{\boldsymbol{B}}}\frac{\partial \mathcal{W}}{\partial II_{\overline{\boldsymbol{B}}}}\right)\right]\boldsymbol{I}. \tag{7.11}$$

where $\mathcal{W}$ is the material's strain energy density function (specified in the following), and $I_{\overline{\boldsymbol{B}}}$ and $II_{\overline{\boldsymbol{B}}}$ the first and second invariants (2.44) of the modified left Cauchy–Green tensor. Equation (7.11) provides a relation between adhesive stresses σ_{xx}, σ_{zz} and τ_{xz} and adhesive strains ε_{xx}, ε_{zz} and γ_{xz}. Despite assuming small strains, it describes a nonlinear stress–strain relation.

System of differential equations. Owing to the physical nonlinearity of the adhesive, the field equations and constitutive equations presented above yield a system of differential equations that describes a nonlinear multi-point boundary value problem.

The first set of differential equations is derived by inserting the adhesive's constitutive equation (7.11) into the equilibrium equations (7.1). Introducing the abbreviations

$$\eta_0 = \sqrt[3]{4\,(1+\varepsilon_{xx})(1+\varepsilon_{zz}) - \gamma_{xz}^2},\quad \eta_1 = \eta_0^2 \frac{\partial \mathcal{W}}{\partial I_{\bar{\boldsymbol{B}}}},\quad \eta_2 = 2\sqrt[3]{2}\,\frac{\partial \mathcal{W}}{\partial II_{\bar{\boldsymbol{B}}}},\quad \eta_3 = \frac{\partial \mathcal{W}}{\partial J}, \tag{7.12}$$

this yields

$$N_{1x}' = -8\sqrt[3]{2}\,(2+\varepsilon_{xx}+\varepsilon_{zz})\,\gamma_{xz}\,(\eta_1+\eta_2)\eta_0^{-7}, \tag{7.13}$$

$$\begin{aligned} V_{1x}' = \frac{2\sqrt[3]{2}}{3}\Big[&(16\varepsilon_{xx}+\varepsilon_{xx}^2)\,(\eta_1 - (\varepsilon_{zz}(2+\varepsilon_{zz})-1)\eta_2) \\ &+ \eta_2(6+4\varepsilon_{zz}+4\varepsilon_{xx}(1+\varepsilon_{zz}) - \gamma_{xz}^2)\,\gamma_{xz}^2 \\ &- 16\varepsilon_{zz}(2+\varepsilon_{zz})\,(\eta_1+\eta_2) - \eta_1\Big]\eta_0^{-7} - \eta_3, \end{aligned} \tag{7.14}$$

$$M_{1x}' = V_{1x} + \frac{h_1+t}{2}N_{1x}'. \tag{7.15}$$

Another two equations are derived from the adhesive kinematics. Differentiating Eqs. (7.7a) and (7.7c) with respect to x, and using the adherends' constitutive equations (7.6), yields

$$\begin{aligned} \gamma_{xz}' = &\frac{1}{t\Delta_2}\left[\left(D_2^{11} + \frac{h_2+t}{2}B_2^{11}\right)N_{2x} - \left(B_2^{11} + \frac{h_2+t}{2}A_2^{11}\right)M_{2x}\right] \\ &- \frac{1}{t\Delta_1}\left[\left(D_1^{11} - \frac{h_1+t}{2}B_1^{11}\right)N_{1x} + \left(-B_1^{11} + \frac{h_1+t}{2}A_1^{11}\right)M_{1x}\right] \\ &- \frac{1}{2}\left(\frac{1}{k_2A_2^{55}} - \frac{1}{k_1A_1^{55}}\right)V_{1x}', \end{aligned} \tag{7.16}$$

$$\begin{aligned} \varepsilon_{zz}'' = &\frac{1}{t\Delta_1}\left(-B_1^{11}N_{1x} + A_1^{11}M_{1x}\right) + \frac{1}{t\Delta_2}\left(B_2^{11}N_{2x} - A_2^{11}M_{2x}\right) \\ &- \frac{1}{t}\left(\frac{1}{k_1A_1^{55}} + \frac{1}{k_2A_2^{55}}\right)V_{1x}'. \end{aligned} \tag{7.17}$$

Expressing the axial strain ε_{xx} in terms of section forces using Eqs. (7.6) and (7.7b),

$$\begin{aligned} \varepsilon_{xx} = &\frac{1}{2\Delta_1}\left[\left(D_1^{11} - \frac{h_1}{2}B_1^{11}\right)N_{1x} - \left(B_1^{11} - \frac{h_1}{2}A_1^{11}\right)M_{1x}\right] \\ &+ \frac{1}{2\Delta_2}\left[\left(D_2^{11} + \frac{h_2}{2}B_2^{11}\right)N_{2x} - \left(B_2^{11} + \frac{h_2}{2}A_2^{11}\right)M_{2x}\right], \end{aligned} \tag{7.18}$$

and replacing the section forces and moments of the lower adherend using Eq. (7.2), allows for transforming the system of nonlinear equations (7.13) to (7.17) into a system of first-order differential equations of the form

$$\boldsymbol{y}' = f(x, \boldsymbol{y}), \tag{7.19}$$

where

$$\boldsymbol{y} = \left(N_{1x}, V_{1x}, M_{1x}, \gamma_{xz}, \varepsilon_{zz}, \varepsilon'_{zz}\right)^{\mathrm{T}}, \tag{7.20}$$

is a vector containing the six free functions. Accordingly, the boundary value problem requires six boundary conditions, which are determined from the equality of applied general loading and section forces and moments at the upper adherend ends, i.e.,

$$\begin{aligned} N_{1x}\left(x = -\tfrac{l}{2}\right) &= N_{11}, & V_{1x}\left(x = -\tfrac{l}{2}\right) &= V_{11}, & M_{1x}\left(x = -\tfrac{l}{2}\right) &= M_{11}, \\ N_{1x}\left(x = \tfrac{l}{2}\right) &= N_{12}, & V_{1x}\left(x = \tfrac{l}{2}\right) &= V_{12}, & M_{1x}\left(x = \tfrac{l}{2}\right) &= M_{12}. \end{aligned} \tag{7.21}$$

For the present system, the nonlinear multi-point boundary value problem solver `bvp4c` of the MATLAB (2016) library is used.

This solver for ordinary differential equations is an implementation of the three-stage Lobatto IIIa implicit Runge–Kutta method in a finite difference code. The collocation formula provides a $\mathcal{C}^1$-continuous piecewise cubic polynomial. That is, the solution and its first derivative are continuous. The code subdivides the domain based on error estimation, enforces boundary conditions and collocation conditions on the subintervals, and repeatedly solves a global system of algebraic equations and refines the mesh until a specified tolerance criterion is met. The stress solution of an arbitrary joint is obtained within milliseconds.

7.3 Stress and strain analysis

In order to validate the above sandwich-type model, its stress and strain predictions are compared against detailed finite element analyses. For this validation we consider DOWSIL™ TSSA, which is typically applied as a 1 mm thick adhesive layer. The silicone is modeled using the isochoric Neo-Hooke strain energy density function (2.101) and the simple volumetric model (2.119) common in commercial FEA software, i.e.,

$$\mathcal{W}(I_{\bar{\boldsymbol{B}}}, J) = \frac{\mu}{2}(I_{\bar{\boldsymbol{B}}} - 3) + \frac{\mu(1+\nu)}{3(1-2\nu)}(J-1)^2, \tag{7.22}$$

where $\mu = 2.67$ MPa is the shear modulus and $\nu = 0.475$ the Poisson's ratio providing slight compressibility. Of course, any other potential may be used. Properties of isotropic

Table 7.1
Adherend elastic properties.

Property	Steel	Aluminum	Glass
E (GPa)	210.0	70.0	70.0
ν (−)	0.30	0.33	0.23

Table 7.2
Carbon fiber reinforced plastic adherend ply elastic properties.

Property	E_1 (GPa)	E_2 (GPa)	μ_{12} (GPa)	ν_{12} (−)
Value	135.0	10.0	5.0	0.27

adherends are specified in Table 7.1 and ply elastic properties of carbon fiber reinforced plastic (CFRP) adherends used in the analyses are listed in Table 7.2.

The finite element benchmark model comprises a two-dimensional plane strain model of the adherend–adhesive–adherend overlap domain. Corresponding section forces and moments are applied as Neumann boundary conditions at the adherend ends (cf. Table 7.3). A dense and locally refined mesh ensures that stress solutions extracted in the adhesive mid-plane are fully converged. This comprises at least 20 eight-noded biquadratic elements through the adherend thickness and at least 10 eight-noded biquadratic hybrid elements with linear pressure through the adhesive thickness. Laminated adherends are assembled from individual homogeneous anisotropic plies. In the following, stress solutions of the FEA are shown as dotted lines. Stress predictions of the present model are plotted using solid lines.

Figure 7.5 shows the stress and strain analysis of one of the most common adhesive joints: a balanced single-lap joint (SLJ). The present SLJ consists of two glass adherends (Table 7.1) of thickness $h_1 = h_2 = 4\,\text{mm}$ bonded by a $t = 1\,\text{mm}$ thick DOWSIL™ TSSA adhesive layer. Bond length and width amount to $l = 100\,\text{mm}$ and $b = 25\,\text{mm}$, respectively. The joint is simply supported at its ends with an unsupported adherend length of 200 mm. The general loading applied at the sandwich element is calculated using the bending moment factor proposed by Goland and Reissner (1944) with a correction for

Table 7.3
Section forces and moments per unit width applied at the segment ends. Section forces N and V in N/mm, section moments M in Nmm/mm.

Fig.	N_{11}	V_{11}	M_{11}	N_{12}	V_{12}	M_{12}	N_{21}	V_{21}	M_{21}	N_{22}	V_{22}	M_{22}
7.5	400.0	13.35	332.27	0.0	0.0	0.0	0.0	0.0	0.0	400.0	13.35	−332.27
7.6	40.0	1.05	23.84	0.0	0.0	0.0	0.0	0.0	0.0	40.0	1.05	−23.84
7.7	0.0	0.0	0.0	0.0	20.0	2000.0	0.0	0.0	0.0	0.0	−20.0	−2000.0
7.8	0.0	0.0	0.0	20.0	0.0	−540.0	20.0	6.8	−170.0	0.0	6.8	170.0

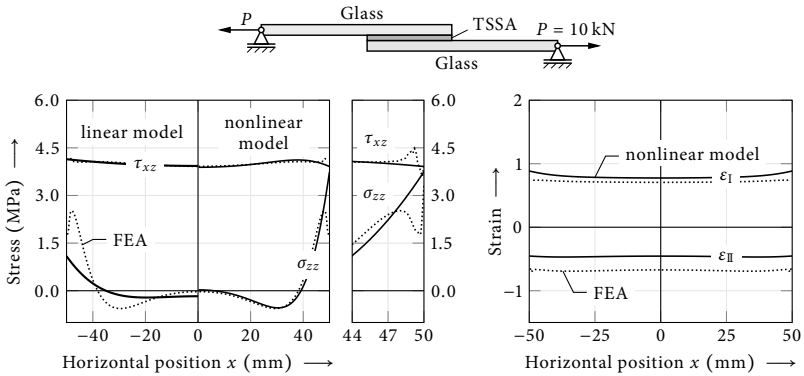

Fig. 7.5 Modeled adhesive stresses and strains (solid) in comparison to FEA solutions (dotted) for an axially loaded balanced glass–TSSA–glass single-lap joint. The bondline has the length $l = 100$ mm, thickness $t = 1$ mm and width $b = 25$ mm. The adherends are $h_1 = h_2 = 4$ mm thick and have an unsupported length of 200 mm. While the linear elastic model of Goland and Reissner (1944) (linear model, $x < 0$) captures the homogeneous shear stresses well, it provides poor predictions of peel stresses. The present model (nonlinear model, $x > 0$) provides a good description of both stress components except at the overlap ends and accurately predicts principal strains.

the transverse shear force suggested by Chen and Cheng (1983), i.e.,

$$N = \frac{P}{b}, \qquad V = k^* \frac{P}{b}, \qquad M = k \frac{h}{2} \frac{P}{b}, \tag{7.23}$$

where $h = h_1 = h_2$ and

$$k^* = \frac{(1-k)h + t}{l}, \qquad k = \left[1 + 2\sqrt{2} \tanh\left(\sqrt{\frac{3(1-\nu^2)P}{2Ehb}} \frac{l}{2h} \right) \right]^{-1}. \tag{7.24}$$

The section forces and moments computed for an axial loading of the joint of $P = 10$ kN are listed in Table 7.3.

While the Goland–Reissner bending moment factor was derived for linear elastic joints only, it provides reasonable estimates of section forces and moments for thin nonlinear adhesive layers (max. 20 % deviation to section moments determined from a finite element analysis of a corresponding full single-lap joint model). For the validation of the stress solutions provided by the present model, the same general loading is applied to the semi-analytical model and the FEA model of the sandwich element. That is, inaccuracies of general loading computation have no impact. More importantly, using Goland and Reissner's bending moment factor allows for assessing the performance of

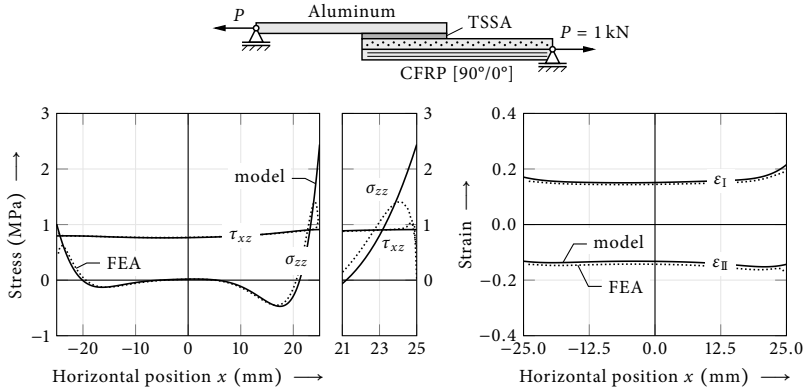

Fig. 7.6 Stress and strain solutions of the present model (solid) and FEA (dotted) for an unbalanced aluminum–TSSA–CFRP single-lap joint. The upper aluminum adherend is $h_1 = 2$ mm thick. The lower adherend is a [90°/0°] cross ply laminate of thickness $h_2 = 2$ mm. Both feature an unsupported length of 100 mm. The overlap is of length $l = 50$ mm, width $b = 25$ mm and thickness $t = 1$ mm.

their linear elastic single-lap joint model (Goland and Reissner, 1944) for soft nonlinear adhesives.

In Fig. 7.5, the symmetric distributions of shear and peel stresses obtained from FEA are shown as dotted lines. The left half of Fig. 7.5 (horizontal position $x < 0$) displays predictions of the Goland and Reissner (1944) model as solid lines using the Young's modulus $E = 7.88$ MPa computed from shear modulus and Poisson's ratio of DOWSIL™ TSSA. The solid lines in the right half of the figure ($x \geq 0$) correspond to stress distributions predicted by the present model. The linear elastic model of Goland and Reissner accurately captures the shear stresses τ_{xz} that are almost constant owing to the adhesive's low stiffness. However, peel stresses σ_{zz} are underestimated significantly and deviate considerably from the FEA reference. In contrast, the present nonlinear model reproduces both stress component distributions well. The zoom-in in Fig. 7.5 allows for an assessment of the quality of stress solutions provided by the present model in the vicinity of the boundaries. In a small domain, both the predicted peel and shear stresses deviate from the FEA solution. In particular, the zero shear stress boundary condition at the bondline ends is not satisfied. This is a common shortcoming of weak interface models. However, such highly localized differences are no significant disadvantage if nonlocal failure models such as finite fracture mechanics (Chapter 6) are used. Principal strains required for the evaluation of the strain failure model proposed in the present work (Section 6.2) are modeled adequately by the weak interface model.

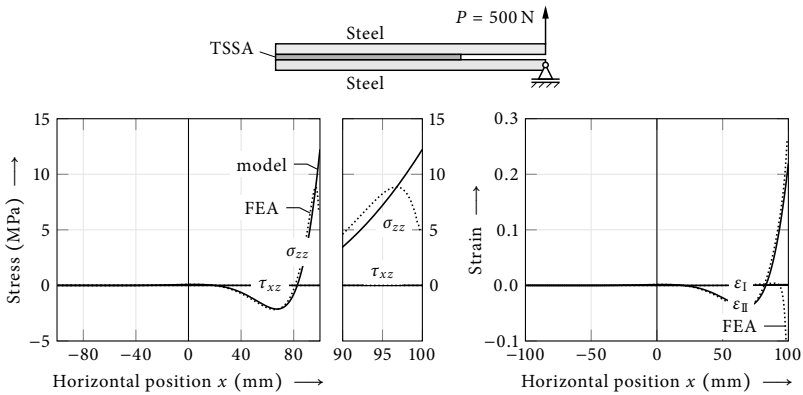

Fig. 7.7 Modeled stresses and strains (solid) in comparison to FEA (dotted) for a steel–TSSA–steel DCB specimen. The adhesive bond has a length of $l = 200$ mm, a width of $b = 25$ mm and a thickness $t = 1$ mm. The adherends have a thickness of $h_1 = h_2 = 6$ mm and an unsupported length of 100 mm.

The adherend kinematics of the present model allow for the use of laminated adherends with bending–extension coupling. To illustrate this, consider the aluminum–TSSA–CFRP single-lap joint examined in Fig. 7.6. The $[90°/0°]$ carbon fiber reinforced plastic cross ply-laminate of thickness $h_2 = 2$ mm exhibits considerable bending extension coupling. The shear correction factor for the present layup, $k = 0.773$, is calculated using the method of Klarmann and Schweizerhof (1993). The upper adherend is a $h_1 = 2$ mm thick aluminum beam. Both adherends are simply supported at their ends and have an unsupported length of 100 mm. The overlap is $l = 50$ mm long, $b = 25$ mm wide and $t = 1$ mm thick. The loading of the sandwich element is computed using the bending moment factor proposed by Talmon l'Armée et al. (2016) (Table 7.3). Again, the factor is derived for linear elastic joints but proves usable for thin nonlinear adhesives as well. Deviations to FEA section forces and moments are of the same order of magnitude as the Goland–Reissner bending moment factor. Despite the roughly equivalent extensional stiffness of the adherends, the transfer of peel stresses is concentrated at the right overlap end owing to the laminate's bending extension coupling. The effect is captured well by the present model and an overall good agreement between model and FEA solution is observed for both stresses and strains. As discussed above, deviations of the stress solution at the overlap ends are present.

The stress and strain analysis of a double cantilever beam (DCB) specimen is shown in Fig. 7.7. DCB specimens are loaded in pure mode I so that no shear stresses τ_{xz} are present. The loading of the sandwich element can be computed using linear statics

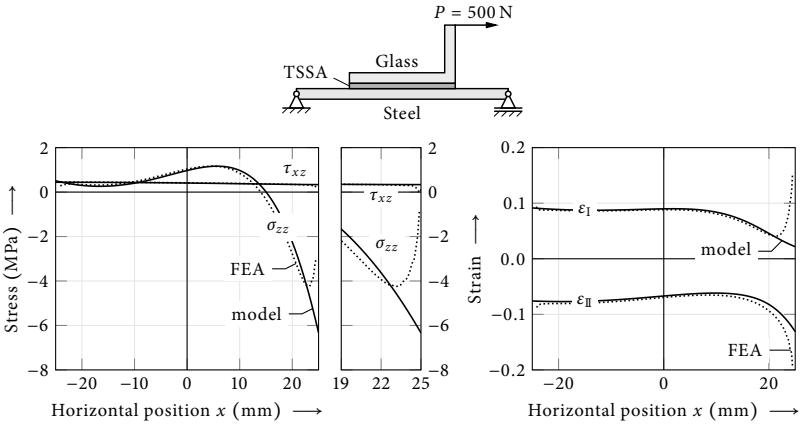

Fig. 7.8 Stress and strain distributions of the present model (solid) and FEA (dotted) for a glass–TSSA–steel T-joint. The joint is bonded across the length $l = 50$ mm, width $b = 25$ mm and thickness $t = 1$ mm. The upper glass adherend is $h_1 = 4$ mm thick and extends 25 mm vertically. The lower steel adherend is $h_2 = 4$ mm thick and extends 25 mm to the left and right of the overlap.

(Table 7.3). The present steel–TSSA–steel DCB specimen has an adhesive bondline of length $l = 200$ mm, width $b = 25$ mm and thickness $t = 1$ mm. The steel adherends are $h_1 = h_2 = 6$ mm thick and have an unsupported length of 100 mm. A good agreement between FEA and present model is observed for both stress and strain (Fig. 7.7). The weak interface approach presumes constant stresses through the adhesive thickness. This assumption is typically valid in terms of shear stress for thin adhesive layers. However, if peel stresses are dominant, the present model allows for the treatment of thick adhesives as well. Again, small deviations are present towards the overlap boundaries.

The glass–TSSA–steel T-joint shown in Fig. 7.8 causes considerable compressive stresses within the adhesive. Its upper glass adherend is $h_1 = 4$ mm thick and extends 25 mm vertically. The lower steel base is $h_2 = 4$ mm thick and extends 25 mm to the left and to the right of the overlap. The DOWSIL™ TSSA layer is $t = 1$ mm thick, $l = 50$ mm long and $b = 25$ mm wide. The loading of the sandwich element is obtained from linear statics (Table 7.3). The axial loading of the T-joint yields moderate shear stresses and considerable compressive peel stresses, which are reproduced well by the present model. Modeled principal strains are in good agreement with the FEA solution.

All of the above specimens indicate a good agreement between the present model and the finite element analysis reference solutions for typical dimensions of DOWSIL™ TSSA applications. The load transfer in classical glass–glass or glass–metal joints, as well as in

joints with laminated adherends with bending–extension coupling can be modeled and is represented accurately.

7.4 Failure prediction

The weak interface model provides good estimates for stresses and strains in hyperelastic adhesive layers and, hence, can be employed to predict failure of thin hyperelastic adhesive joints. For this purpose, we use principal strains to evaluate the mixed-mode failure model for hyperelastic materials developed in Section 6.2. The energy criterion of this finite fracture mechanics failure model permits only cracks with a certain minimum length, which means that the equivalent strain function of the coupled strain and energy criterion is evaluated in a certain distance from notches. Hence, the failure model is almost unaffected by local inaccuracies of the weak interface approach at the overlap boundaries but harnesses its efficiency.

Computation of energy release rates. The major performance advantage of the weak interface model results from the computation of energy release rates. The incremental energy release rate $\overline{\mathcal{G}}$ of a finite crack Δa used in the coupled criterion (6.5) is obtained from an integration of the differential energy release rate $\mathcal{G}$ and, hence, requires multiple evaluations of $\mathcal{G}$. In the present setting, the differential energy release rate can be computed using either the *J*-integral (2.168) or a compliance analysis of the adherends. Both approaches, the evaluation of the *J*-integral (Fraisse and Schmit, 1993; Hu, 1995) and the compliance model (Krenk, 1992), independently yield the same result:

$$\mathcal{G} = t\,\mathcal{W}\left(x \pm \tfrac{l}{2}\right), \tag{7.25}$$

where t is the adhesive thickness, and $\mathcal{W}$ the adhesive's strain energy density function evaluated at the overlap ends. In this context, $\mathcal{G}$ corresponds to the energy release rate of infinitesimal crack growth from one end of the overlap. It is nonzero in the present weak interface setting and can be interpreted as the energy stored in springs directly ahead of the crack tip. Both derivations require the assumptions of small strains and a thin interface. However, neither of them requires linearity of the adhesive, which is important for the present model.

Crack advance is represented by a shortening of the bonded length. For a crack of length a in a joint of initial bonded length l_0, the differential release rate $\mathcal{G}(a)$ is obtained by computing the weak interface solution for a joint of length $l = l_0 - a$ and evaluating Eq. (7.25) at the ends of the joint of reduced length. The incremental energy release rate $\overline{\mathcal{G}}$ of a finite crack Δa is then obtained by integrating repeatedly computed differential energy release rates $\mathcal{G}$ of crack increments a using Eq. (2.178).

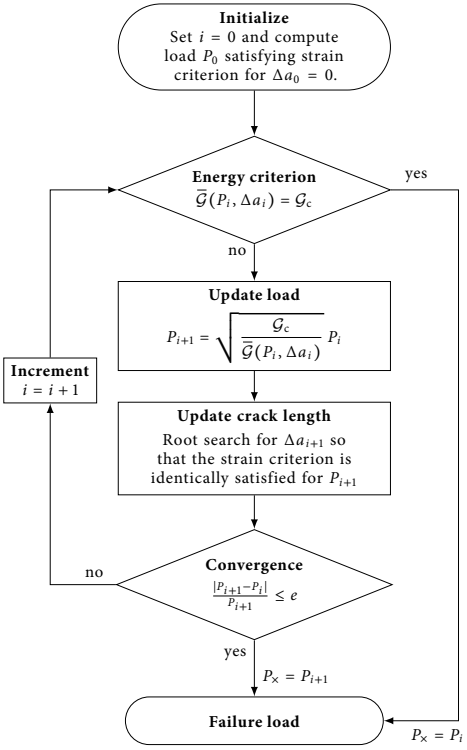

Fig. 7.9 Flowchart of the iterative solution algorithm for the optimization problem.

The integration is performed numerically using 30 crack increments to resolve a finite crack of length Δa.

Iterative solution of the coupled criterion. Thin adhesive joints typically fail under the formation of short finite cracks that originate from the bi-material notch between adherend and adhesive. Closely around this notch, both the equivalent strain function (6.4) and the incremental energy release rate (2.178) are monotonic. Hence, the inequalities in Eq. (6.7) revert to equalities and the optimization problem can be solved efficiently using an iterative algorithm (Fig. 7.9).

The scheme is initialized for an iteration index $i = 0$. Using a root search, the initial load P_0 that satisfies the strain criterion (6.3) for $\Delta a_0 = 0$, i.e., at the overlap end, is

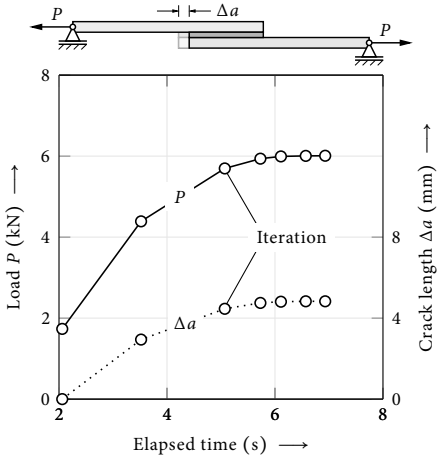

Fig. 7.10 Convergence of the iterative solver for the optimization problem.

computed. In every consecutive iteration i, the energy condition (6.1) is evaluated. If the energy condition is met, the failure load $P_\times$ and the finite crack length $\Delta a_\times$ are found and returned. Otherwise, the load is updated according to

$$P_{i+1} = \sqrt{\frac{\mathcal{G}_c}{\bar{\mathcal{G}}(P_i, \Delta a_i)}}\, P_i, \tag{7.26}$$

assuming a quadratic dependence of the total energy potential on the loading. Using a root search, the new crack length Δa_{i+1} is computed so that the strain criterion is satisfied identically at the distance Δa_{i+1} from the overlap end for the updated load P_{i+1}. The iteration index i is incremented and the procedure repeated until the convergence criterion

$$\frac{|P_{i+1} - P_i|}{P_{i+1}} \leq e, \tag{7.27}$$

is met. For engineering purposes a tolerance of $e = 10^{-3}$ suffices.

This solver typically converges within less than 10 s requiring less than 10 iterations. An illustration of the iterative procedure is shown in Fig. 7.10 for a single-lap joint. In Fig. 7.10, one plot mark (circle) corresponds to one iteration. In the present example, the root search for the initial load value takes about 2 s. As the iteration progresses, load increments decrease and root searches for the crack length update become less expensive. Quick convergence of both load P and crack length Δa is observed. Both the iterative solver and the weak interface model are implemented in MATLAB (2016).

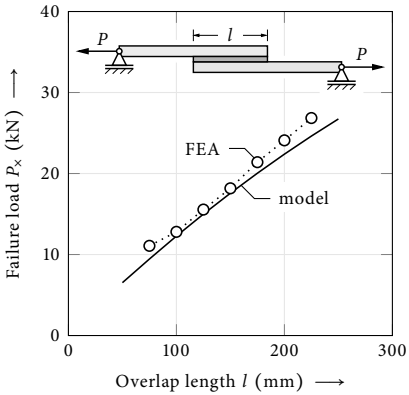

Fig. 7.11 Failure predictions of the weak interface model (solid) and a detailed FEA model (dotted) plotted against the overlap length l of an aluminum–TSSA–aluminum single-lap joint of adhesive thickness $t = 1$ mm and width $b = 25$ mm. The aluminum adherends are $h_1 = h_2 = 8$ mm thick and extend 100 mm beyond the overlap.

Failure loads. Except for pancake specimens, which require involved constitutive models (Section 6.3.3), no experimental data on DOWSIL™ TSSA samples is available. DOWSIL™ 993 specimens tested in the present work are too thick to satisfy the assumptions of the weak interface model. Hence, failure predictions of the weak interface model are validated in comparison to evaluations of the finite fracture mechanics failure criterion using a detailed finite element model of the overlap domain.

Figure 7.11 compares FEA and weak interface model failure predictions for an aluminum–TSSA–aluminum single-lap joint in dependence of its overlap length. The SLJ has an adhesive thickness of $t = 1$ mm and a width of $b = 25$ mm. The aluminum adherends of thickness $h_1 = h_2 = 8$ mm have an unsupported length of 100 mm. Section forces at the overlap boundaries are calculated using the bending moment factor of Goland and Reissner (1944), and the correction for the transverse shear force suggested by Chen and Cheng (1983), and are applied to both the FEA and the weak interface model. Both models predict increasing failure loads with increasing overlap length and are in close agreement. Since no experimental data are available, no assessment of the absolute accuracy of the results can be given.

Because DOWSIL™ TSSA is supplied in sheets of 1 mm thickness, consider the hypothetical very thin application of DOWSIL™ 993 as a peel joint (Fig. 7.12), in order to explore different adhesive dimensions. The constitutive behavior of DOWSIL™ 993 is modeled using Eq. (7.22) with a shear modulus of $\mu = 0.63$ MPa and a Poisson's ratio of

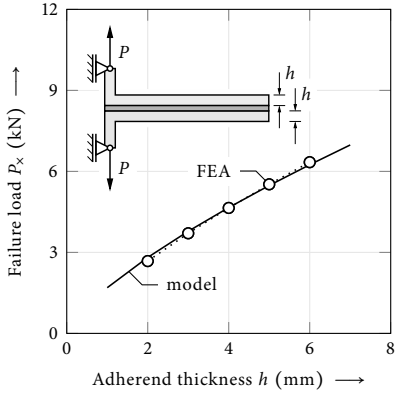

Fig. 7.12 Failure predictions of the weak interface model (solid) and a detailed FEA model (dotted) plotted against the adherend thickness $h = h_1 = h_2$ of an aluminum–993–aluminum peel joint of adhesive thickness $t = 0.1\,\text{mm}$ and width $b = 25\,\text{mm}$.

$\nu = 0.475$. For this very thin adhesive layer ($t = 0.1\,\text{mm}$), the agreement between model and FEA is excellent (Fig. 7.12). The effective strength of the aluminum–993–aluminum peel joint increases with increasing adherend thickness $h = h_1 = h_2$ because the load is transferred through a larger section of the adhesive. Section forces at the overlap boundaries are calculated using linear statics and are applied to both the FEA and the weak interface model.

The above observations together with findings of excellent predictions of FFM models for brittle linear elastic adhesive joints, in particular using weak interface models (Stein et al., 2015, 2016b), suggest the conclusion that the present failure model can yield accurate results for many brittle nonlinear elastic adhesive joints as well. The nonlocal nature of finite crack initiation promotes the use of weak interface models for the failure assessment. It is to note that the accuracy of the present model depends on a reliable computation of boundary loads of the sandwich-type element. For practical applications of joints with severe nonlinearities, adequate methods for the calculation of loads, e.g., bending moment factors for single-lap joints, are required. On account of the weak interface assumptions, adhesive layers are well represented when they are thin in comparison to all other characteristic dimensions. While this typically applies to DOWSIL™ TSSA, most practical applications of DOWSIL™ 993 are not covered by the model.

Chapter 8

Conclusions and perspectives

This work provides a theoretical and experimental framework for the characterization and description of static failure of nearly incompressible nonlinear elastic materials. The procedure is developed and validated using two hyperelastic silicones with different technical purposes: DOWSIL™ 993 typically applied in thick but narrow beads and DOWSIL™ TSSA used in thin and flat adhesive joints. The methodology is not restricted to the investigated silicones but may be applied to other hyperelastic media, as well.

Experimental characterization. The present work shows experiments suitable for the characterization of the constitutive behavior, bulk failure properties, and fracture properties. It provides benchmark experiments for the validation of failure models for notch-induced crack nucleation. To characterize the isochoric material behavior uniaxial tension, biaxial tension and shear tests prove important. The volumetric material behavior can be identified from pancake tests. This work employs a strain-based description of bulk material failure, which is best examined using uniaxial and biaxial tension tests. While these two tests determine the principal shape of the deviatoric failure surface, shear test can further particularize it. Appropriate models allow for the use of standardized test setups for the measurement of the fracture toughnesses of hyperelastic materials. Employing the J-integral, approximate expressions for the mode I and mode III energy release rates in slightly modified double cantilever beam samples are given and used for measurements of the corresponding fracture toughnesses.

Bulk material failure. Hyperelastic materials possess two failure modes: they can rupture owing to dilatational or distortional loading. For a comprehensive description of failure surfaces of such materials, this work describes volumetric and isochoric failure independently and combines the respective failure surfaces using the so-called failure mode concept. To allow for the description of deviatoric bulk failure using a single, smooth, and convex failure surface, a new, more general deviatoric function capable of describing relevant shape transitions between the upper and lower deviatoric convexity limits is proposed. Using this function, a highly accurate strain-based representation of deviatoric failure surfaces of hyperelastic materials is given. The corresponding

shape parameters are identified for many hyperelastic materials. The representation of the failure surfaces of these materials requires only certain features of the suggested deviatoric function and a simplified equivalent strain function is given. It is shown that volumetric bulk material failure can be described using a critical volumetric strain criterion. Combining this simple dilatational criterion with the above deviatoric strain function using the failure mode concept finally provides a complete picture of the failure surface of nearly incompressible hyperelastic media.

Notch-induced crack nucleation. Notches are locations of so-called weak singularities. Here, stresses and strains are infinite, yet, the energy release rate of an infinitesimal crack originating from a weak singularity is zero. Hence, local bulk material failure concepts predict vanishing failure loads and linear elastic fracture mechanics permit indefinitely high loads. It is shown that this contradiction can be resolved assuming the nucleation of finite sized cracks, which are associated to a nonzero incremental energy release rate and finite stresses and strains. Cracks can nucleate when both an equivalent strain criterion and an energetic condition are satisfied simultaneously. In the present work, this coupled strain and energy criterion is applied to hyperelastic materials. The model is validated using a large number of different silicone adhesive joints such as simple shear, pull-off, tubular lap shear and pancake samples. It provides excellent predictions of critical loads and physical explanations for size effects such as the adhesive thickness effect. Interestingly, even in structures with pronounced volumetric loading such as pancake tests, ultimate failure is governed by distortional deformations. Because the size of nucleating finite cracks is almost constant across all examined specimens a simple design tool applicable to practically relevant structural dimensions can be derived. The critical distances tool only evaluates the proposed equivalent strain function, does not require the computation of energy release rates and provides conservative predictions. Not monotonic energy release rates in simple shear tests are shown to cause crack nucleation, instable crack growth, crack arrest, stable crack growth and finally ultimate unstable crack propagation.

Weak interface model. The characteristics of adhesive joints are similar in many technical applications. Often, flat and thin adherends are bonded using a thin adhesive layer. This also applies to DOWSIL™ TSSA and can be exploited to provide an efficient model for stresses and strains within the adhesive. The present work proposes a weak interface model for thin hyperelastic adhesive joints. In combination with the suggested coupled strain and energy failure criterion, it allows for quick estimates of effective joint strengths. Linking this nonlocal failure model with a weak interface approach is particularly powerful because the failure model is not affected by local inaccuracies of the weak interface ansatz. A validation of the interface model using detailed finite element analyses shows that estimates for stresses, strains and effective joint strengths are accurate.

Limitations. The present work is concerned with bulk material and notch-induced failure in ambient conditions and under static loads. A comprehensive toolkit for the design of hyperelastic components undoubtedly also requires concepts for the prediction of fatigue life. The principles and mechanisms of static crack nucleation described by the present failure model may inspire models for cyclic failure. This is of particular concern for hyperelastic materials that exhibit the Mullins effect, i.e., cyclic effects in the constitutive behavior. Although the silicones investigated in the present work do not exhibit significant viscoelastic effects, nonlinear elastic materials are generally sensitive to temperature, humidity and strain rate. The present description of the failure surface can incorporate temperature, humidity and strain rate dependent parameters. Together with fracture toughnesses measured in dependence of these influences, the finite fracture mechanics failure model can account for environmental impacts.

Future experiments. Complementing the description of DOWSIL™ 993 bulk failure requires volumetric, i.e., pancake tests of this material. More importantly, however, it is of great interest how the volumetric and distortional failure modes interact. Using the failure mode concept, the present work provides a theoretical framework to account for the interaction of different failure modes. However, an experimental design allowing for measuring this dependence is missing. The proposed failure model for hyperelastic materials yields good results in its validation against specimen tests. However, it can only prove its capabilities in its use for the design of full-scale structures and corresponding experiments.

Theoretical extensions. Although this work determines the crack tearing fracture toughness $\mathcal{G}_{\text{III}c}$ for DOWSIL™ TSSA, the property is not used. The nonlinear crack opening integral, which allows for mode separation, increases the computational cost of failure predictions considerably. However, it can improve insights into the mechanisms triggering crack nucleation considerably. Assuming the equivalence of crack sliding and crack tearing, all tools for the evaluation of a mixed-mode energy criterion for DOWSIL™ TSSA are available and can be used to re-evaluate experiments reported here. The kinematics of the proposed weak interface model are restricted to thin adhesive layers. However, many hyperelastic adhesives such as DOWSIL™ 993 are applied as thick beads. Hence, this simple joint analysis tool cannot be used. To broaden the applicability of the weak interface approach, a model with more complete kinematics capable of describing thick adhesive layers is required.

The present work is a contribution to the description of bulk material and notch-induced failure of nearly incompressible hyperelastic media and extends finite fracture mechanics to nonlinear elastic materials.

References

Abaqus. *User's Manual Version 2018*. Dassault Systèmes Simulia Corp., 2018.

R. D. Adams and N. A. Peppiatt. Stress Analysis of Adhesive Bonded Tubular Lap Joints. *The Journal of Adhesion*, 9(1):1–18, 1977.

N. Aït Hocine, A. Hamdi, M. Naït Abdelaziz, P. Heuillet, and F. Zaïri. Experimental and finite element investigation of void nucleation in rubber-like materials. *International Journal of Solids and Structures*, 48(9):1248–1254, 2011.

H. Alexander. A constitutive relation for rubber-like materials. *International Journal of Engineering Science*, 6(9):549–563, 1968.

H. Altenbach. *Kontinuumsmechanik*. Springer, Berlin, Heidelberg, 2015.

H. Altenbach, J. Altenbach, and A. Zolochevsky. *Erweiterte Deformationsmodelle und Versagenskriterien der Werkstoffmechanik*. Deutscher Verlag für Grundstoffindustrie, Stuttgart, 1995.

H. Altenbach, A. Bolchoun, and V. A. Kolupaev. Phenomenological Yield and Failure Criteria. In H. Altenbach and A. Öchsner, editors, *Plasticity of Pressure-Sensitive Materials*, Engineering Materials, pages 49–152. Springer, Berlin, Heidelberg, 1st edition, 2014.

H. Altenbach, V. A. Eremeyev, and K. Naumenko. On the use of the first order shear deformation plate theory for the analysis of three-layer plates with thin soft core layer. *ZAMM – Journal of Applied Mathematics and Mechanics / Zeitschrift für Angewandte Mathematik und Mechanik*, 95 (10):1004–1011, 2015.

H. Altenbach, P. L. Rosendahl, W. Becker, and V. A. Kolupaev. Isogonal and isotoxal hexagons as extremal yield figures. In K. Wiśniewski and T. Burczyński, editors, *41st Solid Mechanics Conference, Book of abstracts*, Warsaw, Poland, 2018.

A. F. Amin, S. I. Wiraguna, A. R. Bhuiyan, and Y. Okui. Hyperelasticity Model for Finite Element Analysis of Natural and High Damping Rubbers in Compression and Shear. *Journal of Engineering Mechanics*, 132(1):54–64, 2006.

L. Anand. On H. Hencky's Approximate Strain-Energy Function for Moderate Deformations. *Journal of Applied Mechanics*, 46:78, 1979.

L. Anand. Moderate deformations in extension-torsion of incompressible isotropic elastic materials. *Journal of the Mechanics and Physics of Solids*, 34(3):293–304, 1986.

T. Andersson and A. Biel. On the effective constitutive properties of a thin adhesive layer loaded in peel. *International Journal of Fracture*, 141(1-2):227–246, 2006.

T. Andersson and U. Stigh. The stress–elongation relation for an adhesive layer loaded in peel using equilibrium of energetic forces. *International Journal of Solids and Structures*, 41(2):413–434, 2004.

J. H. Argyris, G. Faust, J. Szimmat, E. P. Warnke, and K. J. Willam. Recent developments in the finite element analysis of prestressed concrete reactor vessels. *Nuclear Engineering and Design*, 1974.

E. M. Arruda and M. C. Boyce. A three-dimensional constitutive model for the large stretch behavior of rubber elastic materials. *Journal of the Mechanics and Physics of Solids*, 41(2): 389–412, 1993.

M. Aßmus. *Structural Mechanics of Anti-Sandwiches*. SpringerBriefs in Applied Sciences and Technology. Springer International Publishing, Cham, 2019.

M. Aßmus, K. Naumenko, and H. Altenbach. A multiscale projection approach for the coupled global–local structural analysis of photovoltaic modules. *Composite Structures*, 158:340–358, 2016.

M. Aßmus, S. Bergmann, J. Eisenträger, K. Naumenko, and H. Altenbach. Consideration of Non-uniform and Non-orthogonal Mechanical Loads for Structural Analysis of Photovoltaic Composite Structures. In H. Altenbach, R. V. Goldstein, and E. Murashkin, editors, *Mechanics for Materials and Technologies*, volume 46 of *Advanced Structured Materials*, pages 73–122. Springer International Publishing, Cham, 2017.

M. Aßmus, K. Naumenko, A. Öchsner, V. A. Eremeyev, and H. Altenbach. A generalized framework towards structural mechanics of three-layered composite structures. *Technische Mechanik*, 39 (2):202–219, 2019.

ASTM Standard C1401. *Standard Guide for Evaluating Failure of Structural Sealant Glazing*. ASTM International, West Conshohocken, PA, 2014.

ASTM Standard D3433. *Standard Test Method for Fracture Strength in Cleavage of Adhesives in Bonded Metal Joints*. ASTM International, West Conshohocken, PA, 2012.

ASTM Standard D3492. *Standard Specification for Rubber Contraceptives (Male Condoms)*. ASTM International, West Conshohocken, PA, 2016.

ASTM Standard D412. *Standard Test Methods for Vulcanized Rubber and Thermoplastic Elastomers — Tension*. ASTM International, West Conshohocken, PA, 2016.

ASTM Standard D4762. *Standard Guide for Testing Polymer Matrix Composite Materials*. ASTM International, West Conshohocken, PA, 2018.

ASTM Standard D5528. *Standard Test Method for Mode I Interlaminar Fracture Toughness of Unidirectional Fiber-Reinforced Polymer Matrix Composites*. ASTM International, West Conshohocken, PA, 2013.

ASTM Standard D624. *Standard Test Method for Tear Strength of Conventional Vulcanized Rubber and Thermoplastic Elastomers*. ASTM International, West Conshohocken, PA, 2000.

ASTM Standard D638. *Standard Test Method for Tensile Properties of Plastics*. ASTM International, West Conshohocken, PA, 2014.

ASTM Standard D6976. *Standard Specification for Rubber Contraceptives — Vaginal Diaphragms*. ASTM International, West Conshohocken, PA, 2013.

ASTM Standard E2712. *Standard Test Methods for Bulge-Forming Superplastic Metallic Sheet*. ASTM International, West Conshohocken, PA, 2015.

ASTM Standard E399. *Standard Test Method for Linear-Elastic Plane-Strain Fracture Toughness KIc of Metallic Materials*. ASTM International, West Conshohocken, PA, 2017.

M. M. Attard and G. W. Hunt. Hyperelastic constitutive modeling under finite strain. *International Journal of Solids and Structures*, 41(18-19):5327–5350, 2004.

J. Awerbuch and M. S. Madhukar. Notched Strength of Composite Laminates: Predictions and Experiments–A Review. *Journal of Reinforced Plastics and Composites*, 4(1):3–159, 1985.

M. R. Ayatollahi, M. Heydari-Meybodi, M. Dehghany, and F. Berto. A New Criterion for Rupture Assessment of Rubber-Like Materials under Mode-I Crack Loading: The Effective Stretch Criterion. *Advanced Engineering Materials*, 18(8):1364–1370, 2016.

J. M. Ball. Convexity conditions and existence theorems in nonlinear elasticity. *Archive for Rational Mechanics and Analysis*, 63(4):337–403, 1976.

J. M. Ball. Discontinuous Equilibrium Solutions and Cavitation in Nonlinear Elasticity. *Philosophical Transactions of the Royal Society A: Mathematical, Physical and Engineering Sciences*, 306 (1496):557–611, 1982.

M. D. Banea, L. F. M. da Silva, and R. D. S. G. Campilho. Temperature Dependence of the Fracture Toughness of Adhesively Bonded Joints. *Journal of Adhesion Science and Technology*, 24(11-12): 2011–2026, 2010.

M. D. Banea, L. F. M. da Silva, and R. D. S. G. Campilho. The Effect of Adhesive Thickness on the Mechanical Behavior of a Structural Polyurethane Adhesive. *The Journal of Adhesion*, 91(5): 331–346, 2015.

G. I. Barenblatt. Concerning equilibrium cracks forming during brittle fracture. The stability of isolated cracks. Relationships with energetic theories. *Journal of Applied Mathematics and Mechanics*, 23(5):1273–1282, 1959.

J. D. Barrett and R. O. Foschi. Mode II stress-intensity factors for cracked wood beams. *Engineering Fracture Mechanics*, 9(2):371–378, 1977.

Z. P. Bažant. Size Effect in Blunt Fracture: Concrete, Rock, Metal. *Journal of Engineering Mechanics*, 110(4):518–535, 1984.

Z. P. Bažant. Size effect on structural strength: a review. *Archive of Applied Mechanics*, 69(9-10): 703–725, 1999.

M. F. Beatty. An Average-Stretch Full-Network Model for Rubber Elasticity. *Journal of Elasticity*, 70(1-3):65–86, 2003.

M. F. Beatty. On Constitutive Models for Limited Elastic, Molecular Based Materials. *Mathematics and Mechanics of Solids*, 13(5):375–387, 2008.

H. Bechir, L. Chevalier, and M. Idjeri. A three-dimensional network model for rubber elasticity: The effect of local entanglements constraints. *International Journal of Engineering Science*, 48 (3):265–274, 2010.

E. Becker and W. Bürger. *Kontinuumsmechanik*. Vieweg+Teubner, Wiesbaden, 1975.

F. Becker. *Entwicklung einer Beschreibungsmethodik für das mechanische Verhalten unverstärkter Thermoplaste bei hohen Deformationsgeschwindigkeiten*. Dissertation, Martin-Luther-Universität Halle-Wittenberg, 2009.

G. F. Becker. The finite elastic stress-strain function. *American Journal of Science*, 46:337–356, 1893.

T. Beda. Modeling hyperelastic behavior of rubber: A novel invariant-based and a review of constitutive models. *Journal of Polymer Science Part B: Polymer Physics*, 45(13):1713–1732, jul 2007.

T. Beda. An approach for hyperelastic model-building and parameters estimation a review of constitutive models. *European Polymer Journal*, 50:97–108, 2014.

T. Belytschko, W. K. Liu, B. Moran, and K. Elkhodary. *Nonlinear Finite Elements for Continua and Structures*. John Wiley & Sons, Ltd., Chichester, 2nd edition, 2013.

Y. Benveniste and T. Miloh. Imperfect soft and stiff interfaces in two-dimensional elasticity. *Mechanics of Materials*, 33(6):309–323, 2001.

F. Berto. A criterion based on the local strain energy density for the fracture assessment of cracked and V-notched components made of incompressible hyperelastic materials. *Theoretical and Applied Fracture Mechanics*, 76:17–26, 2015.

A. Biel and U. Stigh. Cohesive zone modelling of nucleation, growth and coalesce of cavities. *International Journal of Fracture*, 204(2):159–174, 2017.

D. Bigoni and A. Piccolroaz. Yield criteria for quasibrittle and frictional materials. *International Journal of Solids and Structures*, 41(11–12):2855–2878, 2004.

D. A. Bigwood and A. D. Crocombe. Elastic analysis and engineering design formulae for bonded joints. *International Journal of Adhesion and Adhesives*, 9(4):229–242, 1989.

D. A. Bigwood and A. D. Crocombe. Non-linear adhesive bonded joint design analyses. *International Journal of Adhesion and Adhesives*, 10(1):31–41, 1990.

J. F. W. Bishop and R. Hill. A theory of the plastic distortion of a polycrystalline aggregate under combined stresses. *The London, Edinburgh, and Dublin Philosophical Magazine and Journal of Science*, 42(327):414–427, 1951.

B. Blackman, J. P. Dear, A. J. Kinloch, and S. Osiyemi. The calculation of adhesive fracture energies from double-cantilever beam test specimens. *Journal of Materials Science Letters*, 10(5):253–256, 1991.

B. R. K. Blackman, A. J. Kinloch, M. Paraschi, and W. S. Teo. Measuring the mode I adhesive fracture energy, GIC, of structural adhesive joints: the results of an international round-robin. *International Journal of Adhesion and Adhesives*, 23(4):293–305, 2003.

P. J. Blatz. Application of Finite Elastic Theory to the Behavior of Rubberlike Materials. *Rubber Chemistry and Technology*, 36(5):1459–1496, 1963.

D. B. Bogy. Two Edge-Bonded Elastic Wedges of Different Materials and Wedge Angles Under Surface Tractions. *Journal of Applied Mechanics*, 38(2):377, 1971.

A. Bolchoun, V. A. Kolupaev, and H. Altenbach. Konvexe und nichtkonvexe Fließflächen. *Forschung im Ingenieurwesen*, 75(2):73–92, 2011.

M. C. Boyce and E. M. Arruda. Constitutive Models of Rubber Elasticity: A Review. *Rubber Chemistry and Technology*, 73(3):504–523, 2000.

L. Brochard, S. Souguir, and K. Sab. Scaling of brittle failure: strength versus toughness. *International Journal of Fracture*, 210(1-2):153–166, 2018.

L. Brochard, S. Souguir, and K. Sab. Fundamentals of brittle failure at the atomic scale. In *Proceedings of the 10th International Conference on Fracture Mechanics of Concrete and Concrete Structures*, pages 1–11, 2019.

O. T. Bruhns, H. Xiao, and A. Meyers. Hencky's elasticity model with the logarithmic strain measure: A study on Poynting effect and stress response in torsion of tubes and rods. *Archives of Mechanics*, 52(4-5):489–509, 2000.

O. T. Bruhns, H. Xiao, and A. Meyers. Constitutive inequalities for an isotropic elastic strain-energy function based on Hencky's logarithmic strain tensor. *Proceedings of the Royal Society of London. Series A: Mathematical, Physical and Engineering Sciences*, 457(2013):2207–2226, 2001.

BS Standard 7991. *Determination of the mode I adhesive fracture energy, GIc, of structural adhesives using the double cantilever beam (DCB) and tapered double cantilever beam (TDCB) specimens*. British Standards Institution, London, 2001.

M. K. Budzik, J. Jumel, K. Imielińska, and M. E. R. Shanahan. Effect of Adhesive Compliance in the Assessment of Soft Adhesives with the Wedge Test. *Journal of Adhesion Science and Technology*, 25(1-3):131–149, 2011.

W. Burzyński. *Study on material effort hypotheses*. Dissertation, Polish Academy of Technical Sciences, Lwów, 1928.

W. F. Busse. Physics of Rubber as Related to the Automobile. *Journal of Applied Physics*, 9(7): 438–451, 1938.

M. Cabello, J. Zurbitu, J. Renart, A. Turon, and F. Martínez. A non-linear hyperelastic foundation beam theory model for double cantilever beam tests with thick flexible adhesive. *International Journal of Solids and Structures*, 80:19–27, 2016.

R. D. S. G. Campilho, D. C. Moura, M. D. Banea, and L. F. M. da Silva. Adhesive thickness effects of a ductile adhesive by optical measurement techniques. *International Journal of Adhesion and Adhesives*, 57:125–132, 2015.

M. Capurso. Yield conditions for incompressible isotropic and orthotropic materials with different yield stress in tension and compression. *Meccanica*, 2(2):118–125, 1967.

T. Carlberger and U. Stigh. Influence of Layer Thickness on Cohesive Properties of an Epoxy-Based Adhesive—An Experimental Study. *The Journal of Adhesion*, 86(8):816–835, 2010.

A. Carpinteri, P. Cornetti, N. Pugno, A. Sapora, and D. Taylor. A finite fracture mechanics approach to structures with sharp V-notches. *Engineering Fracture Mechanics*, 75(7):1736–1752, 2008.

A. Carpinteri, P. Cornetti, and A. Sapora. A Finite Fracture Mechanics approach to the asymptotic behaviour of U-notched structures. *Fatigue and Fracture of Engineering Materials and Structures*, 35(5):451–457, 2012.

N. Carrère, E. Martin, and D. Leguillon. Comparison between models based on a coupled criterion for the prediction of the failure of adhesively bonded joints. *Engineering Fracture Mechanics*, 138:185–201, 2015.

M. M. Carroll. A Strain Energy Function for Vulcanized Rubbers. *Journal of Elasticity*, 103(2): 173–187, 2011.

J. Casey. A remark on Cauchy-elasticity. *International Journal of Non-Linear Mechanics*, 40(2-3): 331–339, 2005.

G. Catalanotti and P. P. Camanho. A semi-analytical method to predict net-tension failure of mechanically fastened joints in composite laminates. *Composites Science and Technology*, 76: 69–76, 2013.

H. Chai and S. Mall. Design aspects of the end-notch adhesive joint specimen. *International Journal of Fracture*, 36(1):3–8, 1988.

Y.-W. Chang, A. N. Gent, and J. Padovan. Expansion of a cavity in a rubber block under unequal stresses. *International Journal of Fracture*, 60(3):283–291, 1993.

E. W. V. Chaves. *Notes on Continuum Mechanics*. Lecture Notes on Numerical Methods in Engineering and Sciences. Springer Netherlands, Dordrecht, 2013.

D. Chen and S. Cheng. An Analysis of Adhesive-Bonded Single-Lap Joints. *Journal of Applied Mechanics*, 50(1):109, 1983.

W.-F. Chen and H. Zhang. *Structural plasticity: theory, problems, and CAE software*. Springer, New York, 1991.

G. P. Cherepanov. Crack propagation in continuous media. *Journal of Applied Mathematics and Mechanics*, 31(3):503–512, 1967.

R. Christensen. Stress based yield/failure criteria for fiber composites. *International Journal of Solids and Structures*, 34(5):529–543, 1997a.

R. M. Christensen. Yield functions/failure criteria for isotropic materials. *Proceedings of the Royal Society of London. Series A: Mathematical, Physical and Engineering Sciences*, 453:1473–1491, 1997b.

R. M. Christensen. *The theory of materials failure*. Oxford University Press, 2013.

J. D. Clark and I. J. McGregor. Ultimate Tensile Stress over a Zone: A New Failure Criterion for Adhesive Joints. *The Journal of Adhesion*, 42(4):227–245, 1993.

C. D. Clift, L. D. Carbary, P. Hutley, and J. H. Kimberlain. Next generation structural silicone glazing. *Journal of Facade Design and Engineering*, 2(3–4):137–161, 2014.

B. D. Coleman and W. Noll. The thermodynamics of elastic materials with heat conduction and viscosity. *Archive for Rational Mechanics and Analysis*, 13(1):167–178, 1963.

P. Cornetti and A. Sapora. Penny-shaped cracks by Finite Fracture Mechanics. *International Journal of Fracture*, 219(1):153–159, sep 2019.

P. Cornetti, N. Pugno, A. Carpinteri, and D. Taylor. Finite fracture mechanics: A coupled stress and energy failure criterion. *Engineering Fracture Mechanics*, 73(14):2021–2033, 2006.

P. Cornetti, A. Sapora, and A. Carpinteri. Mode mixity and size effect in V-notched structures. *International Journal of Solids and Structures*, 50(10):1562–1582, 2013.

P. Cornetti, M. Muñoz-Reja, A. Sapora, and A. Carpinteri. Finite fracture mechanics and cohesive crack model: Weight functions vs. cohesive laws. *International Journal of Solids and Structures*, 2018.

C. A. Coulomb. Essai sur une application des règles des maximis et minimis à quelques problèmes de statique relatifs, à l'architecture. *Mémoires de Mathématique et de Physique, présentés a l'Academie Royale des Sciences, par divers Savans, & Iûs dans ses Assemblées*, 7:343–382, 1773.

C. Creton and M. Ciccotti. Fracture and adhesion of soft materials: a review. *Reports on Progress in Physics*, 79(4):046601, 2016.

C. Creton, J. Hooker, and K. R. Shull. Bulk and Interfacial Contributions to the Debonding Mechanisms of Soft Adhesives: Extension to Large Strains. *Langmuir*, 17(16):4948–4954, 2001.

J. C. Criscione, J. D. Humphrey, A. S. Douglas, and W. C. Hunter. An invariant basis for natural strain which yields orthogonal stress response terms in isotropic hyperelasticity. *Journal of the Mechanics and Physics of Solids*, 48(12):2445–2465, 2000.

A. D. Crocombe and D. A. Bigwood. Development of a full elasto-plastic adhesive joint design analysis. *The Journal of Strain Analysis for Engineering Design*, 27(4):211–218, 1992.

R. G. Cuntze. Fracture-type strength criteria formulated by invariants which consider the material symmetries of the isotropic/anisotropic material used. In W. R. Burke, editor, *Proceedings of Spacecraft Structures, Materials and Mechanical Engineering*, pages 399–409, Noordwijk, 1996.

R. G. Cuntze. The failure mode concept – A new comprehensive 3D-strength analysis concept for any brittle and ductile behaving material. In *Proceedings of the European Conference on Spacecraft Structures, Materials and Mechanical Testing*, pages 296–287, Braunschweig, 1999.

R. G. Cuntze. The predictive capability of failure mode concept-based strength criteria for multidirectional laminates—part B. *Composites Science and Technology*, 64(3-4):487–516, 2004.

R. G. Cuntze. Failure conditions for isotropic materials, unidirectional composites, woven fabrics – their visualization and links. In *Conference on Damage in Composite Materials*, pages 1–18, Stuttgart, 2006.

R. G. Cuntze and A. Freund. The predictive capability of failure mode concept-based strength criteria for multidirectional laminates. In *Failure Criteria in Fibre-Reinforced-Polymer Composites*, pages 429–489. Elsevier, 2004.

L. F. M. da Silva, P. J. C. das Neves, R. D. Adams, and J. K. Spelt. Analytical models of adhesively bonded joints—Part I: Literature survey. *International Journal of Adhesion and Adhesives*, 29(3): 319–330, 2009.

H. Dal and M. Kaliske. A micro-continuum-mechanical material model for failure of rubber-like materials: Application to ageing-induced fracturing. *Journal of the Mechanics and Physics of Solids*, 57(8):1340–1356, 2009.

P. J. C. das Neves, L. F. M. da Silva, and R. D. Adams. Analysis of Mixed Adhesive Bonded Joints Part I: Theoretical Formulation. *Journal of Adhesion Science and Technology*, 23(1):1–34, 2009.

J. D. Davidson and N. C. Goulbourne. A nonaffine network model for elastomers undergoing finite deformations. *Journal of the Mechanics and Physics of Solids*, 61(8):1784–1797, 2013.

J. Diani and P. Gilormini. Combining the logarithmic strain and the full-network model for a better understanding of the hyperelastic behavior of rubber-like materials. *Journal of the Mechanics and Physics of Solids*, 53(11):2579–2596, 2005.

V. Dias, C. Odenbreit, O. Hechler, F. Scholzen, and T. Ben Zineb. Development of a constitutive hyperelastic material law for numerical simulations of adhesive steel–glass connections using structural silicone. *International Journal of Adhesion and Adhesives*, 48:194–209, 2014.

R. A. Dickie and T. L. Smith. Ultimate tensile properties of elastomers. VI. Strength and extensibility of a styrene–butadiene rubber vulcanizate in equal biaxial tension. *Journal of Polymer Science Part A-2: Polymer Physics*, 7(4):687–707, 1969.

DIN Standard 743-2. *Calculation of load capacity of shafts and axles – Part 2: Theoretical stress concentration factors and fatigue notch factors*. Deutsches Institut für Normung e.V., Berlin, 2012.

J. Dispersyn, S. Hertelé, W. D. Waele, and J. Belis. Assessment of hyperelastic material models for the application of adhesive point-fixings between glass and metal. *International Journal of Adhesion and Adhesives*, 77(March):102–117, 2017.

A. Doitrand and D. Leguillon. Comparison between 2D and 3D applications of the coupled criterion to crack initiation prediction in scarf adhesive joints. *International Journal of Adhesion and Adhesives*, 85:69–76, 2018a.

A. Doitrand and D. Leguillon. 3D application of the coupled criterion to crack initiation prediction in epoxy/aluminum specimens under four point bending. *International Journal of Solids and Structures*, 143:175–182, 2018b.

A. Doitrand and A. Sapora. Nonlinear implementation of Finite Fracture Mechanics: A case study on notched Brazilian disk samples. *International Journal of Non-Linear Mechanics*, page 103245, 2019.

A. Doitrand, R. Estevez, and D. Leguillon. Comparison between cohesive zone and coupled criterion modeling of crack initiation in rhombus hole specimens under quasi-static compression. *Theoretical and Applied Fracture Mechanics*, 99:51–59, 2019.

S. Dölling, J. Hahn, J. Felger, S. Bremm, and W. Becker. A scaled boundary finite element method model for interlaminar failure in composite laminates. *Composite Structures*, (under review), 2020.

A. Dorfmann, K. N. G. Fuller, and R. W. Ogden. Shear, compressive and dilatational response of rubberlike solids subject to cavitation damage. *International Journal of Solids and Structures*, 39 (7):1845–1861, 2002.

Dow Automotive Systems. *BETAFORCE Composite Bonding Adhesives for Lightweight Multimaterial Vehicles*. Product sheet, Form No. 299-52330-0816, 2019.

Dow Chemical Company. *Silicone Structural Glazing Manual*. Seneffe, Belgium, Form Number: 62-0979-01, 2018.

Dow Chemical Company. *DOWSIL™ TSSA/TSSL Technical Manual*. Seneffe, Belgium, Form Number: 62-2010-01, 2019.

Dow Corning Corporation. *Silicone Structural Glazing Manual*. Seneffe, Belgium, Form Number: 62-0979H-01, 2011.

M. Drass. *Constitutive Modelling and Failure Prediction for Silicone Adhesives in Facade Design*. Dissertation, Technische Universtität Darmstadt, Wiesbaden, 2020.

M. Drass, V. A. Kolupaev, P. L. Rosendahl, J. Schneider, and W. Becker. Generalized cavitation criterion for poro-hyperelastic materials. In J. Schneider and N. Kiziltoprak, editors, *Baustatik-Baupraxis e.V. Forschungskolloquium 2018 Grasellenbach*, pages 20–23. Springer, Wiesbaden, 2018a.

M. Drass, V. A. Kolupaev, J. Schneider, and S. Kolling. On cavitation in transparent structural silicone adhesive: TSSA. *Glass Structures & Engineering*, 3(2):237–256, 2018b.

M. Drass, J. Schneider, and S. Kolling. Novel volumetric Helmholtz free energy function accounting for isotropic cavitation at finite strains. *Materials & Design*, 138:71–89, 2018c.

M. Drass, J. Schneider, and S. Kolling. Damage effects of adhesives in modern glass façades: a micro-mechanically motivated volumetric damage model for poro-hyperelastic materials. *International Journal of Mechanics and Materials in Design*, 14(4):591–616, 2018d.

M. Drass, G. Schwind, J. Schneider, and S. Kolling. Adhesive connections in glass structures—part I: experiments and analytics on thin structural silicone. *Glass Structures & Engineering*, 3(1): 39–54, 2018e.

M. Drass, G. Schwind, J. Schneider, and S. Kolling. Adhesive connections in glass structures—part II: material parameter identification on thin structural silicone. *Glass Structures & Engineering*, 3(1):55–74, 2018f.

M. Drass, J. Muth, C. Louter, and J. Schneider. Stress whitening effects in transparent structural silicone adhesives. *Glass Structures & Engineering*, 2019.

M. Drass, P. L. Rosendahl, and M. A. Kraus. Coupled distortional-dilatational failure mode concept for rubber-like materials. *Mechanics of Materials*, (in press), 2020.

A. D. Drozdov. Constitutive equations in finite elasticity of rubbers. *International Journal of Solids and Structures*, 44(1):272–297, 2007.

D. C. Drucker and W. Prager. Soil mechanics and plastic analysis or limit design. *Quarterly of Applied Mathematics*, 10(2):157–165, 1952.

D. S. Dugdale. Yielding of steel sheets containing slits. *Journal of the Mechanics and Physics of Solids*, 8(2):100–104, 1960.

B. Duncan and G. Dean. Measurements and models for design with modern adhesives. *International Journal of Adhesion and Adhesives*, 23(2):141–149, 2003.

G. Duvaut and J. L. Lions. *Inequalities in Mechanics and Physics*, volume 219 of *Grundlehren der mathematischen Wissenschaften*. Springer, Berlin, Heidelberg, 1976.

S. F. Edwards and T. A. Vilgis. The effect of entanglements in rubber elasticity. *Polymer*, 27(4): 483–492, 1986.

M. H. El Haddad, N. E. Dowling, T. H. Topper, and K. N. Smith. J integral applications for short fatigue cracks at notches. *International Journal of Fracture*, 16(1):15–30, 1980.

A. Elías-Zúñiga and M. F. Beatty. Constitutive equations for amended non-Gaussian network models of rubber elasticity. *International Journal of Engineering Science*, 40(20):2265–2294, 2002.

EOTA. *ETAG 002 – European Technical Approval Guideline for Structural Sealant Glazing Systems*. European Organization for Technical Approvals EOTA, Brussels, 2012.

J. D. Eshelby. The Force on an Elastic Singularity. *Philosophical Transactions of the Royal Society A: Mathematical, Physical and Engineering Sciences*, 244(877):87–112, 1951.

J. D. Eshelby. Energy Relations and the Energy-Momentum Tensor in Continuum Mechanics. In J. M. Ball, D. Kinderlehrer, P. Podio-Guidugli, and M. Slemrod, editors, *Fundamental Contributions to the Continuum Theory of Evolving Phase Interfaces in Solids*, pages 82–119. Springer, Berlin, Heidelberg, 1999.

E. Euchler, K. Schneider, G. Heinrich, S. Wießner, R. Bernhardt, S. V. Roth, and T. Tada. Failure of rubber vulcanizates. *Tire Technology International Annual Review*, pages 100–103, 2018.

J. Felger, P. L. Rosendahl, N. Stein, and W. Becker. Finite Bruchmechanik: Bewertung von singulären und nichtsingulären Spannungskonzentrationen. In *DVM-Bericht 249*, pages 111–120. Deutscher Verband für Materialforschung und -prüfung e.V., 2017a.

J. Felger, N. Stein, and W. Becker. Asymptotic finite fracture mechanics solution for crack onset at elliptical holes in composite plates of finite-width. *Engineering Fracture Mechanics*, 182:621–634, 2017b.

J. Felger, N. Stein, and W. Becker. Mixed-mode fracture in open-hole composite plates of finite-width: An asymptotic coupled stress and energy approach. *International Journal of Solids and Structures*, 122-123:14–24, 2017c.

J. Felger, P. L. Rosendahl, C. Frey, and W. Becker. Das Konzept der finiten Bruchmechanik zur Analyse von Rissentstehung an Materialübergängen. In *DVM-Bericht 250*, pages 99–109. Deutscher Verband für Materialforschung und -prüfung e.V., Paderborn, Germany, 2018.

J. Felger, P. L. Rosendahl, D. Leguillon, and W. Becker. Predicting crack patterns at bi-material junctions: A coupled stress and energy approach. *International Journal of Solids and Structures*, 164:191–201, 2019a.

J. Felger, N. Stein, C. Frey, and W. Becker. Scaling laws for the adhesive composite butt joint strength derived by finite fracture mechanics. *Composite Structures*, 208:546–556, 2019b.

M. M. Filonenko-Boroditsch. *Theory of elasticity*. Peace Publishers, Moscow, 2nd edition, 1963.

P. J. Flory. Network Structure and the Elastic Properties of Vulcanized Rubber. *Chemical Reviews*, 35(1):51–75, 1944.

P. J. Flory. Thermodynamic relations for high elastic materials. *Transactions of the Faraday Society*, 57:829–838, 1961.

P. J. Flory. Theory of elasticity of polymer networks. The effect of local constraints on junctions. *The Journal of Chemical Physics*, 66(12):5720–5729, 1977.

P. J. Flory and J. Rehner. Statistical Mechanics of Cross-Linked Polymer Networks I. Rubberlike Elasticity. *The Journal of Chemical Physics*, 11(11):512–520, 1943.

C. Fond. Cavitation criterion for rubber materials: A review of void-growth models. *Journal of Polymer Science Part B: Polymer Physics*, 39(17):2081–2096, 2001.

M. Fonselius. Effect of size on the bending strength of laminated veneer lumber. *Wood Science and Technology*, 31(6):399–413, 1997.

P. Fraisse and F. Schmit. Use of J-integral as fracture parameter in simplified analysis of bonded joints. *International Journal of Fracture*, 63(1):59–73, 1993.

G. A. Francfort and J.-J. Marigo. Revisiting brittle fracture as an energy minimization problem. *Journal of the Mechanics and Physics of Solids*, 46(8):1319–1342, 1998.

L. B. Freund. *Dynamic Fracture Mechanics*. Cambridge University Press, Cambridge, 1990.

Y. Frostig, O. T. Thomsen, and F. Mortensen. Analysis of Adhesive-Bonded Joints, Square-End, and Spew-Fillet—High-Order Theory Approach. *Journal of Engineering Mechanics*, 125(11): 1298–1307, 1999.

I. G. García, V. Mantič, and E. Graciani. A model for the prediction of debond onset in spherical-particle-reinforced composites under tension. Application of a coupled stress and energy criterion. *Composites Science and Technology*, 106:60–67, 2015.

I. G. García, B. J. Carter, A. R. Ingraffea, and V. Mantič. A numerical study of transverse cracking in cross-ply laminates by 3D finite fracture mechanics. *Composites Part B: Engineering*, 95(1): 475–487, 2016.

I. G. García, V. Mantič, and A. Blázquez. The effect of residual thermal stresses on transverse cracking in cross-ply laminates: an application of the coupled criterion of the finite fracture mechanics. *International Journal of Fracture*, 51, 2018a.

I. G. García, V. Mantič, and A. Blázquez. The effect of residual thermal stresses on transverse cracking in cross-ply laminates: an application of the coupled criterion of the finite fracture mechanics. *International Journal of Fracture*, 211(1-2):61–74, 2018b.

I. G. García, J. Justo, A. Simon, and V. Mantič. Experimental study of the size effect on transverse cracking in cross-ply laminates and comparison with the main theoretical models. *Mechanics of Materials*, 128(September 2018):24–37, 2019.

T. C. Gasser and G. A. Holzapfel. Modeling 3D crack propagation in unreinforced concrete using PUFEM. *Computer Methods in Applied Mechanics and Engineering*, 194(25-26):2859–2896, 2005.

E. E. Gdoutos. *Fracture Mechanics Criteria and Applications*. Springer Netherlands, Dordrecht, 1990.

A. N. Gent and P. B. Lindley. Internal Rupture of Bonded Rubber Cylinders in Tension. *Proceedings of the Royal Society A: Mathematical, Physical and Engineering Sciences*, 249(1257):195–205, 1959.

A. N. Gent and A. G. Thomas. Forms for the stored (strain) energy function for vulcanized rubber. *Journal of Polymer Science*, 28(118):625–628, 1958.

G. Geymonat, F. Krasucki, and S. Lenci. Mathematical Analysis of a Bonded Joint with a Soft Thin Adhesive. *Mathematics and Mechanics of Solids*, 4(2):201–225, 1999.

M. Goland and E. Reissner. The stresses in cemented joints. *Journal of Applied Mechanics*, 11(1): A17–A27, 1944.

A. E. Green and W. Zerna. *Theoretical elasticity*. Clarendon Press, Oxford, 1954.

A. A. Griffith. The Phenomena of Rupture and Flow in Solids. *Philosophical Transactions of the Royal Society A: Mathematical, Physical and Engineering Sciences*, 221(582-593):163–198, 1921.

D. Gross and T. Seelig. *Bruchmechanik*. Springer, Berlin, Heidelberg, 6th edition, 2016.

A. L. Gurson. Continuum Theory of Ductile Rupture by Void Nucleation and Growth: Part I—Yield Criteria and Flow Rules for Porous Ductile Media. *Journal of Engineering Materials and Technology*, 99(1):2, 1977.

M. E. Gurtin. *An Introduction to Continuum Mechanics*. Academic Press, New York, 1st edition, 1981.

E. Guth and H. Mark. Zur innermolekularen, Statistik, insbesondere bei Kettenmolekiilen I. *Monatshefte für Chemie*, 65(1):93–121, 1934.

A. Hagl. Development and test logics for structural silicone bonding design and sizing. *Glass Structures & Engineering*, 1(1):131–151, 2016.

B. P. Haigh. Strain-energy function and the elastic limit. In *Report of the Eighty-Seventh Meeting of the British Association for the Advancement of Science*, pages 486–495, Bournemouth, 1920. John Murray.

D. W. Haines and W. D. Wilson. Strain-energy density function for rubberlike materials. *Journal of the Mechanics and Physics of Solids*, 27(4):345–360, 1979.

A. Hamdi and H. Mahjoubi. Design criterion for rubbery parts under biaxial loading. *Theoretical and Applied Fracture Mechanics*, 78:51–55, 2015.

A. Hamdi, M. Naït Abdelaziz, N. Aït Hocine, P. Heuillet, and N. Benseddiq. A fracture criterion of rubber-like materials under plane stress conditions. *Polymer Testing*, 25(8):994–1005, 2006a.

A. Hamdi, M. Naït Abdelaziz, N. A. Hocine, and P. Heuillet. Fracture criteria of rubber-like materials under plane stress conditions. *Fracture of Nano and Engineering Materials and Structures – Proceedings of the 16th European Conference of Fracture*, 2006b.

A. Hamdi, N. Aït Hocine, M. N. Abdelaziz, and N. Benseddiq. Fracture of elastomers under static mixed mode: The strain-energy-density factor. *International Journal of Fracture*, 144(2):65–75, 2007a.

A. Hamdi, M. Naït Abdelaziz, N. Aït Hocine, P. Heuillet, and N. Benseddiq. A new generalized fracture criterion of elastomers under quasi-static plane stress loadings. *Polymer Testing*, 26(7): 896–902, 2007b.

L. J. Hart-Smith. Elasticity parameters for finite deformations of rubber-like materials. *Zeitschrift für angewandte Mathematik und Physik ZAMP*, 17(5):608–626, 1966.

L. J. Hart-Smith. Adhesive-bonded double-lap joints. Technical report, CR-112235, Langley Research Center, NASA, Hampton, Virginia, 1973a.

L. J. Hart-Smith. Adhesive bonded scarf and stepped-lap joints. Technical report, CR-112237, Langley Research Center, NASA, Hampton, Virginia, 1973b.

L. J. Hart-Smith. Adhesive-bonded single lap joints. Technical report, CR-112236, Langley Research Center, NASA, Hampton, Virginia, 1973c.

L. J. Hart-Smith. Stress Analysis: A Continuum Mechanics Approach. In A. J. Kinloch, editor, *Developments in Adhesives 2*, pages 1–43. Applied Science Publishers, London, 1981.

S. Hartmann and P. Neff. Polyconvexity of generalized polynomial-type hyperelastic strain energy functions for near-incompressibility. *International Journal of Solids and Structures*, 40(11): 2767–2791, 2003.

S. Hashemi, A. J. Kinloch, and J. G. Williams. The Analysis of Interlaminar Fracture in Uniaxial Fibre-Polymer Composites. *Proceedings of the Royal Society A: Mathematical, Physical and Engineering Sciences*, 427(1872):173–199, 1990.

Z. Hashin. Finite thermoelastic fracture criterion with application to laminate cracking analysis. *Journal of the Mechanics and Physics of Solids*, 44(7):1129–1145, 1996.

Z. Hashin. Thin interphase/imperfect interface in elasticity with application to coated fiber composites. *Journal of the Mechanics and Physics of Solids*, 50(12):2509–2537, 2002.

R. M. Haythornthwaite. Mechanics of the triaxial test for soils. *Journal of the Soil Mechanics and Foundations Division*, 86(5):35–62, 1960.

J. Hebel, R. Dieringer, and W. Becker. Modelling brittle crack formation at geometrical and material discontinuities using a finite fracture mechanics approach. *Engineering Fracture Mechanics*, 77 (18):3558–3572, 2010.

G. Heinrich and M. Kaliske. Theoretical and numerical formulation of a molecular based constitutive tube-model of rubber elasticity. *Computational and Theoretical Polymer Science*, 7(3-4): 227–241, 1997.

S. Hell and W. Becker. The scaled boundary finite element method for the analysis of 3D crack interaction. *Journal of Computational Science*, 9:76–81, 2015.

S. Hell, P. Weißgraeber, J. Felger, and W. Becker. A coupled stress and energy criterion for the assessment of crack initiation in single lap joints: A numerical approach. *Engineering Fracture Mechanics*, 117:112–126, 2014.

H. Hencky. Über die Form des Elastizitätsgesetzes bei ideal elastischen Stoffen. *Zeitschrift für technische Physik*, 9:215–220, 1928.

H. Hencky. The Law of Elasticity for Isotropic and Quasi-Isotropic Substances by Finite Deformations. *Journal of Rheology*, 2(2):169–176, 1931.

H. Hencky. The Elastic Behavior of Vulcanized Rubber. *Rubber Chemistry and Technology*, 6(2): 217–224, 1933.

M. Heydari-Meybodi, M. R. Ayatollahi, M. Dehghany, and F. Berto. Mixed-mode (I/II) failure assessment of rubber materials using the effective stretch criterion. *Theoretical and Applied Fracture Mechanics*, 91:126–133, 2017.

References

M. Heydari-Meybodi, M. R. Ayatollahi, and F. Berto. Rupture analysis of rubber in the presence of a sharp V-shape notch under pure mode-I loading. *International Journal of Mechanical Sciences*, 146-147:405–415, 2018.

R. Hill. The essential structure of constitutive laws for metal composites and polycrystals. *Journal of the Mechanics and Physics of Solids*, 15(2):79–95, 1967.

R. Hill. On the elasticity and stability of perfect crystals at finite strain. *Mathematical Proceedings of the Cambridge Philosophical Society*, 77(1):225–240, 1975.

G. A. Holzapfel. *Nonlinear solid mechanics*. John Wiley & Sons Ltd., Chichester, 1st edition, 2000.

C. O. Horgan and J. G. Murphy. Limiting Chain Extensibility Constitutive Models of Valanis–Landel Type. *Journal of Elasticity*, 86(2):101–111, 2007.

C. O. Horgan and G. Saccomandi. Phenomenological Hyperelastic Strain-Stiffening Constitutive Models for Rubber. *Rubber Chemistry and Technology*, 79(1):152–169, 2006.

H.-S. Hou and R. Abeyaratne. Cavitation in elastic and elastic-plastic solids. *Journal of the Mechanics and Physics of Solids*, 40(3):571–592, 1992.

S. S. Hsieh, E. C. Ting, and W. F. Chen. A plastic-fracture model for concrete. *International Journal of Solids and Structures*, 18(3):181–197, 1982.

G. Hu. Mixed mode fracture analysis of adhesive lap joints. *Composites Engineering*, 5(8):1043–1050, 1995.

G. R. Irwin. Analysis of Stresses and Strains near the End of a Crack Traversing a Plate. *Journal of Applied Mechanics*, 24:351–369, 1957.

G. R. Irwin. Fracture. In S. Flügge, editor, *Encyclopedia of Physics: Elasticity and Plasticity*, volume 3/6, pages 551–590. Springer, Berlin, Heidelberg, 1958.

G. R. Irwin. Plastic zone near a crack and fracture toughness. In *Proceedings of the 7th Sagamore Ordnance Materials Research Conference*, pages 63–78. Syracuse University Press, 1960.

G. R. Irwin. Relation of crack toughness measurements to practical applications. *Welding Journal, Research Supplement*, 41(11):519–528, 1962.

G. R. Irwin and J. A. Kies. Critical energy rate analysis of fracture strength. *Welding Journal*, 33: 193–198, 1954.

A. Y. Ishlinsky and D. D. Ivlev. *Mathematical theory of plasticity (russ.: Matematicheskaja teorija plastichnosti)*. Fizmatlit, Moscow, 2003.

A. Isihara, N. Hashitsume, and M. Tatibana. Statistical Theory of Rubber-Like Elasticity. IV. (Two-Dimensional Stretching). *The Journal of Chemical Physics*, 19(12):1508–1512, 1951.

ISO Standard 7743. *Rubber, vulcanized or thermoplastic – determination of compression stress-strain properties*. International Organization for Standardization, Geneva, Switzerland, 2017.

M. Itskov, A. E. Ehret, and R. Dargazany. A Full-Network Rubber Elasticity Model based on Analytical Integration. *Mathematics and Mechanics of Solids*, 15(6):655–671, 2010.

D. D. Ivlev. The theory of fracture of solids. *Journal of Applied Mathematics and Mechanics*, 23(3): 884–895, 1959.

A. G. James, A. Green, and G. M. Simpson. Strain energy functions of rubber. I. Characterization of gum vulcanizates. *Journal of Applied Polymer Science*, 19(7):2033–2058, 1975.

H. M. James and E. Guth. Theory of the Elastic Properties of Rubber. *The Journal of Chemical Physics*, 11(10):455–481, 1943.

Z. Javanbakht, M. Aßmus, K. Naumenko, A. Öchsner, and H. Altenbach. On thermal strains and residual stresses in the linear theory of anti-sandwiches. *ZAMM – Journal of Applied Mathematics and Mechanics / Zeitschrift für Angewandte Mathematik und Mechanik*, 99(8):1–17, 2019.

S. Jemioło and A. Szwed. Construction of the Deviatoric Shape Function for the Cross-Sections of the Limit Surfaces. In *Seria Monografie Zakładu Wytrzymałości Materiałów, Teorii Sprężystości i Plastyczności ZWMTSiP, Deformacje i Wytrzymałość Materiałów i Elementów Konstrukcji*, pages 51–66. Wydział Inżynierii Lądowej Politechniki Warszawskiej, Warszawa, 2013.

R. M. Jones. *Mechanics of Composite Materials*. Taylor & Francis Inc., Philadelphia, 2nd edition, 1998.

T. M. Jones and R. B. Kruse. Failure behavior of composite hydrocarbon fuel binder propellants. *Journal of Spacecraft and Rockets*, 3(2):265–267, 1966.

J. Jumel, N. Ben Salem, M. K. Budzik, and M. E. R. Shanahan. Measurement of interface cohesive stresses and strains evolutions with combined mixed mode crack propagation test and Backface Strain Monitoring measurements. *International Journal of Solids and Structures*, 52:33–44, 2015.

M. Kaliske and G. Heinrich. An Extended Tube-Model for Rubber Elasticity: Statistical-Mechanical Theory and Finite Element Implementation. *Rubber Chemistry and Technology*, 72(4):602–632, 1999.

S. Kawabata. Fracture and Mechanical Behavior of Rubber-Like Polymers under Finite Deformation in Biaxial Stress Field. *Journal of Macromolecular Science-Physics, Part B*, 8(3-4):605–630, 1973.

S. Kawabata, M. Matsuda, K. Tei, and H. Kawai. Experimental survey of the strain energy density function of isoprene rubber vulcanizate. *Macromolecules*, 14(1):154–162, 1981.

E. A. Kearsley. Note: Strain Invariants Expressed as Average Stretches. *Journal of Rheology*, 33(5): 757–760, 1989.

H. Khajehsaeid, J. Arghavani, and R. Naghdabadi. A hyperelastic constitutive model for rubber-like materials. *European Journal of Mechanics - A/Solids*, 38:144–151, 2013.

A. Khayer Dastjerdi, E. Tan, and F. Barthelat. Direct Measurement of the Cohesive Law of Adhesives Using a Rigid Double Cantilever Beam Technique. *Experimental Mechanics*, 53(9):1763–1772, 2013.

V. N. Khiêm and M. Itskov. Analytical network-averaging of the tube model: Rubber elasticity. *Journal of the Mechanics and Physics of Solids*, 95:254–269, 2016.

H.-G. Kilian. Equation of state of real networks. *Polymer*, 22(2):209–217, 1981.

R. Klarmann and K. Schweizerhof. A Priori Verbesserung von Schubkorrekturfaktoren zur Berechnung von geschichteten anisotropen Schalentragwerken. *Archive of Applied Mechanics*, 63(2):73–85, 1993.

M. Klüppel and J. Schramm. A generalized tube model of rubber elasticity and stress softening of filler reinforced elastomer systems. *Macromolecular Theory and Simulations*, 9(9):742–754, 2000.

W. G. Knauss. An upper bound of failure in viscoelastic materials subjected to multiaxial stress states. *International Journal of Fracture Mechanics*, 3(4):267–277, 1967.

W. L. Ko. *Application of finite elastic theory to the behavior of rubber-like materials*. PhD thesis, California Institute of Technology, Pasadena, 1963.

V. A. Kolupaev. Generalized Strength Criteria as Functions of the Stress Angle. *Journal of Engineering Mechanics*, 143(9):04017095, 2017.

V. A. Kolupaev. *Equivalent Stress Concept for Limit State Analysis*, volume 86 of *Advanced Structured Materials*. Springer International Publishing, Cham, 2018.

V. A. Kolupaev and H. Altenbach. Einige Überlegungen zur Unified Strength Theory von Mao-Hong Yu. *Forschung im Ingenieurwesen*, 74(3):135–166, 2010.

S. Krenk. Energy release rate of symmetric adhesive joints. *Engineering Fracture Mechanics*, 43(4): 549–559, 1992.

M. Kroon. An 8-chain model for rubber-like materials accounting for non-affine chain deformations and topological constraints. *Journal of Elasticity*, 102(2):99–116, 2011.

R. Krueger. Virtual crack closure technique: History, approach, and applications. *Applied Mechanics Reviews*, 57(2):109, 2004.

W. Kuhn. Über die Gestalt fadenförmiger Moleküle in Lösungen. *Kolloid-Zeitschrift*, 68(1):2–15, feb 1934.

W. Kuhn. Die Bedeutung der Nebenvalenzkräfte für die elastischen Eigenschaften hochmolekularer Stoffe. *Angewandte Chemie*, 51(37):640–647, 1938.

W. Kuhn. Dependence of the average transversal on the longitudinal dimensions of statistical coils formed by chain molecules. *Journal of Polymer Science*, 1(5):380–388, 1946.

W. Kuhn and F. Grün. Beziehungen zwischen elastischen Konstanten und Dehnungsdoppelbrechung hochelastischer Stoffe. *Kolloid-Zeitschrift*, 101(3):248–271, 1942.

S. Kumar. Analysis of tubular adhesive joints with a functionally modulus graded bondline subjected to axial loads. *International Journal of Adhesion and Adhesives*, 29(8):785–795, 2009.

S. Kumar and J. P. Scanlan. Stress Analysis of Shaft-Tube Bonded Joints Using a Variational Method. *The Journal of Adhesion*, 86(4):369–394, 2010.

H. Kupfer. *Das Verhalten des Betons unter mehrachsiger Kurzzeitbelastung unter besonderer Berücksichtigung der zweiachsigen Beanspruchung*. PhD thesis, Technische Universtität München, 1972.

H. Kupfer and K. H. Gerstle. Behavior of Concrete Under Biaxial Stresses. *Journal of the Engineering Mechanics Division*, 99(4):853–866, 1973.

H. Kupfer and C. Zelger. Das Verhalten des Betons unter mehrachsiger Kurzzeitbelastung unter besonderer Berücksichtigung der zweiachsigen Beanspruchung. In *Deutscher Ausschuss für Stahlbeton 229*. Ernst & Sohn, Berlin, 1973.

H. Kupfer, H. K. Hilsdorf, and H. Rusch. Behavior of Concrete Under Biaxial Stresses. *Journal of the American Concrete Institute*, 8:656–666, 1969.

P. V. Lade. Modelling the strengths of engineering materials in three dimensions. *Mechanics of Cohesive-frictional Materials*, 2(4):339–356, 1997.

P. V. Lade and M. K. Kim. Single hardening constitutive model for soil, rock and concrete. *International Journal of Solids and Structures*, 32(14):1963–1978, 1995.

J. Lambert-Diani and C. Rey. New phenomenological behavior laws for rubbers and thermoplastic elastomers. *European Journal of Mechanics - A/Solids*, 18(6):1027–1043, 1999.

K. A. Lazopoulos and R. W. Ogden. Nonlinear Elasticity Theory with Discontinuous Internal Variables. *Mathematics and Mechanics of Solids*, 3(1):29–51, 1998.

P. Lazzarin and R. Zambardi. A finite-volume-energy based approach to predict the static and fatigue behavior of components with sharp V-shaped notches. *International Journal of Fracture*, 112(3):275–298, 2001.

D. Leguillon. Strength or toughness? A criterion for crack onset at a notch. *European Journal of Mechanics – A/Solids*, 21(1):61–72, 2002.

D. Leguillon. A simple model of thermal crack pattern formation using the coupled criterion. *Comptes Rendus Mécanique*, 341(6):538–546, 2013.

D. Leguillon and E. Martin. The strengthening effect caused by an elastic contrast – part I: the bimaterial case. *International Journal of Fracture*, 179(1-2):157–167, 2013a.

D. Leguillon and E. Martin. The strengthening effect caused by an elastic contrast—part II: stratification by a thin stiff layer. *International Journal of Fracture*, 179(1-2):169–178, 2013b.

D. Leguillon and Z. Yosibash. Failure initiation at V-notch tips in quasi-brittle materials. *International Journal of Solids and Structures*, 122-123:1–13, 2017.

D. Leguillon, O. Haddad, M. Adamowska, and P. Da Costa. Cracks Pattern Formation and Spalling in Functionalized Thin Films. *Procedia Materials Science*, 3:104–109, 2014.

D. Leguillon, É. Martin, and M.-C. Lafarie-Frenot. Flexural vs. tensile strength in brittle materials. *Comptes Rendus Mécanique*, 343(4):275–281, 2015a.

D. Leguillon, E. Martin, O. Ševeček, and R. Bermejo. Application of the coupled stress-energy criterion to predict the fracture behaviour of layered ceramics designed with internal compressive stresses. *European Journal of Mechanics - A/Solids*, 54:94–104, 2015b.

D. Leguillon, E. Martin, O. Sevecek, and R. Bermejo. What is the tensile strength of a ceramic to be used in numerical models for predicting crack initiation? *International Journal of Fracture*, 212(1):89–103, 2018.

S. Lenci. Analysis of a crack at a weak interface. *International Journal of Fracture*, 108(3):275–290, 2001.

M. Y. Leonov and V. V. Panasyuk. Development of the smallest cracks in a solid. *Prikladnaya Mechanika*, 5(4):391–401, 1959.

J. Li, E. Martin, D. Leguillon, and C. Dupin. A finite fracture model for the analysis of multi-cracking in woven ceramic matrix composites. *Composites Part B: Engineering*, 139:75–83, 2018.

V. C. Li and R. J. Ward. A novel testing technique for post-peak tensile behaviour of cementitious materials. In H. Mihashi, H. Takahashi, and F. Wittmann, editors, *Fracture Toughness and Fracture Energy*, pages 183–195. CRC Press, 1989.

G. H. Lindsey. Triaxial Fracture Studies. *Journal of Applied Physics*, 38(12):4843, 1967.

Z. Liu, Y. Huang, Z. Yin, S. Bennati, and P. S. Valvo. A general solution for the two-dimensional stress analysis of balanced and unbalanced adhesively bonded joints. *International Journal of Adhesion and Adhesives*, 54:112–123, 2014.

W. Lode. Versuche über den Einfluss der mittleren Hauptspannung auf das Fließen der Metalle Eisen, Kupfer und Nickel. *Zeitschrift für Physik*, 36(11-12):913–939, 1926.

L. Loh and S. Marzi. An Out-of-plane Loaded Double Cantilever Beam (ODCB) test to measure the critical energy release rate in mode III of adhesive joints. *International Journal of Adhesion and Adhesives*, 83(March):24–30, 2018a.

L. Loh and S. Marzi. Mixed-mode I+III tests on hyperelastic adhesive joints at prescribed mode-mixity. *International Journal of Adhesion and Adhesives*, 85:113–122, 2018b.

L. Loh and S. Marzi. A Mixed-Mode Controlled DCB test on adhesive joints loaded in a combination of modes I and III. *Procedia Structural Integrity*, 13:1318–1323, 2018c.

L. Loh and S. Marzi. A novel experimental methodology to identify fracture envelopes and cohesive laws in mixed-mode I+III. *Engineering Fracture Mechanics*, 214(December 2018):304–319, 2019.

O. Lopez-Pamies. A new I1-based hyperelastic model for rubber elastic materials. *Comptes Rendus Mécanique*, 338(1):3–11, 2010.

O. Lopez-Pamies, M. I. Idiart, and T. Nakamura. Cavitation in elastomeric solids: I - A defect-growth theory. *Journal of the Mechanics and Physics of Solids*, 59(8):1464–1487, 2011a.

O. Lopez-Pamies, T. Nakamura, and M. I. Idiart. Cavitation in elastomeric solids: II—Onset-of-cavitation surfaces for Neo-Hookean materials. *Journal of the Mechanics and Physics of Solids*, 59(8):1488–1505, 2011b.

A. L. Loureiro, L. F. M. da Silva, C. Sato, and M. A. V. Figueiredo. Comparison of the Mechanical Behaviour Between Stiff and Flexible Adhesive Joints for the Automotive Industry. *The Journal of Adhesion*, 86(7):765–787, 2010.

J. Lubliner. A model of rubber viscoelasticity. *Mechanics Research Communications*, 12(2):93–99, 1985.

I. Lubowiecka, M. Rodríguez, E. Rodríguez, and D. Martínez. Experimentation, material modelling and simulation of bonded joints with a flexible adhesive. *International Journal of Adhesion and Adhesives*, 37:56–64, 2012.

G. Machado, D. Favier, and G. Chagnon. Membrane Curvatures and Stress-strain Full Fields of Axisymmetric Bulge Tests from 3D-DIC Measurements. Theory and Validation on Virtual and Experimental results. *Experimental Mechanics*, 52(7):865–880, 2012.

K. Machalická and M. Eliášová. Adhesive joints in glass structures: effects of various materials in the connection, thickness of the adhesive layer, and ageing. *International Journal of Adhesion and Adhesives*, 72:10–22, 2017.

J. Mandel. Contribution théorique à l'étude de l'écrouissage et des lois de l'écoulement plastique. In *Applied Mechanics*, pages 502–509. Springer, Berlin, Heidelberg, 1966.

M. R. Mansouri and H. Darijani. Constitutive modeling of isotropic hyperelastic materials in an exponential framework using a self-contained approach. *International Journal of Solids and Structures*, 51(25-26):4316–4326, 2014.

V. Mantič. Interface crack onset at a circular cylindrical inclusion under a remote transverse tension. Application of a coupled stress and energy criterion. *International Journal of Solids and Structures*, 46(6):1287–1304, 2009.

G. Marckmann and E. Verron. Comparison of Hyperelastic Models for Rubber-Like Materials. *Rubber Chemistry and Technology*, 79(5):835–858, 2006.

G. Marckmann, E. Verron, L. Gornet, G. Chagnon, P. Charrier, and P. Fort. A theory of network alteration for the Mullins effect. *Journal of the Mechanics and Physics of Solids*, 50(9):2011–2028, 2002.

H. Mardani, N. Stein, P. L. Rosendahl, and W. Becker. An effcient stress and deformation model for arbitrary elastic–perfectly plastic adhesive lap joints. *International Journal of Adhesion and Adhesives*, (under review), 2020.

R. S. Marlow. A general first-invariant hyperelastic constitutive model. In J. J. C. Busfield and A. H. Muhr, editors, *Constitutive Models for Rubber III*, pages 157–160. A. A. Balkema Publishers, Lisse, 2003.

W. V. Mars and A. Fatemi. A literature survey on fatigue analysis approaches for rubber. *International Journal of Fatigue*, 24(9):949–961, 2002.

W. V. Mars and A. Fatemi. Multiaxial fatigue of rubber: Part I: equivalence criteria and theoretical aspects. *Fatigue & Fracture of Engineering Materials and Structures*, 28(6):515–522, 2005.

W. V. Mars and A. Fatemi. Nucleation and growth of small fatigue cracks in filled natural rubber under multiaxial loading. *Journal of Materials Science*, 41(22):7324–7332, 2006.

J. Marsden and T. J. R. Hughes. *Mathematical foundations of elasticity*. Prentice-Hall, Inc., Englewood Cliffs, 1983.

E. Martin, B. Poitou, D. Leguillon, and J. M. Gatt. Competition between deflection and penetration at an interface in the vicinity of a main crack. *International Journal of Fracture*, 151(2):247–268, 2008.

E. Martin, D. Leguillon, and N. Carrère. A twofold strength and toughness criterion for the onset of free-edge shear delamination in angle-ply laminates. *International Journal of Solids and Structures*, 47(9):1297–1305, 2010.

S. Marzi, O. Hesebeck, M. Brede, and F. Kleiner. A Rate-Dependent Cohesive Zone Model for Adhesively Bonded Joints Loaded in Mode I. *Journal of Adhesion Science and Technology*, 23(6): 881–898, 2009a.

S. Marzi, O. Hesebeck, M. Brede, and F. Kleiner. An End-Loaded Shear Joint (ELSJ) Specimen to Measure the Critical Energy Release Rate in Mode II of Tough, Structural Adhesive Joints. *Journal of Adhesion Science and Technology*, 23(15):1883–1891, 2009b.

S. Marzi, A. Biel, and U. Stigh. On experimental methods to investigate the effect of layer thickness on the fracture behavior of adhesively bonded joints. *International Journal of Adhesion and Adhesives*, 31(8):840–850, 2011.

S. Marzi, A. Rauh, and R. M. Hinterhölzl. Fracture mechanical investigations and cohesive zone failure modelling on automotive composites. *Composite Structures*, 111(1):324–331, 2014.

MATLAB. *Version 9.1.* The MathWorks Inc., Natick, Massachusetts, 2016.

W. Mayland. *Untersuchungen zu Spannungssingularitätsordnungen in linear- elastischen und piezoelektrischen Multimaterialkonfigurationen mit der Rand-Finite-Elemente-Methode*. Dissertation, Technische Universität Darmstadt, Studienbereich Mechanik, 2012.

B. Meissner and L. Matějka. A Langevin-elasticity-theory-based constitutive equation for rubberlike networks and its comparison with biaxial stress–strain data. Part I. *Polymer*, 44(16):4599–4610, 2003.

C. Miehe. Aspects of the formulation and finite element implementation of large strain isotropic elasticity. *International Journal for Numerical Methods in Engineering*, 37(12):1981–2004, 1994.

C. Miehe and L.-M. Schänzel. Phase field modeling of fracture in rubbery polymers. Part I: Finite elasticity coupled with brittle failure. *Journal of the Mechanics and Physics of Solids*, 65:93–113, 2014.

C. Miehe and E. Stein. A canonical model of multiplicative elasto-plasticity: formulation and aspects of the numerical implementation. *European Journal of Mechanics – A/Solids*, 11:25–43, 1992.

C. Miehe, S. Göktepe, and F. Lulei. A micro-macro approach to rubber-like materials–Part I: the non-affine micro-sphere model of rubber elasticity. *Journal of the Mechanics and Physics of Solids*, 52(11):2617–2660, 2004.

O. Mohr. Welche Umstände bedingen die Elastizitätsgrenze und den Bruch eines Materials. *Zeitschrift des Vereins Deutscher Ingenieure*, 46:1572–1577, 1900.

G. Molnár, P. Ganster, A. Tanguy, E. Barthel, and G. Kermouche. Densification dependent yield criteria for sodium silicate glasses – An atomistic simulation approach. *Acta Materialia*, 111: 129–137, 2016.

M. Mooney. A Theory of Large Elastic Deformation. *Journal of Applied Physics*, 11(9):582–592, 1940.

A. Moradi, N. Carrère, D. Leguillon, E. Martin, and J.-Y. Cognard. Strength prediction of bonded assemblies using a coupled criterion under elastic assumptions: Effect of material and geometrical parameters. *International Journal of Adhesion and Adhesives*, 47:73–82, 2013.

F. Mortensen and O. T. Thomsen. Simplified linear and non-linear analysis of stepped and scarfed adhesive-bonded lap-joints between composite laminates. *Composite Structures*, 38(1-4):281–294, 1997.

F. Mortensen and O. T. Thomsen. Analysis of adhesive bonded joints: a unified approach. *Composites Science and Technology*, 62(7-8):1011–1031, 2002.

A. Müller, W. Becker, D. Stolten, and J. Hohe. A hybrid method to assess interface debonding by finite fracture mechanics. *Engineering Fracture Mechanics*, 73(8):994–1008, 2006.

P. M. Naghdi, F. Essenburg, and W. Koff. An experimental study of initial and subsequent yield surfaces in plasticity. *Journal of Applied Mechanics*, 25:201–209, 1958.

T. Nakamura and O. Lopez-Pamies. A finite element approach to study cavitation instabilities in non-linear elastic solids under general loading conditions. *International Journal of Non-Linear Mechanics*, 47(2):331–340, 2012.

K. Naumenko and V. A. Eremeyev. A layer-wise theory for laminated glass and photovoltaic panels. *Composite Structures*, 112(1):283–291, 2014.

P. Neff, I.-D. Ghiba, and J. Lankeit. The Exponentiated Hencky-Logarithmic Strain Energy. Part I: Constitutive Issues and Rank-One Convexity. *Journal of Elasticity*, 121(2):143–234, 2015.

P. Neff, B. Eidel, and R. J. Martin. Geometry of Logarithmic Strain Measures in Solid Mechanics. *Archive for Rational Mechanics and Analysis*, 222(2):507–572, 2016.

A. Nelson. *Modellierung und Finite-Elemente-Berechnung form- und stoffschlüssiger Fügeverbindungen*. Dissertation, Universität Kassel, kassel university press GmbH, 2019.

H. Neuber. Theorie der technischen Formzahl. *Forschung auf dem Gebiete des Ingenieurwesens*, 7 (6):271–274, 1936.

H. Neuber. *Kerbspannungslehre*. Springer, Berlin, Heidelberg, 1st edition, 1958.

H. Neuber. *Kerbspannungslehre*. Springer, Berlin, Heidelberg, 4th edition, 2001.

M. Nguyen-Hoang and W. Becker. Tension failure analysis for bolted joints using a closed-form stress solution. *Composite Structures*, 238:111931, apr 2020.

F. Nilsson. A Tentative Method for Determination of Cohesive Zone Properties in Soft Materials. *International Journal of Fracture*, 136(1-4):133–142, 2005.

V. V. Novozhilov. On a necessary and sufficient criterion for brittle strength. *Journal of Applied Mathematics and Mechanics*, 33(2):201–210, 1969.

R. W. Ogden. Large Deformation Isotropic Elasticity - On the Correlation of Theory and Experiment for Incompressible Rubberlike Solids. *Proceedings of the Royal Society A: Mathematical, Physical and Engineering Sciences*, 326:565–584, 1972a.

R. W. Ogden. Large Deformation Isotropic Elasticity: On the Correlation of Theory and Experiment for Compressible Rubberlike Solids. *Proceedings of the Royal Society A: Mathematical, Physical and Engineering Sciences*, 328:567–583, 1972b.

R. W. Ogden. *Non-linear elastic deformations*. Dover Publications, Inc., Mineola, New York, 1997.

R. W. Ogden and D. G. Roxburgh. A pseudo–elastic model for the Mullins effect in filled rubber. *Proceedings of the Royal Society of London. Series A: Mathematical, Physical and Engineering Sciences*, 455(1988):2861–2877, 1999.

I. U. Ojalvo and H. L. Eidinoff. Bond Thickness Effects upon Stresses in Single-Lap Adhesive Joints. *AIAA Journal*, 16(3):204–211, 1978.

P. Olsson and U. Stigh. On the determination of the constitutive properties of thin interphase layers - An exact inverse solution. *International Journal of Fracture*, 41(4):R71–R76, 1989.

M. Ortiz and A. Pandolfi. Finite-deformation irreversible cohesive elements for three-dimensional crack-propagation analysis. *International Journal for Numerical Methods in Engineering*, 44(9): 1267–1282, 1999.

N. S. Ottosen. A failure criterion for concrete. *Journal of the Engineering Mechanics Division, Proceedings of the American Society of Civil Engineers*, 103(4):527–353, 1977.

A. J. Paris and P. C. Paris. Instantaneous evaluation of J and C*. *International Journal of Fracture*, 38(1):R19–R21, 1988.

H. Parisch. *Festkörper-Kontinuumsmechanik*. Vieweg+Teubner, Wiesbaden, 2003.

B. Paul. Macroscopic criteria for plastic flow and brittle fracture. In H. Liebowitz, editor, *Fracture*, pages 313–496. Academic Press, New York, 1968.

R. W. Penn. Volume Changes Accompanying the Extension of Rubber. *Transactions of the Society of Rheology*, 14:509–517, 1970.

R. E. Peterson. Methods of correlating data from fatigue tests of stress concentration specimens. In *Stephen Timoshenko Anniversary Volume*, pages 179–183. Macmillan, New York, 1938.

A. Philipps. Experimental plasticity. Some thoughts on its present status and possible future trends. In A. A. Sawczuk, editor, *Problems of plasticity*, pages 193–233. Nordhoff International Publishing, Leyden, 1974.

W. D. Pilkey and D. F. Pilkey. *Peterson's Stress Concentration Factors*. John Wiley & Sons, Inc., 3. auflage edition, 2008.

R. B. Pipes, R. C. Wetherhold, and J. W. Gillespie. Notched Strength of Composite Materials. *Journal of Composite Materials*, 13(2):148–160, 1979.

G. S. Pisarenko and A. A. Lebedev. On the Shape of a Limit Surface for a Mechanical Strength Criterion. *Prikladnaja Mekhanika*, 4(3):45–50, 1968.

J. Podgórski. General Failure Criterion for Isotropic Media. *Journal of Engineering Mechanics*, 111 (2):188–201, 1985.

E. Pucci and G. Saccomandi. A Note on the Gent Model for Rubber-Like Materials. *Rubber Chemistry and Technology*, 75(5):839–852, 2002.

A. Puck and H. Schürmann. Failure analysis of FRP laminates by means of physically based phenomenological models. *Composites Science and Technology*, 58:1045–1067, 1998.

A. Puck and H. Schürmann. Failure analysis of FRP laminates by means of physically based phenomenological models. *Composites Science and Technology*, 62(12–13):1633–1662, 2002.

A. Puck and H. Schürmann. Failure analysis of FRP laminates by means of physically based phenomenological models. In *Failure Criteria in Fibre-Reinforced-Polymer Composites*, pages 832–876. Elsevier, 2004.

H. J. Qi and M. C. Boyce. Constitutive model for stretch-induced softening of the stress–stretch behavior of elastomeric materials. *Journal of the Mechanics and Physics of Solids*, 52(10):2187–2205, 2004.

W. J. M. Rankine. *Manual of Applied Mechanics*. Griffin, London, 1876.

J. N. Reddy. *Mechanics of Laminated Composite Plates and Shells: Theory and Analysis*. CRC Press, Boca Raton, 2nd edition, 2003.

W. J. Renton and J. R. Vinson. The Efficient Design of Adhesive Bonded Joints. *The Journal of Adhesion*, 7(3):175–193, 1975.

J. Rice. A Path Independent Integral and the Approximate Analysis of Strain Concentration by Notches and Cracks. *Journal of Applied Mechanics*, 35(2):379, 1968.

E. Riks. An incremental approach to the solution of snapping and buckling problems. *International Journal of Solids and Structures*, 15(7):529–551, 1979.

R. S. Rivlin. Large Elastic Deformations of Isotropic Materials. IV. Further Developments of the General Theory. *Philosophical Transactions of the Royal Society A: Mathematical, Physical and Engineering Sciences*, 241(835):379–397, 1948.

R. S. Rivlin and D. W. Saunders. Large Elastic Deformations of Isotropic Materials. VII. Experiments on the Deformation of Rubber. *Philosophical Transactions of the Royal Society A: Mathematical, Physical and Engineering Sciences*, 243(865):251–288, 1951.

G. Ronca and G. Allegra. An approach to rubber elasticity with internal constraints. *The Journal of Chemical Physics*, 63(11):4990–4997, dec 1975.

P. L. Rosendahl and P. Weißgraeber. Modeling snow slab avalanches caused by weak-layer failure – Part 1: Slabs on compliant and collapsible weak layers. *The Cryosphere*, 14(1):115–130, 2020a.

P. L. Rosendahl and P. Weißgraeber. Modeling snow slab avalanches caused by weak-layer failure – Part 2: Coupled mixed-mode criterion for skier-triggered anticracks. *The Cryosphere*, 14(1): 131–145, 2020b.

P. L. Rosendahl, P. Weißgraeber, N. Stein, and W. Becker. A numerical finite fracture mechanics approach on asymmetric cracks in open-hole plates. *Procedia Structural Integrity*, 2:1991–1998, 2016a.

P. L. Rosendahl, P. Weißgraeber, N. Stein, and W. Becker. Assessment of asymmetric crack initiation in open-hole plates using a coupled stress and energy criterion. *Proceedings in Applied Mathematics and Mechanics (PAMM)*, 16(1):165–166, 2016b.

P. L. Rosendahl, Y. Staudt, C. Odenbreit, J. Schneider, and W. Becker. Silicone selants: A finite fracture mechanics model for nonlinear materials. In *14th International Conference on Fracture*, Rhodes, Greece, 2017a.

P. L. Rosendahl, N. Stein, and W. Becker. Stress solutions for joints with nonlinear adhesives. *Proceedings in Applied Mathematics and Mechanics (PAMM)*, 17(1):341–342, 2017b.

P. L. Rosendahl, N. Stein, and W. Becker. A general stress analysis and failure model for ductile adhesive joints. In *4th International Conference on Structural Adhesive Bonding*, page 28, Porto, Portugal, 2017c.

P. L. Rosendahl, P. Weißgraeber, N. Stein, and W. Becker. Asymmetric crack onset at open-holes under tensile and in-plane bending loading. *International Journal of Solids and Structures*, 113-114:10–23, 2017d.

P. L. Rosendahl, M. Drass, J. Schneider, and W. Becker. Crack nucleation in hyperelastic adhesive bonds. *ce/papers*, 2(5-6):409–425, 2018.

P. L. Rosendahl, M. Drass, J. Felger, J. Schneider, and W. Becker. Equivalent strain failure criterion for multiaxially loaded incompressible hyperelastic elastomers. *International Journal of Solids and Structures*, 166:32–46, 2019a.

P. L. Rosendahl, V. A. Kolupaev, and H. Altenbach. Extreme Yield Figures for Universal Strength Criteria. In H. Altenbach and A. Öchsner, editors, *State of the art and future trends in material modeling*, chapter 12, pages 259–324. Springer, Berlin, 1st edition, 2019b.

P. L. Rosendahl, Y. Staudt, C. Odenbreit, J. Schneider, and W. Becker. Measuring mode I fracture properties of thick-layered structural silicone sealants. *International Journal of Adhesion and Adhesives*, 91:64–71, 2019c.

P. L. Rosendahl, Y. Staudt, A. P. Schneider, J. Schneider, and W. Becker. Nonlinear elastic finite fracture mechanics: Modeling mixed-mode crack nucleation in structural glazing silicone sealants. *Materials & Design*, 182:108057, 2019d.

P. L. Rosendahl, Y. Staudt, A. P. Schneider, J. Schneider, and W. Becker. Hyperelastic adhesive joints: from crack nucleation to ultimate failure. In T. Gleim and S. Lange, editors, *Proceedings of the 8th GACM Colloquium on Computational Mechanics, Kassel, Germany*, pages 363–366. Kassel University Press, 2019e.

P. L. Rosendahl, N. Stein, A. P. Schneider, and W. Becker. A general stress analysis and failure model for hyperelastic adhesive composite joints. *Composite Structures*, (under review), 2020.

E. F. Rybicki and M. F. Kanninen. A finite element calculation of stress intensity factors by a modified crack closure integral. *Engineering Fracture Mechanics*, 9(4):931–938, 1977.

M. Santarsiero, C. Louter, and A. Nussbaumer. A novel triaxial failure model for adhesive connections in structural glass applications. *Engineering Structures*, 166:195–211, 2018.

A. Sapora and P. Cornetti. Crack onset and propagation stability from a circular hole under biaxial loading. *International Journal of Fracture*, 214(1):97–104, 2018.

A. Sapora, P. Cornetti, A. Carpinteri, and D. Firrao. An improved Finite Fracture Mechanics approach to blunt V-notch brittle fracture mechanics: Experimental verification on ceramic, metallic, and plastic materials. *Theoretical and Applied Fracture Mechanics*, 78:20–24, 2015.

A. Sapora, P. Cornetti, A. Campagnolo, and G. Meneghetti. Fatigue crack onset by Finite Fracture Mechanics. *Procedia Structural Integrity*, 18:501–506, 2019.

M. Sasso, G. Palmieri, G. Chiappini, and D. Amodio. Characterization of hyperelastic rubber-like materials by biaxial and uniaxial stretching tests based on optical methods. *Polymer Testing*, 27 (8):995–1004, 2008.

C. Sator. *Asymptotische Nahfeldanalysen ebener Multi-Materialverbindungsstellen mit der Methode komplexer Potentiale*. Dissertation, Technische Universität Darmstadt, Studienbereich Mechanik, 2010.

C. Sator and W. Becker. Closed-form solutions for stress singularities at plane bi- and trimaterial junctions. *Archive of Applied Mechanics*, 82(5):643–658, 2012.

M. Sayir. Zur Fließbedingung der Plastizitätstheorie. *Ingenieur-Archiv*, 39(6):414–432, 1970.

M. Sayir and H. Ziegler. Der Verträglichkeitssatz der Plastizitätstheorie und seine Anwendung auf räumlich unstetige Felder. *Zeitschrift für angewandte Mathematik und Physik*, 20(1):78–93, 1969.

L.-M. Schänzel, H. Dal, and C. Miehe. Phase field modeling of fracture in rubbery polymers. *Constitutive Models for Rubber VIII*, 31(1975):335, 2013.

C. Schmandt and S. Marzi. Effect of crack opening velocity and adhesive layer thickness on the fracture behaviour of hyperelastic adhesive joints subjected to mode I loading. *International Journal of Adhesion and Adhesives*, 83:9–14, 2018a.

C. Schmandt and S. Marzi. Effect of crack opening velocity on fracture behavior of hyperelastic semi-structural adhesive joints subjected to mode I loading. *Procedia Structural Integrity*, 13: 799–805, 2018b.

E. Schmid and W. Boas. *Kristallplastizität*. Springer, Berlin, Heidelberg, 1st edition, 1935.

D. J. Seibert and N. Schöche. Direct Comparison of Some Recent Rubber Elasticity Models. *Rubber Chemistry and Technology*, 73(2):366–384, 2000.

A. P. S. Selvadurai and M. Shi. Fluid pressure loading of a hyperelastic membrane. *International Journal of Non-Linear Mechanics*, 47(2):228–239, 2012.

M. H. B. M. Shariff. Strain Energy Function for Filled and Unfilled Rubberlike Material. *Rubber Chemistry and Technology*, 73(1):1–18, 2000.

M. G. Sharma. Failure of polymeric materials under biaxial stress fields. *Polymer Engineering and Science*, 6(1):30–35, 1966.

M. G. Sharma and C. K. Lim. Experimental investigations on fracture of polymers. *Polymer Engineering and Science*, 5(4):254–262, 1965.

G. C. Sih. Strain-energy-density factor applied to mixed mode crack problems. *International Journal of Fracture*, 10(3):305–321, 1974.

Sika Services AG. *Sealing & Bonding: Joint sealants for building envelope waterproofing*. Brochure, Zurich, Switzerland, 2019a.

Sika Services AG. *Sealing & Bonding: Sika construction adhesives*. Brochure, Zurich, Switzerland, 2019b.

J. C. Simo and R. L. Taylor. Penalty function formulations for incompressible nonlinear elastostatics. *Computer Methods in Applied Mechanics and Engineering*, 35(1):107–118, 1982.

J. C. Simo and R. L. Taylor. Quasi-incompressible finite elasticity in principal stretches. continuum basis and numerical algorithms. *Computer Methods in Applied Mechanics and Engineering*, 85 (3):273–310, 1991.

J. C. Simo, R. L. Taylor, and K. S. Pister. Variational and projection methods for the volume constraint in finite deformation elasto-plasticity. *Computer Methods in Applied Mechanics and Engineering*, 51(1-3):177–208, sep 1985.

S. Sitte, M. J. Brasseur, L. D. Carbary, A. T. Wolf, and S. W. Dean. Preliminary Evaluation of the Mechanical Properties and Durability of Transparent Structural Silicone Adhesive (TSSA) for Point Fixing in Glazing. *Journal of ASTM International*, 8(10):104084, 2011.

T. L. Smith and J. A. Rinde. Ultimate tensile properties of elastomers. V. Rupture in constrained biaxial tensions. *Journal of Polymer Science Part A-2: Polymer Physics*, 7(4):675–685, 1969.

V. V. Sokolovsky. *Theory of plasticity (russ.: Teorija plastichnosti)*. Visshaja Shkola, Moscow, 1969.

B. F. Sørensen. Cohesive law and notch sensitivity of adhesive joints. *Acta Materialia*, 50(5): 1053–1061, 2002.

G. Stamoulis, N. Carrere, J.-Y. Cognard, P. Davies, and C. Badulescu. On the experimental mixed-mode failure of adhesively bonded metallic joints. *International Journal of Adhesion and Adhesives*, 51:148–158, 2014.

G. Stamoulis, N. Carrere, J.-Y. Cognard, P. Davies, and C. Badulescu. Investigating the fracture behavior of adhesively bonded metallic joints using the Arcan fixture. *International Journal of Adhesion and Adhesives*, 66:147–159, 2016.

Y. Staudt. *Proposal of a Failure Criterion of Adhesively Bonded Connections with Silicone*. Dissertation, University of Luxembourg, 2017.

Y. Staudt, J. Schneider, and C. Odenbreit. Investigation of the material behaviour of bonded connections with silicone. In *engineered tranparency. International Conference at glasstec*, Düsseldorf, 2014.

Y. Staudt, C. Odenbreit, and J. Schneider. Failure behaviour of silicone adhesive in bonded connections with simple geometry. *International Journal of Adhesion and Adhesives*, 82:126–138, 2018.

N. Stein, P. Weißgraeber, and W. Becker. A model for brittle failure in adhesive lap joints of arbitrary joint configuration. *Composite Structures*, 133:707–718, 2015.

N. Stein, H. Mardani, and W. Becker. An efficient analysis model for functionally graded adhesive single lap joints. *International Journal of Adhesion and Adhesives*, 70:117–125, 2016a.

N. Stein, P. Weißgraeber, and W. Becker. Brittle failure in adhesive lap joints – a general Finite Fracture Mechanics approach. *Procedia Structural Integrity*, 2:1967–1974, 2016b.

N. Stein, P. Weißgraeber, and W. Becker. Stress solution for functionally graded adhesive joints. *International Journal of Solids and Structures*, 97-98:300–311, 2016c.

N. Stein, J. Felger, and W. Becker. Analytical models for functionally graded adhesive single lap joints: A comparative study. *International Journal of Adhesion and Adhesives*, 76:70–82, 2017a.

N. Stein, P. L. Rosendahl, and W. Becker. Homogenization of mechanical and thermal stresses in functionally graded adhesive joints. *Composites Part B: Engineering*, 111:279–293, 2017b.

N. Stein, P. L. Rosendahl, and W. Becker. Modelling load transfer and mixed-mode fracture of ductile adhesive composite joints. *International Journal of Adhesion and Adhesives*, 82(January): 299–310, 2018.

P. Steinmann, M. Hossain, and G. Possart. Hyperelastic models for rubber-like materials: consistent tangent operators and suitability for Treloar's data. *Archive of Applied Mechanics*, 82(9):1183–1217, 2012.

E. Straube, V. Urban, W. Pyckhout-Hintzen, and D. Richter. SANS Investigations of Topological Constraints and Microscopic Deformations in Rubber-Elastic Networks. *Macromolecules*, 27 (26):7681–7688, 1994.

E. Straube, V. Urban, W. Pyckhout-Hintzen, D. Richter, and C. J. Glinka. Small-Angle Neutron Scattering Investigation of Topological Constraints and Tube Deformation in Networks. *Physical Review Letters*, 74(22):4464–4467, 1995.

Z. Sun, E. T. Ooi, and C. Song. Finite fracture mechanics analysis using the scaled boundary finite element method. *Engineering Fracture Mechanics*, 134:330–353, 2015.

A. Szwed. *Strength Hypotheses and Constitutive Relations of Materials Including Degradation Effects*. Dissertation, Warsaw University of Technology, Faculty of Civil Engineering, 2000.

H. Tada, P. C. Paris, and G. R. Irwin. *The Stress Analysis Of Cracks Handbook*. Wiley, New York, 3rd edition, 2000.

A. Talmon l'Armée. *Analyse interlaminarer Rissentstehung in einschnittigen Überlappungsklebungen zwischen Laminatfügeteilen*. Dissertation, Technische Universität Darmstadt, Studienbereich Mechanik, 2019.

A. Talmon l'Armée, N. Stein, and W. Becker. Bending moment calculation for single lap joints with composite laminate adherends including bending-extensional coupling. *International Journal of Adhesion and Adhesives*, 66:41–52, 2016.

A. Talmon l'Armée, S. Hell, P. L. Rosendahl, J. Felger, and W. Becker. Nonlinear crack opening integral: Mode mixity for finite cracks. *Engineering Fracture Mechanics*, 186:283–299, 2017.

S. C. Tan. Fracture strength of composite laminates with an elliptical opening. *Composites Science and Technology*, 29(2):133–152, 1987.

E. Tanné, T. Li, B. Bourdin, J.-J. Marigo, and C. Maurini. Crack nucleation in variational phase-field models of brittle fracture. *Journal of the Mechanics and Physics of Solids*, 110:80–99, 2018.

D. Taylor. *The theory of critical distances: a new perspective in fracture mechanics*. Elsevier, 2007.

D. Taylor. The theory of critical distances. *Engineering Fracture Mechanics*, 75(7):1696–1705, 2008.

D. Taylor, M. Merlo, R. Pegley, and M. P. Cavatorta. The effect of stress concentrations on the fracture strength of polymethylmethacrylate. *Materials Science and Engineering: A*, 382(1-2): 288–294, 2004.

A. Torabi, S. Etesam, A. Sapora, and P. Cornetti. Size effects on brittle fracture of Brazilian disk samples containing a circular hole. *Engineering Fracture Mechanics*, 186:496–503, 2017.

L. R. G. Treloar. The elasticity of a network of long-chain molecules. I. *Transactions of the Faraday Society*, 39:36–41, 1943a.

L. R. G. Treloar. The elasticity of a network of long-chain molecules. II. *Transactions of the Faraday Society*, 39:241–246, 1943b.

L. R. G. Treloar. Stress-Strain Data for Vulcanized Rubber under Various Types of Deformation. *Rubber Chemistry and Technology*, 17(4):813–825, 1944.

L. R. G. Treloar. The elasticity of a network of long-chain molecules. III. *Transactions of the Faraday Society*, 42:83–94, 1946.

L. R. G. Treloar. The photoelastic properties of short-chain molecular networks. *Transactions of the Faraday Society*, 50:881, 1954.

L. R. G. Treloar and G. Riding. A Non-Gaussian Theory for Rubber in Biaxial Strain. II. Optical Properties. *Proceedings of the Royal Society A: Mathematical, Physical and Engineering Sciences*, 369(1737):281–293, 1979.

H. E. Tresca. Mémoire sur l'écoulement des corps solids. *Mémoires Presentés par Divers Savants*, 18:733–799, 1868.

C. Truesdell and W. Noll. *The Non-Linear Field Theories of Mechanics*. Springer, Berlin, Heidelberg, 3rd edition, 2004.

M. Y. Tsai, D. W. Oplinger, and J. Morton. Improved theoretical solutions for adhesive lap joints. *International Journal of Solids and Structures*, 35(12):1163–1185, 1998.

N. W. Tschoegl. Failure surfaces in principal stress space. *Journal of Polymer Science Part C: Polymer Symposia*, 32(1):239–267, 1971.

K. C. Valanis and R. F. Landel. The Strain-Energy Function of a Hyperelastic Material in Terms of the Extension Ratios. *Journal of Applied Physics*, 38(7):2997–3002, 1967.

O. Volkersen. Die Nietkraftverteilung in zugbeanspruchten Nietverbindungen mit konstanten Laschenquerschnitten. *Luftfahrtforschung*, 15(1/2):41–47, 1938.

K. Y. Volokh. On modeling failure of rubber-like materials. *Mechanics Research Communications*, 37(8):684–689, 2010.

R. von Mises. Mechanik der festen Körper im plastisch-deformablen Zustand. *Nachrichten von der Gesellschaft der Wissenschaften zu Göttingen, Mathematisch-Physikalische Klasse*, 20:582–592, 1913.

M. E. Waddoups, J. R. Eisenmann, and B. E. Kaminski. Macroscopic Fracture Mechanics of Advanced Composite Materials. *Journal of Composite Materials*, 5(4):446–454, 1971.

A. S. D. Wang and F. W. Crossman. Initiation and Growth of Transverse Cracks and Edge Delamination in Composite Laminates Part 1. An Energy Method. *Journal of Composite Materials*, 14 (1):71–87, 1980.

M. C. Wang and E. Guth. Statistical Theory of Networks of Non-Gaussian Flexible Chains. *The Journal of Chemical Physics*, 20(7):1144–1157, 1952.

Z.-Y. Wang, Y. Shi, Y. Wu, Q. Wang, and S. Luo. Shear behaviour of structural silicone adhesively bonded steel-glass orthogonal lap joints. *Journal of Adhesion Science and Technology*, 0(0):1–16, 2018.

P. Weißgraeber. *Neue Ansätze zur Analyse der Lastübertragung und Initiierung finiter Risse in Klebverbindungen*. Dissertation, Technische Universität Darmstadt, Studienbereich Mechanik, 2014.

P. Weißgraeber and W. Becker. Finite Fracture Mechanics model for mixed mode fracture in adhesive joints. *International Journal of Solids and Structures*, 50(14-15):2383–2394, 2013.

P. Weißgraeber, N. Stein, and W. Becker. A general sandwich-type model for adhesive joints with composite adherends. *International Journal of Adhesion and Adhesives*, 55:56–63, 2014.

P. Weißgraeber, J. Felger, D. Geipel, and W. Becker. Cracks at elliptical holes: Stress intensity factor and Finite Fracture Mechanics solution. *European Journal of Mechanics - A/Solids*, 55:192–198, 2015a.

P. Weißgraeber, J. Felger, A. Talmon l'Armée, and W. Becker. Crack initiation in single lap joints: effects of geometrical and material properties. *International Journal of Fracture*, 192(2):155–166, 2015b.

P. Weißgraeber, S. Hell, and W. Becker. Crack nucleation in negative geometries. *Engineering Fracture Mechanics*, 168:93–104, 2016a.

P. Weißgraeber, D. Leguillon, and W. Becker. A review of Finite Fracture Mechanics: crack initiation at singular and non-singular stress raisers. *Archive of Applied Mechanics*, 86(1-2):375–401, 2016b.

H. M. Westergaard. On the resistance of ductile materials to combined stresses in two or three directions perpendicular to one another. *Journal of the Franklin Institute*, 189(5):627–640, 1920.

J. M. Whitney and R. J. Nuismer. Stress Fracture Criteria for Laminated Composites Containing Stress Concentrations. *Journal of Composite Materials*, 8(3):253–265, 1974.

K. Wieghardt. Über das Spalten und Zerreißen elastischer Körper. *Zeitschrift für Mathematik und Physik*, 55(2):60–103, 1907.

J.-Y. Wu and V. P. Nguyen. A length scale insensitive phase-field damage model for brittle fracture. *Journal of the Mechanics and Physics of Solids*, 119:20–42, 2018.

P. D. Wu and E. van der Giessen. On improved 3-D non-Gaussian network models for rubber elasticity. *Mechanics Research Communications*, 19(5):427–433, 1992.

P. D. Wu and E. van der Giessen. On improved network models for rubber elasticity and their applications to orientation hardening in glassy polymers. *Journal of the Mechanics and Physics of Solids*, 41(3):427–456, 1993.

H. Xiao. An explicit, direct approach to obtaining multiaxial elastic potentials that exactly match data of four benchmark tests for rubbery materials—part 1: incompressible deformations. *Acta Mechanica*, 223(9):2039–2063, 2012.

Y. I. Yagn. New methods of strength prediction. *Vestnik inzhenerov i tekhnikov*, 6(237-244), 1931.

C. Yang and S.-S. Pang. Stress-Strain Analysis of Single-Lap Composite Joints Under Tension. *Journal of Engineering Materials and Technology*, 118(2):247, 1996.

C. Yang, H. Huang, J. S. Tomblin, and W. Sun. Elastic-Plastic Model of Adhesive-Bonded Single-Lap Composite Joints. *Journal of Composite Materials*, 38(4):293–309, 2004.

O. H. Yeoh. Characterization of Elastic Properties of Carbon-Black-Filled Rubber Vulcanizates. *Rubber Chemistry and Technology*, 63(5):792–805, 1990.

O. H. Yeoh and P. D. Fleming. A new attempt to reconcile the statistical and phenomenological theories of rubber elasticity. *Journal of Polymer Science Part B: Polymer Physics*, 35(12):1919–1931, 1997.

F. L. Yerzley. Adhesion of Neoprene to Metal. *Industrial & Engineering Chemistry*, 31(8):950–956, 1939.

Z. Yosibash, E. Priel, and D. Leguillon. A failure criterion for brittle elastic materials under mixed-mode loading. *International Journal of Fracture*, 141(1-2):291–312, 2006.

M.-H. Yu. *Unified Strength Theory and Its Applications*. Springer Berlin Heidelberg, Berlin, Heidelberg, 1st edition, 2004.

M.-H. Yu. *Unified Strength Theory and Its Applications*. Springer, Singapore, 2nd edition, 2018.

X. Zhao, R. D. Adams, and L. F. M. da Silva. A new method for the determination of bending moments in single lap joints. *International Journal of Adhesion and Adhesives*, 30(2):63–71, 2010.

H. Ziegler. *An introduction to thermomechanics*. North-Holland Publishing Company, Amsterdam, 1983.

This document has 483 references.